Downloaded from orbit.dtu.dk on: May 04, 2023

DTU Library

Tribology of a Combined Yaw Bearing and Brake for Wind Turbines

Poulios, Konstantinos

Publication date:
2014

Document Version
Publisher's PDF, also known as Version of record

Link back to DTU Orbit

Citation (APA):
Poulios, K. (2014). *Tribology of a Combined Yaw Bearing and Brake for Wind Turbines*. DTU Mechanical Engineering. DCAMM Special Report No. S159

General rights
Copyright and moral rights for the publications made accessible in the public portal are retained by the authors and/or other copyright owners and it is a condition of accessing publications that users recognise and abide by the legal requirements associated with these rights.

- Users may download and print one copy of any publication from the public portal for the purpose of private study or research.
- You may not further distribute the material or use it for any profit-making activity or commercial gain
- You may freely distribute the URL identifying the publication in the public portal

If you believe that this document breaches copyright please contact us providing details, and we will remove access to the work immediately and investigate your claim.

Tribology of a Combined Yaw Bearing and Brake for Wind Turbines

PhD Thesis

$$(EIv'')'' = q - \rho A \ddot{v}$$

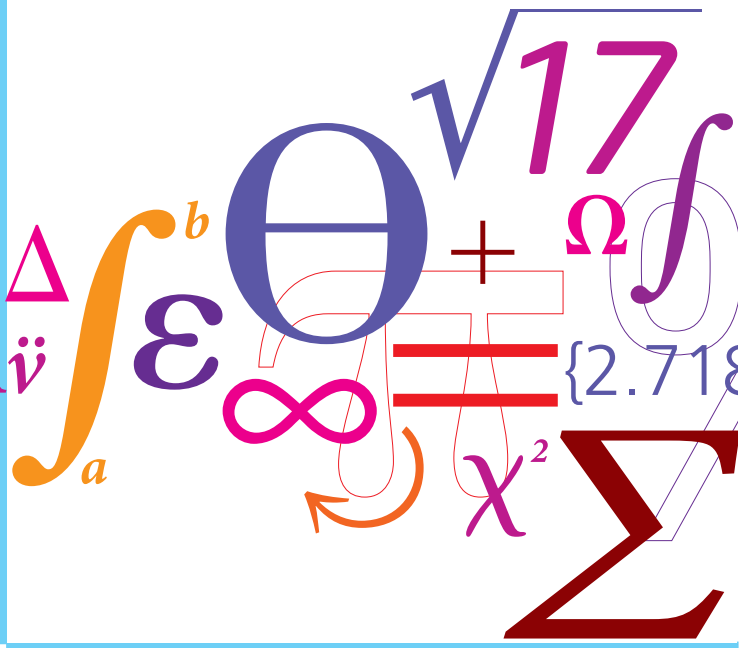

Konstantinos Poulios
DCAMM Special Report No. S159
September 2013

DTU Mechanical Engineering
Department of Mechanical Engineering

Tribology of a Combined Yaw Bearing and Brake for Wind Turbines

Konstantinos Poulios

Technical University of Denmark
Mechanical Engineering Department, Solid Mechanics Section
Building 404, DK-2800 Kongens Lyngby, Denmark

DCAMM Special Report no.: S159
ISBN: 978-87-7475-367-4

Preface

This thesis is submitted in partial fulfillment of the requirements for obtaining the degree of Ph.D. in mechanical engineering at the Technical University of Denmark (DTU). The Ph.D. project was funded by the Danish National Advanced Technology Foundation and DTU Mechanical Engineering, in the framework of the "Yaw Drive Unit" project. It was carried out mainly at the Solid Mechanics section of DTU Mechanical Engineering, in the period between October 2010 and September 2013.

My involvement in this Ph.D. project dealing with tribological aspects of a combined brake and sliding bearing for the yaw system of wind turbines, was motivated by my interest in both fields of tribology and wind energy. In the past three years, I had the opportunity not only to deal with exciting experimental and numerical modeling assignments, but also to follow the development of the corresponding real application by our industry partners.

I consider that many persons have contributed in making the period of this Ph.D. project flow as smooth as possible. To begin with, I would like to thank my supervisor Peder Klit, who was the one that first introduced me to the project and accompanied me till the end, for his confidence in my work and his support in both technical and practical issues. Next, I would like to thank my co-supervisor Kjeld Bruno Pedersen, especially for his careful approach, his attentive attitude and his project management contribution. He has often recognized mistakes, early enough for them to be corrected without unnecessary stress.

I would also like to express my gratitude to the major industry partner within the "Yaw Drive Unit" project, the company Svendborg Brakes. With their openness and interest in the project, they have contributed to the quality of my work and the applicability of the results very significantly. In particular, I direct my thank to Poul

Sejer Nielsen and Peter Hornskov who provided me with all necessary information and technical details about the actually designed system. I am especially grateful to Ole Gunneskov for his deep interest in my work, his guidance and constructive criticism and for his big effort in reviewing the present thesis. Concerning the second industry partner, the company Kirkholm Maskiningeniører A/S, apart from my co-surpervisor and founder of the company, I would also like to thank Jasmus Rust for his technical contribution, especially with respect to wind turbine loads and the modeling work presented in Chapter 2. Very much, I would also like to thank Gustav Winther Svendsen, who has, in the framework of his Master's thesis, conducted with great care many of the tests presented in Chapter 4.

An important part of this thesis relies on surface analysis and characterization. With respect to this point, I would like to thank professor Leonardo De Chiffre from the Manufacturing Engineering section and his group, for carrying out many of the topographic measurements presented in this work, for instructing me in the usage of metrological equipment and for giving valuable advice with regard to metrological aspects. More specifically, I thank Rene Sobiecki, Nicola Drago, Kamran Mohaghegh, Alessandro Godi and Jochen Hiller. Together with the group of professor Leonardo De Chiffre, I would also like to thank Rolf Jensen for his instructions and assistance in the usage of scanning-electron microscopy equipment.

Last, I would like to express my deepest thank to my family. To my wife for her unlimited support and hard work and to my daughter, born during this Ph.D. project, for being my greatest inspiration and motivation for bringing this project forward.

Lyngby, 30 September 2013

Konstantinos Poulios

Summary (English)

A common goal among many countries worldwide is to increase the share of renewable energy in the overall energy supply. As response to such an aspiration, wind energy is becoming more and more cost effective through improved technology and increased size of wind turbines. One of the subsystems that are affected by the tendency for building larger units, is the yaw system of horizontal axis wind turbines.

State of the art wind turbine yaw systems consist of either a large roller element bearing or a corresponding segmented sliding bearing that connects the wind turbine nacelle and tower. An additional disc brake is typically included as an independent system. However, the increasing size of wind turbines makes roller element bearings an economically costly option. Moreover, the additional brake system increases complexity and consequently adds further production and maintenance costs. One of the innovations aiming at reducing complexity in the yaw system consists in combining a segmented sliding bearing and a brake into a single system.

This thesis studies the tribological implications of such a hybrid sliding bearing and brake for the yaw system of wind turbines. Based to a large extent on experimental testing, it aims at providing designers with friction coefficient and wear rate values for different material candidates, to serve as a basis for appropriate material selection and proper dimensioning of the system. Moreover, the experimentally studied cases are put into a theoretical framework by identifying known friction and wear mechanisms, supported by topography measurements and micrographs. Finally, a numerical model for contact between rough surfaces was developed and used for studying friction phenomena in a more quantitative manner.

Summary (Danish)

Mange lande har som mål at forøge andelen af vedvarende energi i deres energiforsyning. For at imødekomme dette behov arbejder vindmøllebranchen på at reducere deres omkostningsniveau gennem udvikling af ny teknologi og på at øge størrelsen af vindmøllene. Et af de delsystemer i en vindmølle, som bliver påvirket af at møllerne bliver større, er krøjemekanismen. Denne mekanisme sikrer krøjning for en horisontalt akslet vindmølle.

De nyeste krøjesystemer til vindmøller består af enten store rullelejer eller segmentopbyggede glidelejer. Begge forbinder vindmøllens nacelle med tårnet. Yderligere er der ofte i vindmøllerne monteret en skivebremse som er uafhængig af den øvrige mekanik. Som følge af at vindmøllene bliver stadig større bliver løsningen med rullelejer mere og mere uøkonomisk. Desuden bliver det uafhængige skivebremsesystem mere og mere komplekst i sin opbygning jo større møllen bliver, og som følge heraf dyrere at fremstille og vedligeholde. Et af formålene med dette projekt er at kombinere et segmentopbygget glideleje med en bremsefunktion, således at kompleksiteten af det samlede krøjesystem reduceres.

Denne afhandling beskæftiger sig med de smøringsmekaniske problemstillinger for en sådan hybridkonstruktion mellem en vindmølles bremse- og krøjemekanisme. På grundlag af omfattende eksperimentelle undersøgelser giver afhandlingen konstruktionsingeniørerne viden om friktionskoefficienter og slidrater på kandiderende leje- og bremsematerialer. Afhandlingen kan således fungere som et referenceværk i forbindelse med korrekt dimensionering og hensigtsmæssigt materialevalgfor krøjesystemet. Desuden er de eksperimentelle resultater sammenlignet med kendte teoretiske modeller for slid og friktion. Dette understøttes yderligere af topografiske målinger og mikrografer. Slutteligt er en numerisk model af kontakten mellem ru overflader udviklet og brugt til kvantitativt at studere friktionsfænomener.

Nomenclature

α	Pressure dependence coefficient for the interfacial shear strength
α_v	Negative relative slope of the friction coefficient with respect to the sliding speed
$\bar{A}$	Real contact area ratio
δh	Wear displacement
ϵ	Strain tensor
Γ_C	Contact boundary
Γ_D	Dirichlet boundary
Γ_N	Neumann boundary
$\mathcal{A}$	Elasticity tensor
μ_0	Friction coefficient at reference sliding speed
μ_k	Kinetic/dynamic coefficient of friction
μ_L	Representative friction coefficient for the lower brake/sliding pads
μ_R	Representative friction coefficient for the radial sliding pads
μ_s	Static coefficient of friction
μ_U	Representative friction coefficient for the upper brake/sliding pads
ν	Poisson's ratio

ψ	Plasticity index
σ	Stress value or stress tensor
σ_n	Normal stress component
σ_p	Standard deviation of th asperity peak heights distribution
σ_{yc}	Compressive strength
σ_{yt}	Tensile strength
τ	Interfacial shear strength
τ_0	Initial (pressure independent) interfacial shear strength
τ_{lim}	Upper limit of interfacial shear strength
A_L	Apparent contact area of the lower brake/sliding pad
A_p	Nominal contact area of a pin specimen
A_R	Apparent contact area of the radial sliding pad
A_U	Apparent contact area of the upper brake/sliding pad
C_{dw}	Coefficient of sensitivity between normal force and the dead weight position in the pin-on-disc test-rig
E	Young's modulus
E'	Effective elasticity modulus (also known as plane stress modulus)
f	Volume force field
F_C	Clamping force of a brake caliper
F_f	Friction force
F_n	Normal force
F_w	Weight force applied to nacelle bottom interface
F_x	Yaw system thrust force with respect to the nacelle reference system
F_y	Yaw system lateral force with respect to the nacelle reference system
F_z	Yaw system vertical force with respect to the nacelle reference system
F_{FT}	Force transducer measured force
F_{n0}	Initial normal force

$F_{R,i}$	Radial force exerted by the flange to the i-th segment
$F_{r_{x,y,z}}$	Force components applied to nacelle rotor-side interface with respect to a local system
$F_{V,i}$	Vertical force exerted by the flange to the i-th segment
g	Gap between the proximity sensor and the moving plate of the pin-on-plate test-rig
g_0	Gap between the proximity sensor and the moving plate of the pin-on-plate test-rig at a reference time point
g_N	Gap in the surface normal direction
H	Ball indentation hardness
K	Archard's wear coefficient
k	Specific wear rate
L_a	Length of arm for measuring the reaction torque on the pin-on-disc test-rig motor
m	Mass
M_b	Yaw braking torque
M_x	Yaw system roll moment with respect to the nacelle reference system
M_y	Yaw system tilt moment with respect to the nacelle reference system
M_z	Yaw system yaw moment with respect to the nacelle reference system
M_{fB}	Friction torque in the pin-on-disc main shaft bearings
n	Surface normal vector
p	Contact pressure
$P_{L,i}$	Apparent contact pressure on the lower brake/sliding pad of the i-th segment
$P_{R,i}$	Apparent contact pressure on the radial sliding pad of the i-th segment
$P_{U,i}$	Apparent contact pressure on the upper brake/sliding pad of the i-th segment
R_p	Asperity peak curvature radius
r_p	Pin-on-disc testing track radius
R_{mean}	Mean radius of the yaw flange track corresponding to the upper and lower brake/sliding pads

R_{min}	Inner radius of the yaw flange
Ra	Arithmetic average roughness
s	Covered sliding distance
u	Deformation field
v	Sliding speed
v_0	Reference sliding speed
W_h	Wear height
w_h	Wear rate
W_V	Wear volume
w_V	Volumetric wear rate
x_p	Pin position along the loading arm of the pin-on-disc test-rig
x_r, z_r	Coordinates of the nacelle rotor-side interface center
x_w	Coordinate corresponding to the gravity center of the weight applied to nacelle bottom interface
x_{dw}	Dead weight position along the loading arm of the pin-on-disc test-rig

Contents

Chapter 1

Introduction

1.1 Problem definition

The yaw system of horizontal axis wind turbines fulfills three functions. It connects the nacelle and the tower, it drives the nacelle-rotor compound to a new orientation with respect to the tower when it is necessary and it prevents any relative rotation, acting as a brake, otherwise. Traditional yaw system designs, like the one shown in Figure 1.1, incorporate a bearing, a driving mechanism and a brake as independent sub-systems. The bearing can either be a large roller element bearing or a segmented sliding bearing, while the driving mechanism consists of a number of motors engaging corresponding pinion gears against a large ring gear. Normally, the driving motors are mounted on the nacelle and the gear teething is located at the exterior of the tower top, although other configurations are also possible. The brake functionality is provided partially by the driving mechanism but it is also assisted by a separate disk brake of dimension comparable to the wind turbine tower diameter.

Figure 1.2 shows a novel yaw system architecture that consists of a segmented sliding bearing with integrated hydraulic pistons that can apply a clamping force so that no additional disk brake is necessary. Each segment of the system is mounted on the nacelle and it is driven against a steel flange connected to the tower. Three surfaces of the segment come into contact with the upper, lower and inner lateral surfaces of the flange. An essential part of designing the system segments is the choice of appropriate

friction materials for these three interfaces, so that the system can provide the desired braking torque while maintaining an acceptable lifetime.

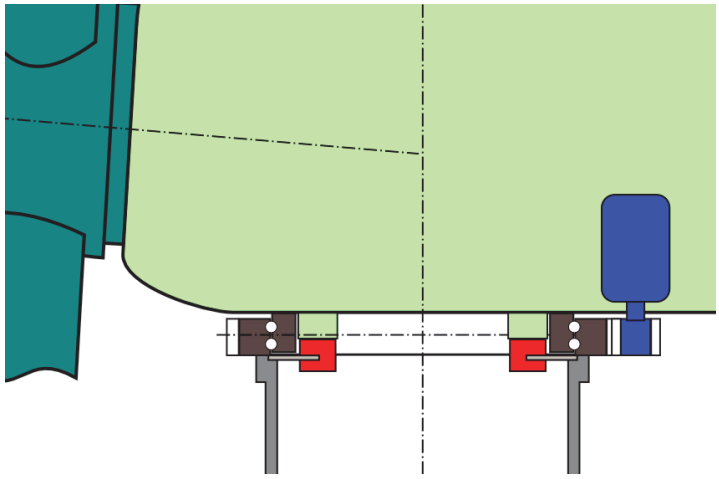

Figure 1.1: Traditional yaw system architecture

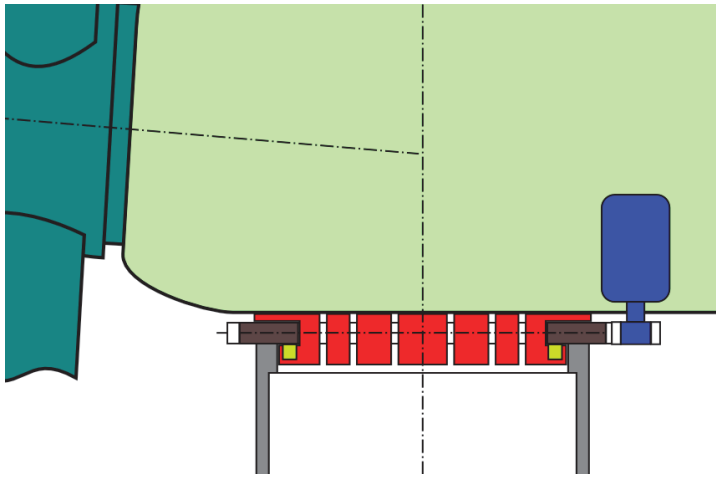

Figure 1.2: Novel yaw system architecture

Depending on specified, applied load, required friction force and tolerated amount of total wear, it is possible to choose three independent friction materials to run against the three above mentioned flange surfaces. It is even possible for a single surface of the flange to run against more than one friction material, if the contact surfaces of the system segments are split, for example, into a sliding and a braking area. Using the upper flange surface as an example, Figure 1.3 presents the possibilities of a single friction material, two friction materials running against independent tracks

of the flange surface and two friction materials running on a common track. The latter case, with possible interactions between neighbor friction materials through a common counter surface, can be relevant also for some practical applications, however it will not be considered in the present work.

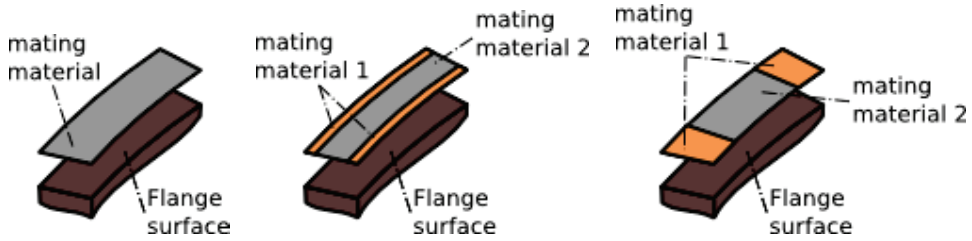

Figure 1.3: Different possibilities of mating friction materials with a flange surface

The present thesis studies, from a tribological viewpoint, the behavior of different friction material candidates, running against a predefined counter surface, under conditions that are relevant to the wind turbine yaw system. It includes experimental testing which aims at providing designers with friction coefficient and wear rate values that will serve as basis for appropriate material selection and dimensioning of the yaw system. Moreover, understanding the mechanisms behind the observed friction and wear in a given tribosystem, is crucial for doing further optimizations as well as for evaluating the sensitivity to changes in the operational or environmental conditions. In order to contribute to a better understanding of the experimentally studied tribosystems, the present thesis employees examination of all test specimen surfaces after testing and numerical modeling of the contact between rough surfaces.

1.2 State of the art

This section summarizes the state of the art with respect to friction materials, tribological testing as well as understanding and modeling the physical phenomena studied in the present thesis. Although the exact definition of the tribopair corresponding to the considered real life application depends on the final design, it is necessary to assume some of its characteristics a priori, in order to limit the relevant literature. Based on the system description provided in the previous section, the basic concept shown in Figure 1.2 and a typically very low yawing speed, it is reasonable to assume a conformal contact, reciprocating operation under either dry or boundary lubrication conditions. Hence, the below discussed literature references are selected under consideration of these characteristics.

Automotive brakes, even if their operational conditions are significantly different to the wind turbine yaw system, represent a very extensively studied case of brake system

with contact between conformal surfaces. A detailed overview of the composition of typical automotive brake pad materials is provided in [1] and [2], whereas references [3] and [4] describe the corresponding friction mechanisms and formation of transfer film layers.

Limited slip clutches is another application from the automotive industry that show significant similarity to the tribological conditions considered in the present work. This kind of clutches normally operate under higher contact pressures and lower sliding speeds than normal transmission clutches and they may also undergo bidirectional sliding. Actually, the operational data reported with respect to wet clutches in [5] partially overlap the operational conditions that will be considered in this work.

Apart from friction applications like brakes and clutches, relevant information for the considered hybrid bearing and brake system can be found in the literature on sliding bearing materials. Textbook [6] is a classical work that provides a very detailed overview on sliding bearings. Among other, it analyses the use of sintered and polymer materials in sliding bearing applications. Of special interest for the present work is the category of polymer sliding bearings, also summarized in [7].

Independent of the kind of materials to be considered, a very fundamental discipline in tribology and important part of this work is friction and wear testing. Textbooks [8], [9], [10] and [11] are some of the most recognized modern resources with respect to tribological testing. In total, apart from listing possible tribological problems that can be studied experimentally, they also provide an overview of the corresponding testing equipment that can be used for carrying out the test itself as well as for examining the contact surfaces and wear particles independently. Moreover, they provide information and recommendations on the testing procedure as well as about the interpretation and presentation of results.

Representative values of friction coefficient and wear rate for different material combinations are available in references like [12], [13] and [14] (vol. 18). However, the vast majority of friction and wear data that can be found in literature, refers to unidirectional sliding and to speeds considerably higher than expected in a wind turbine yaw system. Only few sources report on friction and wear rate testing under reciprocating sliding at very low sliding speeds, e.g. [15], [16] and [17].

A further step beyond experimental quantification of the friction and wear that are observed in the macroscopic scale, consists in explaining these phenomena through mechanisms defined in the microscopic or atomic scale.

Since the classical works of Bowden and Tabor [18], Archard [19] and Greenwood and Williamson [20], who tried to explain dry friction in the microscopic scale, a lot of research has been conducted in this area providing new or improved explanations for the source of friction in the microscopic or atomic scale. A summary and evaluation of

the most accepted among these theories can be found in general tribology textbooks, like [21] (chap. 5), [14] (vol. 18, chap. "Basic Theory of Solid Friction") and [22] (chap. 10). Despite many years of relevant research, most tribologists will agree that the very nature of dry friction is still an open question. In particular, it is still very difficult to determine the dominant friction mechanisms for a given real life contact pair and specify the extent of their relative contributions to the total friction in a more quantitative manner.

Similar to friction, the phenomenon of wear observed in the macroscopic scale can only be explained by considering the contact in the microscopic scale. The aforementioned textbooks [21], [14] (vol. 18) and [22] also dedicate relevant chapters to present the most established wear mechanisms that can be found in published research of the past years. Reference [23] contains a quite extensive overview of the most important efforts for expressing the assumed wear mechanism through simple mathematical expressions.

In an effort to study the assumed friction and wear mechanisms in a rather quantitative manner, an important amount of research work has focused on creating numerical models for simulating the contact between rough surfaces at microscopic level. One category of such models builds upon the pioneering works of Bowden and Tabor [18], Archard [19] and Greenwood and Williamson [20]. A different approach based on a fractal description of the contact surfaces is presented in reference [24] and other relevant publications, while reference [25] introduced another novel approach for calculating the real contact area between conformal rough surfaces.

With the increasing computational power that has become available in recent years, numerical models for simulating the contact between deterministically described surface topographies have been developed. The most efficient ones rely on half space elasticity equations, like for instance, the Fast-Fourier-Transformation (FFT) based implementation described in reference [26]. Finite-element modeling is a less efficient but more generic approach that is used in many works that either study the contact between single asperities or between representative surface topography samples. Some indicative publications with respect to finite-element based models for dry contact can be found in references [27], [28] and [29].

Most of the aforementioned models refer to the microscopic scale. However, there is a relatively recent trend to extend the field of simulations also to the atomic scale by implementing corresponding numerical models, like e.g. molecular dynamics models. Reference [30] provides a very comprehensive literature overview on the most important models at both microscopic and atomic level. Despite the very promising advancements in simulation in the atomic scale, a major disadvantage of such simulations is their limitation to extremely low sliding speeds. In the present work, the effort put into numerical modeling is focused on contact phenomena in the microscopic scale.

1.3 Structure of the thesis

The chapters of the present thesis are organized in such manner that more practical aspects and larger size scales are treated earlier, while more theoretical aspects along with smaller size scales come later. However, this is just a general rule which is subject to several exceptions throughout the entire thesis.

More specifically, the second chapter discusses the loads and operational conditions that the overall wind turbine and its yaw system are subjected to. External global loads and internal loads per yaw system segment are defined and a parametric finite-element model for the entire yaw system is presented as a tool for calculating the load distribution among the system segments.

In the third chapter, general information about possible friction materials and lubricants is given. The chemical composition and structural properties of the most important constituents are outlined along with the relevant literature sources. Moreover, the terminology and the conventions that are used in this work for the classification of the investigated materials, are introduced.

Both chapters four and five present experimental results from a purely phenomenological viewpoint with the fourth chapter being specifically dedicated to coefficient of friction testing on a pin-on-disc test-rig. The testing procedure is described in detail and results from dry and lubricated tests are presented. In particular, the evolution of the friction coefficient during the running-in phase and the impact of the nominal contact pressure on the steady-state friction are commented. Break-away friction testing results for dry running conditions are also included.

Wear testing on a pin-on-plate test-rig is the subject of the fifth chapter. Details about the test-rig and the testing procedure are presented along with wear measurements for a selected group of materials. A study about the impact of the contact pressure on the observed wear rate is also included. Finally, the friction level recorded as part of the wear testing is presented and compared with the corresponding results from the previous chapter.

The sixth chapter explains how the presented experimental data can be utilized in practical calculations of the braking torque and the wear height as part of the design and dimensioning procedure. It also provides information about mechanisms of friction-induced noise and how break-away friction tests presented in the fourth chapter, can be taken into account in practical designs.

The seventh chapter describes friction and wear mechanisms that correspond to selected cases from the testing results presented in chapters four and five. The assumed

friction and wear mechanisms are supported by optical microscope and scanning-electron-microscope (SEM) pictures.

The fundamentals of contact between two nominally flat but rough surfaces are presented in chapter eight along with a corresponding finite-element model, to be referred as a micro-contact model. The key role of the real area of contact is explained and the different mechanisms contributing to the friction force are presented through simulation examples.

The last chapter summarizes the most important conclusions of this thesis and proposes tasks for future work.

Chapter 2

Loads and operational conditions

The three main operational parameters affecting friction and wear of a given tribological system are the contact pressure, the sliding velocity and the sliding distance. In order to estimate these quantities in a hybrid yaw bearing and brake, the overall loading and operation of the system has to be considered along with the distribution of loads within the system. In the next sections, general information on the operation of the yaw system is provided, an estimation of the sliding speed and distance is presented, the major loads are described and a finite-element model for calculating the load distribution among the yaw system segments is presented.

2.1 Operational conditions

Ideally the rotor of a horizontal axis wind turbine should always be perpendicular to the wind direction. In practice however, there can be small or bigger deviations from this ideal situation which are referred to as yaw error or yaw misalignment.

Depending on the installation site, the wind direction can change less or more often. Anemometers that are normally installed on top of the nacelle determine the wind direction and provide this information to the control system responsible for deciding

if orientation of the turbine should be changed at this time to minimize yaw error for optimal power production. There is a trade off between power losses due to periods of misaligned operation and energy spent in activating the yaw motors as well as a reduced life time of yaw system components as well as an increased accumulated sliding distance.

In general, modern wind turbine control systems will typically evaluate all monitored data in intervals of ten minutes, which is a basic time interval according to [31]. It is quite safe to consider this interval as a low limit of how often the yaw system can be activated. In the extreme case of a very sensitive control system that would activate the yaw system every ten minutes for correcting even the slightest yaw misalignment, approximately one million activations would happen during a calculated lifetime of 20 years, without accounting for any standstill periods. In practice the total number of activations depends on the installation site and the control strategy in terms of maximum allowable yaw error, but it should be expected to be one order of magnitude lower than this theoretical maximum.

Another aspect concerns the distance run in every activation of the yaw system. It can be expected that the more sensitive to changes of the wind direction the control system is, the smaller the necessary corrections and the shorter the corresponding sliding distances will be. On the other side, a more tolerant control system will activate the system less often but will have to perform on average larger corrections. In practice, it is not required to maintain an average yaw error below $3°$, while for less sensitive control strategies values of up to $15°$ are not very uncommon, [31]. Consequently, one can assume that yaw corrections will be mainly between $3°$ and $15°$. Using a 3 m in diameter yaw system as an example, the corresponding sliding distance would be between 80 mm and 400 mm.

However, unidirectional rotation of the nacelle with respect to the tower is not unlimited. Due to the cabling that connects the nacelle to the ground, its rotation is limited to two or three revolutions in each direction. When this limit is reached, the cables need to be unwound by activating an unwinding procedure in the control system to bring the nacelle to its neutral position. For a 3 m in diameter yaw system three revolutions correspond to a sliding distance of approximately 28 m.

Regarding the yawing speed, a typical value for the rotational speed of the nacelle with respect to the tower is $1°$ per second, see e.g. reference [32] (chap. 5). For this rotational speed and a tower diameter of 3 m, the sliding velocity in the yaw system can be estimated equal to 26 mm/s. One practical example of a wind turbine yaw system is given in appendix A of reference [33]. It refers to a system of approximately 1.5 m in diameter with a rotational speed of $1.71°$ per second, corresponding to a circumferential speed in the bearing equal to 22 mm/s. In the remaining part of the present thesis a value of 20 mm/s will be considered as reference sliding speed for all further considerations.

One characteristic, that is very specific to the wind turbine yaw system, is the need for damping during yawing. As described in the previous chapter, the driving system consists of motors driving the yaw system flange through gears. Impacts in the gear teeth contact, as a combined result of the dynamic loads acting on the wind turbine and the gear backlash may be catastrophic for the gears. For this reason it is common practice to partially activate the yaw brake during yawing. In this situation an increased driving torque is required from the motors, with the benefit of minimizing the effect of dynamic loads and protecting the gears.

2.2 Yaw system loads

Forces in mechanical systems are always distributed. However, for well-defined elements like roller element bearings, a concentrated load consisting of six force and moment components is normally sufficient for assessing strength or lifetime.

In wind turbines, aerodynamic, gravity and inertia loads exerted on rotor and nacelle have to be transferred through the yaw system to the tower. It is common practice to define the overall yaw system load through three force components F_x, F_y and F_z and three moment components M_x, M_y and M_z with respect to the nacelle reference system, illustrated in Figure 2.1. The nacelle reference system is defined in document [34], with its origin at the center of the yaw bearing, its x-axis pointing downwind and its z-axis pointing upward. According to the established wind turbine terminology, the yaw system force components F_x, F_y and F_z are called thrust, lateral and vertical forces respectively and the moment components M_x, M_y and M_z are called, roll, tilt and yaw moments respectively.

For a complex system like a segmented yaw system of a wind turbine, providing the total applied load may not be sufficient for studying the behavior of the system. For instance, in the case that the deformation of the nacelle and the tower have to be taken into account, it is important to also consider the location where loads are introduced.

Figure 2.2 shows the nacelle, yaw system and top tower portion, separated from the rest of a wind turbine. It defines the rotor-side interface of the nacelle and the corresponding loads F_{r_x}, F_{r_y}, F_{r_z}, M_{r_x}, M_{r_y} and M_{r_z} that can be exerted on the nacelle, mainly from the rotor. It also defines the bottom interface of the nacelle, to which the yaw system segments are attached. The weight force F_w contained in the figure may represent the self-weight of the nacelle and the weight of contained components, like gearbox, generator, etc. The center of the rotor-side interface is located at coordinates x_r and z_r with respect to the nacelle reference system, while

the weight force is applied at a horizontal coordinate x_w. Last, the surface denoted as the supporting interface, is between tower top and remainder of the tower.

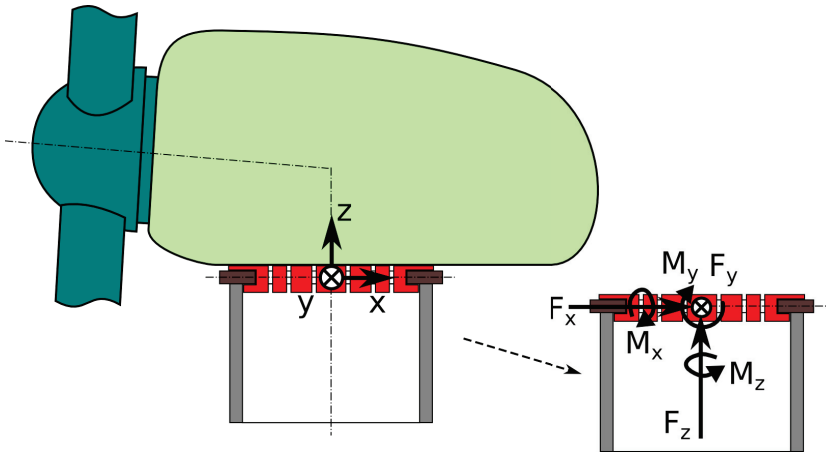

Figure 2.1: Reference coordinate system and yaw system loads

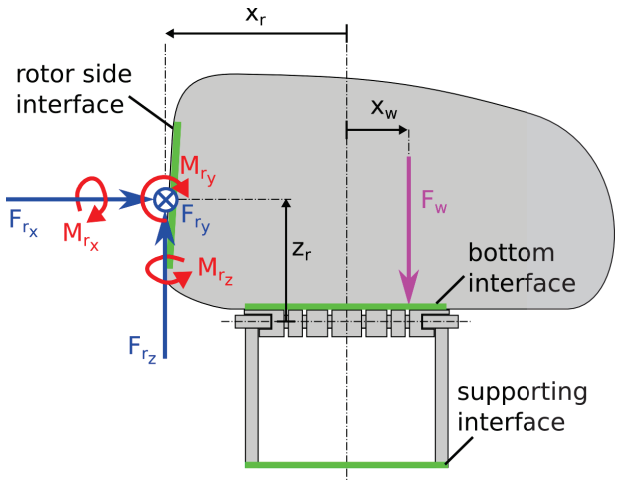

Figure 2.2: Loads carried by the wind turbine yaw system

Given the coordinates of the rotor-side interface center, a concentrated load acting on the interface center, can also be expressed in the nacelle reference system according to the following transformation:

$$\begin{aligned} F_{x,rotor} &= F_{r_x} & M_{x,rotor} &= M_{r_x} - F_{r_y} \cdot z_r \\ F_{y,rotor} &= F_{r_y} & M_{y,rotor} &= M_{r_y} + F_{r_x} \cdot z_r - F_{r_z} \cdot x_r \\ F_{z,rotor} &= F_{r_z} & M_{z,rotor} &= M_{r_z} + F_{r_y} \cdot x_r \end{aligned} \tag{2.1}$$

with x_r being negative in the example illustrated in Figure 2.2.

Given the coordinate x_w of the nacelle center of gravity, also the weight load can be expressed in the nacelle reference system as a force and a moment:

$$\begin{aligned} F_{z,bottom} &= -F_w \\ M_{y,bottom} &= F_w \cdot x_w \end{aligned} \tag{2.2}$$

with the weight F_w considered positive in downward direction.

Finally, the total load carried by the yaw system according to Figure 2.1 can be written as the sum of both loads expressed in the common reference system:

$$\begin{aligned} F_x &= F_{x,rotor} & M_x &= M_{x,rotor} \\ F_y &= F_{y,rotor} & M_y &= M_{y,rotor} + M_{y,bottom} \\ F_z &= F_{z,rotor} + F_{z,bottom} & M_z &= M_{z,rotor} \end{aligned} \tag{2.3}$$

2.3 Load distribution

Apart from determining the overall load transferred through the yaw system by obtaining the corresponding six force and moment components, it is essential to specify how this load is distributed among the different segments of the yaw system. What is relevant for assessing lifetime of the friction materials in each segment is the corresponding contact pressure in the individual sliding interfaces.

The load distribution among the segments, depends not only on the overall load carried by the yaw system, but also on the deformation of the involved components. For this reason, a simplified parametric finite-element model, corresponding to the sub-system shown in Figure 2.2, had to be developed. The model implementation was based on the public domain finite-element library GetFem++ [1] .

Figure 2.3 shows an example of a finite-element mesh corresponding to the whole model and Figure 2.4 shows the geometry and mesh of a single segment in larger detail. Actually, the model consists of five components, the upper end of the wind turbine tower, a transition tube at the end of the tower, the yaw system flange, a variable number of yaw system segments and the nacelle. Required input are the basic component dimensions as well as the number and positions of the segments. Based on this info, all components except the nacelle are meshed automatically with linear hexahedral solid elements. The meshed nacelle geometry has to be imported from an external file that can be generated by appropriate third-party software, like NetGen or ANSYS®.

Continuity between the tower, the transition tube and the flange is enforced through corresponding constraints implemented in the model using the Lagrange multipliers

[1] `http://download.gna.org/getfem/html/homepage/`

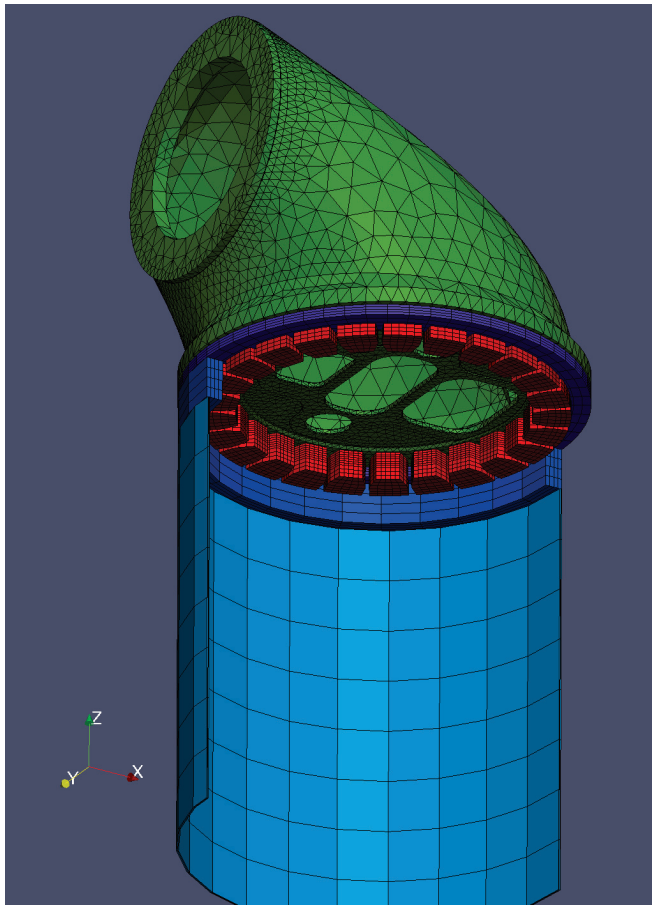

Figure 2.3: Parametric finite-element model of the yaw system

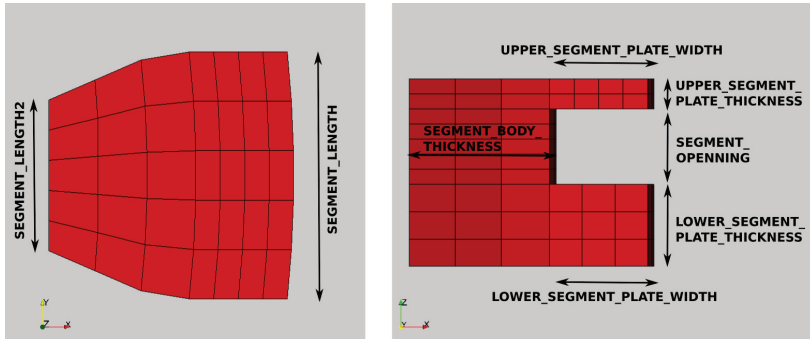

Figure 2.4: Dimensions of the simplified yaw system segment

method in a similar manner like described in reference [35]. The same type of connection is established between the nacelle and each of the yaw system segments. At importing the nacelle mesh, the nacelle bottom interface is detected automatically and the nacelle is aligned to the vertical position of the yaw system segments. The connection between the segments and the flange is modeled as frictionless contact on three faces, the upper, the lower and the radially inner flange surfaces. More details about the mathematical treatment of the frictionless contact condition are provided in Chapter 8.

The modeling of both structural deformation and contact conditions is valid under the small deformations assumption. In particular, the material behavior is modeled as isotropic linearized elasticity. For the sake of simplicity, the model accepts a single Young's modulus E and a single Poisson's ratio ν and associates them with all components. Optionally, a separate Young's modulus value can be specified only for the nacelle. The motivation for providing this option is that the nacelle can often be made of cast iron instead of steel.

With respect to loads, the model expects as input the six components $F_{x,rotor}$, $F_{y,rotor}$, $F_{z,rotor}$, $M_{x,rotor}$, $M_{y,rotor}$ and $M_{z,rotor}$, described in the previous section. These loads are defined in the nacelle reference system according to Figure 2.1. Internally however, the model solves the system of equations (2.1) for calculating the rotor loads F_{r_x}, F_{r_y}, F_{r_z}, M_{r_x}, M_{r_y} and M_{r_z}, defined in the local coordinate system of the rotor-side interface. These loads are then applied uniformly distributed on the rotor-side interface of the nacelle.

The nacelle weight F_w and the coordinate x_w for the nacelle gravity center are optional input parameters for the model. If they are provided, Equation (2.2) is used for calculating $F_{z,bottom}$ and $M_{y,bottom}$ which are introduced as uniformly distributed loads on the nacelle bottom interface.

Applying loads either to the rotor-side interface or the nacelle bottom interface is a convention that intends to approximate reality, while requiring only little information about the system.

In reality, loads are transferred from the rotor to the nacelle either through one large or through two smaller roller element bearings. The exact location of these bearings, certainly has some impact on the deformation of the nacelle. However, without knowing the details of a specific design, a reasonable approximation is to assume that rotor loads act on the area denoted in Figure 2.2 as the rotor-side interface.

Regarding the weight force F_w, the nacelle self-weight is of course uniformly distributed as a gravity force and consequently contributes very little to the overall deformation of the nacelle. The weight of the nacelle content, is applied to certain areas of the nacelle bottom and the exact location of these areas will affect the na-

celle deformation to some extent. However, to avoid restricting the model to a specific design, the safest option is to introduce this load directly on the nacelle bottom interface, where it will affect the deformation of the nacelle only minimally while it will still have a contribution to its static equilibrium.

It should be underlined that the weight F_w does not include the rotor weight, which is actually part of the vertical force component $F_{z,rotor}$ and it also contributes to the tilt moment $M_{y,rotor}$. Moreover, for direct drive wind turbines that include a very heavy generator close to the rotor side, it is completely reasonable not to express this weight as F_w with negative x_w coordinate but to include it in the rotor loads.

Detailed lists of all mandatory and optional input parameters for the model along with additional information can be found in Appendix B.

Figure 2.5 shows the calculated results of an example corresponding to the input data summarized in Table 2.1. Load data in this table are based on a load case from reference [33] that corresponds to a wind speed of 17.9 m/s. The original load data were extended here through a lateral force and a roll moment that correspond to 10% of the provided thrust force and tilt moment respectively. Common material parameters for steel were considered both for the nacelle and the rest of the system. The model output consists of one vertical and one radial force per segment. The data presented in Figure 2.5 graphically, are also available in numerical form in Table 2.2.

The mean contact pressure $P_{R,i}$ at the radial interface between a segment i and the flange can be estimated by dividing the calculated radial force $F_{R,i}$ from Table 2.2 by an approximate surface area A_R of the sliding material attached to the corresponding segment surface.

Since the segments of the yaw system are supposed to incorporate hydraulic pistons for providing braking functionality, the corresponding clamping force needs to be taken into account for estimating the contact pressure at the upper and lower contact interfaces between a segment and the yaw system flange. Utilizing the notation $F_{V,i}$ for the vertical force corresponding to segment i and F_C for the hydraulic clamping force applied on the lower pad, the mean pressure in the upper and lower contact interface can be estimated as follows:

$$P_{U,i} = \frac{\max\left(F_C + F_{V,i}, 0\right)}{A_U}$$
$$P_{L,i} = \frac{\max\left(F_C, -F_{V,i}\right)}{A_L} \tag{2.4}$$

with A_U and A_L representing the areas of the upper and lower segment interfaces that are covered with sliding material.

Table 2.1: Major input data for the calculated example

Tower diameter	1500	mm
Tower thickness	15	mm
Tower height	2500	mm
Transition thickness	100	mm
Transition height	180	mm
Flange width	180	mm
Flange thickness	60	mm
Segment length	200	mm
Segment body thickness	110	mm
Upper segment plate width	80	mm
Lower segment plate width	70	mm
Number of segments	12	-
Thrust force	40.9	kN
Lateral force	4.09	kN
Vertical force	-226	kN
Roll moment	27.3	kNm
Tilt moment	273	kNm

Table 2.2: Calculated loads per yaw system segment

	Segment position	Vertical force [kN]	Radial force [kN]
1	15°	65.4	24.3
2	45°	84.9	0.9
3	75°	41.5	0
4	105°	-13.3	0
5	135°	-33.7	0
6	165°	-53.5	0
7	195°	-50.1	0
8	225°	-25.3	0
9	255°	1.1	0
10	285°	61.7	0
11	315°	89.2	0
12	345°	58.0	16.8

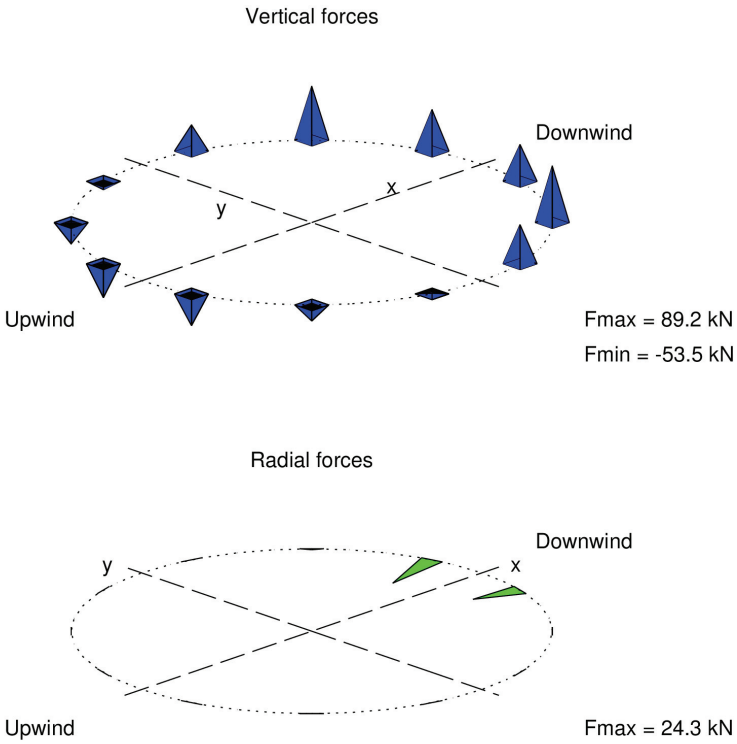

Figure 2.5: Calculated load distribution among yaw system segments

A hydraulic pressure of 160 bar is typical for industrial brake applications. Moreover, it can be assumed that during yawing a lower hydraulic pressure in the order 40 bar will be sufficient for avoiding uncontrolled vibrations within the clearances of the driving system. These pressure levels combined with a piston area corresponding to 50% of the area of the segment lower plate would result in clamping forces of 28 kN and 112 kN during yawing and in parked state respectively. The three segment pads are assumed to cover 70% of the corresponding segment surfaces. Using the rough dimensions of the segments and the flange from Table 2.1 this assumption results to contact areas of A_R=8400 mm^2, A_U=11 200 mm^2 and A_L=9800 mm^2. Based on the so far presented data, one can calculate the corresponding mean pressures per segment interface. Table 2.3 shows the calculated pressures corresponding to the load distribution of Table 2.2.

Table 2.3 gives an impression of the expected pressure levels and variations among the different segments. This example will serve as reference also for further demonstrations later.

Table 2.3: Calculated pressures in each yaw system segment

		F_C=28 kN		F_C=112 kN		
i	Segment position	$P_{U,i}$ [MPa]	$P_{L,i}$ [MPa]	$P_{U,i}$ [MPa]	$P_{L,i}$ [MPa]	$P_{R,i}$ [MPa]
1	15°	8.3	2.9	15.8	11.4	2.9
2	45°	10.1	2.9	17.6	11.4	0.1
3	75°	6.2	2.9	13.7	11.4	0
4	105°	1.3	2.9	8.8	11.4	0
5	135°	0	3.4	7.0	11.4	0
6	165°	0	5.5	5.2	11.4	0
7	195°	0	5.1	5.5	11.4	0
8	225°	0.2	2.9	7.7	11.4	0
9	255°	2.6	2.9	10.1	11.4	0
10	285°	8.0	2.9	15.5	11.4	0
11	315°	10.5	2.9	18.0	11.4	0
12	345°	7.7	2.9	15.2	11.4	2.0

2.4 Load variation

In reality, the load applied to the yaw system is not constant as in the above presented example but a function of time. A representative sample of such a load history can be made available either through simulations or through monitoring of appropriately instrumented wind turbines. However, working with time histories of force and moment components is not practical for assessing ultimate and fatigue strength or wear of specific components of the yaw system. A common practice for presenting or interpreting load histories in wind turbines, consists in considering all load data in intervals of ten minutes. Each such interval is assumed to represent a certain set of wind conditions (average velocity and turbulence level). This convention is used extensively in simulations and is also acknowledged by the relevant standard [31].

Regarding fatigue strength in particular, it is important to account for all possible dynamic amplitudes occurring at all average load levels experienced during the wind turbine lifetime. For this reason, each load time history is analyzed using rainflow counting, so that the dynamic content of the load curve is extracted for the specific average load level, corresponding to the considered time interval. The result of this process, accumulated over all considered ten minutes intervals, is stored in a so called Markov matrix. Each row of a Markov matrix corresponds to an average of the considered load component and each column corresponds to a certain dynamic amplitude value. The matrix value at a given row and column represents the probability that the corresponding average and dynamic amplitude values can be experienced in com-

bination during the whole lifetime. This probability is normally expressed in number of ten minute intervals per 20 years of lifetime.

A Markov matrix can be determined for each load component but also for a stress magnitude at a specific component, if the corresponding time history is available. One further step in the pre-processing of loads for assessing fatigue strength is the extraction of damage equivalent fatigue loads. Such fatigue loads are defined for an assumed slope of the considered material S-N curve and an assumed mean load as described in standard [31]. Neither Markov matrices nor the damage equivalent fatigue loads can capture the correlation between different load components or provide information about the relative phase between them.

Ultimate strength of components in wind turbines is assessed by means of extreme loads. Extreme loads are normally derived from simulated or measured load histories by statistical extrapolation for a certain probability level. By convention, two probability levels are used for defining extreme loads in wind turbines corresponding to one occurrence per year and one occurrence per fifty years respectively.

Extreme loads refer to maximizing or minimizing a specific load component considering an extensive number of load cases. However, not all load components reach their extreme under the same load case. Moreover, there is no general rule determining if the maximum or the minimum of a load component yields to higher stressing of the considered component. Hence, all possible load combinations have to be taken into account. It is common to provide a matrix of extreme loads, where each row contains information about the load case that maximizes or minimizes each of the load components. The different columns of the matrix contain the other load components that occur concurrently to the maximized or minimized load component. Apart from the 12 rows that refer to the maximum and minimum of F_x, F_y, F_z, M_x, M_y, M_z, it is common to have four additional rows corresponding to the maximum and minimum of the F_{xy} and M_{xy} resultant force and moment respectively. Specifying the extreme loads is useful for dimensioning the braking system and for checking the compressive strength of the utilized sliding materials in the yaw system.

Wear in the wind turbine yaw system is expected to occur mainly during yawing time, which corresponds to a relatively small portion of the system lifetime. In parked state, extreme and dynamic loads should not contribute to the observed wear significantly, provided that sufficient clamping pressure is available in order to avoid fretting. The normal pressure which is relevant for wear calculations is determined per time interval through Equation (2.4) for a minimum clamping force, applied during yawing, and average external loads. The dynamic content of the external load is assumed to be considerably lower than the corresponding average load supplemented by the applied clamping force. Moreover, assuming an approximately linear relationship between wear rate and normal load, the impact of dynamic load fluctuations during yawing on the estimated amount of wear should be negligible.

A simplified but relatively accurate way of processing load history data for wear calculations would require the following steps:

- calculate the average of each load component per 10 minute interval
- quantize the calculated averages into a finite number of intervals
- list all experienced load sets along with the corresponding yawing time per reference lifetime
- remove all load sets with zero yawing time

The result of such a process would be a table with six columns corresponding to force and moment components and one column corresponding to yawing time. Often, for practical reasons, only the most important load components are considered. Reference [33] provides such a load table that is presented here in Table 2.4. It includes only the F_x and M_y load components, while the vertical load component is assumed to be constant in all cases with F_z=-226 kN. The yawing time periods and the corresponding sliding distances in the table are based on the time percentages provided in [33], an assumed total yawing time corresponding to 8% of 20 years total lifetime and the reference sliding speed of 20 mm/s. Under these assumptions, the total sliding distance sums up to approximately 1000 km. Hereafter, this value will be considered by convention as a reference sliding distance for any further lifetime considerations. Of course this is a very rough estimation, since the actually experienced sliding distance depends very much on installation site specific conditions.

Table 2.4: Example loads format for assessing wear

Load case	F_x [kN]	M_y [kNm]	Yawing time [h/(20 years)]	Sliding distance [km]
1	30.6	89.3	4500	324
2	53.0	178.4	2250	162
3	57.2	233.7	2109	152
4	52.5	251.3	2812	202
5	40.9	273.2	2109	152
6	36.1	299.9	281	20

Utilizing the parametric finite-element model presented in the previous section and Equation (2.4) it is possible to convert Table 2.4 into an equivalent table of surface pressures per segment. As an example, Table 2.5 shows such data only for segments at 15° and 165° from downwind direction (segments no. 1 and 6 respectively).

Table 2.5: Calculated pressure spectrum for different system segments

Load case	$P_{U,1}$ [MPa]	$P_{L,1}$ [MPa]	$P_{R,1}$ [MPa]	$P_{U,6}$ [MPa]	$P_{L,6}$ [MPa]
1	5.1	2.9	1.8	1.9	2.9
2	6.7	2.9	3.0	0.1	2.9
3	7.6	2.9	3.2	0	4.2
4	7.9	2.9	3.1	0	4.6
5	8.1	2.9	2.1	0	5.3
6	8.5	2.9	1.7	0	6.0

These results show how the pressure in the upper interface of segment 1 and the lower interface of segment 6 increases with increasing load case number due to the larger tilt moment M_y. At the same time the pressure in the upper interface of segment 6 is decreasing and the pressure in the lower interface of segment 1 remains constant, determined exclusively by the clamping force. The pressure in the radial interface of segment 1 depends on the thrust force F_x and consequently reaches its maximum at an intermediate wind speed corresponding to the third load case. Being at the front side of the yaw system, segment 6 is not loaded radially.

Chapter 3

Friction materials and lubricants

A tribological system includes at least the two materials corresponding to the contacting bodies and possibly an additional third body present at their interface acting as a lubricant or friction modifier. This chapter presents some of the possible materials and lubricants that can be used for the considered wind turbine yaw system.

3.1 Steel flange material

As described in Chapter 1, it is very common that the tower top incorporates a steel flange of corresponding diameter serving as one of the contacting surfaces of a yaw sliding bearing. In principle, the material of the flange can either be some structural steel like S355 or some alloy steel. Since the tower top flange often incorporates the gear toothing of the driving system, it is convenient to use alloy steels appropriate for quenching and tempering, like e.g. 42CrMo4 (1.7225) or 34CrNiMo6 (1.6582). These steels in unhardened condition possess a relatively low surface hardness, similar to normal structural steel, [36].

For some of the friction materials with abrasive constituents it is possible that an unhardened flange surface will undergo abrasive wear. However, due to the additional

cost of surface treatments like hardening or coating, the scope of the present work is limited to investigating the combination of different materials with an untreated steel surface.

Another issue related to the yaw system flange material, is the possibility of surface oxidation, especially in harsh environmental conditions typically encountered in offshore applications. Oxidation of the flange surface can be avoided or minimized either by coatings or by the presence of lubricant. Oxidation can also be tolerated under the condition that it will never reach an extent that will affect the long term operation of the system. For instance, the maximum oxidation layer thickness expected after a long standstill of the system can be tolerated if the friction pad material is capable of removing such layer within the first sliding meters after the operation of the yaw system is resumed. In any case, specific testing with respect to this issue has to be conducted, but it is beyond the scope of the present work to study possible implications caused by excessive oxidization of the flange surface.

3.2 Friction materials

Friction materials can be classified in different ways. In the present work, the following classification is considered:

- Molded thermoset compounds
- Thermoplastic materials
- Fiber composites
- Sintered materials
- Elastomer materials
- Ceramic materials

The first four groups are the ones actually represented in the performed testing. More information about the definition and the general properties of these groups is provided in the paragraphs below. Elastomer and ceramic materials are listed here only for the sake of completeness although they were not included in the testing plan. Ceramic materials were excluded mainly because of their brittleness. Elastomer materials weren't included either although they are known to be used in bearings supporting traffic bridges, under similar load conditions to the ones defined in the previous section. In such applications, when considerable sliding is expected elastomer bearings are normally coated with a polytetrafluoroethylene (PTFE) layer, [37]. Once this layer is consumed, the wear process is expected to accelerate rapidly. For a total

sliding distance in the order of 1000 km, the lifetime of the friction pad would be practically limited by the thickness of the PTFE layer.

3.2.1 Molded thermoset compounds

Molded thermoset compounds are based on a thermosetting polymer matrix which acts as a binder for a mixture of organic, metallic or ceramic components that actually determine the friction and wear performance of the final compound. Molded thermoset compounds is the most common type of friction materials for automotive brake and clutch applications. For this reason they are often characterized simply as organic brake pad materials. References [38], [2] and [1] provide a very comprehensive overview of this material group and the following paragraphs only aim at summarizing the most relevant info with respect to the present work.

Thermosetting polymers are produced by an irreversible chemical process consisting of hardening an initially liquid polymer by creating so called cross-link bonds between the polymer molecule chains. This process is called curing and normally requires heat, pressure or radiation to be applied. After curing, thermosets cannot be reshaped anymore by reheating and subsequent cooling. However, the fact that they are initially in liquid form ensures excellent binding performance when they are cured in molded form, enclosing all other components of the final compound.

Some common thermosetting polymers are phenol-formaldehyde, urea-formaldehyde, melamine-formaldehyde, unsaturated polyester and epoxy. Regarding binders for friction materials, phenol-formaldehyde, also called phenolic resin, is the most commonly used thermoset, mostly because of its low cost and its high heat resistance. The toxicity of phenol that is used for its production and possible residues of phenol due to incomplete curing, can be mentioned as the main disadvantage of phenolic resin binders. In theory, due to the low heat generation expected in the yaw system, other types of thermosets might also be considered. However, the molded thermoset compounds tested in the present work are all based on phenolic resins as binding material.

Apart from the binder material, the other components of a molded thermoset compound can be in form of fibers, flakes or grains and they can be categorized as reinforcing fibers, frictional additives and fillers. However, one may find components that can be classified into more than one of these categories at the same time.

Reinforcing fibers

Glass fiber is a very common type of reinforcing fiber in composite materials in general. It typically consists of approximately 60% silica (SiO_2) with the rest comprised

of oxides Al_2O_3, CaO and MgO and possibly also B_2O_3, [14] (vol. 18). Depending on their exact formulation, different variants of glass fibers are commercially available. E-glass and S-glass are two denominations used for the most basic variant and a high strength variant respectively. Typical diameters for glass fibers vary from 5 to 25 µm. Glass fibers are in general brittle, however, the smaller the fiber diameter the higher their flexibility. Because of the amorphous nature of glass, their bulk material behavior is isotropic. Young's modulus for E-glass is around 80 GPa while its tensile strength is approximately 3.5 GPa. For S-glass these values are increased to 90 GPa and 4.5 GPa respectively.

Aramid (aromatic polyamide) fibers is a category of synthetic fibers with their molecular chains, typically $(C_7H_5NO)_n$, highly oriented along the fiber length. Kevlar® variants are the most known commercially available aramid fibers. The stiffness and the tensile strength of aramid fibers vary within a quite wide range depending on the exact variant under consideration. The strongest ones with a tensile strength around 3.5 GPa are comparable to glass fibers and also stiffer than the latter, exhibiting a Young's Modulus of 130 GPa or higher, [39]. A typical diameter for aramid fibers is around 12 µm and they are normally available in form of pulp, either wet or dry. Unlike glass and carbon fibers, aramid fibers exhibit a very low compressive strength, typically one order of magnitude less than their tensile strength. Aramid fibers are often used for friction material composites because they exhibit high wear resistance without being abrasive against steel or cast iron.

Carbon fibers consist of graphite mixed with amorphous carbon. The carbon in graphite is structured in parallel layers of hexagonally arranged atoms, which exhibit high in-plane stiffness and strength. With the graphitic layers in carbon fibers oriented along the fiber length the elasticity modulus of carbon fibers in longitudinal direction can be in the order of 200 GPa or higher and their tensile strength can exceed 3 GPa. Depending on the exact orientation of the graphitic planes with respect to the radial and circumferential direction, carbon fibers may exhibit significantly higher stiffness at the expense of reduced strength. Carbon fibers are not very widespread in composites for friction applications, mainly because of their high price.

Metallic fibers like steel, brass or copper are not uncommon in organic brake pads. Apart from their reinforcing action they also increase the thermal conductivity of the compound. Steel fibers in particular have the disadvantage of rusting and being abrasive for the counter surface, probably preventing the formation of a transfer film. Hence, in cases of low heat generation like the wind turbine yaw system, utilization of steel fibers is a less attractive option.

Ceramic fibers is one more option for molded thermoset compounds and other composites. Two representative groups of ceramic fibers are those based on silicon carbide (SiC) and those based on aluminum oxide (Al_2O_3). The stiffness of ceramic fibers is comparable to high modulus carbon fibers and they can be found in a wide range

of sizes from 1 to 140 µm, with their tensile and compressive strength depending on the fiber diameter. Cost is a major disadvantage of ceramic fibers, limiting their application mostly to high temperature conditions.

Reinforcing fibers, in general, can be found in short-cut form, in form of filament yarn or as a pulp. Short-cut fibers of different lengths are very common in molded thermoset compounds, while fibers in pulp form are often used also. The use of the yarn form will be discussed further in the section about fiber composites, which are considered here as a separate category of friction materials. One important aspect of reinforcing fibers is their adhesion to the binding material. Normally some kind of surface treatment, e.g. etching, is necessary in order to improve adhesion between glass, aramid or carbon fibers and the binder.

Frictional additives

According to reference [1], frictional additives can be divided into abrasives and lubricants. Hard particles like metal oxides and silicates, e.g. SiO_2, $ZrSiO_4$ and Al_2O_3, are typically used as abrasives, contributing to an increased coefficient of friction at the expense of a higher wear on the counter material and a less stable coefficient of friction. Graphite and metal sulphides, e.g. MoS_2, are the most common types of solid lubricants. Their role is to stabilize the coefficient of friction, especially at higher temperatures and reduce the tendency for stick-slip phenomena. One disadvantage of graphite compared to other solid lubricants is its poor bonding with a thermoset matrix.

Fillers

Fillers are used for increasing the volume and heat capacity of brake pads or for reducing the tendency for noise generation. According to reference [1], they can be divided into inorganic and organic types. Typical inorganic fillers are barium sulphate ($BaSO_4$) and calcium carbonate ($CaCO_3$) for increasing heat stability, mica and vermiculite for reducing noise generation. Cashew dust and rubber dust are the most common organic fillers utilized for suppressing noise generation. Reduction of noise is normally at the expense of wear resistance due to the low strength of the corresponding inorganic fillers or due to the poor bonding of the organic types.

3.2.2 Thermoplastic materials

Thermoplastic materials are polymers that are solid at room temperature, they can be melted by heating and recover their initial state when cooled down again. Thermoplastics can be found either in amorphous or semi-crystalline form. Semi-crystalline thermoplastics normally exhibit a relatively sharp melting point, retaining their stiff-

ness and strength properties even at temperatures close to their melting point. On the contrary, amorphous thermoplastics tend to lose their stiffness and strength as temperature increases towards their glass transition temperature before finally becoming liquid at their melting temperature. Moreover, semi-crystalline thermoplastics usually exhibit better chemical resistance.

A very common classification of thermoplastics is according to their mechanical properties and their glass transition temperature. Thermoplastics with low stiffness, strength and glass transition temperature are characterized as standard or commodity thermoplastics. Engineering thermoplastics are in the middle strength and temperature range, while thermoplastics at the high end of strength and glass transition temperature are referred to as high performance thermoplastics.

Both groups of engineering and high performance thermoplastics include materials that can be considered either in pure or reinforced form as candidates for the brake or sliding pads of the wind turbine yaw system. However, due to the large dimensions of the system and the comparatively much higher price of high performance thermoplastics like e.g. Polyetheretherketone (PEEK), the present work focuses only on engineering thermoplastics.

Three chemical families of polymers cover the majority of engineering thermoplastics. These are polyamides, polyesters and polyacetals. Most common polyamide thermoplastics are Polyamide 6 (PA 6) and Polyamide 66 (PA 66), also known as Nylon 6 and Nylon 66 respectively. Some very common polyester thermoplastics are Polyethylene terephthalate (PET), Polybutylene terephthalate (PBT) and Polycarbonate (PC). Polyoxymethylene (POM), also known as Acetal, is the most common representative of polyacetals. Table 3.1 summarizes some indicative values for different properties of the above mentioned thermoplastics, along with their molecular formulas. Since the exact properties of every thermoplastic depend on the level of crystallinity and the exact manufacturing process, the values presented here are only indicative. They are based on references [40], [41], [42] and [43].

For demanding tribological applications like the one studied in the present work, it is very common to use thermoplastics reinforced with fibers. Typically, glass, aramid and carbon fibers are used to improve the creeping behavior as well to increase the stiffness and wear resistance of the base polymer.

In this work, thermoplastic materials reinforced with short fibers, will by convention still be categorized as thermoplastics provided that the volume of the matrix polymer exceeds in percentage the volume of the reinforcing fibers. Moreover, materials categorized here as thermoplastics may contain reinforcing elements, friction modifiers and other fillers in form of particles or flakes.

Table 3.1: Indicative properties of common thermoplastics: Young's modulus E [GPa], Rockwell hardness, density ρ [kg/m^3], water absorption at 50% humidity [%]

	PA 6	PA 66	PET	PBT	PC	POM
	$(C_6H_{11}NO)_n$	$(C_{12}H_{22}N_2O_2)_n$	$(C_{10}H_8O_4)_n$	$(C_{12}H_{12}O_4)_n$	$(C_{16}H_{14}O_3)_n$	$(CH_2O)_n$
E	1.9	2.0	3.0	2.6	2.5	2.7
Rockwell	R 85	R 114	R 120	-	R 118	R 120
ρ	1130	1140	1370	1300	1210	1410
water abs.	3.0	3.2	0.3	0.5	0.15	0.22

3.2.3 Fiber composites

Materials that incorporate either a significant content of long fibers or a well-defined reinforcing network of fibers, like woven fabrics, will be treated in this work as a separate group of materials and will be referred to as fiber composites. The matrix material can either be a thermoplastic or a thermosetting polymer.

It was already mentioned that thermoplastic materials or molded thermoset compounds as defined in the two previous sections, may also contain reinforcing fibers. Thus, classification of materials in either of these categories or as a fiber composite, is not straightforward. A simple practical test for determining if a material classifies as a fiber composite, is by breaking a plate of the considered material through bending. If the fracture surface mostly contains faces that are either perpendicular or approximately at 45° with respect to the plate mean plane, one can assume that the reinforcing fibers are too short for the material to be categorized here as a fiber composite. If the fracture surface consists mainly of spikes or wedges with flanks very parallel to the plate mean plane, it can be assumed that the length and amount of the contained fibers justifies classification of the material as a fiber composite. Figure 3.1 shows pictures of fracture surfaces corresponding to a molded thermoset compound, a thermoplastic reinforced with short fibers and a fiber composite.

Theoretically both thermoplastic and thermoset materials can serve as base material for fiber composites. In practice, it is more common to find fiber composites based on thermoset materials. This is because of the liquid form of thermoset prior to curing, which allows a better wetting of the reinforcing fibers and consequently a stronger adhesion between the fibers and the matrix.

Independent of the binding material, fiber composites can be further categorized as materials based on woven or knitted fabrics or on non-woven fabrics. In composites

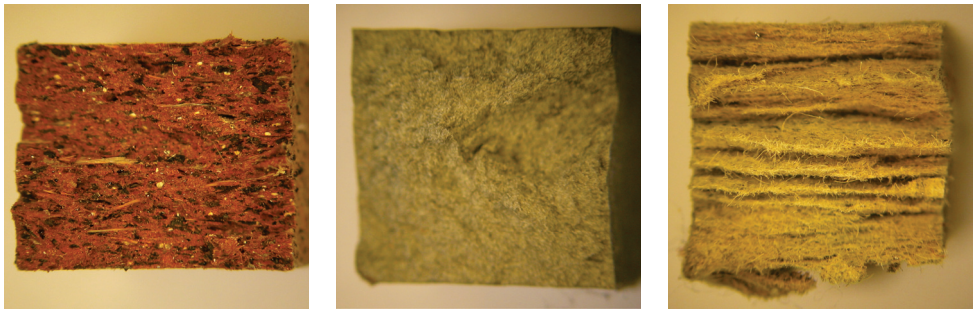

Figure 3.1: Fracture surfaces of a short fiber reinforced molded thermoset compound (left), a short fiber reinforced thermoplastic (middle) and a fiber composite with non-woven fibers in pulp form (right)

of woven or knitted fabrics, the reinforcing fibers are oriented in a predetermined highly ordered way, while in non-woven fabric composites, fibers are not ordered or oriented in a specific manner. One kind of non-woven fabric composites are the so called paper-like materials. In such materials fibers are provided in the manufacturing process in form of pulp that can be impregnated by the matrix material and dried.

3.2.4 Sintered materials

Sintered materials are produced from raw materials in form of powder. They are named after the process of sintering, that is one of the final steps in their production. In principle, sintering applies to a wide range of materials including metals, ceramics and polymers. However, metallic sintered materials are the most common group and the technology of their production is more accurately referred to as powder metallurgy. Independent disc brakes incorporated in traditional yaw systems corresponding to Figure 1.1 are often based on sintered friction materials that are either metallic or metallic-ceramic and the present work is limited to these two kinds of sintered materials. Detailed information about powder metallurgy can be found in reference [44] (chap. 23).

A typical process for production of sintered materials involves preparation and mixing of the powders, compaction under high pressure in an appropriate mold and heating at a temperature below the melting point, which causes welding between powder particles. The last phase of heating is the actual sintering process. Post-treatment of the produced sintered parts, like rolling, machining or heat treatment is also possible. An alternative technique for producing sintered materials for friction applications is by sprinkling the raw powders on the surface of a substrate plate, optionally compacting it under high pressure and finally sintering it.

Metallic sintered materials can be based on iron, copper or aluminum as their main component and they can also include metals like lead, cobalt, molybdenum and nickel. Ceramics similar to the abrasives mentioned in the section on molded thermoset compounds can also be included. Sintered materials used in clutch or brake applications normally contain a high amount of copper in form of bronze along with abrasive elements like metal oxides and silicates as well as solid lubricants like graphite.

Apart from the chemical composition of the raw powders, the size and the shape of the particles in the powder are of major importance for the properties of final material. Due to the powder form of the raw material, sintered materials retain some degree of porosity also in their final form. In tribological applications, this property can be exploited in two different ways. Self lubricated bearings can be produced by filling sintered bushing materials with oil. Furthermore, in wet friction applications like wet clutches, the porosity of sintered materials may reduce the risk of squeeze or hydrodynamic film formation.

3.3 Lubricants

It has already been mentioned above, that solid lubricants are often included in friction materials in order to reduce friction, increase wear resistance and avoid noise generation. However, solid lubricants may not be sufficient. This section summarizes some fundamentals about fluid lubricants.

In the context of the considered yaw system, oil or grease lubrication might be necessary either in order to achieve a low wear rate to ensure long lifetime of the friction materials or just in order to prevent oxidation of the steel flange. In practice, due to the difficulty of sealing an oil filled system of such dimensions, the present work is limited to the most practical case of utilizing grease lubrication. The drawback of utilizing grease is that it requires an appropriate design for redistributing the grease on the flange surface during operation.

Greases consist of three basic components, a base oil, a thickener and additives, with the base oil covering approximately 85% and the thickener around 10% of the total weight, cf. references [45] (chap. 14) and [22] (chap. 3). The base oil can either be mineral oil or a synthetic one. Mineral oils are normally paraffins while there are many categories of synthetic oils like polyalphaolefins (PAO), esters, polyglycols, silicones, etc. The main advantage of synthetic oils is that they maintain their properties in a wider range of temperatures than mineral oils. Concerning the thickener, it functions as a semi-solid container for the base oil. Thickeners are divided into soap and non-soap types. Sodium, calcium, lithium and barium soaps are some typical thickeners. Some commonly used non-soap thickeners are silica, bentonite clay and

polyurea (diurea). Additives used in greases serve as anti-oxidants, they offer rust and corrosion protection, they can improve the adhesion properties (tackiness) and they can also lower the friction coefficient and minimize wear (e.g. extreme pressure additives).

The basic properties of greases refer to their consistency, drop point, evaporation, oxidation, base oil viscosity and apparent viscosity, [22] (chap. 3). The consistency or hardness of greases expresses their shear resistance and is quantified as the NLGI (National Lubricating Grease Institute) grade. The higher the grade in a nine step scale, the higher the grease consistency. The drop point is the highest temperature limit at which the grease basically maintains its consistency. The evaporation loss expresses the weight of volatile components of a grease that are released during an elevated temperature test. Oxidation stability refers mainly to the ability of the base oil to resist oxidation at elevated temperature. The thickener can also suffer oxidation but typically to lesser extent compared to the base oil. Apart from the dynamic viscosity of the base oil, which is normally relatively independent of the shear rate, the apparent viscosity of greases typically decreases rapidly with increasing shear rate.

Regarding the wind turbine yaw system, the expected wide range of operational conditions suggests utilization of synthetic greases, despite their higher cost. However, no extreme temperatures at the high end of the temperature range are expected, hence, the anti-oxidation performance of the used grease is not a very critical parameter. Due to the long lifetime of the system and the long maintenance intervals, good adhesion properties of the grease is important, so that grease leakage is avoided. Due to the very low sliding speed and the high nominal pressure, the grease is expected to act as a boundary lubricant, no hydrodynamic phenomena should be expected. Under such conditions the bulk viscosity and hardness of the grease is not a key parameter for its lubrication performance, lesser than its behavior at nano level, related to the so called boundary liquid and its chemical ability to bond with the contacting surfaces.

Chapter 4

Friction testing

A device used to measure the friction force between two solid bodies in contact, sliding against each other, is characterized as a tribometer. Chapter three of textbook [8] is devoted to tribometers, providing a very detailed overview of the different designs. In the present work, a pin-on-disc test-rig was utilized as tribometer for studying a number of selected friction materials running against a steel surface. This chapter describes the testing equipment as well as the testing procedures and presents the obtained results. Part of the information provided in this chapter is included in Publication P1.

4.1 Pin-on-disc test-rig

Figure 4.1 shows a simplified illustration of the utilized pin-on-disc test-rig, cf. [46]. The normal load on the flat ended pin (1) is determined by the position of mass (2) on the loading arm (3). The rotating disc (4) is driven by an electric motor (5). In order to record the torque generated on the disc by the friction force, the rotation of the motor housing with respect to the test-rig frame (6) is restricted exclusively through arm (7), wire (8) and force transducer (9).

One of the previously discussed particularities of the yaw system, namely its reciprocating operation, had to be taken into account in the test-rig design. Motor (5)

should be able to drive disc (4) in periodically alternated directions and friction measuring should be possible in both directions. For this reason, wire (8) along with force transducer (9) are preloaded through the weight of an additional mass (10). Consequently, the measured friction force should not exceed the weight of mass (10), otherwise the mass will be lifted.

One important aspect about utilizing a pin-on-disc test-rig for reciprocating testing is that the turning points of the reciprocal motion can be at fixed locations on the disc. This means that if the stroke length of the reciprocation is longer than one circumference, the pin will run over the turning points one or more times in every half stroke. It is expected that the disc surface in the area of the fixed turning points will develop different characteristics than for the rest of the used disc track and yield to friction peaks or valleys when these locations are overrun. In order to avoid this possibility and maintain the cyclic symmetry of the test, in the tests presented in this section the stroke length in the reversing direction was shortened by 1%. In this manner, the turning points are not at fixed positions of the disc, but they are moving as the test progresses.

Taking additional care in the test-rig design was necessary in order to fulfill the low sliding speed and relatively high pressure conditions of 20 mm/s and 20 MPa respectively, that are according to the estimations and the calculated example presented in Chapter 2. A gearbox of transmission ratio 30, integrated in the test-rig motor (5), was used in order to achieve a low rotational speed and a correspondingly higher torque on disc (4).

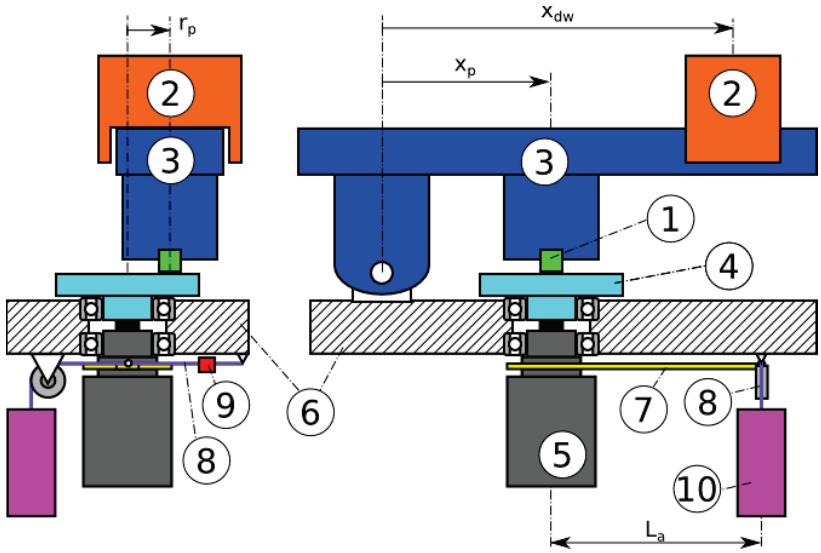

Figure 4.1: Simplified illustration of the pin-on-disc test-rig

The calibration of the normal force applied to the pin and the friction force corresponding to the signal of transducer (9) are part of the testing procedure.

By neglecting the friction in the roller element bearing connecting loading arm (3) and frame (6), the normal force F_n applied to the pin can be expressed according to Equation (4.1) as the sum of an initial load F_{n0} due to the weight of loading arm (3) and a variable load proportional to the linear position x_{dw} of the dead weight mass (2). A calibration line correlating the mass position with the normal force was determined by placing a pre-calibrated compressive force transducer below the pin and moving the mass to different positions. The coefficients F_{n0} and C_{dw} could be determined by fitting a line to the probed points. During the tests the dead weight position x_{dw} is adjusted through a stepper motor in order to achieve the desired nominal pressure on the pin surface.

$$F_n = F_{n0} + C_{dw} \cdot x_{dw} \tag{4.1}$$

The calibration of force transducer (9) was done in-place by adding and removing mass to the dead weight (10). The zero level of the force transducer measurement F_{FT} corresponds to loading only through the original dead weight (10). Any additional force applied to wire (8) through arm (7) will result in a positive value for F_{FT} if it acts in the same direction like the dead weight force and it will result in a negative F_{FT} if it acts against the weight. Finally, Equation (4.2) can be used to relate the measured force F_{FT} to the friction force F_f under consideration of the length L_a of arm (7) and the actual pin track radius r_p.

$$F_f = \frac{F_{FT} \cdot L_a - M_{fB}}{r_p} \tag{4.2}$$

In Equation (4.2), M_{fB} stands for the friction torque in the bearings supporting the rotating disc. Since M_{fB} is load dependent, it is difficult to estimate or measure independently. Nevertheless, its impact on the measured coefficient of friction should be comparable to the friction coefficient of the utilized bearings, which in the case of ball bearings is in the order of 0.001, while the friction coefficient to be measured is above 0.1. For this reason, in the present work M_{fB} is neglected.

The length of arm (7) in the actually utilized test-rig is $L_a = 193$ mm and all tests in the present work were carried out on tracks with radii r_p equal to 40, 51 and 62 mm.

With respect to the pin specimens (1), flat ended pins were used in all tests, in order to avoid changes in the apparent area of contact as the relatively soft pin material wears down. However, because of the flat form of the pins, a good alignment with

respect to the disc surface is very important. For this purpose, pressure sensitive paper is used before every test in order to verify that the pin surface is in full contact with the disc. Figure 4.2 shows two imprints corresponding to a misaligned pin and a pin in full contact. For obtaining a good alignment at the beginning of each test, the height of loading arm (3) has to be adjusted by appropriate screws integrated in the test-rig design.

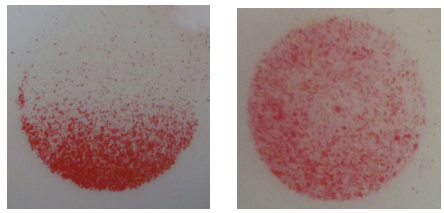

Figure 4.2: Pin imprint on pressure sensitive paper, before and after alignment (left and right picture respectively)

It should be noted however, that a good alignment between the pin and the disc at any arbitrary circumferential position depends on the flatness of the disc and the perpendicularity between its upper surface and the rotation axis. Relatively compliant pin materials, like most of the friction materials presented in Section 4.3 , are more tolerant to geometrical deviations than stiffer ones.

Regarding the size of the pin specimens, one has to consider that relatively coarse grained or inhomogeneous friction materials cannot be represented adequately by too small pin specimens. On the other side, for achieving a nominal contact pressure of up to 20 MPa, the required normal force and the corresponding friction force increase quadratically with the pin diameter. The pin diameter of 10 mm that was kept constant for all tests in the present work, was based on the capabilities of an already available pin-on-disc test-rig, [46]. For the chosen pin diameter, the apparent contact area is $A_p = 78.5\,\mathrm{mm}^2$ and the normal force corresponding to a nominal contact pressure of 20 MPa is $F_n = 1571$ N. Assuming a coefficient of friction of 0.5 and a track radius of 50 mm, a friction force $F_f = 785.5$ N and a corresponding disc torque of approximately 40 Nm can be calculated as indicative values.

The manufacturing of all pin specimens was done by turning plates or bars of the different materials to be tested. In case of raw materials provided in form of plates, the pin axis corresponded to the direction perpendicular to the plate mean plane and in case of raw materials in form of bars the pin axis coincided with the bar axis.

Regarding the disc that served as counter surface for the testing, alloy steel 34CrNiMo6 (1.6582) was chosen as the disc material and the disc top surface was fine turned and left in unhardened state. In order to achieve a possibly constant surface roughness on the disc surface, independent of the track radius, the turning was carried out on a

CNC lathe that retained constant cutting speed. After each use, the disc surface has to be re-machined before it can be used in another test again. In total, the arithmetic average surface roughness *Ra* of the different discs and re-machined disc surfaces used in the tests, varied between 0.5 and 1 µm. The disc outer diameter was 134 mm and the thickness of the utilized discs varied from 17 to 19 mm, depending on how many times the top disc surface was re-machined.

The temperature in the area close to the contact interface between pin and disc was monitored through a laser infrared thermometer of the type Optris® CT, that came pre-installed with the pin-on-disc test-rig. The laser beam of this non-contact temperature sensor, with a focus point of approximately 1 mm, was targeted against the edge of the pin at the boundary of the contact between the pin and the disc. The temperature measured at this location is an indicative temperature probably a few degrees lower than the temperature in the center of the contact area.

4.2 Testing procedure

In general, a single coefficient of friction value is not sufficient for describing the frictional behavior of a given tribopair. Friction may depend strongly on the environmental and lubrication conditions, the nominal pressure, the sliding speed and the covered sliding distance. The testing procedure described in this section intends to reveal the evolution of friction as a function of the covered sliding distance until a steady state is reached and show the impact of the nominal contact pressure on the friction coefficient. Moreover, both dry and grease-lubricated conditions are taken into account. All in all, the friction testing on the utilized pin-on-disc test-rig is meant to achieve the below listed goals for a relatively big number of friction material candidates.

- Determine the running-in behavior.
- Obtain indicative values for the friction coefficient at steady state.
- Determine the pressure dependence of the friction coefficient.
- Study the impact of grease lubrication.

The testing procedure begins with mounting a pin specimen and aligning it as described in the previous section. Thereafter, both the disc and the pin are cleaned thoroughly using isopropyl alcohol in more than one passes of cleaning and drying. After the final cleaning pass the surfaces are left to dry for a few minutes. The purpose of cleaning is not to achieve absolutely clean surfaces but to ensure a similar level of cleanliness among the different experiments. For this reason, the previous processing

of the disc and the pin specimens is also important. Utilization of the same type of cutting tools, cutting fluid and cleaning after the machining is important.

After pin and disc are aligned and cleaned, an initial running-in test takes place on the disc track with a radius of 40 mm. Its purpose is to ensure that any remaining geometrical misalignment between the pin and the disc is eliminated through the wear process. During this initial running-in, a normal load of 472 N corresponding to a nominal pressure of 6 MPa in applied on the pin, the sliding speed is kept constant to 20 mm/s and the sliding direction is alternated every 0.9 m. The necessary sliding distance for reaching a steady coefficient of friction value, depends on the material. Typically, for the materials presented in the next section the initial running-in covers a distance between 50 and 400 m.

Once this first running-in is completed, the pin is moved on the disc track with a radius of 51 mm, where the actual measurement under dry conditions takes place. On this track a second running-in is carried out under the same conditions as the first one until the recorded coefficient of friction approximates a steady state again. The evolution of the coefficient of friction observed in this testing phase is only due to microscopic geometrical changes on the pin and disc surfaces and possible chemical changes on the disc surface, e.g. material transfer.

The next testing phase involves varying the applied nominal pressure from 3 MPa to 18 MPa in steps of 3 MPa. For each pressure level, a sliding distance of 10 m is covered under conditions otherwise matching the ones during the running-in test. For materials with moderate or low coefficient of friction, one additional step at a pressure level of 20 MPa is possible to include.

The last testing phase is carried out on a third track with a radius of 62 mm, initially covered with an approximately 1 mm thick layer of grease. During a similar running-in period like in the previous cases, the grease layer is wiped from the track due to the motion of the pin. However, a minimal quantity of lubricant remains in the contact during a longer period, so that the contact runs under boundary lubrication conditions with a much lower coefficient of friction than under dry conditions. The lubricant stored in the contact may be in form of a very thin layer adhered on the contacting surfaces, that is very difficult if not impossible to squeeze out only through normal loading and sliding, cf. [47]. Moreover, additional lubricant may be trapped in the porous structure of the tested friction material and it can be released progressively as the tested material wears down.

Despite the ability of most materials to run longer distances under boundary lubrication without re-lubrication of the track, the running-in tests with grease are by convention stopped after 50 to 60 m. At this point a pressure variation in 10 m long intervals takes place in the same manner like in the dry testing.

The steps of the whole testing procedure with the pin-on-disc test-rig, after the alignment and cleaning, are summarized below:

Step 1: Initial dry running-in at p=6 MPa on track with r_p=40 mm
Step 2: Dry running-in at p=6 MPa on track with r_p=51 mm
Step 3: Pressure variation from 3 to 20 MPa on track with r_p=51 mm
Step 4: Greased running-in at p=6 MPa on track with r_p=62 mm
Step 5: Pressure variation from 3 to 20 MPa on track with r_p=62 mm

4.3 Tested materials

In order to cover a wide spectrum of the friction material groups presented in Section 3.2, three to five representative materials of each group were included in the friction tests with only one sample per tested material. Tables 4.1 to 4.4 provide an overview and some basic data about the tested materials, divided according to the groups defined in Section 3.2. Most material data are extracted from the supplier data-sheets, when available, while the estimated sizes of contained particles and fibers are based on microscope pictures to be presented in the next chapters.

Table 4.1: Molded thermoset compounds tested in the pin-on-disc tribometer

Name	Image	Material information
MTC1		- phenolic resin and elastomer (rubber) binder - reinforcing fibers in form of short yarn pieces - further friction modifiers in form of particles and flakes - coarse grained (500 µm)
MTC2		- phenolic resin binder - short reinforcing fibers - fine grained (10 µm)
MTC3		- phenolic resin binder - short reinforcing fibers - medium grained (50 µm)

The materials in Table 4.1, referred as MTC1, MTC2 and MTC3, are all molded thermoset compounds based on a phenolic resin matrix and provided by two different suppliers. One distinct characteristic of MTC1 is that it also includes a portion of

elastomer (rubber) in its binding matrix. It is also a very coarse grained material, with contained particles and flakes with a size in the order of 0.5 mm and fiber yarn pieces of similar diameter and a length of up to 3 mm. On the contrary, material MTC2 is very fine grained and material MTC3 has a medium grain size and they are both reinforced with very short fibers.

Table 4.2: Thermoplastic materials tested in the pin-on-disc tribometer

Name	Image	Material information
TP1		- PET (semi-crystalline) - E=3.5 GPa, ν=0.43, σ_{yt}=90 MPa, σ_{yc}=100 MPa - H=170 MPa
TP2		- PET (semi-crystalline) - E=3.0 GPa, σ_{yt}=85 MPa - 85 Shore-D, H=170 MPa
TP3		- PA 6 (semi-crystalline) - E=4.0 GPa, σ_{yt}=87 MPa, σ_{yc}=67 MPa - H=170 MPa
TP4		- PA 66 (semi-crystalline, reinforced) - short glass and aramid fibers - MoS_2 as solid lubricant
TP5		- PA 66 (semi-crystalline, reinforced) - short glass and aramid fibers - MoS_2 as solid lubricant (less than in TP4)

Table 4.2 summarizes the five tested thermoplastic materials. Materials TP1 and TP2 are both unreinforced PET thermoplastics obtained from two different suppliers. Material TP3 is an unfilled PA 6 thermoplastic, while both TP4 and TP5 are based on PA 66, reinforced with short glass and aramid fibers and filled with solid lubricant MoS_2. TP5 contains a lower percentage of solid lubricant in comparison to TP4. Both reinforced thermoplastics TP4 and TP5 are very fine grained with size of contained particles similar to the diameter of the contained glass fibers in the order of 12 µm.

Table 4.3 summarizes materials FC1, FC2 and FC3, that can be classified as fiber composites according to the convention explained in Section 3.2. Fiber composite FC1 is based on aramid fibers provided in form of pulp and bonded with a phenolic resin thermoset. Material FC2 consists of a woven textile which is mainly made of glass fiber yarn, impregnated in a thermoset matrix. The yarn diameter has a

Table 4.3: Fiber composite materials tested in the pin-on-disc tribometer

Name	Image	Material information
FC1		- based on aramid fibers pulp - thermoset matrix - E=9.2 GPa, ν=0.24, σ_{yt}=23 MPa, σ_{yc}=120 MPa - 83 Shore-D
FC2		- glass fibers yarn (300 µm) - woven coarse textile bonded with thermoset - E=8.4 GPa, ν=0.19, σ_{yt}=73 MPa, σ_{yc}=360 MPa - 90 Shore-D
FC3		- non-woven fibers (10 µm) - high porosity - metallic particles (100 µm)

diameter of approximately 300 µm, which size also determines the pitch length of the impregnated textile. The individual glass fibers forming the yarn have a diameter of approximately 8 µm. The last fiber composite FC3 is a paper-like material typical for wet clutch applications. It consists of non-woven thermoset bonded fibers with diameter in the order of 10 µm and it also contains dispersed metallic particles with a characteristic size of approximately 100 µm. As it can be seen on the corresponding picture in Table 4.3, material FC3 is in form of an only 1 mm thick layer glued on a steel substrate.

The last group of tested friction materials are four sintered materials listed in Table 4.4, provided by two different suppliers. They are all four copper based with different grain sizes, abrasives and manufacturing methods. S1 is a very fine grained and dense bronze-based sintered material that has a structure very close to a corresponding cast part but incorporates solid lubricant particles. Sintered material S2 incorporates both bronze particles and ceramic particles as abrasives along with graphite as solid lubricant. It is very coarse grained with a characteristic grain size in the order of 300 µm. Material S3 is also bronze-based and contains additional abrasives and lubricants but its grains, with a size of about 100 µm, instead of being pressed in a mold they are sprinkled on a steel substrate before the material is heated in the sintering furnace . This production method results in a high porosity structure appropriate for wet clutch applications. Finally, material S4 is similar in grain size and composition with material S2, however it incorporates a surface layer enhanced in abrasives.

Table 4.4: Sintered materials tested in the pin-on-disc tribometer

Name	Image	Material information
S1		- bronze based, metallic sintered material - very fine grained (<10 µm)
S2		- bronze-based, metallic-ceramic sintered material - graphite particles and other frictional additives - coarse grained (300 µm)
S3		- bronze-based, sprinkled sintered material - significant porosity - relatively coarse grained (100 µm)
S4		- copper based - surface layer enhanced with abrasives - coarse grained (300 µm)

Regarding the greased testing, it is important to provide information about the utilized lubricant. All below presented pin-on-disc testing results that refer to lubricated conditions are carried out utilizing a full synthetic grease with the commercial name Rivolta F.L.G. GT-2. It is based on a synthetic oil of the type PAO (cf. Section 3.3) with a kinematic viscosity of 46 mm^2/s. Its thickener is a calcium sulfonate complex soap and its consistency corresponds to an NLGI grade equal to 2.

4.4 Testing results

4.4.1 Running-in

This section includes results corresponding to steps 2 and 4 of the testing procedure described in Section 4.2. The diagrams in Figure 4.3, show the evolution of the coefficient of friction during the running-in phase under dry conditions (procedure step 2), while Figure 4.5 contains the corresponding running-in diagrams under lubricated conditions (procedure step 4). All presented coefficient of friction curves are based on average friction force values, calculated per reciprocation stroke. In this way they demonstrate the long term evolution of the measured coefficient of friction without revealing any possible fluctuation withing each single stroke.

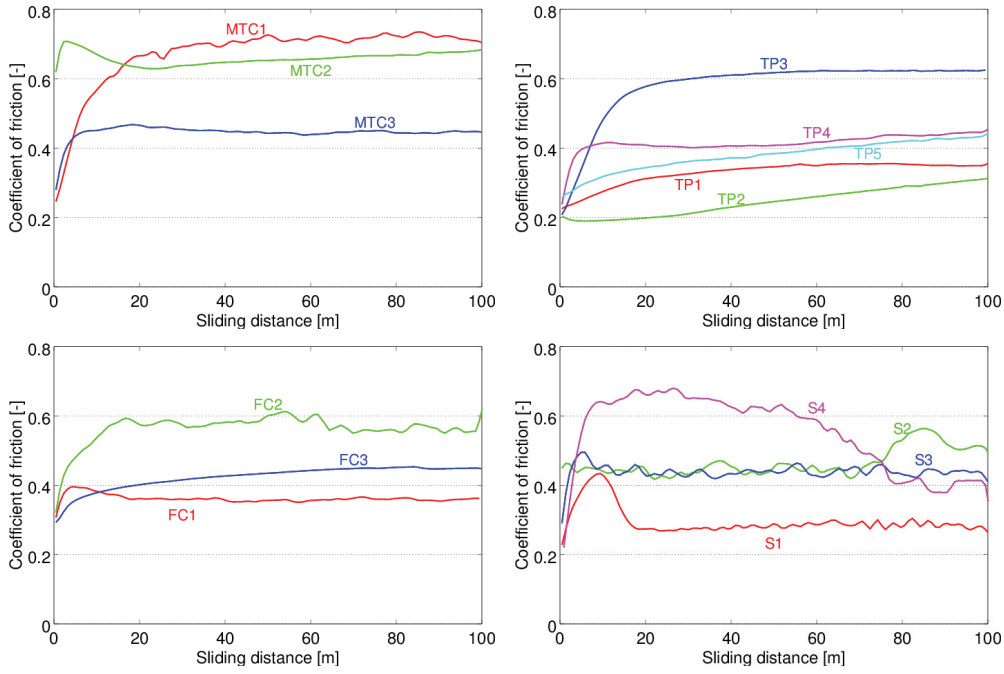

Figure 4.3: Measured coefficient of friction during running-in under dry conditions

Under dry conditions, one can observe a very big variation of the steady-state coefficient of friction and the running-in behavior within each of the four material groups. With graphs in Figure 4.3 representing the dry running-in on the clean track r=51 mm but with a pin surface that was already run in on track r=40 mm, the initially increasing friction is mainly because of changes on the disc track surface and small changes on the pin surface topography. Molded thermoset compounds, fiber composites and sintered materials exhibited rather short running-in distances in the order of 20 m. In some cases, like for materials MTC2, MTC3, FC1, S2 an S3, the running-in distance was as low as 5 m. Thermoplastics exhibited a variable behavior with TP3 and TP4 running-in relatively fast, while TP2 and TP5 exhibited a very slow running-in. It is surprising that TP1 and TP2 pins, made both of unfilled PET, exhibit so different running-in behaviors.

Motivated by this observation, a further study with more than one specimens of the TP1 material has demonstrated a very high variability of the running-in distance even among pins of exactly the same material. The corresponding testing results are shown in Figure 4.4. Three pins made of the PET material TP1 were tested against steel discs that were machined in the same batch. Roughness measurements on the discs surfaces verified that not only they had very similar roughness parameters but also the form of asperities was almost identical. In all three repetitions, the test

was interrupted after 250 m of accumulated sliding distance, the pin surface was measured and the test was resumed. The testing of pin specimens number 2 and 3 was interrupted two additional times at the beginning of the test when the measured coefficient of friction reached the limits of 0.23 and 0.33. In every interruption the pin surfaces were measured with a stylus profilometer.

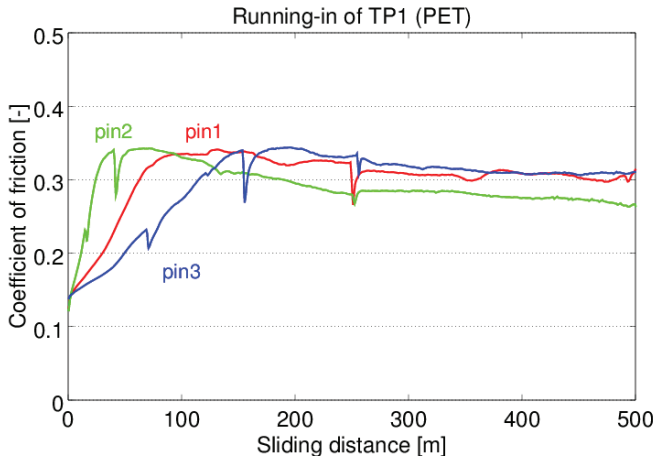

Figure 4.4: Measured coefficient of friction during running-in of PET under dry conditions

In total, the following comments can be made with respect to Figure 4.4:

- All three pins begin with very similar friction coefficient around 0.14 .
- The measured steady-state coefficients of friction vary from 0.26 to 0.31 .
- The three pins exhibit very different running-in distances from 40 to 150 m.
- After each interruption the coefficient of friction drops significantly but within only 10 m it recovers the value prior to the interruption.

The monitored temperature close to the contact interface, varied during the testing of all three PET specimens from 24° to 29° C. No relationship between the measured temperatures and the different friction coefficient curves could be found.

Figure 4.5 summarizes all running-in testing results under grease lubrication (procedure step 4). The measured coefficient of friction approximates a steady-state value between 0.13 and 0.16 for all pin materials except FC2 and S4. Considering that each tested material is represented by one single repetition, such small variation cannot be considered as statistically significant for ranking the tested materials with respect to the measured coefficient of friction. A general conclusion is that the measured

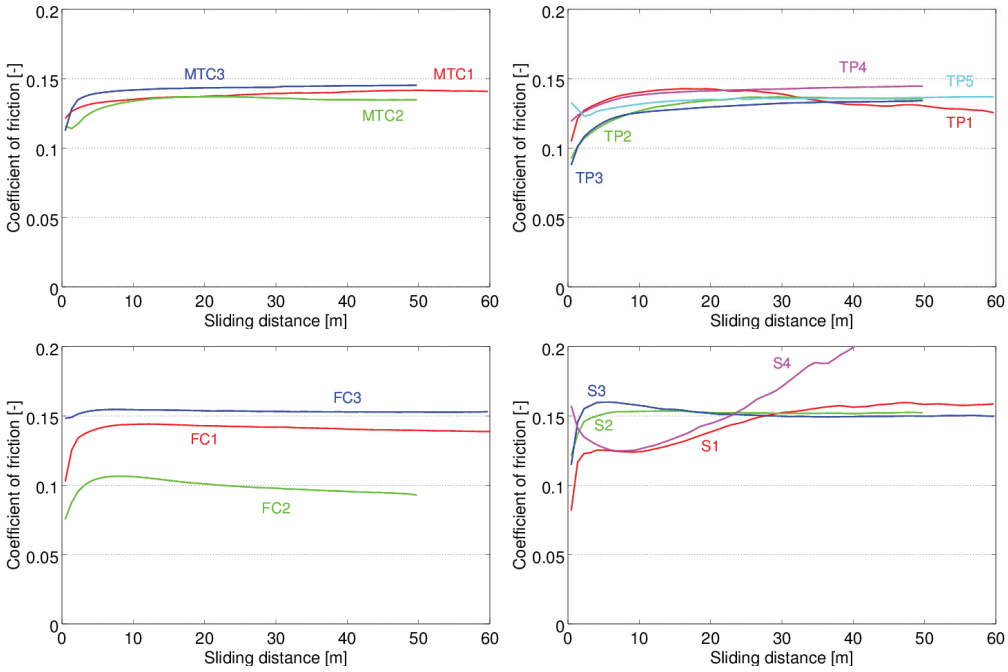

Figure 4.5: Measured coefficient of friction during running-in with grease

friction is dominated by the used grease. With very few exceptions, materials of very different compositions and structures provided very similar friction levels.

The fiber composite material FC2 is the only material that exhibited, under grease lubrication, a significantly lower coefficient of friction than the rest of the tested materials. It is reminded that FC2 mainly consists of a textile of glass fiber yarn bonded together with a thermoset.

The sintered material S4 also deviated from the typical behavior of the rest of the tested materials. After a sliding distance of 60 m, the measured coefficient of friction did not reach a steady value. This means that the material is not able to remain under boundary lubrication conditions without adding further grease on the disc track. For this reason material S4 was eliminated from further testing under variable pressure.

4.4.2 Pressure variation

Results corresponding to the testing procedure steps 3 and 5 are reported in Figures 4.6 and 4.7 respectively.

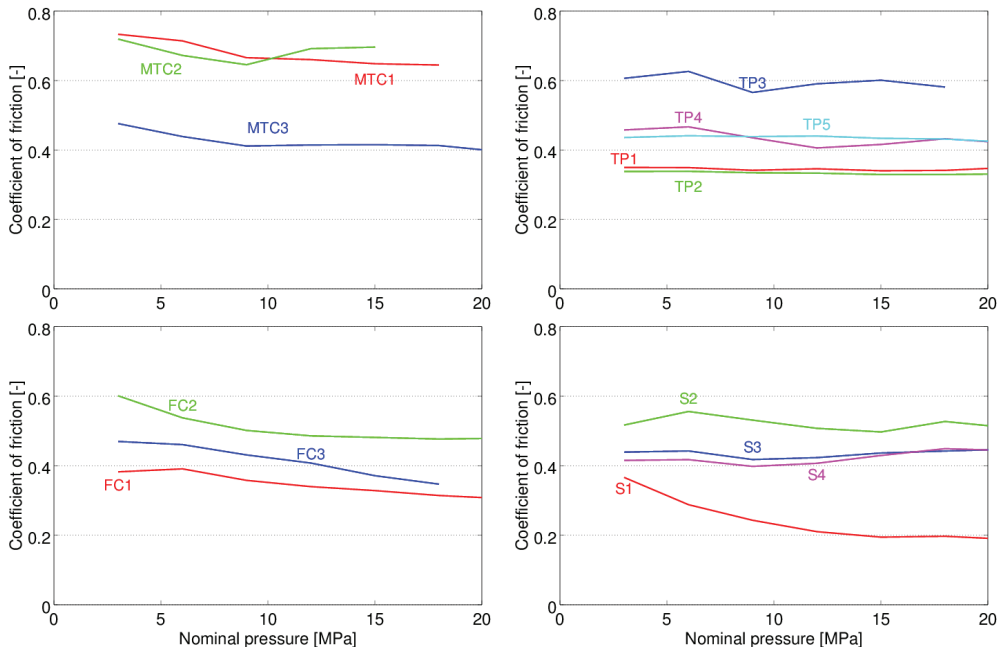

Figure 4.6: Measured coefficient of friction under dry conditions at different pressure levels

Under dry conditions, the coefficient of friction for the tested molded thermoset compounds drops only slightly with increasing pressure, while the friction coefficient for the tested thermoplastics seem practically unaffected by the applied pressure. All three tested fiber composites exhibit a decreasing coefficient of friction with increasing pressure, while the frictional performance of the tested sintered materials with respect to the applied pressure is mixed. For the fine grained material S1 the measured friction coefficient drops to a very low value of 0.2 at the highest pressure of 20 MPa, while the other three coarse grained sintered materials exhibit a rather stable coefficient of friction through the whole pressure range.

Under lubricated conditions, the friction coefficient of all three tested molded thermoset compounds exhibits a slightly negative slope with respect to pressure. A similar behavior is observed for the reinforced thermoplastics TP4 and TP5 while all three non-reinforced thermoplastics TP1, TP2 and TP3 exhibit a more significant negative slope in their friction coefficient curves. The coefficient of friction for fiber composites FC1 and FC2 drops significantly with increasing pressure as well. The higher porosity fiber composite FC3, exhibits a higher and less sensitive to pressure friction coefficient. Regarding the sintered materials, material S1 failed to complete the test under boundary lubrication conditions. The increased coefficient of friction at high pressures reflects the lack of lubricant in the contact, similar to the behavior of ma-

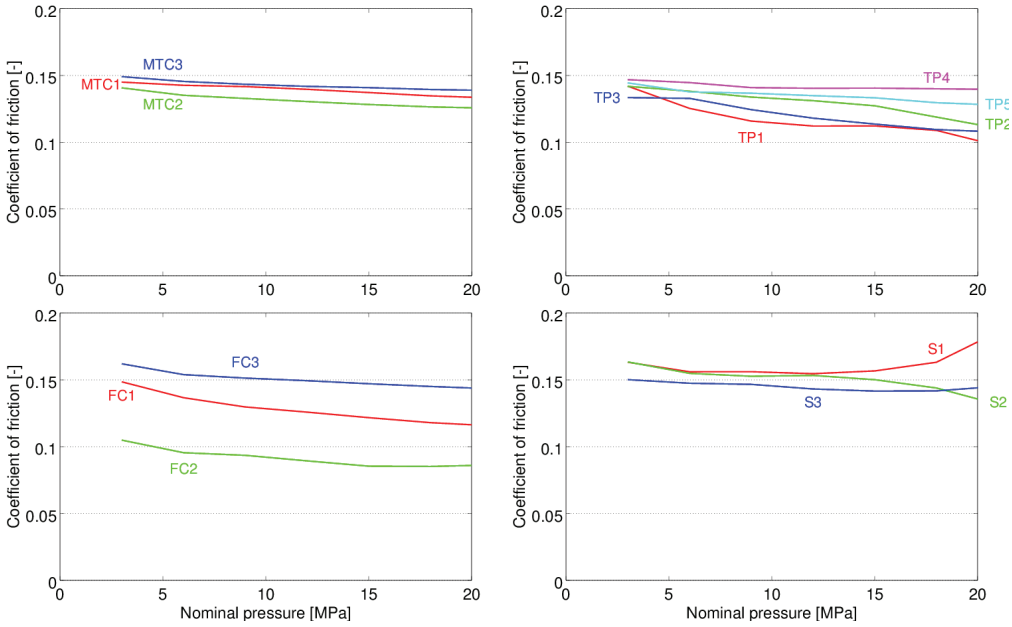

Figure 4.7: Measured coefficient of friction with grease at different pressure levels

terial S4 during the running-in test (procedure step 4). Sintered materials S2 and S3 exhibited, within the tested pressures range, decreasing and rather constant friction coefficients respectively.

4.4.3 Sliding speed variation

Although the sliding speed range expected in the wind turbine yaw system, as explained in Chapter 2, is very limited, in extreme cases like total failure of the yaw driving system, higher sliding speeds may be experienced. An increasing coefficient of friction with increasing sliding speed can act as a stabilizing factor in such emergency cases. On the contrary, a decreasing coefficient of friction may result in an out-of-control movement.

In order to provide some basic information about the speed dependency of the coefficient of friction under dry and grease-lubricated conditions, two selected thermoplastic materials, TP2 and TP4 were tested not only under variable pressure but also under different sliding speeds from 10 to 50 mm/s. The testing procedure steps 3 and 5, were repeated for five different speed levels. Figure 4.8 presents the results of these tests only for three pressure levels at 6, 12 and 18 MPa. The rest of the intermediate pressure levels are omitted for the sake of simplicity.

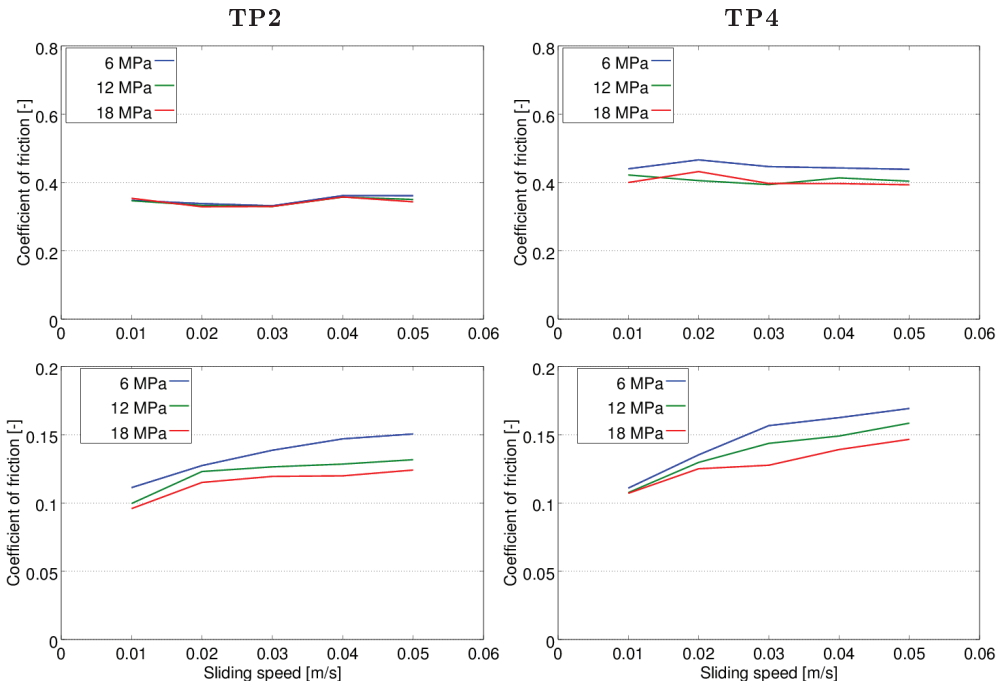

Figure 4.8: Coefficient of friction of thermoplastics at different pressure levels under dry conditions (top) and with grease lubrication (bottom)

The testing results presented in Figure 4.8, show no significant impact of the sliding speed on the coefficient of friction under dry conditions and a positive impact under grease-lubricated conditions. It is assumed that thermoplastics similar to the non-reinforced PET variant TP2 and the reinforced PA 66 variant TP4 will exhibit the same tendencies.

It should be noted that all tests presented so far were conducted at ambient temperatures in the range between 18° and 28° C and with relative humidity varying from 25 to 35%. The monitored temperature in the area near the contact interface was only a few degrees higher than the room temperature. The highest recorded peak was at 40° C during dry testing of material TP4 under the maximum pressure of 20 MPa and sliding speed of 50 mm/s.

4.4.4 Break-away friction

The capability of friction materials to operate without inducing noise during sliding is one further performance criterion to take into account. As explained in Section 6.3, the tendency of friction materials to generate noise or not, depends on the relationship between their static and dynamic coefficients of friction and the slope of the friction coefficient curve with respect to the sliding speed. In order to provide information about the ratio between the static and dynamic coefficients of friction, a series of so called brake-away friction tests were carried out under dry conditions for a selected group of materials.

As it can be seen in the running-in diagrams of Figure 4.3, there is normally an important difference between the initial and the steady-state coefficient of friction, after running-in. For this reason, it is crucial to complete the running-in phase before carrying out any study on the static coefficient of friction. Measuring the static to dynamic friction ratio without a prior running-in would have little relevance for the considered real life application.

All break-away friction measurements to be presented here, were carried out on disc track with radius r_p=40 mm of the pin-on-disc test-rig. After completing the initial running-in according to the procedure step 1, the disc was repeatedly started in a very controlled manner, was accelerated up to a sliding speed of 20 mm/s and was stopped again. Five sequential starts and stops took place within a stroke width of 1 m and then the same steps were repeated in reversed rotational direction. In total, the test included three pressure levels at 6, 12 and 18 MPa. As an example, Figure 4.9 shows the coefficient of friction measurement corresponding to material FC1, tested under a nominal pressure of 18 MPa. The negative values on the coefficient of friction axis, simply represent the friction force during the reversed rotation of the disc. Along with the measured coefficient of friction, the graph also shows the evolution of the sliding speed. In total, it covers two full strokes. Within each stroke, it is easy to recognize when the disc is stopped by considering the points where the sliding velocity drops to zero. After each stop, the sliding speed increases again up to 20 mm/s before the disc is stopped again.

Since the objective of the test is to capture the static coefficient of friction, a very progressive and free of oscillations start-up of the disc is essential. By prescribing the rotational speed of the driving motor as a cubic function of time, combined with the high reduction ratio in the incorporated gear transmission and the small track radius of 40 mm, very satisfactory results could be achieved. Figure 4.10 illustrates one single start-up extracted from the test presented in Figure 4.9. Each single start-up, like the one shown in Figure 4.10, is analyzed in the same way by determining an average coefficient of friction just before the stop and by detecting the highest friction peak during the start-up. By convention, the average coefficient of friction,

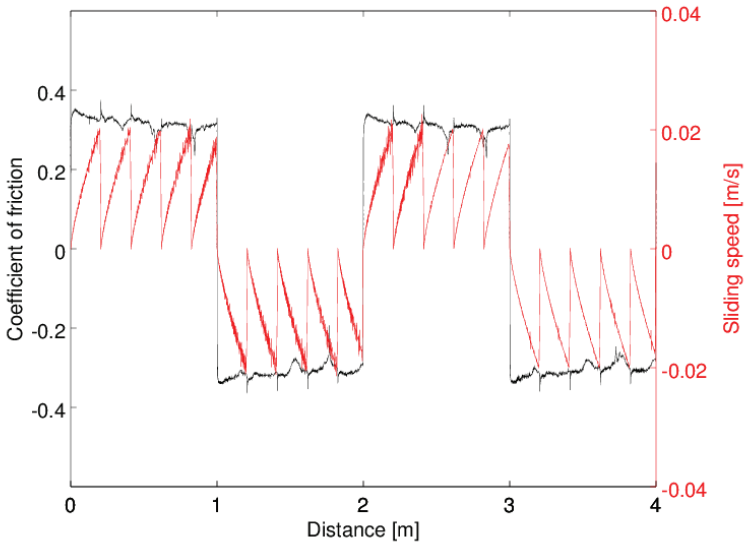

Figure 4.9: Break-away friction testing of material FC1 at 18 MPa

representing the dynamic friction, is evaluated in the interval between 20 mm and 5 mm prior to the stopping point.

Table 4.5 summarizes the results from break-away friction testing of four materials, including both thermoplastics TP1 and TP5 and both fiber composites FC1 and FC2. For each start-up, like the one shown in Figure 4.10, the ratio between the static and dynamic coefficients of friction was calculated. Some of the start-ups recorded during the test had to be eliminated from further processing because their form was evaluated as unnatural. The remaining start-ups were used for the calculation of the average and standard deviation values listed in Table 4.5. The number of the evaluated start-ups per case is listed in the last column of the table.

According to the results of Table 4.5, ranking the four tested materials with respect to their static to dynamic friction coefficients ratio is quite straightforward. Thermoplastic TP5 performed best exhibiting the lowest ratio, followed by fiber composites FC2 and FC1. Thermoplastic TP1 exhibited the highest ratio of static to dynamic friction under all three tested pressure levels. In general, a negative trend of the static to dynamic friction ratio with increasing nominal pressure is quite clear to find in almost all tests.

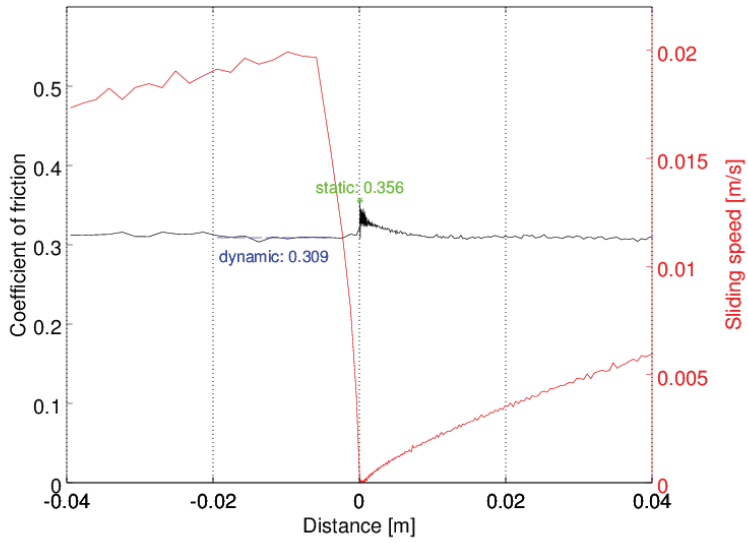

Figure 4.10: A single start-up within break-away friction testing of material FC1 at 18 MPa

Table 4.5: Static to dynamic coefficient of friction ratio

Material	Pressure	Mean μ_s/μ_k	Std. dev.	No. of start-ups
TP1	6 MPa	1.284	0.049	9
	12 MPa	1.226	0.029	11
	18 MPa	1.252	0.036	14
TP5	6 MPa	1.061	0.013	15
	12 MPa	1.051	0.012	13
	18 MPa	1.044	0.015	14
FC1	6 MPa	1.163	0.038	11
	12 MPa	1.150	0.018	12
	18 MPa	1.142	0.018	12
FC2	6 MPa	1.100	0.022	14
	12 MPa	1.093	0.008	4
	18 MPa	1.081	0.013	10

4.5 Friction testing summary

The tests described in this chapter were meant to provide an overview on the frictional behavior of a wide range of different materials running against a steel surface under a quite limited range of operational conditions that are applicable to the wind turbine yaw system. Despite the lack of many test repetitions, it was possible to draw a number of phenomenological conclusions, summarized below:

- Under dry conditions, the friction coefficient variation among the materials of the same group was higher than the differences between the material groups.
- Under grease-lubricated conditions, different materials exhibited very similar friction, with very few exceptions.
- Under dry conditions, the friction coefficient of thermoplastics was not affected by the nominal pressure.
- Under dry conditions, the tested fiber composites exhibited decreasing coefficient of friction with increasing pressure.
- Under dry conditions, the measured friction coefficient for thermoplastics remained constant in the tested sliding speed range.
- Under grease-lubricated conditions, the measured friction coefficient for thermoplastics increased with increasing sliding speed.
- Under dry conditions, the running-in distance of PET thermoplastic was very variable for the 10 mm pin specimens taken into account here.
- Under dry conditions, the static to dynamic coefficient of friction ratio dropped with increasing pressure.

Chapter 5

Wear testing

Quantifying material loss as a function of the sliding distance is the purpose of wear testing. Current standards [48] and [49] are very common references regarding wear testing on a pin-on-disc or a pin-on-plate test-rig respectively. Even if this possibility is not covered in standard [48], a pin-on-disc test-rig can also operate in reciprocating sense like shown in the previous chapter. Nevertheless, a pin-on-plate test-rig was utilized for all conducted wear tests, because it can easily be designed as a multiple implementation for testing more than one specimen in parallel. Part of the information provided in this chapter is included in Publication P3.

5.1 Pin-on-plate test-rig

Figure 5.1 illustrates the concept of the utilized pin-on-plate test-rig. Like in the pin-on-dic test-rig presented in the previous chapter, the material to be tested is in form of a flat ended cylindrical pin (1) that is vertically loaded through a dead weight (3) and a lever arm (2). This loading arm is connected to the intermediate lever (5) at the pivot point (A). With respect to the fixed sub-frame (6), lever (5) is free to rotate around pivot (B). Its rotation is restricted exclusively through force transducer (4). According to the equilibrium of moments for lever (5) around pivot (B), the horizontal force component transferred from loading arm (2) to lever (5) through pivot (A),

generates a proportional reaction in force transducer (4). By choosing the vertical distances between pivot (B) and pivots (A) and (C) to be equal, the horizontal force recorded by force transducer (4) is equal to the horizontal force component applied to pivot (A) and consequently equal to the friction force exerted on pin (1).

The counter surface consists of the interchangeable insert plate (8) which is mounted on the moving plate (7). Plate (7) is connected to the stationary frame (9) through linear bearings and is driven by a motor through a worm gear and a threaded shaft that are not included in the illustration. Its motion is linear apart from a very limited distance near the stroke ends, where the plate motion is decelerated and reversed.

This test-rig concept allows multiple instances of the loading arm substructure (1-6) and the insert plate (8) to be implemented against a common moving plate (7). The tests presented in the next section were conducted on a quadruplet implementation of the here presented pin-on-plate test-rig.

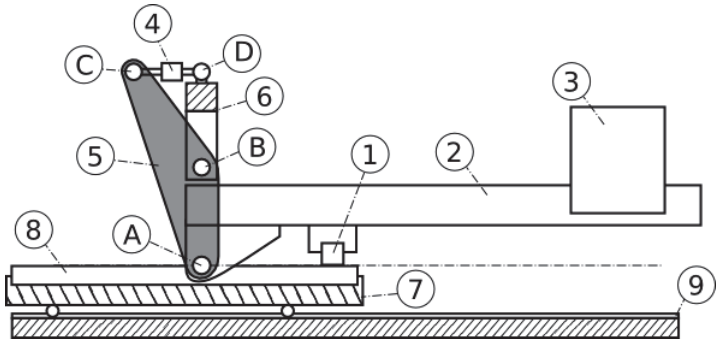

Figure 5.1: Pin-on-plate test-rig design

The construction of pivots (A) and (B) is a practical aspect that requires some further attention. Friction in pivot (A) affects the normal force applied on the pin, while friction in pivot (B) can yield to a reduced measured force in load-cell (4). In the present work, oil lubricated bronze bushings were utilized for both pivots (A) and (B). In comparison to roller element bearings, lubricated sliding bushings exhibit relatively higher static friction. However, they are more robust and they can consequently be designed with a smaller diameter so that the total friction torque will remain low. Moreover, roller element bearings under stationary load are prone to plastic deformation between the roller elements and the bearing races, which may compromise the function of the bearing and yield to unpredictable behavior.

Figure 5.2 shows the structure that supports the pin specimen. Pin (1a) with dimensions of 10 mm in diameter and 8 mm in height is glued in holder (1b) which is bolted to the intermediate plate (1c). The purpose of the intermediate plate (1c) is to provide a rigid support for the Eddy-current proximity sensor (11). Plate (1c) is

connected directly to loading arm (2) and its position in height is adjustable through an appropriate screw (10).

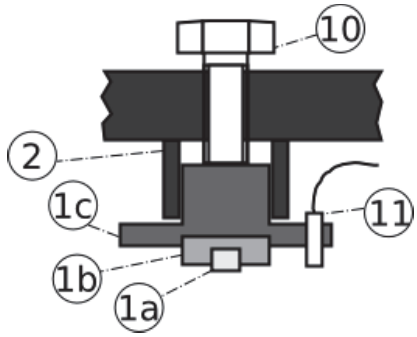

Figure 5.2: Pin holder design

The Eddy-current proximity sensor (11) provides a signal that is proportional to the gap between its free end and the counter surface (8), Figure 5.1. In case the protruding part of sensor (11) with respect to its holder (1c) is too small its linearity may be disturbed significantly, because the steel part (1c) intersects the magnetic field of the sensor. For the 5 mm in diameter sensor that was used in the implementation shown in Figure 5.3, the system was dimensioned in such a way that a minimum distance of 7 mm between the free end of sensor (11) and its holder (1c) was available, when the sensor was adjusted at a distance of 1.5 mm from the counter surface (8). The linearity of the assembled sensor was verified by mounting the compound (1b), (1c) and (11) on a height gauge and varying its vertical position in steps of 0.1 mm. At the same time the linearity coefficients between measured signal and monitored gap were specified for a gap range between 0.5 and 2.5 mm.

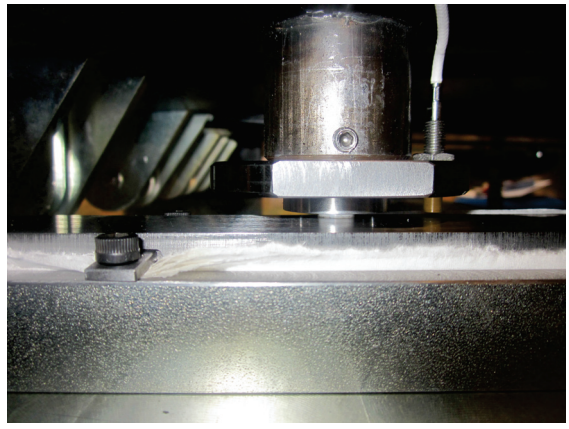

Figure 5.3: Picture of the assembled pin and proximity sensor

In order to estimate the wear displacement based on the monitored gap, one has to also take into account the different axial positions of pin (1a) and sensor (11) with respect to the pivot point (A). The wear displacement δh is equal to the difference between the monitored gap g at the current time point during a test and the gap g_0 at a reference time point, multiplied by a geometrical factor:

$$\delta h = \frac{x_{(1)}}{x_{(11)}} \cdot (g - g_0) \tag{5.1}$$

with $x_{(1)}$ and $x_{(11)}$ representing the horizontal distance from pivot point (A) to the center of the pin and the Eddy-current sensor respectively.

It should be noted that due to geometrical deviations and deformations of the construction, the gap monitored by the proximity sensor may not be completely constant during a single stroke. For this reason, the actual gap g and the reference gap g_0, to be used for the calculation of the wear displacement, they should be defined as stroke averages.

In comparison to other systems that record the wear displacement on the loading arm, the advantage of mounting the proximity sensor close to the pin sample is the minimization of possible errors from deformation and thermal expansion of the parts between the pin sample and the displacement sensor. Moreover, this setup utilizes directly the counter surface as the reference surface. In this way, any inaccuracies between this surface and the test-rig frame have no impact on the measurement. The choice of Eddy-current proximity sensors instead of capacitive sensors was based on their lower sensitivity to contaminants on the target surface.

The preparation of the pin specimens is the same as described in Chapter 4 about the pin-on-disc test-rig. Regarding the insert plate (8), it can be either ground or also polished if required. Polished surfaces are appropriate for fundamental tribological testing, whereas simply ground surfaces are relevant for testing with respect to a specific real life application with similar roughness characteristics, [49].

Both the pin sample and the corresponding plate have to be cleaned before testing. Cleaning with ethyl alcohol or isopropyl alcohol and consequently drying, repeated one or more times, was part of the testing presented in this chapter. ASTM standards [48] and [49] additionally recommend an ultrasound bath and drying in oven, however these measures were not followed here.

For each test, an unused track on plate (8) has to be used. Reusing the same track for tests with different pin materials should be avoided, because in most cases, the presence of an already formed transfer film is expected to have a non-negligible impact on the new test.

In order to ensure a correct operation of the test-rig a few alignments are required before each test. As a first step, a digital level is used in order to verify that pivot points (A) and (B) of Figure 5.1 are aligned on the same vertical line. If not, the distance CD is adjusted by modifying the length of the connectors of force transducer (4).

In order to avoid self energizing and de-energizing of the friction force, the free surface of pin (1a) and the center of pivot (A) have to lie in the same horizontal plane, when the loading arm (2) is horizontal. If not, screw (10) is adjusted until this condition is fulfilled. Next, it is ensured that when the pin is loaded against plate (8), the loading arm is horizontal and the pressure on the pin surface is uniform. For this purpose, pressure sensitive paper is put between pin (1) and plate (8) and the height of the sub-frame (6) is adjusted iteratively until a uniform imprint of the pin on the pressure sensitive paper is achieved, cf. also Figure 4.2.

5.2 Tested materials

Only a selected subgroup of the materials presented in Section 4.3 was included in the friction and wear rate testing with the pin-on-plate test-rig. Table 5.1 shows the relevant testing plan. Each of the seven test cases listed in Table 5.1 include four simultaneously tested specimens.

Table 5.1: Testing plan with respect to the pin-on-plate test-rig

Material	Conditions	Pressure	Total distance
FC1	Dry	6 MPa	5.3 km
FC2	Dry	6, 9, 12 MPa	12.3 km
TP1	Dry	6 MPa	5.3 km
TP5	Dry	6, 9, 12 MPa	10.3 km
FC3	Greased	6 MPa	5.3 km
TP1	Greased	6 MPa	5.3 km
TP5	Greased	6 MPa	5.3 km

Unlike the pin-on-disc testing that included both dry and lubricated condition for all materials, here only thermoplastics TP1 and TP5 were tested under both conditions. Fiber composites FC1 and FC2 were tested only under dry conditions while fiber composite FC3 was tested only under grease lubrication.

In this chapter, in order to proceed with wear volume estimations through weighing, the specific gravity of the tested materials is needed. The values 1.40, 1.51, 1.38 and 1.32 could be specified for materials FC1, FC2, TP1 and TP5 respectively.

Compared to the pin-on-disc testing a different grease type, with the commercial name Shell Gadus S5 T460 (HDS Stamina), was utilized for all lubricated tests with the pin-on-plate test-rig. It is a non-soap type grease that employs a diurea thickener and a mixture of PAO and esters as a synthetic base oil. The kinematic viscosity of the base oil is $460\,\mathrm{mm}^2/\mathrm{s}$, i.e. ten times higher than the base oil viscosity of the Rivolta grease described in Section 4.3. However, this Shell grease has a lower consistency of NLGI grade 1.5.

5.3 Testing results

5.3.1 Measured wear

Figure 5.4 presents the measured wear displacement for materials FC1, FC2, TP1 and TP5 during a 5.3 km long test under dry conditions at a nominal contact pressure of 6 MPa. Figure 5.5 shows the corresponding measurements for materials FC3, TP1 and TP5 under grease lubrication. All graphs in these two figures, except the graph for material TP5 with grease, have the same aspect ratio with respect to the represented data. This means that the slopes of the curves represented in the first six graphs can be compared directly. The last graph is scaled differently, stretched by a factor of five in the vertical direction, because of the very low wear observed in this case.

Two different kinds of wear behavior can be identified in the results corresponding to dry testing. Materials FC1 and TP1 exhibit an initially high wear rate that evolves rather progressively to a lower steady-state value, while materials FC2 and TP5 exhibit a very low initial wear rate which at some point shifts to a higher level, through a relatively sharp transition. Thanks to the common scaling, it is possible to rank the four materials tested under dry conditions with respect to their steady-state wear rate even visually. PET thermoplastic TP1 exhibits the lowest wear rate followed by the aramid based fiber composite FC1. Fiber composite FC2 exhibits a slightly higher steady-state wear rate, while the highest wear rate was measured for material TP5.

Regarding the three materials tested with grease, TP5 exhibits the lowest wear rate and FC3 is the middle one in the ranking. The wear rate of PET material TP1 is considerably high. It is very remarkable that material TP1 wears much faster with

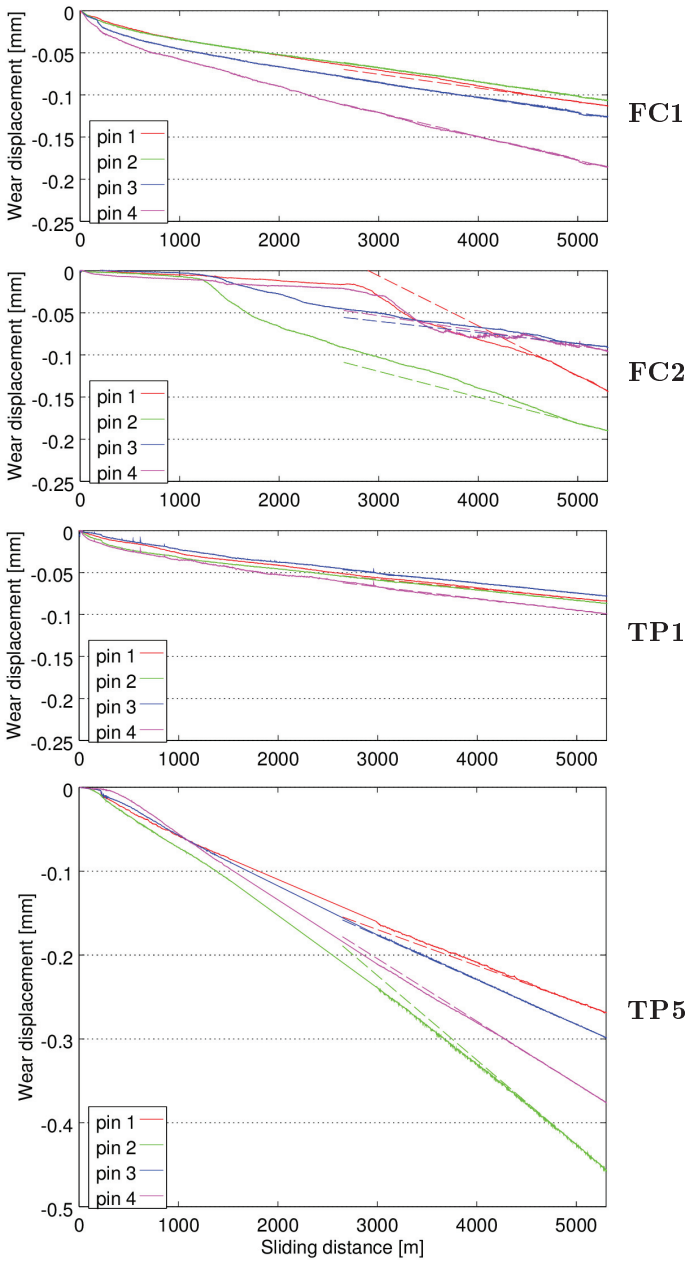

Figure 5.4: Measured wear displacement under a nominal contact pressure of 6 MPa and dry conditions

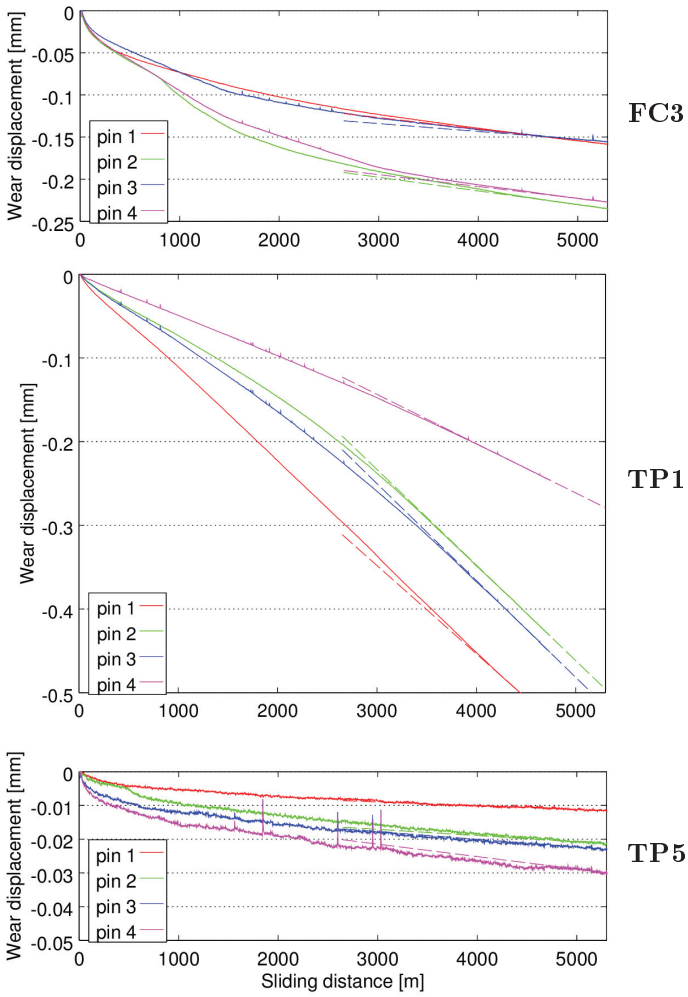

Figure 5.5: Measured wear displacement under a nominal contact pressure of 6 MPa and grease-lubricated conditions

grease lubrication than under dry conditions. This particular case is discussed further in Chapter 7. For materials FC3 and TP5, the wear evolution begins with a steeper slope which is progressively reduced until a steady state is reached, while the wear curve of material TP1 has a relatively constant slope during the whole test.

Most of the results presented in Figures 5.4 and 5.5 are validated through an independent estimation of the final wear height, based either on a coordinate-measuring machine (CMM) measurement of the pin height or on weighing of pin specimens before and after the test. Table 5.2 summarizes the total wear heights extracted from

Figures 5.4 and 5.5 and compares them to alternative estimations. By convention, wear displacement measurements that deviate less than 15% from the corresponding reference estimation, they are considered valid. In Table 5.2, only pins 3 and 4 of material FC1 and pin 4 of material FC2 exceed this limit. However, looking at the wear displacement measurements for material FC1, pins 3 and 4 exhibit an abrupt increase of the wear displacement approximately at 200 m of sliding distance. This artifact can explain the observed differences, so that the part of the corresponding curve near the end of the test can still be considered as valid for wear rate estimation. On the contrary, the wear displacement curve corresponding to pin 4 of material FC2 seems to contain artifacts near the end of the testing distance and it was consequently eliminated from further processing.

Table 5.2: Overview of measured and estimated total wear height

		Measured wear displacement	CMM based wear height measurement	Weight based wear height estimation
FC1, dry	pin 1	114 µm	-	105 µm
	pin 2	107 µm	-	100 µm
	pin 3	126 µm	-	100 µm
	pin 4	187 µm	-	154 µm
FC2, dry	pin 1	148 µm	141 µm	135 µm
	pin 2	189 µm	192 µm	172 µm
	pin 3	90 µm	103 µm	105 µm
	pin 4	93 µm	143 µm	139 µm
TP1, dry	pin 1	85 µm	92 µm	83 µm
	pin 2	88 µm	91 µm	88 µm
	pin 3	79 µm	79 µm	74 µm
	pin 4	100 µm	95 µm	92 µm
TP5, dry	pin 1	271 µm	286 µm	275 µm
	pin 2	461 µm	490 µm	478 µm
	pin 3	301 µm	310 µm	294 µm
	pin 4	379 µm	388 µm	352 µm
TP1, greased	pin 5	532 µm	520 µm	498 µm
	pin 6	432 µm	436 µm	401 µm
	pin 7	452 µm	479 µm	438 µm
	pin 8	246 µm	248 µm	221 µm

As it is mentioned in Table 5.1, materials FC2 and TP5 were tested further under dry conditions at increased pressures up to 12 MPa. For material FC2 the additional testing includes a 4 km long repetition of the testing at 6 MPa, a 2 km long test at 9 MPa and a 1 km long test at 12 MPa. Material TP5 was tested for additional 2 km

at 6 MPa, for 2 km at 9 MPa and 1 km at 12 MPa. Figures 5.6 and 5.7 show the measured wear corresponding to these additional tests. The scaling of the presented graphs was defined in such way that wear rates proportional to the nominal contact pressure would result in curves of visually equal slopes in all three graphs for 6, 9 and 12 MPa.

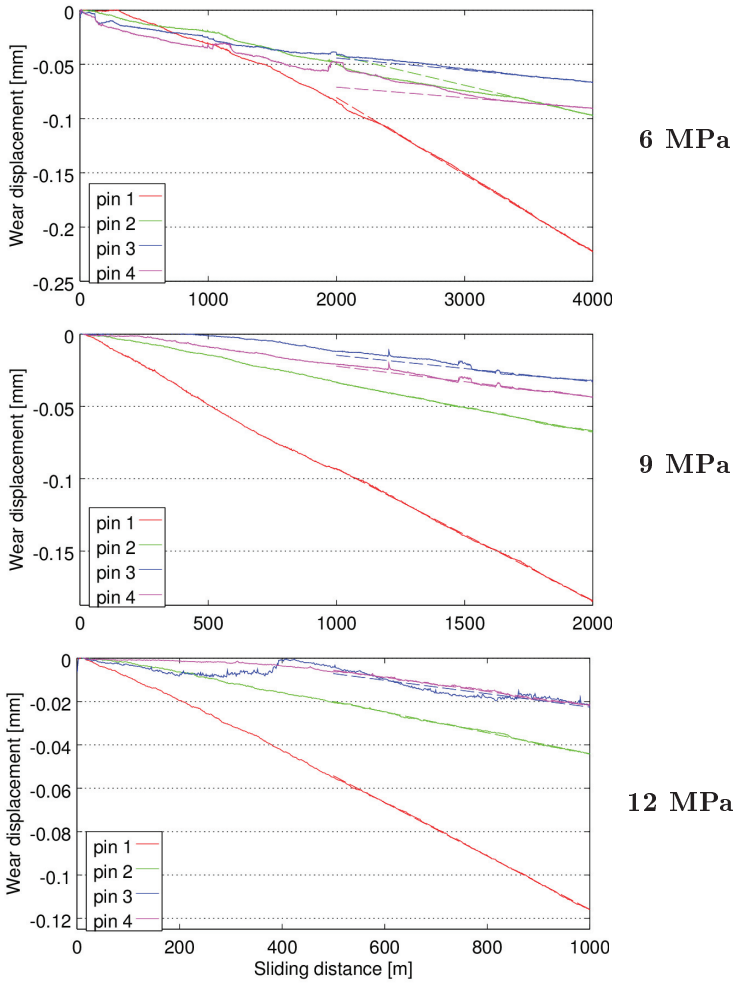

Figure 5.6: Measured wear displacement for material FC2 under dry conditions at three different pressure levels

One first observation regarding Figure 5.6 is about the running-in distance for the repeated test at 6 MPa being minimal compared to the running-in distance shown in Figure 5.4 for the original test of material FC2. This is according to one's expectation, since the already run in pins and tracks from the first test were reused for the repeated

test. Moreover, the steady-state slopes of the wear curves during the repeated test at 6 MPa are similar to the corresponding slopes from the original test. Finally, the corresponding wear curves in the three subgraphs of Figure 5.6, referring to 6, 9 and 12 MPa respectively, they appear to be relatively parallel. Given the previously explained axes scaling, this means that the wear rate for material FC2 under dry conditions is approximately proportional to the applied contact pressure.

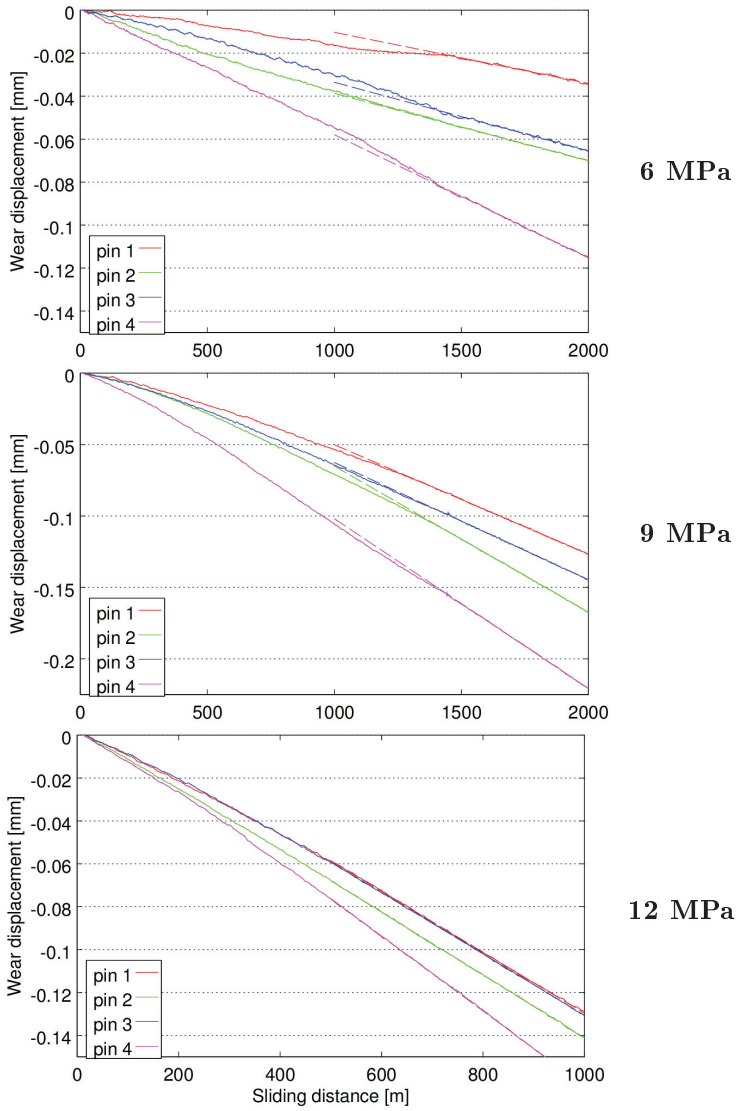

Figure 5.7: Measured wear displacement for material TP5 under dry conditions at three different pressure levels

Concerning the extended testing of material TP5, presented in Figure 5.7, there are some important differences compared to the above discussed case of material FC2. The running-in period in the repeated test of thermoplastic TP5 at 6 MPa, is not only shorter but is practically inexistent. Moreover, the steady-state wear rate defined at the end of the repeated test at 6 MPa is not the same like in the original test of TP5, presented in Figure 5.4, it is significantly lower. This result is explained by the fact, that strong vibrations observed in the original test, were not present in the second test. Slight modification of the test-rig mass distribution and aging of the pins and track surfaces may have contributed to suppressing the vibration in the repeated test.

Table 5.3: Calculated wear rates for dry testing

		6 MPa	6 MPa (2)	9 MPa	12 MPa	
FC1, dry	pin 1	16	-	-	-	µm/km
	pin 2	17	-	-	-	µm/km
	pin 3	18	-	-	-	µm/km
	pin 4	28	-	-	-	µm/km
	avg.	20	-	-	-	µm/km
	c.o.v.	28%	-	-	-	
FC2, dry	pin 1	59	71	91	123	µm/km
	pin 2	31	28	34	48	µm/km
	pin 3	13	11	18	31	µm/km
	pin 4	-	10	21	33	µm/km
	avg.	34	30	41	59	µm/km
	c.o.v.	68%	95%	82%	74%	
TP1, dry	pin 1	11	-	-	-	µm/km
	pin 2	12	-	-	-	µm/km
	pin 3	12	-	-	-	µm/km
	pin 4	14	-	-	-	µm/km
	avg.	12	-	-	-	µm/km
	c.o.v.	9%	-	-	-	
TP5, dry	pin 1	43	24	77	142	µm/km
	pin 2	101	31	102	147	µm/km
	pin 3	53	32	82	143	µm/km
	pin 4	75	57	119	175	µm/km
	avg.	68	36	95	152	µm/km
	c.o.v.	38%	40%	20%	10%	

One fundamental difference between the wear behavior of materials FC2 and TP5 is related to the increased impact of the contact pressure on the wear rate of thermo-

plastic TP5. It is demonstrated in Figure 5.7 that at higher pressure the wear curves of all four tested pins exhibit steeper slopes, although the graph axes are carefully scaled so that a linear impact of the applied pressure would be compensated. This means that, unlike the case of material FC2, the wear rate of material TP5 is not directly proportional to the applied contact pressure.

Table 5.4: Calculated wear rates for testing with grease at 6 MPa

FC3, greased	pin 1	14 µm/km
	pin 2	16 µm/km
	pin 3	9 µm/km
	pin 4	14 µm/km
	avg.	13 µm/km
	c.o.v.	22%
TP1, greased	pin 1	105 µm/km
	pin 2	114 µm/km
	pin 3	116 µm/km
	pin 4	59 µm/km
	avg.	99 µm/km
	c.o.v.	27%
TP5, greased	pin 1	1.1 µm/km
	pin 2	1.8 µm/km
	pin 3	2.3 µm/km
	pin 4	3.7 µm/km
	avg.	2.2 µm/km
	c.o.v.	50%

Besides the visual inspection of the so far presented graphs, which relies on appropriately scaled axes, the steady-state wear can also be expressed quantitatively. By considering the last 500 m of each test as a representative interval for the steady state, a straight line can be fitted to the data contained in this last portion of the test and the slope of the fitted line expresses the actual wear rate. The fitted lines at the end of each test are depicted as dashed lines in the presented graphs. Tables 5.3 and 5.4 summarize all calculated wear rate values corresponding to the previously presented graphs. Apart from the individual values per pin specimen, an average per tested material and the corresponding coefficient of variance are also listed in the tables.

One further aspect to be discussed, is the variability of the wear measurements per material. With four pin specimens per tested material, some of the tested materials exhibited quite reproducible results, whether for other materials there was a high variation in the estimated wear rates. The case with the best reproducibility was for the testing of material TP1 under dry conditions, while material FC1 under dry

conditions and materials TP1 and FC3 under lubricated conditions, also exhibited relatively small variations. Regarding the test of material TP5 with grease, capturing so low wear levels accurately is difficult and some of the observed variation among the pins may be due to inherent limitations of the testing setup itself. The highest variations were observed during testing of materials FC2 and TP5 under dry conditions at 6 MPa. However, for increased pressure levels the variation in the results of material TP5 dropped significantly.

5.3.2 Measured coefficient of friction

As explained in Section 5.1, the utilized pin-on-plate test-rig is equipped with force transducers for recording the actual friction force per pin specimen. In order to complete the documentation of the presented experiments, Tables 5.5 and 5.6 list the average coefficient of friction and the corresponding coefficients of variance for the pin-on-plate testing under dry and grease-lubricated conditions respectively. The corresponding coefficient of friction values from the pin-on-disc testing, presented in Chapter 4, are given in the last column as reference.

Table 5.5: Measured coefficients of friction in dry testing

		6 MPa	6 MPa (repetition)	9 MPa	12 MPa	pin-on-disc 6 MPa
FC1, dry	avg.	0.33	-	-	-	0.39
	c.o.v.	6%	-	-	-	
FC2, dry	avg.	0.53	0.56	0.53	0.49	0.54
	c.o.v.	18%	18%	17%	9%	
TP1, dry	avg.	0.26	-	-	-	0.35
	c.o.v.	9%	-	-	-	
TP5, dry	avg.	0.39	0.44	0.43	0.43	0.44
	c.o.v.	11%	3%	3%	3%	

In general there is relatively good agreement between the friction levels measured via the pin-on-disc and pin-on-plate test-rigs. One important mismatch is observed for the PET thermoplastic TP1. This is assumed to be related to the formation of different transfer layers on the steel surface and is explained further in Chapter 7. The deviation observed in the grease-lubricated tests with the fiber composite FC3 and thermoplastic TP1 are assumed to be related to the amount of grease trapped on the testing track. In the case of the pin-on-disc test-rig the pin runs on a closed circular track, which is a more favorable situation for retaining grease in the contact than the open-ended track on the steel plate of the pin-on-plate test-rig. Regarding

Table 5.6: Measured coefficients of friction in testing with grease

		6 MPa	pin-on-disc 6 MPa
FC3, greased	avg.	0.21	0.15
	c.o.v.	11%	
TP1, greased	avg.	0.17	0.13
	c.o.v.	15%	
TP5, greased	avg.	0.14	0.14
	c.o.v.	33%	

material TP5, it is also assumed to have a better capability of storing grease internally, so that under grease lubrication it exhibits the same low friction on both test setups. Chapter 7 provides more specific information on how grease is stored in a thermoplastic material similar to TP5.

Finally, Figure 5.8 summarizes the results presented in this chapter by showing the measured wear rate values as a function of the corresponding coefficient of friction measurements.

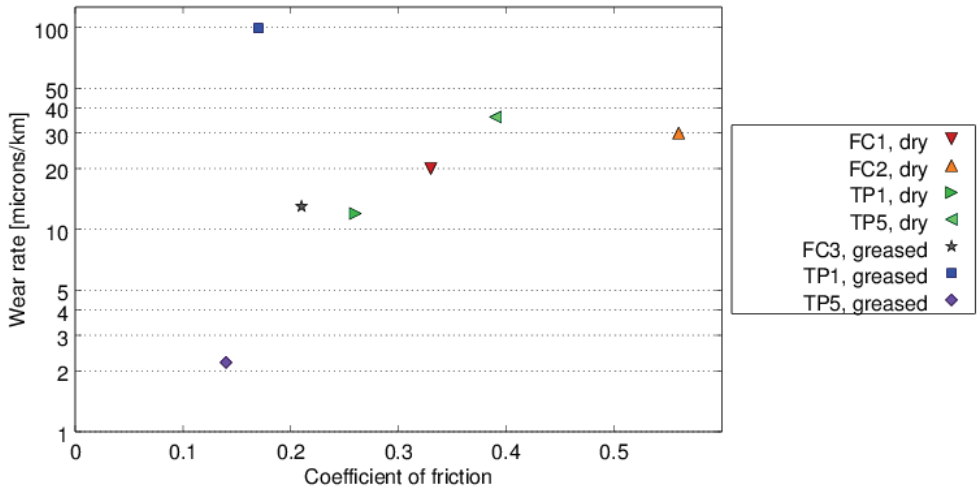

Figure 5.8: Correlation between measured wear rates and coefficients of friction at 6 MPa

Chapter 6

Use of experimental data

In the previous chapters, it was shown how the load distribution among the yaw system segments can be estimated and experimental data about the friction and wear of different friction materials were provided. The present chapter shows how such experimental data, combined with a calculated or assumed load distribution can be utilized in practical estimations of the system braking torque as well as for predicting the expected wear height. Moreover, a general theoretical framework is provided, for interpreting the obtained friction testing results with respect to friction-induced noise issues.

6.1 Braking torque calculation

As described in Chapter 1, the considered yaw system is supposed to provide full braking functionality without further assistance of an additional disc brake. For this reason it is important to assess the braking torque provided by the system, considering both the load distribution discussed in Chapter 2 and the experimental data presented in Chapter 4. If the system fails to provide the required braking torque, the excess load will be transferred to the driving system and can consequently damage the corresponding gears.

Apart from a very limited period at the beginning of the system lifetime, until running-in of the friction materials is completed, the braking torque is a magnitude that is defined at each specific time point by the conditions and loads applying to that very moment. It does not depend significantly on the load history prior to this point. Hence, it is sufficient to simply recognize which operational conditions are less favorable and verify that the braking torque is not lower than the actually applied yaw moment. In this section, it will assumed for demonstration purposes that the load case from Table 2.1 is the critical one for assessing the braking torque capacity of the system. In the general case however, more than one load cases may be necessary to examine.

A straightforward way to derive expression for calculating the yaw system braking torque is the following:

$$M_b = R_{mean} \cdot \sum_i \left(\mu_U P_{U,i} A_U + \mu_L P_{L,i} A_L\right) + R_{min} \cdot \sum_i \mu_R P_{R,i} A_R \tag{6.1}$$

with R_{min} and R_{mean} referring to the radii of the flange where the radial sliding pads and the upper and lower pads act respectively. Different coefficients of friction μ_R, μ_U and μ_L for the three interfaces have to be considered, not only because of the possible different friction material in use, but also because of the possibly different pressure levels in each interface. According to the friction testing results presented in Chapter 4, the coefficients of friction should actually be considered as a function of the applied pressure, in general. For the sake of simplicity however, a constant representative friction coefficient value can be assumed for each of the three interfaces, so that Equation (6.1) can be simplified as following:

$$M_b = R_{mean} \left(\mu_U A_U \sum_i P_{U,i} + \mu_L A_L \sum_i P_{L,i}\right) + R_{min} \mu_R A_R \sum_i P_{R,i} \tag{6.2}$$

Assuming, for demonstration purposes, that the reference yaw system defined in Table 2.1, utilizes pads made of fiber composite FC1 for all three contact interfaces, all three coefficient of friction values μ_R, μ_U and μ_L can be estimated based on the curve corresponding to material FC1 in Figure 4.6. In order not to overestimate the braking torque capacity of the system, the coefficient of friction at the maximum pressure for each interface has to be considered. For the assumed load case, according to Table 2.3, the contact pressure in the radial interface is not expected to exceed 2.9 MPa, while in the upper and lower interfaces the maximum contact pressures under full braking are 18 MPa and 11.4 MPa respectively. For these pressure levels, the corresponding graph of Figure 4.6, provides the values $\mu_R = 0.38$, $\mu_U = 0.315$ and $\mu_L = 0.345$. With these values, the loads from Table 2.3, corresponding to the higher clamping force F_C, and with the estimated radii $R_{mean} = 600$ mm and $R_{min} = 570$ mm, Equation (6.2) results in a braking torque $M_b = 584$ kNm.

Apart from assessing the braking torque capacity of the system, it may be necessary for dimensioning the driving system, to estimate the friction torque in the yaw system under the lower clamping force F_C, corresponding to the yawing phase. In this case, in order to be on the safe side, it is important not to underestimate the actual friction coefficients. For this reason, if one single friction coefficient value is to be used, it is recommended to use the maximum friction coefficient over the tested pressure range. In the case of material FC1 for instance, a friction coefficient of 0.39 would be extracted from Figure 4.6.

Additionally, in order to account for the break-away friction that the driving motors have to overcome, it is necessary to multiply the obtained dynamic friction coefficient with the corresponding static to dynamic friction ratio from Table 4.5. For material FC1 for example, this ratio is equal to 1.163. Utilizing this value, for the assumed configuration with material FC1 employed in all three contact interfaces, a common maximum coefficient of friction for all three interfaces can be estimated as $\mu_R = \mu_U = \mu_L = 0.45$. With this friction coefficient value and the loads from Table 2.3, corresponding to the lower clamping force F_C, the calculated friction torque $M_b = 282$ kNm can be considered as a condition for dimensioning the driving system.

6.2 Wear calculation

As explained in Chapter 2, the complete load spectrum is relevant for calculating the total wear of the yaw system pads during the wind turbine lifetime. In order to demonstrate such a calculation, the loads envelope described in Table 2.4 will be considered as an example. The calculation will be limited to the brake/sliding pad of the upper interface of segment 1, located at 15° from the downwind direction. The calculation procedure can be applied in the same way for all other pads. In this demonstration, it will be assumed that fiber composite material FC2 is utilized as the brake/sliding pad of the upper interface.

Assuming a linear accumulation of wear, the equation for calculating the total wear height $W_{h,U,i}$ for the upper pad of the i-th segment during the system lifetime, is the following:

$$W_{h,U,i} = \sum_k w_U(P_{U,i,k}) s_k \tag{6.3}$$

with w_U representing the wear rate of the upper pad material and s_k referring to the total sliding distance for the k-th load case, e.g. according to Table 2.4. The corresponding expressions for the lower and the radial interfaces are similar.

For the considered pad material FC2 under dry conditions, the wear rate w_U can be expressed as a function of the applied pressure by fitting a linear relation to the wear

rates of 30, 41 and 59 µm/km at 6, 9 and 12 MPa respectively, as they are reported in Table 5.3. The fitted line for w_U is given by the equation below.

$$w_U = 4.8 \cdot P_U \tag{6.4}$$

With this approximation and the pressures reported for segment 1 in Table 2.5, the total wear height for the upper pad of segment 1 can be estimated according to Equation (6.3) as $W_{h,U,1} = 33$ mm.

It should be noted that the pressure range experienced by the considered pad is between 3.8 and 6 MPa and lies slightly outside the range of the experimental data that Equation (6.4) is based on. Looking at the corresponding curve of Figure 6.1, where Equation (6.4) is represented by a dotted line, the performed extrapolation is justified. On the contrary, for material TP5 a similar extrapolation would underestimate wear to a large extent. In cases like this, in order to be on the safe side, it is recommended to use the dashed line between 0 and 6 MPa for extrapolating the experimental data to lower pressures

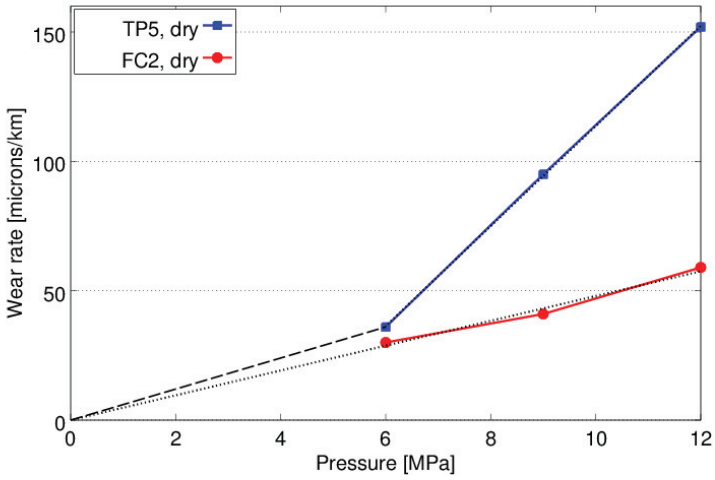

Figure 6.1: Impact of pressure on wear rate, according to Table 5.3

6.3 Noise generation

The motivation for conducting the break-away friction tests presented in Chapter 4 was related to the phenomenon of friction-induced noise. Noise generation as a consequence of the relative sliding in a frictional contact is a phenomenon of dynamic

instability causing vibration of diverging amplitude until non-linear effects will prevent the amplitude from increasing further.

Basically, there are two categories of mechanisms that can cause dynamic instabilities in a system with sliding friction. The first one is one dimensional and is related to self-excited oscillations in direction parallel to the sliding direction while the second category involves both the tangential and normal directions.

Figure 6.2 shows a simplified one dimensional model with a single degree of freedom, which can help in explaining the first category of friction related dynamic instabilities.

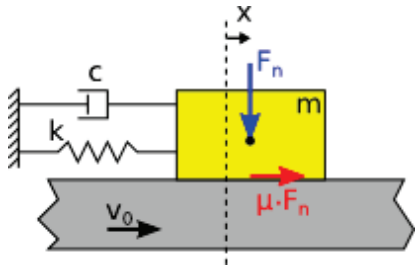

Figure 6.2: Simple model describing self-excited oscillation in frictional sliding

The equation of motion with respect to the position x of the single mass oscillator, depicted in this figure, is the following:

$$m\ddot{x} + c\dot{x} + kx = \mu(v_0 - \dot{x})F_n \tag{6.5}$$

Self-excited oscillation can occur as a consequence of a sliding speed dependent coefficient of friction μ, that decreases with increasing sliding speed. Assuming that the coefficient of friction is equal to μ_0 at a reference speed v_0 and denoting with α_v the negative relative slope with respect to the sliding speed, the coefficient of friction can be expressed as a linear function of the sliding speed v:

$$\mu(v) = \mu_0 \left(1 - \alpha_v(v - v_0)\right) \tag{6.6}$$

It should be noted that α_v has a positive value when the slope of the friction curve with respect to the sliding speed is indeed negative. Substitution of Equation (6.6) into Equation (6.5) yields the following equation of motion:

$$m\ddot{x} + (c - \alpha_v \mu_0 F_n)\dot{x} + kx = \mu_0 F_n \tag{6.7}$$

From Equation (6.7), it becomes obvious that if $\alpha_v \mu_0 F_n$ exceeds the original damping coefficient c, then the effective damping coefficient in Equation (6.7) becomes negative, giving rise to a self-excited oscillation of the mass.

The above described mechanism of self-excited oscillation is related to a negative slope $\alpha_v \mu_0$ in the coefficient of friction curve as a function of the sliding speed. The relevant experimental data from Chapter 4 for evaluating the possibility of this kind of friction-induced noise are available in Figure 4.8 for thermoplastics TP2 and TP4 under both dry and grease-lubricated conditions. The absence of a negative slope suggests that these two materials are not prone to this kind of dynamic instability.

In the case of friction related dynamic instabilities that involve both the tangential and normal directions, self-excited oscillation is consequence of a coupling between the normal force F_n and the displacement x. The coupling may be because of trivial mechanical configurations like the one illustrated in the left part of Figure 6.3, or it can be related to complex mechanical phenomena like frictional slip waves, presented in a very simplified manner in the right part of Figure 6.3. The basic idea of interfacial waves is that the tangential velocities of the surfaces fluctuate spatially around their mean value as well as the vertical displacements but with a different phase. Depending on the exact form of the fluctuations and their phase difference, there can be areas of the interface that are under stick conditions while in other areas there might be slip with higher relative speed than nominally.

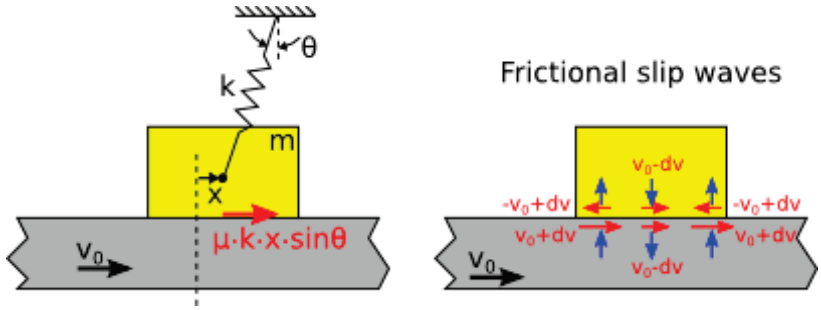

Figure 6.3: Simple model describing dynamic instability in frictional sliding due to normal and tangential force coupling

The cases presented of Figure 6.3 are only for explaining the basic physics. How these physics manifest themselves in each specific case, depends on the stiffness, damping and the eigenvalues of the system but also on the behavior of the coefficient of friction at the interface. Concerning the onset of stick-slip in particular, regardless if it involves a rigid body motion like the example in the left part of Figure 6.3 or if it involves local deformations like the case in the right part, the most important tribological property is the ratio between the static and dynamic coefficient of friction, as provided in Table 4.5. In order for a stick-slip mode of sliding to occur, a combination of high static to dynamic friction ratio, high coefficient of friction and appropriate system eigenvalues and eigenforms are necessary. More in-depth information regarding the above described phenomena and friction-induced noise in general, can be found in textbook [50].

Chapter 7

Friction and wear mechanisms

For a given tribological contact between conformal bodies, the apparent contact area and the nominal pressure are usually known or can be estimated beforehand. However, what is important for studying the coefficient of friction and wear between the contacting surfaces theoretically, is the real contact area and the local pressure within the contact spots at the individual asperity summits. The following sections in this chapter are intended for describing in a qualitative manner the relation between different mechanisms defined at microscale level and the macroscopically observed friction and wear characteristics. The discussion to follow is partly based on published literature but it is also supported by micrographs and surface roughness measurements of specimens from the previously presented testing.

7.1 Collection of measured surfaces

In order to establish a connection between microscale reality and the theoretical considerations to be discussed in the next sections, Figures 7.1 to 7.4 represent a collection of roughness profiles measured on specimens previously used in the pin-on-disc dry testing presented in Chapter 4.

All presented roughness profiles are measured in direction perpendicular to the sliding direction, using a stylus profilometer with a tip radius of 0.2 µm. The 3 mm long profiles on the left side of Figures 7.1 to 7.4 correspond to the middle area of a total

measuring length above 4 mm. The right-side graphs illustrate the first 0.5 mm of the corresponding left-side ones, but with equally scaled axes, so that surface slopes are represented realistically. The red part of the graphs refers to the pin specimen and the blue one to the corresponding disc track after the dry testing phase presented in Chapter 4 (procedure step 3). It can be observed that the feed-rate for the machining of the disc surface is 0.1 mm/rev in all cases except the disc corresponding to pin material TP5, which was unintentionally machined at a smaller feed-rate.

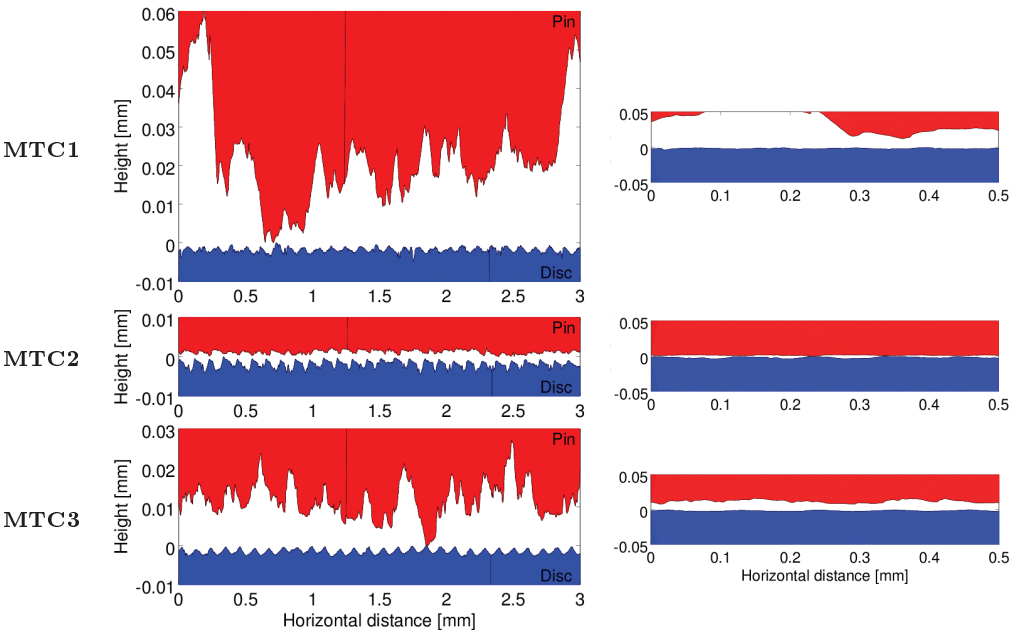

Figure 7.1: Measured surface roughness profiles for specimens from pin-on-disc testing under dry conditions

In Figure 7.1, pins made of the coarse and middle grained materials MTC1 and MTC3 respectively, exhibit at steady state much rougher surfaces compared to the corresponding disc track profiles. Different from this the surface of material MTC2 is somewhat smoother than the disc surface.

Regarding Figure 7.2, the pin specimen made of PET material TP1 exhibits a somewhat smoother surface than the corresponding disc, while for PET material TP2 the pin and disc surfaces have similar roughnesses and the profiles seem to match together. The pin made of material TP3 exhibits quite similar roughness to the disc surface. Finally, both reinforced polyamide materials TP4 and TP5 exhibit similar surfaces, which are in both cases quite rougher compared to the disc surfaces. In both cases, relatively flat plateaus, interrupted by approximately 10 µm deep valleys, can be observed.

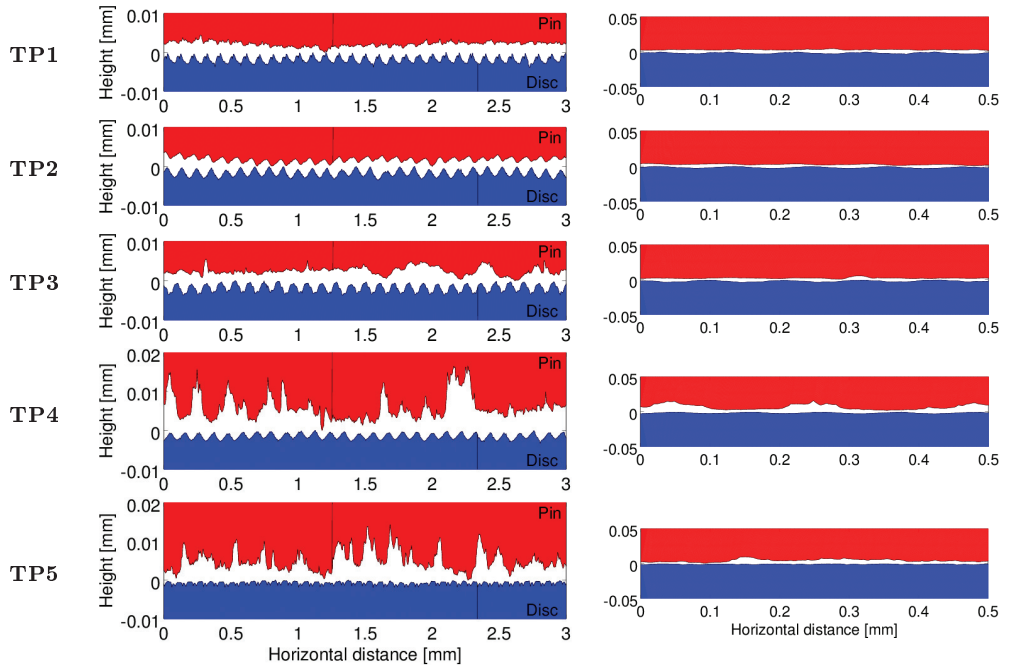

Figure 7.2: Measured surface roughness profiles for specimens from pin-on-disc testing under dry conditions

The surfaces of all three fiber composite pins in Figure 7.3 are very rough in comparison to the disc surfaces. Especially regarding material FC2, the 3 mm long profile consists of several plateaus and craters. Finally, surface roughness profiles from testing of sintered materials in Figure 7.4, show not only very rough pin surfaces but also relatively rough disc track surfaces, due to abrasion of the disc and material transfer.

7.2 Frictionless normal contact

Before considering friction and wear between two contacting surfaces under relative sliding, it is essential to study the normal contact between rough surfaces without relative sliding and friction. A simplified but very insightful explanation on normal contact between two nominally flat rough surfaces was given in the classical paper of Greenwood and Williamson [20]. In this work, the contact between two rough surfaces is reduced to independent contacts between spherical asperities and a rigid plane according to the Hertzian theory. An average curvature radius R_p of all asperity peaks defines the radius of the idealized spherical asperities, while the statistical distribution of the peak heights is assumed to be Gaussian with a standard deviation equal to σ_p.

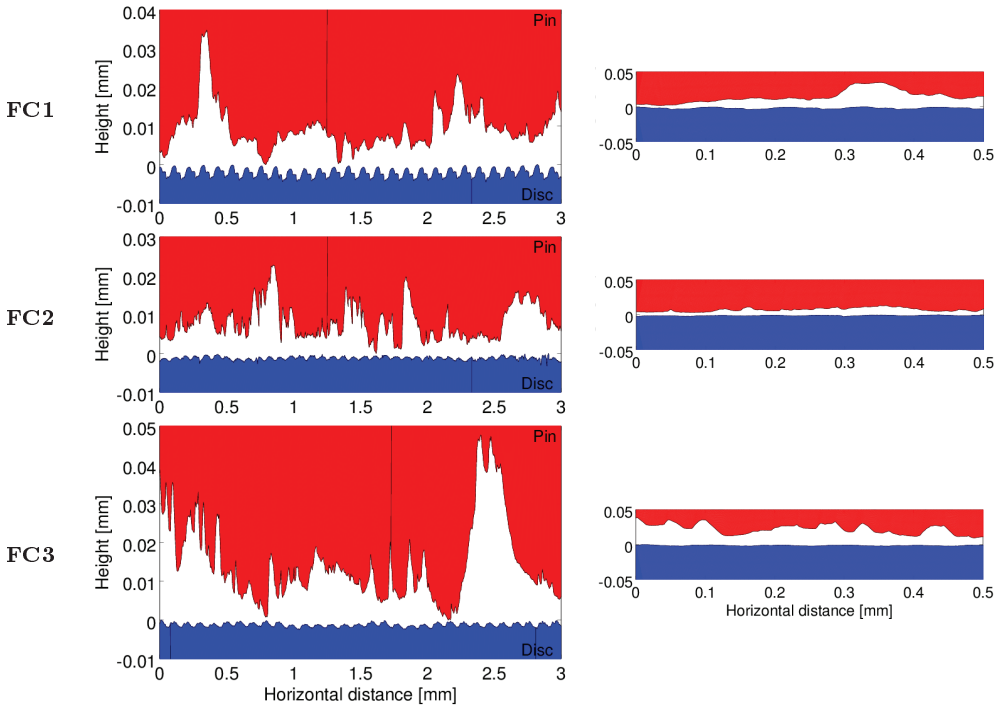

Figure 7.3: Measured surface roughness profiles for specimens from pin-on-disc testing under dry conditions

In this simplified model, the impact of the deformation of one asperity on its neighbor asperities is neglected. Under these assumptions it was demonstrated that the real contact area is approximately proportional to the normal load. Based on a further assumption about the onset of plastic deformation when exceeding a threshold related to the hardness H of the softer of the materials in contact, the Greenwood and Williamson theory [20], can predict if the asperities will mainly deform elastically or plastically. For this purpose the so called plasticity index was introduced:

$$\psi = \frac{E'}{H}\sqrt{\frac{\sigma_p}{R_p}} \tag{7.1}$$

where E' is the effective elasticity modulus. For $\psi < 0.6$, roughness asperities will deform elastically in nearly all contact spots, whereas for $\psi > 1$ plastic deformation will occur almost exclusively.

In an effort for providing a visual explanation of the Greenwood and Williamson theory [20], Figure 7.5 shows three different types of surface roughness. In comparison to the reference surface (A), surface (B) exhibits increased peak heights deviation σ_p but the same peak curvature radius R_p, whereas surface (C) has the same peak

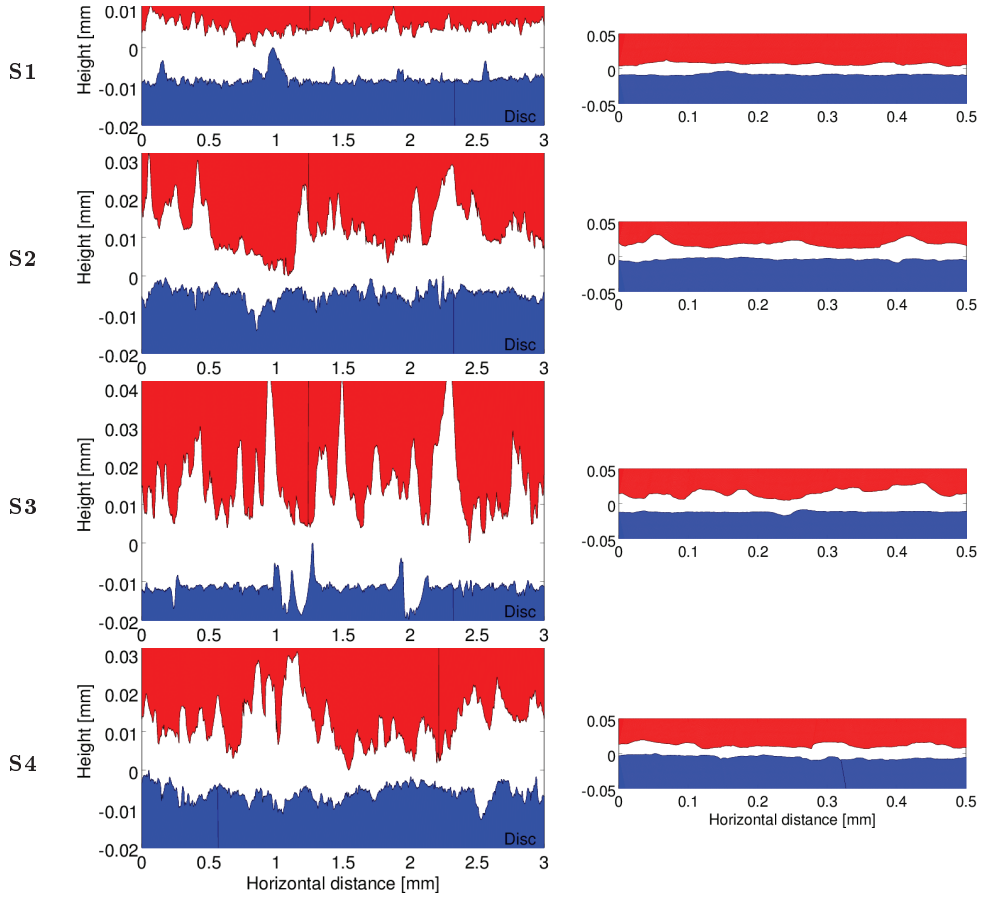

Figure 7.4: Measured surface roughness profiles for specimens from pin-on-disc testing under dry conditions

heights deviation σ_p as surface A but a lower peak curvature radius R_p. When considering the contact between the illustrated surfaces and a rigid flat plane, according to the Greenwood and Williamson theory both surfaces (B) and (C), in comparison to surface (A), for a given load will:

- have lower percentage of asperities in contact
- exhibit a lower real contact area and higher mean pressure
- have a higher plasticity index

In general, when increasing the load transferred through a contact interface with high plasticity index, the already loaded asperity peaks will be loaded further and

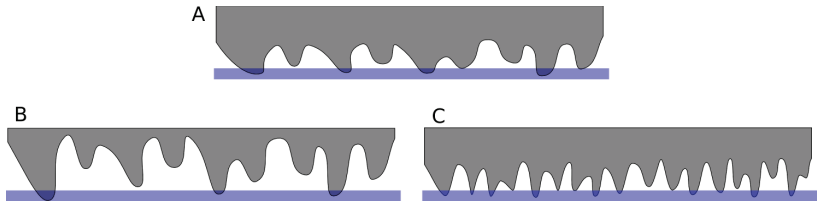

Figure 7.5: Comparison of different roughness types. (A) reference surface, (B) increased peaks height deviation, (C) reduced peak curvature radius

deform plastically, before new asperities will come into contact. For surfaces with low plasticity index, new asperity contacts will carry the majority of the load increase before the already loaded asperities reach their plastic limit.

The Greenwood and Williamson theory, as presented above in its original form, is a very good means of illustrating the basic phenomena governing the behavior of the contact between rough surfaces. Its assumptions about a fixed peak curvature, a Gaussian peak height distribution and negligible inter-asperity interactions, along with the consideration of a single size scale, do not allow its application for a quantitative analysis of the contact between real rough surfaces.

It is well-known and it can also be recognized in some of the profiles presented in Section 7.1, that realistic surfaces are multi-scale. The definition of peaks depends on the size scale under consideration and in practice it is very difficult to approximate a measured surface through spheres of constant curvature distributed at different height positions. The Greenwood and Williamson theory has been extended to include a surface approximation through ellipsoids of variable curvatures and possible compensation of inter-asperity interaction, [51] and [52]. However, each addition is at the cost of moving away from the simplicity of the original model.

As already indicated in Section 1.2, a different approach to the problem of normal contact between rough surfaces is based on a fractal description of the surfaces and represented by the models introduced in references [24] and [25]. Although these two models account for the multi-scale nature of real surface, they are still approximative. The first one neglects inter-asperity interactions and hence is more accurate in the low pressure regime, while the second model is based on the case of full contact and hence it is more accurate at high contact pressures. Reference [53] provides a very comprehensive comparison of the so far discussed contact models and suggests possible improvements.

Finally, deterministic models for the contact between rough surfaces try to draw conclusions about the contact by simulating representative surface samples loaded against each other. The already mentioned in Section 1.2 references [26], [27], [28]

and [29] are characteristic examples. The disadvantage of this kind of models is that they are limited to one size scale or a limited range of size scales and their main advantage is that they inherently account for inter-asperity interactions. Moreover, they do not require any sophisticated analysis of the measured topographies, they use such topographies directly as a model input. They are also easy to extend to plasticity, inhomogeneous materials and relative sliding between the contacting surfaces.

7.3 Friction

7.3.1 Phenomenological friction hypotheses

The following three classical friction hypotheses apply approximately in several practical applications.

- Amonton's first hypothesis: the friction force is proportional to the normal force.
- Amonton's second hypothesis: the friction force is independent of the apparent contact area.
- Coulomb's hypothesis: the friction force is independent of the sliding velocity.

However, in many cases these rules cannot describe the observed coefficient of friction in a given contact. This is the case for the pressure and sliding speed dependent coefficients of friction observed in Figures 4.6, Figures 4.7 and 4.8. The running-in graphs of Figure 4.3 show that coefficient of friction can also depend on the sliding distance. In general the friction coefficient between two nominally flat surfaces may depend on the following parameters:

- Material combinations.
- Contacting surfaces condition (contamination, oxidation and lubrication).
- Contacting surfaces roughness topography.
- Normal load, apparent contact area, nominal contact pressure.
- Sliding velocity.
- Sliding distance (e.g. during running-in).

7.3.2 Friction mechanisms

At microscopic level, there are different mechanisms contributing to the macroscopically observed friction force. Figure 7.6 presents a rough categorization of these mechanisms through an example of a single asperity in contact. When there is no relative sliding or if materials exhibit perfectly elastic behavior, a symmetric pressure field acts on the asperity as a repulsion force from the counter surface. If there is relative sliding and there is viscoelastic or plastic deformation or fracture in the bulk materials, an asymmetric pressure field occurs, like in the first two cases of Figure 7.6 respectively. In this case, there is a horizontal resultant force from integrating the applied pressure, which depends on the slope of the asperity flanks of the strongest of the materials in contact and the deformation behavior of the weakest one. As it can be seen in Figures 7.1 to 7.4 the steel disc which is normally the strongest of the materials in contact, exhibits surface roughness, perpendicular to the sliding direction, with very small asperity slopes. The corresponding slopes in direction parallel to sliding are expected to be even smaller, resulting in a very limited mechanical contribution to the observed coefficient of friction.

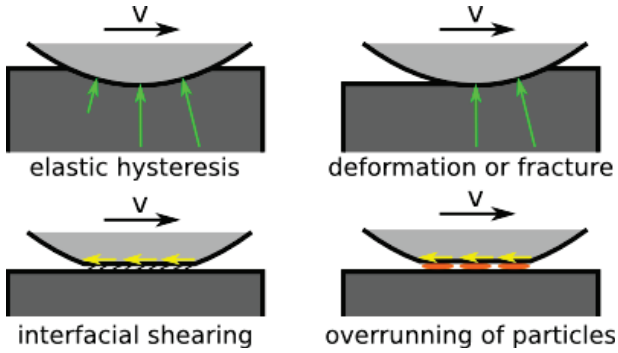

Figure 7.6: Basic mechanisms for dry and boundary lubrication friction

Apart from generating a friction force through normal forces (pressure) on inclined faces of a surface topography, friction can also appear directly in form of shear stress at the interface of the contacting bodies. This case is represented by the third picture of Figure 7.6. The interfacial shearing may occur directly between the bulk materials or it may take place within a third body attached as a thin film on the contacting surfaces. In any case some kind of chemical bonding, either between the two bulk materials or between a bulk material and the third body, is necessary. For this reason, this friction mechanism is often referred to as adhesive friction.

The nature of adhesion in case of metal-to-metal contact is through shared free electrons (metallic bonding) and can also be characterized as co-welding. If the bond strength is higher than the strength of the weakest material, shearing occurs within

the material rather than in the bond. In case of metal-to-ceramic contact the metal atoms tend to bond with the oxygen atoms of the ceramic in a similar manner like in forming metal oxides. Adhesion between polymers and metals is mainly due to van der Waals forces. However, these forces are normally weaker than the cohesion forces in the bulk polymer. More thorough information on adhesion mechanisms can be found in textbook [22] (chap. 12).

Also when interfacial shearing involves a thin layer of a third body between the primary contacting bodies, some bonding between the third body and the bulk materials is necessary. This can be one of the above outlined adhesion mechanisms or it can be based on diffusion of the third body into the bulk material.

Finally, there is the possibility presented in the lower right picture of Figure 7.6, where the third body is not in form of a film attached on the surface, but it consists of loose particles that are overrun by the contacting surfaces during sliding. The friction loss corresponds to the energy consumed in deforming, crushing and compacting the particles. In order for this loss to manifest itself as a friction force, some kind of traction between the particles and the moving surfaces is necessary. This connection can either be in form of the previously discussed adhesion mechanisms or it can simply be due to mechanical interlocking.

It should be noted here that in the microscopic or atomic scale the relationship between normal stress and shear strength within a contact region, not necessarily resembles Amonton's first hypothesis, not even approximately. Considering the limited possibilities of determining such interfacial constitutive laws in the microscopic scale experimentally, quite simple expressions are normally sufficient for representing the currently limited understanding of these systems. Equation (7.2), which assumes a constant shear strength τ, is typically mentioned in connection with the Bowden and Tabor theory, [18]. Equation (7.3), which involves the local contact pressure p, is also used often, especially in cases that involve shearing of adsorbed thin films, [54] (chap. 4) and [55]. Finally, Equation (7.4) is typically used in tribosystems related to metal forming, [56]. In these three equations, τ_0 is an initial pressure independent shear strength, τ_{lim} is an upper limit and coefficient α is equivalent to coefficient of friction in the microscopic scale.

$$\tau = \tau_{lim} \tag{7.2}$$

$$\tau = \tau_0 + \alpha p \tag{7.3}$$

$$\tau = \min(\tau_{lim}, \alpha p) \tag{7.4}$$

Although the behavior in small size scales of contact interfaces may vary very significantly among different tribosystems, macroscopically most tribosystems will follow

Amonton's first hypothesis, at least approximately. This macroscopic behavior is known to occur due to the multiscale nature of surface roughness which leads to an approximately linear relationship between the applied load and the real area of contact, as explained e.g. in reference [57].

In general, the coefficient of adhesive friction μ_{adh} for a given contact can be related to the corresponding microscopic constitutive law by integrating the appropriate equation among Equations (7.2), (7.3) and (7.4) and divide by the total load. In case of Equation (7.3) for example, the result will be:

$$\mu_{adh} = \tau_0/p_m + \alpha \tag{7.5}$$

with p_m expressing the average contact pressure within the real area of contact.

According to Equation (7.5), Amonton's first hypothesis is fulfilled either if τ_0 is zero or if p_m is constant, independent of the applied nominal pressure, or in other words, if the real area of contact is proportional to the nominal pressure.

7.3.3 Running-in

The above presented discussion on friction mechanisms means, that the macroscopically observed friction depends on the chemical properties of the contacting surfaces, their topography and the deformation properties of the bulk materials. Among these three factors, only the bulk material properties can be assumed as constant. The topography of the contacting surfaces can change, e.g. as result of the wear process, until a statistically steady morphology is reached. Similarly, the chemical composition of the contacting surfaces may also change drastically compared to the initial state of the surfaces. These changes result in a variation of the coefficient of friction during the first phase of relative sliding in the contact, which is often referred to as running-in phase.

Regarding changes in surface topographies, they can in general be attributed to wear and material transfer. During running-in wear occurs as the softer material normally tends to adapt to the characteristics of the harder surface, so that the level of conformity between the contacting surfaces is increased. This case is demonstrated very clearly in the roughness profiles of materials MTC2, TP1 and TP2 shown in Figures 7.1 and 7.2 in connection with the pin-on-disc testing. A direct consequence of the increased conformity between the surfaces is a higher real area of contact for the same applied load and a correspondingly lower average pressure. According to Equation (7.5) a further consequence is an increased coefficient of friction.

Figure 7.7 shows the measured roughness topographies for the third of the three PET pins included in the running-in study presented in Figure 4.4. The upper graph

corresponds to the interruption after 70 m of sliding and the lower graph shows the surface topography measured at the end of the test, after 500 m of sliding. The topography shown in the first graph is a combination of turning grooves from the machining of the original pin surface and vertical grooves, parallel to the sliding direction, corresponding to the disc surface topography. In the second graph all traces of the original pin surface have disappeared. The measured coefficients of friction for the considered pin at 70 m and 500 m are 0.23 and 0.31 respectively.

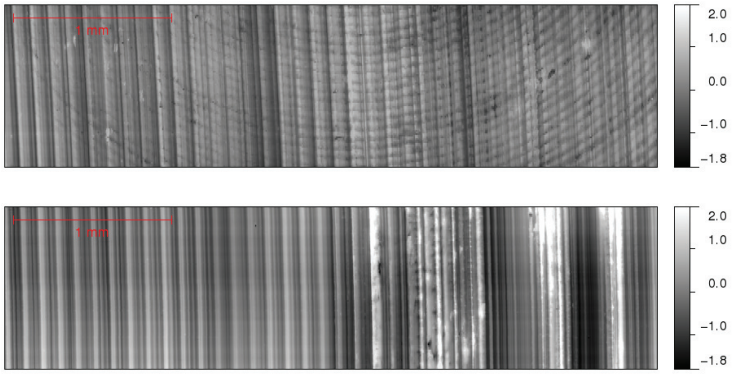

Figure 7.7: Measured roughness topographies of a PET pin specimen during running-in (top) and in steady state (bottom)

Wear, resulting in changes of the surface topography during the running-in phase, is not necessarily limited to the softer of the contacting materials. If hard particles are included in the softer material or if they are embedded into it during sliding, they can abrade the counter surface and change its topography. Moreover, the surface topography of the harder material can be altered due to material transfer from the counter surface and formation of a corresponding surface layer.

One pin-on-disc test with a pin specimen made of reinforced thermoplastic material TP5, is used here as an example for demonstrating changes of the disc roughness topography due to wear and material transfer. The test was conducted on a disc track with radius 62 mm and conditions otherwise equivalent to the testing described in Chapter 4. The total test duration corresponds to a cumulative sliding distance of 4 km. In order to investigate changes in the topography of the disc, a location on the used disc track was marked prior to the testing by machining a 20 µm deep crater of well-defined geometry. Figure 7.8 shows the three-dimensional geometry of the crater along with the roughness topography in its vicinity. Figure 7.9 shows the roughness profiles in the disc radial direction, approximately in the middle of the aforementioned crater, before and after the test. The two profiles are aligned by considering the crater deepest point as a reference.

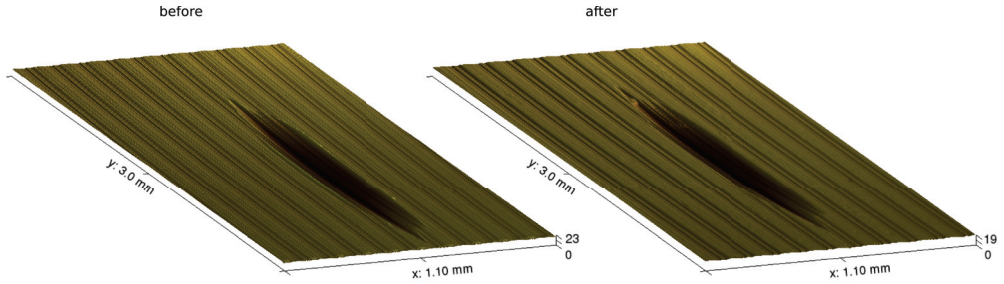

Figure 7.8: Disc track roughness topography before and after testing with material TP5 for 4 km under 6 MPa

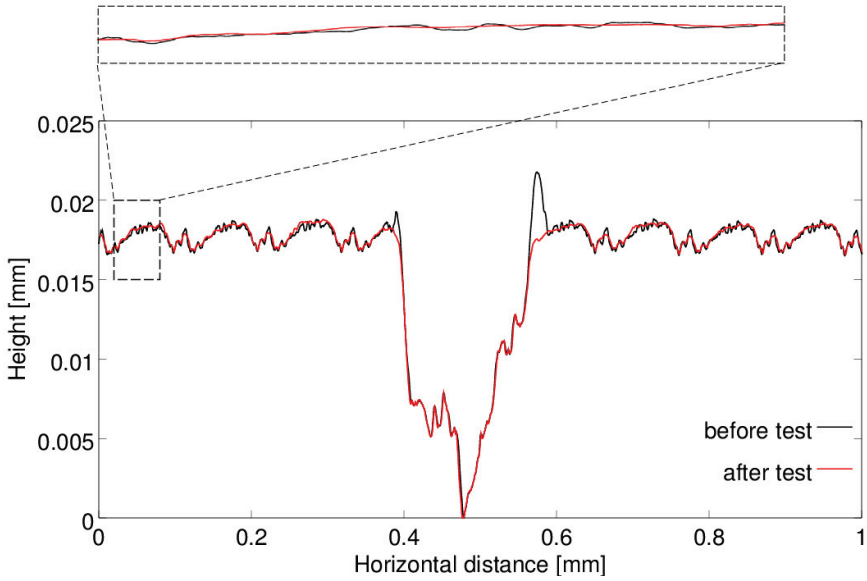

Figure 7.9: Disc track roughness profiles before and after testing with material TP5 for 4 km under 6 MPa

According to the two profiles compared in Figure 7.9, the disc surface becomes significantly smoother after the test. Firstly, asperity peaks appear to be worn and secondly roughness valleys appear to be filled with transferred material. In order to give a visual impression about the real shapes of the surfaces involved in the considered phenomena, Figure 7.9 includes a magnification of the compared profiles from 0.02 to 0.08 mm, represented with equally scaled axes.

As reported in Chapter 5, thermoplastic material TP5 was tested under similar conditions also in the pin-on-plate set-up. During this testing, the steel plate surface should experience similar changes as presented above for the disc surface. Figure 7.10 shows a micrograph and the corresponding topography map of the plate surface after the completed dry testing with material TP5 as presented in Chapter 5. The micrograph and the topography were obtained using focus variation microscopy equipment and their horizontal dimension is parallel to the sliding direction. Areas subjected to more intense material transfer appear as dark areas in the micrograph and they correspond to topography plateaus represented by light color in the topography map on the right.

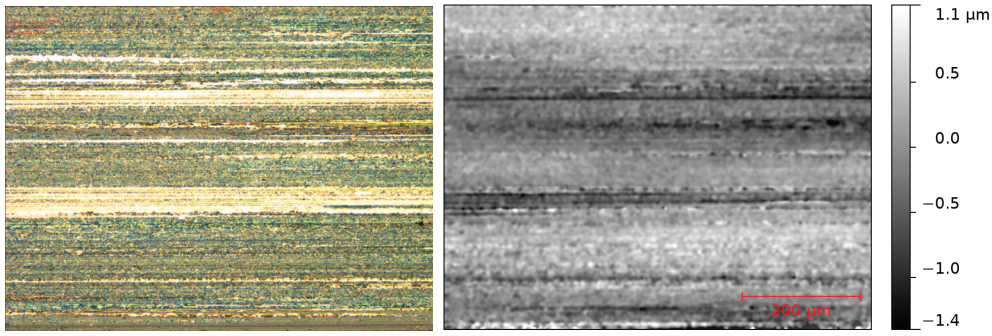

Figure 7.10: Plate track micrograph and roughness topography after testing with material TP5

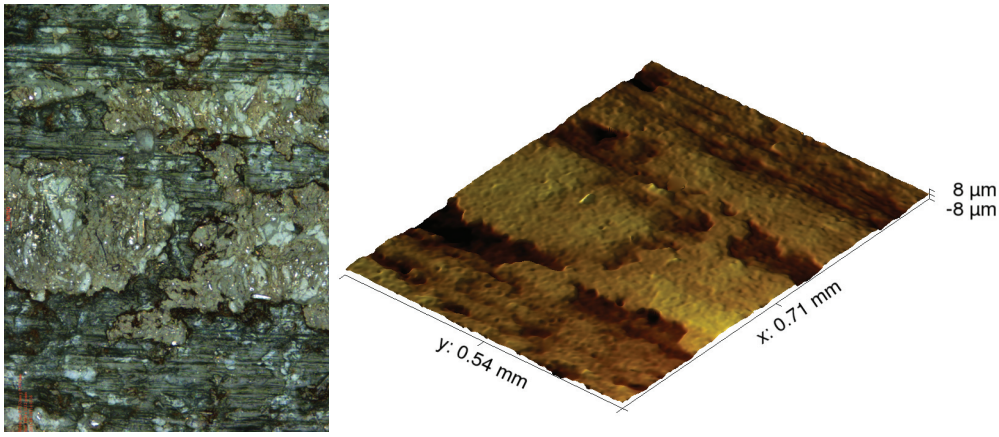

Figure 7.11: Micrograph and topography of TP5 pin surface after pin-on-plate testing

Looking at the counter surface of the plate shown in Figure 7.10, also the topography of the pin changes during running-in as a result of wear and material transfer processes. Figure 7.11 shows a micrograph and the associated topography of the TP5

thermoplastic pin surface corresponding to the plate track shown in Figure 7.10. The pin surface consists of plateaus of compacted wear debris with dimensions in the order of 0.5 and 0.2 mm in directions parallel and perpendicular to sliding respectively. Figure 7.12 shows a two-dimensional roughness profile extracted from the topography of Figure 7.11 along a vertical line close to the right end of the corresponding micrograph. The graph of Figure 7.12 shows an estimated height of 5 µm for the observed plateaus on the TP5 pin surface.

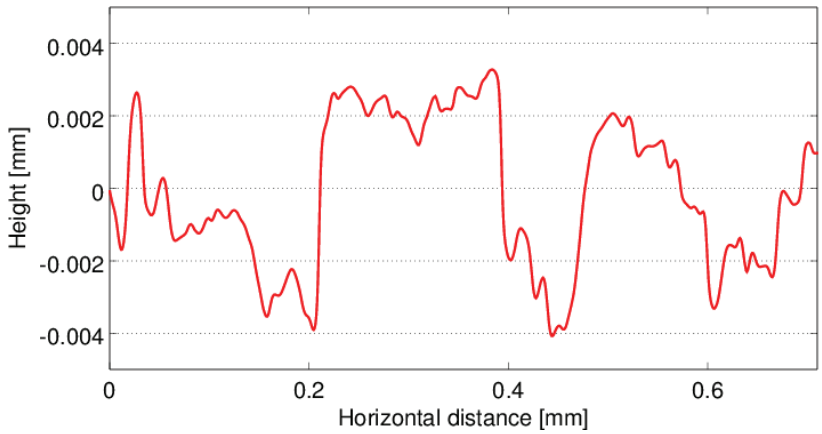

Figure 7.12: Roughness profile of the TP5 pin surface, perpendicular to the sliding direction

Actually the same mechanisms that result in geometrical changes on the contacting surfaces during running-in, namely wear and material transfer, are also responsible for changes on the contacting surfaces with respect to their chemical properties. The abrasive wear process can also be seen as a cleaning process. Mechanical surfaces are normally covered with an adsorbed film of moisture or fluid lubricants. Metals in particular, are normally covered by an oxidation film. As part of the wear process the amount of these superficial features may be reduced during the running-in period. Regarding material transfer, this can affect the chemical properties of the target surface, either by altering the base material e.g. through diffusion of elements from the source surface, or by covering the underlying material with an adhered film of the transferred material. A thorough discussion about running-in can be found in textbook [54] (chap. 8).

7.4 Wear

7.4.1 Phenomenological wear equations

Similar to the simple hypotheses on macroscopically observed friction, there are also corresponding classical equations on macroscopically observed wear. Archard's wear equation, [58], assumes a linear relationship between the wear volume W_V and the independent parameters, applied load F_n and covered sliding distance s:

$$W_V = K \cdot \frac{F_n}{H} \cdot s \tag{7.6}$$

This formulation intends to highlight the idea that wear is proportional to the real area of contact as opposed to the apparent area of contact and equal to the normal load F_n divided by the softer material hardness H. K is dimensionless and is normally referred to as the wear coefficient.

Although some cases confirm the assumed relation between the real area of contact and the observed wear volume, this is not a general law. For this reason, Equation (7.6) is often replaced by a more generic expression highlighting its purely phenomenological nature:

$$W_V = k \cdot F_n \cdot s \tag{7.7}$$

where k is typically referred to as the specific wear rate and normally reported in $\mathrm{mm}^3/(\mathrm{N\,m})$.

Dealing with the applied force F_n and the wear volume W_V, Equation (7.7) implies that the governing parameter is the applied force F_n. This can be interpreted as if two experiments carried out with different test specimen dimensions but the same force and consequently different nominal pressures, were comparable. Even if it is a widely accepted tradition to report wear experiments in terms of wear volume and the applied contact force, in the present work, this convention is intentionally not respected. Instead, wear is reported in terms of the wear height W_h and the nominal contact pressure p, utilizing Equation (7.8) which is derived from Equation (7.7) by simply dividing it by the apparent contact area:

$$W_h = k \cdot p \cdot s \tag{7.8}$$

Even if both Equations (7.7) and (7.8) are theoretically equivalent, the latter underlines the fact that the contact pressure p is the governing parameter and not the applied force F_n. Based on Equation (7.8), one can also define the corresponding wear rate as:

$$w_h = \frac{W_h}{s} = k \cdot p \tag{7.9}$$

The importance of utilizing the pressure p as the load parameter becomes more evident if the aforementioned linear wear rate is considered as a local approximation to a corresponding nonlinear relation $w_h(p)$. Such an equation can be transferred to different contact area dimensions with deviations only due to size effects. A corresponding volumetric wear rate relation $w_V(F_n)$ cannot directly be transferred to contact areas different from the one corresponding to the carried out experiment, directly. Even under a linear wear rate assumption, the range of the validity of such a linear relation is more appropriate to be defined in terms of pressure limits than in terms of normal force limits.

Equation (7.9) can be used for converting the experimentally determined wear rate values presented in Tables 5.3 and 5.4 into the corresponding specific wear rate values. The results of this conversion are presented in Table 7.1.

Table 7.1: Calculated specific wear rates corresponding to testing from Chapter 5

Material and conditions	Pressure [MPa]	Average specific wear rate [$\mathrm{mm}^3/(\mathrm{N\,m})$]
FC1, dry	6	$3.3 \cdot 10^{-6}$
FC2, dry	6	$5.0 \cdot 10^{-6}$
	9	$4.6 \cdot 10^{-6}$
	12	$4.9 \cdot 10^{-6}$
TP1, dry	6	$2.0 \cdot 10^{-6}$
TP5, dry	6	$6.0 \cdot 10^{-6}$
	9	$10.6 \cdot 10^{-6}$
	12	$12.7 \cdot 10^{-6}$
FC3, greased	6	$2.2 \cdot 10^{-6}$
TP1, greased	6	$16.5 \cdot 10^{-6}$
TP5, greased	6	$0.37 \cdot 10^{-6}$

7.4.2 Wear mechanisms

Similar to the above discussed friction mechanisms, macroscopically observed material loss can be attributed to specific mechanisms that cause material removal in the microscopic scale. From all mechanisms that can be found in the relevant literature, adhesive, abrasive, fatigue and oxidative wear are expected to be of relevance for the dry or boundary lubrication conditions, studied in the present work.

Adhesive wear is related to adhesive friction but not every case of adhesive friction will also result in significant adhesive wear. This wear mechanism is particularly observed when the adhesive bonding between the contacting surfaces is stronger than the cohesive strength of the weakest of the bulk materials. In this case, shearing occurs within the bulk material and yields extensive plastic deformation and detachment of material particles from the weaker side. A detailed discussion on adhesive wear is available in textbook [22] (chap. 13). Figure 7.13 shows two micrographs of the pin surface for sintered material S3 before and after dry pin-on-disc testing. The sliding direction is parallel to the horizontal dimension of the micrographs. The pin surface after testing, exhibits extensive plastic deformation which can be attributed to the severe adhesive wear observed during the test.

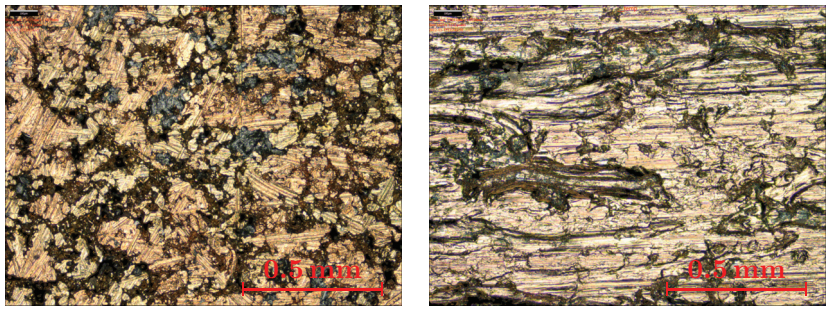

Figure 7.13: S3 pin surface before (left) and after (right) pin-on-disc testing under dry conditions

Abrasive wear is related to the friction mechanism corresponding to the upper right picture in Figure 7.6. Especially when the asperity penetrating the considered surface contains a very hard particle with relatively steep flanks, any relative sliding between the bodies is expected to cause important plastic deformation or fracture of the penetrated material. In case of plastic deformation one normally talks of ploughing.

Fatigue wear is related to crack propagation in the surface or subsurface layers of one of the contacting bodies, because of repeated loading. Even if at macroscopic level loads in both normal and tangential directions are constant, individual asperities are loaded and unloaded, respectively as they encounter asperity peaks or valleys of the moving counter surface. A special case of fatigue wear is related to fiber reinforced friction materials like some of the materials tested in the present work. Exposed fiber material on the contacting surface contributes with its higher strength to the overall wear resistance of the considered material. However, the bonding between a fiber strand and the polymer matrix can fail due to fatigue. When the considered reinforcing material is detached, wear in the area progresses faster until new fibers will be exposed to counterbalance the loss.

Although oxidative wear is normally related to high temperature conditions, it can still contribute to material loss at low temperatures, especially in combination with

abrasive wear. In contact with air, most metals form oxides superficially, at a rate which can be accelerated with increasing temperature and humidity. When the considered metal surface is involved in a sliding contact, the superficial oxide layer that can be as thin as 2 nm, can be removed through the abrasive action of the counter surface. The removed oxides particles, possibly together with detached metal particles, are released in form of wear debris. The metal surface that is exposed after the removal of the protective oxide layer is prone to further oxidation. More information about oxidative wear can be found in textbook [22] (chap. 13).

7.4.3 Practical examples

Fiber composite FC1

Figure 7.14 presents micrographs of the pin surface and wear debris particles corresponding to material FC1 after the corresponding dry test presented in Chapter 5. Micrograph a) shows the pin surface and indicates the existence of plateaus with dimensions in the order of 0.2 mm. Micrographs b) and c) show two isolated wear debris particles observed under a conventional optical microscope and a focus variation microscope respectively. The last two micrographs d) and e) are SEM pictures of a wear debris particle under two different scanning modes. The left one reveals the internal structure of the particle, while the right one illustrates the topography of its surface. Both micrographs c) and d) of Figure 7.14 indicate that the wear debris particles consist of much smaller fragments that are compacted together, while all illustrated particles appear to have a flat form with dimensions comparable to the load carrying plateaus observed on the pin surface. Moreover, visible wear scars on the particles indicate that before being released as free particles, they have been carrying load under sliding.

All these observations resemble a typical wear process of brake materials. Small wear particles with size in the order of 1 µm are released either due to abrasive or adhesive mechanisms. These particles are compressed between the contacting surfaces and form plateaus that carry most of the normal load. At some point as a plateau grows in size, it is sheared away from the underlying material and is released as a flat particle with dimensions in the order of 200 µm. In an effort to estimate the thickness of such flat particles, Figure 7.15 shows a high magnification SEM picture of a particle in a side view. In this micrograph the thickness of the particle can be estimated to the order of 3 µm.

An energy-dispersive spectroscopy (EDS) analysis on wear debris particles has revealed a high amount of iron and oxygen. Hence, despite the aramid fiber based material FC1 is not supposed to be abrasive for steel, it seems that iron oxides on

the plate surface can still be abraded and incorporated in the plateaus formed on the pin surface.

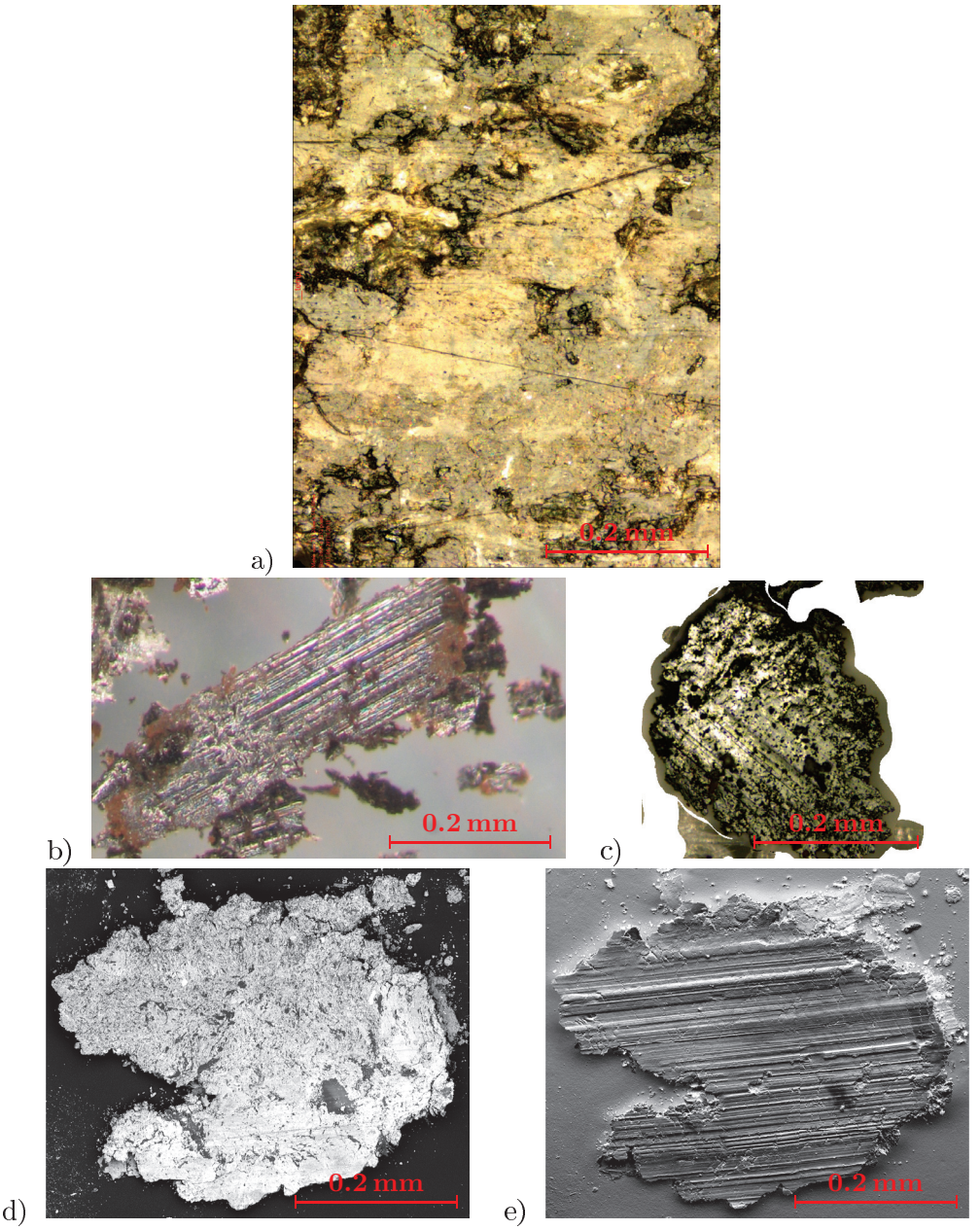

Figure 7.14: Micrographs of pin surface and wear debris particles from dry testing of material FC1

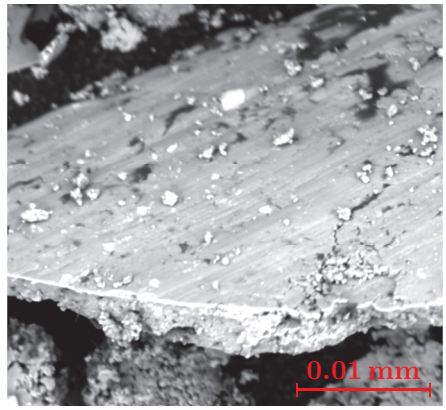

Figure 7.15: High magnification SEM micrograph of wear debris particle from dry testing of material FC1

Fiber composite FC2

Figure 7.16 shows the surface of an FC2 pin after use in pin-on-plate testing. The contact surface of this coarse fiber composite can be divided into three different areas. The dark areas in Figure 7.16 are the actual load carrying plateaus, which correspond to knots of the woven fabric that result in higher contact pressures locally. The light area around the dark spots appears to be lower loaded although it exhibits wear traces parallel to the sliding direction. Finally, there are craters corresponding to voids in the fabric structure.

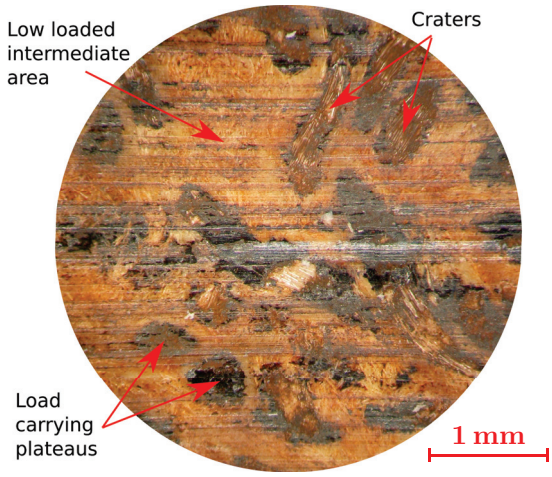

Figure 7.16: Picture of pin surface from dry testing of material FC2

Figure 7.17 shows some further details of the pin surface corresponding to material FC2. Micrograph a) is obtained via a focus variation microscope and shows a portion of the intermediate area between the load carrying plateaus and craters. SEM micrograph b) shows one of the load carrying plateaus which seems to consist of many smaller compacted particles. The shape of the contained light-color particles resembles broken fragments of glass fibers. This assumption is confirmed by an EDS analysis which detected a high content of oxygen, silicon, aluminum and calcium in these spots.

SEM micrograph c) shows part of a crater and the surrounding area. The surface of the crater is formed by free ends of glass fibers. It seems that the craters correspond to voids in the textile, at locations where the glass fiber yarn ends.

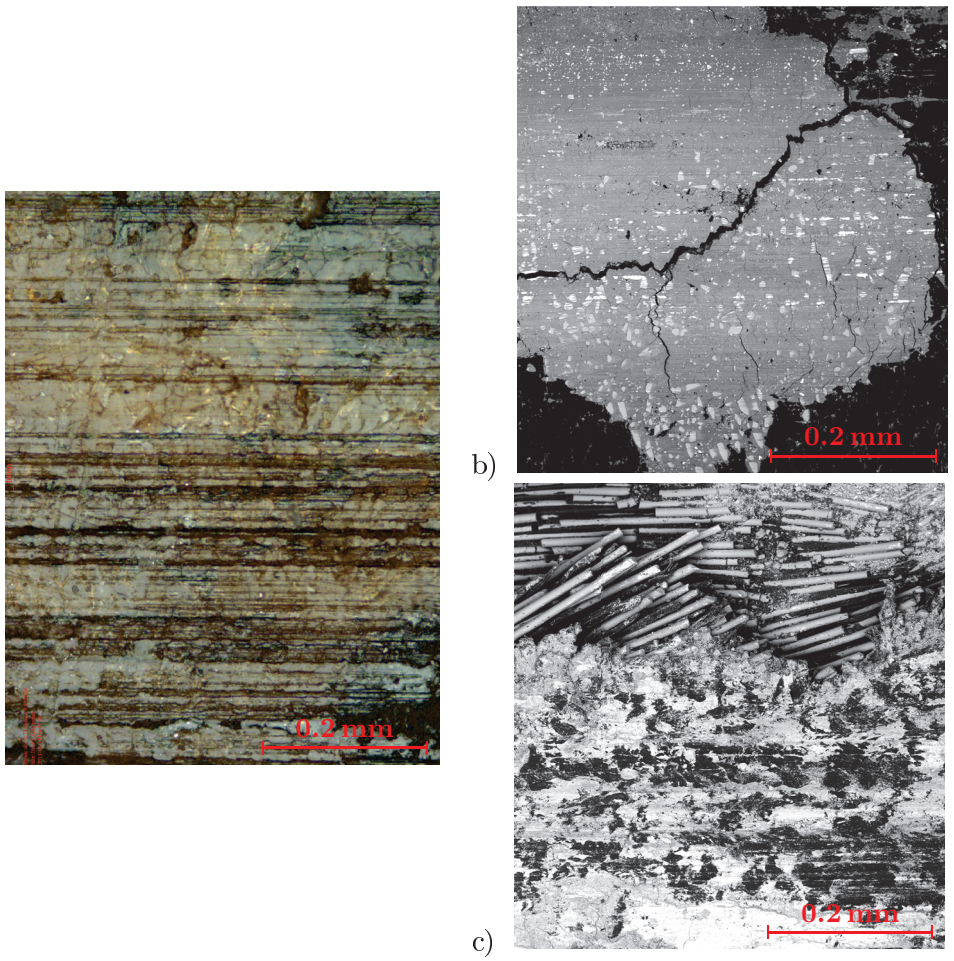

Figure 7.17: Micrographs of pin surface from dry testing of material FC2

Figure 7.18 shows a SEM micrograph of a wear debris particle from the pin-on-plate testing of material FC2. The presented particle seems to consist of compacted small fragments. However, its total size and structure do not resemble the load carrying plateaus like the one shown in Figure 7.17 b). Therefore, material detached from a load carrying plateau through abrasion or fatigue, is expected to undergo further crushing and compaction in order to form the final wear debris.

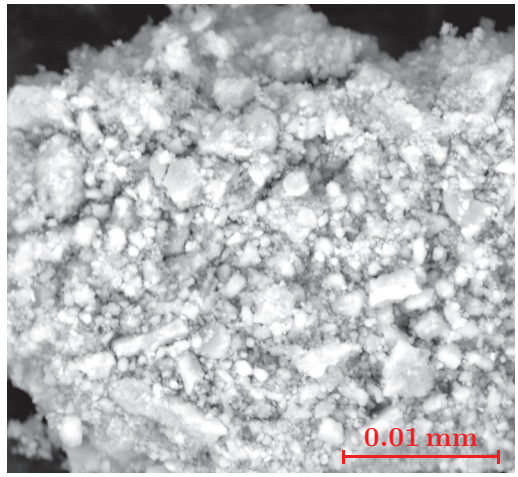

Figure 7.18: High magnification SEM micrograph of wear debris particle from dry testing of material FC2

Thermoplastic TP1

The pin surfaces resulting from testing of PET thermoplastic TP1 under dry and grease-lubricated conditions, are shown in Figure 7.19 on the left and right side respectively.

The very remarkable result from Chapter 5 with PET wearing approximately 8 times faster with grease lubrication than under dry conditions, can partially be explained by Figure 7.19. In the right micrograph corresponding to lubricated conditions it is easy to recognize evidence of significant abrasive wear appearing as horizontal scars. In the left micrograph corresponding to dry conditions a completely different surface morphology is observed. The surface mainly consists of flat plateaus, elongated in the direction of sliding.

This difference between the dry and the lubricated conditions can be explained by looking at the counter surface for the test under dry conditions. Figure 7.20 shows the plate surface corresponding to the dry test as a micrograph captured under polarized

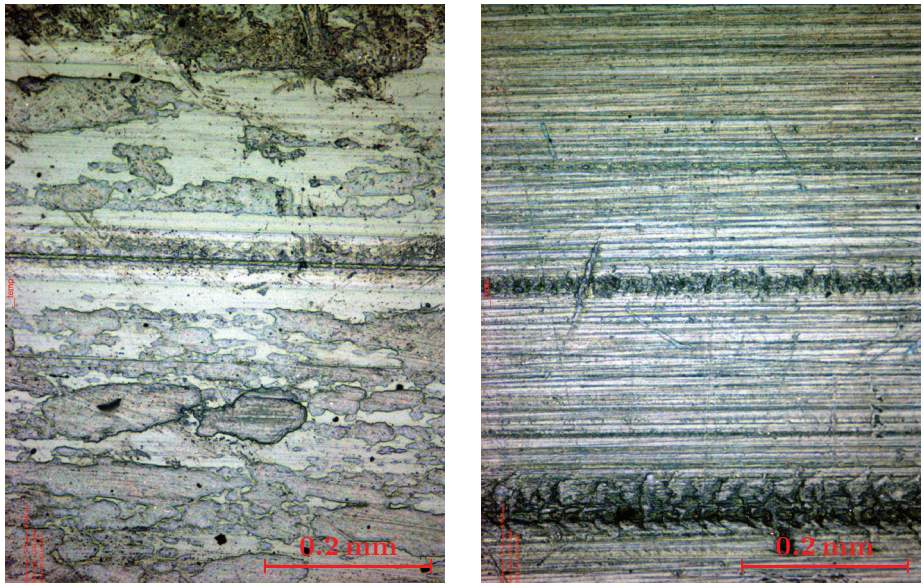

Figure 7.19: Micrographs of pin surfaces from testing of thermoplastic TP1 under dry conditions (left) and with grease lubrication (right)

light. The white area corresponds to a superficial layer of attached PET material which appears to cover more than 50% of the steel plate surface. This layer prevents abrasive wear that would otherwise affect the pin surface. A similar layer could not be observed in the case with grease lubrication. The adsorbed lubricant on the steel surface prevents wear particles of PET from being attached to the surface, reducing its abrasive action. One could say that the lubricant in this case acts as a cutting fluid in a grinding process.

Figure 7.21 compares the roughness profiles of the track surfaces, in direction perpendicular to the sliding direction for the tests of PET thermoplastic TP1 with and without grease lubrication. The upper profiles correspond to the unused track surface, while the lower represent the plate surfaces after the completed wear test. For the grease-lubricated test on the right side of Figure 7.21, no obvious change on the characteristics of the plate surface can be detected. On the contrary, for the test under dry conditions on the left side of Figure 7.21, there is a very clear qualitative difference between the plate surface profiles before and after the test. The relatively smooth plateaus that are visible in the plate surface profile after the dry test, correspond to PET material patches, attached on the steel surface, that are also shown in Figure 7.20. The compared profiles before and after testing do not correspond to exactly the same location on the plate track, but they are representative samples among several repetitions of the roughness measurement in each case.

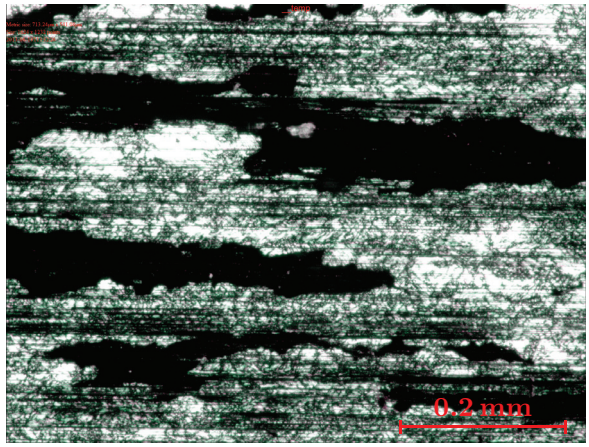

Figure 7.20: Micrograph of plate track surface from dry testing of material TP1 under polarized light

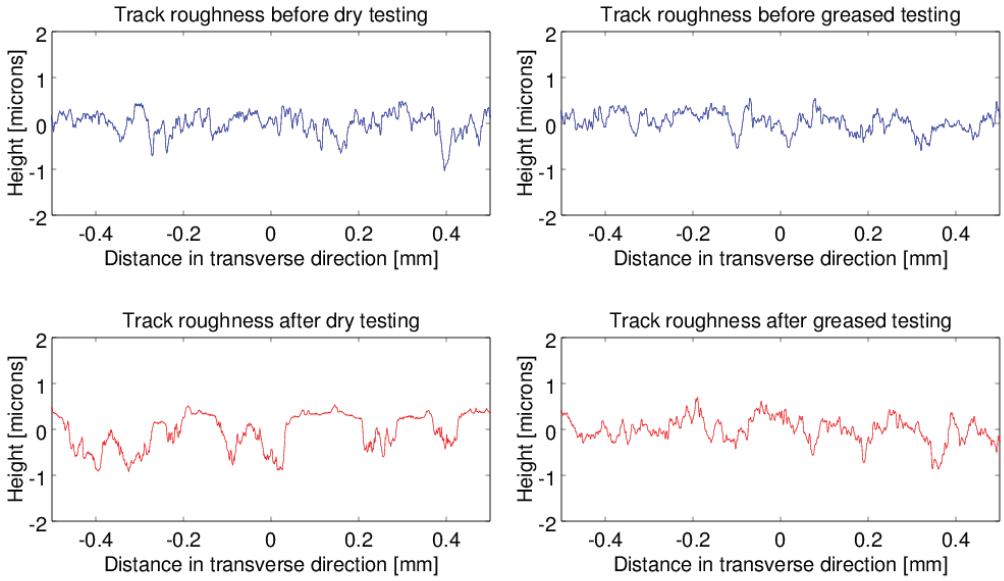

Figure 7.21: Plate track roughness profiles before (top) and after (bottom) testing of material TP1, under dry (left) and grease-lubricated (right) conditions

Thermoplastic TP5

Figure 7.22 shows micrographs of two pin surfaces corresponding to thermoplastic material TP5 under dry and grease-lubricated conditions respectively. As already discussed in the presentation of Figure 7.11, the dry tested pin surface exhibits plateaus formed of compacted wear particles. The wear mechanism is similar to the one described for material FC1. Figure 7.23 shows a micrograph of a wear debris particle with similar characteristics to the case of material FC1.

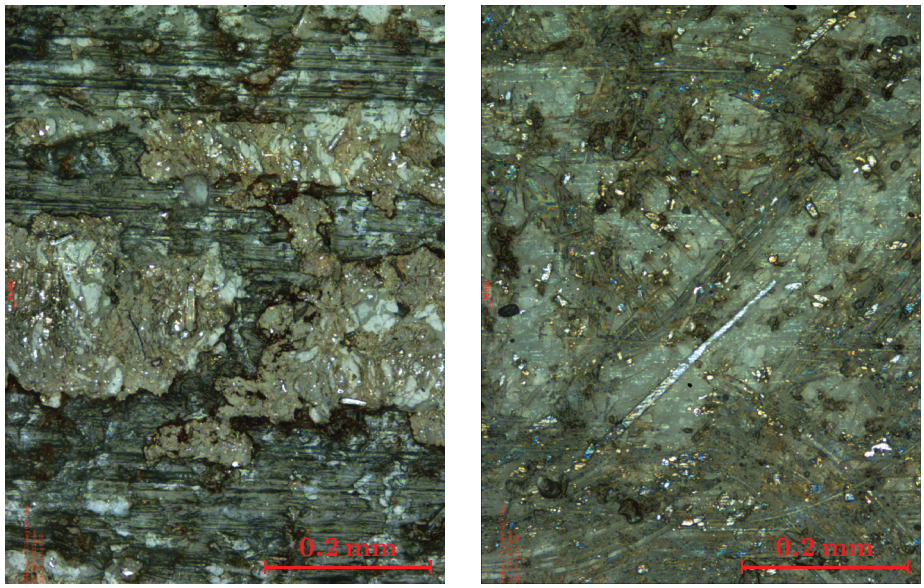

Figure 7.22: Micrographs of pin surfaces from testing of thermoplastic TP5 under dry conditions (left) and with grease lubrication (right)

Considering the right-side micrograph of Figure 7.22 the pin surface for the grease-lubricated case appears to have very different characteristics. Instead of relatively big load carrying plateaus, there are many small individual glass fibers that appear to carry the contact load. There are some fibers lying parallel to the contact surface and many that are perpendicular to the surface. Visible scratches on the exposed fibers indicate that the wear process involves abrasion of the reinforcing fibers. However, since the counter surface, being a steel surface, is softer than the reinforcing fibers of the friction material, abrasion is very limited mainly due to few particles of broken fiber fragments that are overrun during sliding. This situation results in a very low specific wear rate corresponding to the values reported in Table 7.1.

Figure 7.23: Micrograph of wear debris particle from testing of thermoplastic TP5 under dry conditions

Taking the lubricated case as an idealized reference, the wear process and the formation of the corresponding plateaus in the dry case appear to be part of a self-amplifying mechanism. Higher adhesion forces under dry conditions tend to detach more glass fiber fragments from the polymer matrix. The release of reinforcing fibers not only affects the load carrying capacity of the contact, which has to be recovered by exposing new fibers, but it also triggers a third body abrasive wear mechanism that causes even more fiber fragments to be released. The formation of plateaus of compacted debris can be seen as a way of balancing this self-amplifying effect. Glass fiber particles that are embedded into an existing plateau cannot contribute to further abrasion of the pin surface releasing new fiber fragments, until the whole plateau is sheared away.

The contribution of boundary lubrication in this case is to reduce the adhesive forces sufficiently in order to avoid triggering the above described self-amplifying mechanism in the first place. The mechanism of reducing the adhesive friction is via the presence of an adsorbed layer of lubricant on the disc surface. Although such a layer is very difficult to separate from the surface, in the context of an abrasive wear mechanism it is possible to remove the lubricant layer together with particles of the underlying steel. For this reason a constant supply of additional grease may be necessary in order to maintain boundary lubrication conditions. In the tests presented in Chapter 5 no additional grease was provided externally during the test and the tested TP5 material behaved as self-lubricating, remaining under boundary lubrication conditions until the end of the test.

In order to illustrate the self-lubrication mechanism observed for most of the tested materials, Figure 7.24 shows two pin surface micrographs from an approximately 15 km long, grease-lubricated, pin-on-plate test of a thermoplastic reinforced only with glass fibers. The first micrograph is captured without cleaning the pin surface, while the second one is after cleaning. The two pictures do not correspond to exactly the same location on the pin surface but are representative for the whole pin surface. A big number of craters that are visible in the second picture are filled with lubricant in the picture taken before cleaning. Moreover, the craters seem to correspond to locations where fragments of the reinforcing glass fibers have been detached from the matrix. It seems that grease accumulated in the material pores that are being regenerated during the whole test, provides the necessary lubricant supply for maintaining boundary lubrication conditions in the long term.

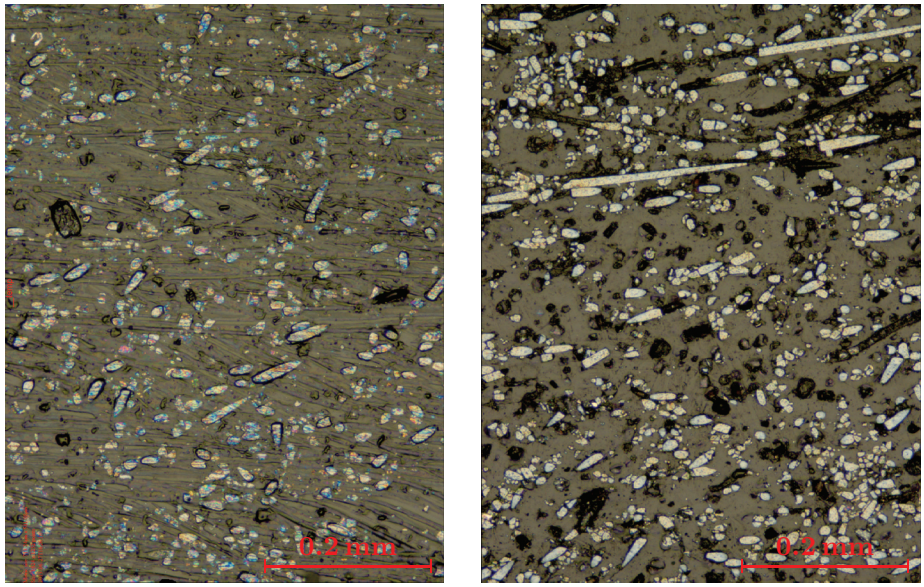

Figure 7.24: Micrograph of pin surface from testing of a glass fiber reinforced polyamide under grease lubrication, before (left) and after cleaning (right)

Chapter 8

Contact mechanics

Even if experimental testing is an indispensable step in the development of products that involve friction and wear, theoretical modeling of friction and wear is still very important. The purpose of theoretical modeling is not to predict the exact friction force and wear rate observed in reality but to help understand the experimental results, evaluate the impact of various operational parameters and expand the application of experimental results to a wider range of operational conditions.

The present chapter is about using numerical modeling for simulating many of the phenomena described in Chapter 7 in order to better understand the different friction and wear mechanisms, not only in qualitative but also in quantitative sense. For this purpose the finite-element method is employed. Part of the information provided in this chapter along with some additional examples is included in Publications P2 and P4.

8.1 Implementation of a micro-contact FEM model

8.1.1 Continuous problem formulation

In continuum mechanics, the deformations u_1 and u_2 of two elastic bodies, identified through the indices $i = 1$ and 2, can be studied by considering the following equations:

$$\nabla\sigma_i(u_i) + f_i = 0 \tag{8.1}$$

$$\sigma_i(u_i) = \mathcal{A}_i\epsilon_i(u_i) \tag{8.2}$$

in the corresponding domains Ω_i shown e.g. in Figure 8.1.

With σ denoting the three by three stress tensor, Equation (8.1) expresses the forces equilibrium in the bulk material under field forces f and Equation (8.2) represents a constitutive law for elastic deformations with $\mathcal{A}$ and ϵ corresponding to the elasticity and the linearized strain tensors respectively.

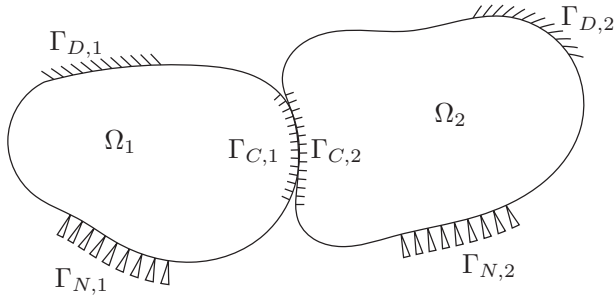

Figure 8.1: Deformable bodies in contact

Additionally, homogeneous Dirichlet conditions on the boundaries $\Gamma_{D,i}$ and surface normal forces t_i on the boundaries $\Gamma_{N,i}$ can be expressed through the following equations respectively:

$$u_i = 0 \text{ , on } \Gamma_{D,i} \tag{8.3}$$

$$\sigma_{N,i} = t_i \text{ , on } \Gamma_{N,i} \tag{8.4}$$

with the stress component $\sigma_{N,i}$ in direction n_i normal to the body surface, defined as:

$$\sigma_{N,i}(u_i) = \sigma_i(u_i)n_i \tag{8.5}$$

For studying the contact interaction between the two elastic bodies, the non-penetration condition can be described on a portion $\Gamma_{C,1}$ of the surface of the first body by using the so-called Karush-Kuhn-Tucker conditions:

$$\sigma_{N,1}(u_1) \leq 0 \text{ , on } \Gamma_{C,1} \tag{8.6}$$

$$g_N(u_1, u_2) \geq 0 \text{ , on } \Gamma_{C,1} \tag{8.7}$$

$$g_N(u_1, u_2)\sigma_{N,1}(u_1) = 0 \text{ , on } \Gamma_{C,1} \tag{8.8}$$

with the normal gap g_N between the bodies, defined as:

$$g_N(u_1, u_2) = g_{N0} - (u_1 - P_1(u_2))\, n_1 \tag{8.9}$$

The variable g_{N0} corresponds to the initial gap between the unloaded bodies and P_1 represents a projection operation on the surface of the first body. In the case of Equation (8.9) the projected quantity is the displacement field u_2.

Equation (8.6) enforces that only compressive stresses can be exerted between the contacting bodies and Equation (8.7) enforces the actual non-penetration condition. Finally, Equation (8.8) expresses that at a specific point either contact will occur or the contact pressure will be zero. A more detailed description of the fundamental problem formulation can be found in [59].

8.1.2 Finite-element discretization

For geometrically complex contacting bodies, the problem stated in the previous section cannot be solved analytically and is typically discretized for numerical solution by using the finite-element method. Geometrically simpler cases such as nominally flat rough surfaces with relatively small roughness asperity slopes cannot justify resorting to a finite-element model and can be solved more efficiently using elastic half-space models, see e.g. [26]. However, if the effect of asperity slopes has to be taken into account or if the bulk material is expected to deform plastically, the finite-element method provides a very straightforward approach to solving this problem.

Two further steps that are typically required before the actual discretization are the conversion of the problem statement into the corresponding weak formulation and the introduction of Lagrange multipliers λ_N for expressing Equations (8.6) to (8.8). Both of these steps are described in detail in [60] and [61]. With respect to the discretization of the contact conditions, the latter paper describes two possible approaches, a nodal based method that enforces Equation (8.6) to (8.8) at each finite-element node and

an integral based method that enforces the condition in an average sense over the contacting face of each finite-element. In the present work the integral approach is used.

The final form of this non-linear problem after its conversion into an iterative series of linear steps according to the Generalized-Newton-Method algorithm presented in [60], is described below:

$$\begin{bmatrix} K_1^k & 0 & B_{N,1}^T \\ 0 & K_2^k & B_{N,2}^T \\ C_{N,1}^k & C_{N,2}^k & D^k \end{bmatrix} \cdot \begin{bmatrix} \delta u_1 \\ \delta u_2 \\ \delta \lambda_N \end{bmatrix} = \begin{bmatrix} R_1^k \\ R_2^k \\ R_\lambda^k \end{bmatrix} \tag{8.10}$$

$$\begin{bmatrix} u_1^{k+1} \\ u_2^{k+1} \\ \lambda_N^{k+1} \end{bmatrix} = \begin{bmatrix} u_1^k \\ u_2^k \\ \lambda_N^k \end{bmatrix} + \alpha \cdot \begin{bmatrix} \delta u_1 \\ \delta u_2 \\ \delta \lambda_N \end{bmatrix} \tag{8.11}$$

with index k corresponding to the current step of the iterative solving process.

The factor α for calculating the next iteration step is determined by performing a line search operation. For linear elastic bulk materials the stiffness sub-matrices K_i are actually independent of the iteration index k. However, for elasto-plastic materials they have to be recalculated at every iteration and can be expressed as $K_i(u_i)$. Sub-matrices $B_{N,i}$ are constant and sub-matrices $C_{N,i}$ and D change as the contact area changes during the numerical iterations and can actually be written as $C_{N,i}(u_1, u_2, \lambda_N)$ and $D(u_1, u_2, \lambda_N)$. The right-hand-side terms of Equation (8.10) are also functions of u_1, u_2 and λ_N.

A practical difficulty with the discretization in form of Equation (8.11) is that the quantities u_1, u_2 and λ_N cannot be represented on a common finite element mesh. In the model to be presented in the next sections, λ_N is by convention defined on the boundary $\Gamma_{C,1}$ of the first body, so that matrices $B_{N,1}$ and $C_{N,1}$ can be calculated easily by a common integration on the corresponding finite-element mesh surface. However, the calculation of matrices $B_{N,2}$ and $C_{N,2}$ requires an integration that involves quantities u_2 and λ_N which are defined on different finite-element meshes. In order to overcome this problem, the base functions defined on body Ω_2 for approximating the displacements u_2 are projected to body Ω_1, like it is shown in Figure 8.2. They are represented by their values at the local Gauss-points of the numerical integration method on body Ω_1. In this way, an integration of quantities that involve both u_2 and λ_N is possible.

All components that were described in this subsection are available in the public domain finite-element library GetFem++ [1] that was utilized for the implementation of the present model. In particular, the possibility of projecting finite-element base

[1] `http://download.gna.org/getfem/html/homepage/`

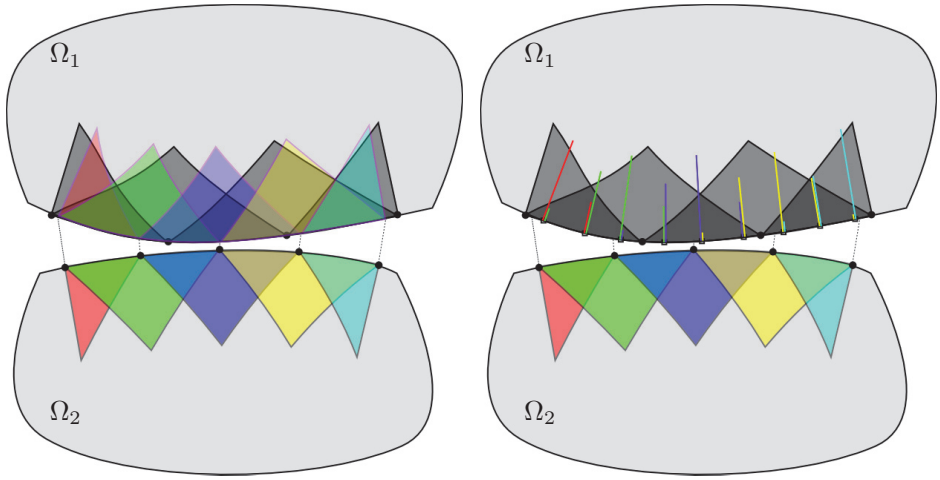

Figure 8.2: Projected finite-element base function between non-matching meshes, continuous (left) and discrete at local Gauss-points (right)

functions between non-matching meshes in two and three dimensions, was added to GetFem++ in the framework of the present work.

8.1.3 Mesh generation

Figure 8.3 shows the mesh discretization used in the model consisting of two rectangular parallelepiped blocks corresponding to the two contacting bodies. Each block is discretized using 8-node hexahedral elements and is divided in layers of different mesh size. Instead of using transition elements, the continuity between the non-matching meshes of neighbouring layers is enforced by applying additional constraints using Lagrange multipliers defined on the finite-element nodes of the finest of the neighbouring layers. More details and examples using this technique for connecting non-matching meshes can be found in [62].

The parameters describing the mesh of each block consist of the block dimensions l_x, l_y, l_z, number of elements in z direction per layer, n_z, and mesh sizes dx, dy and dz of the finest mesh layer. The mesh size in the other layers is determined by a consecutive coarsening factor as close to a value of two as possible and the number of layers is such that the prescribed block height l_z is fulfilled.

For each block, the roughness topography of the contacting surface is imported as a matrix stored in a file and is applied to the nodes of the finest mesh layer as

deviations in the z direction weighted by a factor of one for the nodes on the surface and decreasing to zero for the nodes at the interface with the second mesh layer.

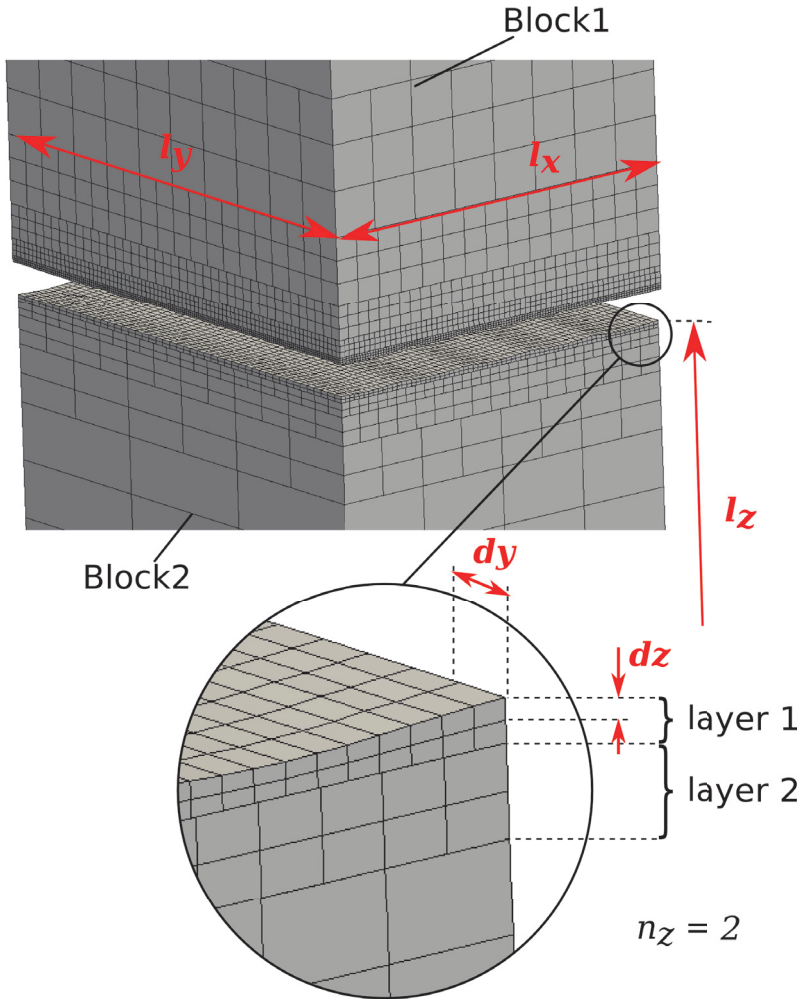

Figure 8.3: Finite-element mesh

8.1.4 Boundary conditions

All results presented later in this paper correspond to a normal loading between the upper and the lower blocks. This condition is achieved by fixing the z displacement of all nodes on the bottom surface of the lower block and loading the top surface of the upper block with a uniform load in z direction. The movement in x and y

directions for both the bottom surface of the lower block and the top surface of the upper block is restricted in an average sense, this means that the individual nodes are free to move in these directions but the average movement over each surface is zero.

The blocks shown in Figure 8.3 correspond to only a small, possibly representative, portion of the two bodies in contact. In order to take this into account and assuming that macroscopically the contact pressure distribution is uniform, periodicity conditions are introduced to the model. The lateral block surfaces in the positive and negative x directions are connected together and this is also the case for the other two lateral surfaces perpendicular to the y direction. The connection is implemented through elimination of finite-element nodes. The degrees of freedom corresponding to one of the connected surfaces are removed and replaced by the corresponding degrees of freedom of the opposite surface. The resulting model should ultimately be interpreted as a rectangular array of infinite blocks like the ones shown in Figure 8.3 extending in x and y directions.

8.1.5 Material properties

Two different material laws, that were already implemented in the GetFem++ library, are supported by the present model. Ideally elastic isotropic materials, expressed by Equation (8.2), and perfectly elasto-plastic materials can be taken into account. Viscoelastic behavior, which is typical for elastomer and thermoplastic materials, is not considered.

Plastic deformation can be considered only in the context of a time dependent process, where the previous time or load step provides the current deformations and stresses, u^0 and σ^0 respectively, as a reference. In this case, a hypothetical elastic relationship between the deformations and stresses can be expressed in incremental sense with respect to the current state as:

$$\tilde{\sigma}(u) = \sigma^0 + \mathcal{A}(\epsilon(u) - \epsilon(u^0)) \tag{8.12}$$

Equation (8.12) is equivalent to Equation (8.2) with the body index i omitted for the sake of simplicity. According to the closest-point projection method described in [63] (chap. 10.7), plastic behavior of a material can be taken into account by projecting the hypothetical elastic stresses $\tilde{\sigma}$ to the space of admissible stresses. By introducing the yield limit σ_y with respect to the Von Mises yield criterion, the constitutive law for a perfectly elasto-plastic material behavior can be expressed based on Equation (8.12), as:

$$\sigma(u) = \begin{cases} \tilde{\sigma} & \text{, for } \tilde{\sigma}_{\mathtt{vm}} \leq \sigma_y \\ \tilde{\sigma}_m + \frac{\sigma_y}{\tilde{\sigma}_{\mathtt{vm}}} \cdot \tilde{\sigma}_d & \text{, for } \tilde{\sigma}_{\mathtt{vm}} > \sigma_y \end{cases} \tag{8.13}$$

whereby, the hydrostatic and deviatoric stress tensors, $\tilde{\sigma}_m$ and $\tilde{\sigma}_d$, are defined respectively as following:

$$\tilde{\sigma}_m = \frac{\tilde{\sigma}_{11} + \tilde{\sigma}_{22} + \tilde{\sigma}_{33}}{3} \cdot I \tag{8.14}$$

$$\tilde{\sigma}_d = \tilde{\sigma} - \tilde{\sigma}_m \tag{8.15}$$

and the scalar function representing the Von Mises stresses can be defined using the Euclidean norm of $\tilde{\sigma}_d$:

$$\tilde{\sigma}_{\mathtt{vm}} = \sqrt{3/2} \cdot |\tilde{\sigma}_d| \tag{8.16}$$

Considering the incremental nature of plasticity phenomena, if at least one of the contacting bodies is expected to deform plastically, the corresponding Equation (8.2) is replaced by Equation (8.13) and a series of quasi-static load steps, beginning from the unloaded state, has to be simulated.

It should be noted that both the elastic and the elasto-plastic material laws, that were included in the present model, are based on the assumption of geometric linearity that is valid only for small deformations.

8.1.6 Performance

As described in Section 8.1.4, each of the blocks shown in Figure 8.3 can be interpreted as part of a periodic space that consists of infinite repetitions of the considered block in form of a rectangular array. In order for the model to represent reality adequately, the dimensions l_x and l_y of each block must be larger than the longest wavelength of interest that is present on the corresponding real surface. In case that this wavelength can be identified as a deterministic pattern on the surface, the corresponding block dimension has to be an exact multiple of it. Additionally, the mesh discretization sizes dx and dy should be lower than the shortest wavelength of interest on the corresponding real surfaces and directions. For this reason, a very high number of elements $n_x = l_x/dx$ and $n_y = l_y/dy$ is necessary in order to cover a range of roughness wavelengths as wide as possible. Therefore, the model size in terms of degrees of freedom and the corresponding computational cost are considerable.

The following measures were taken in order to reduce the computational cost:

- Use variable mesh size in the depth direction in order to reduce the complexity of the problem.
- Reduce the number of Newton-Raphson iterations by using robust contact algorithms like the one mentioned in Section 8.1.2.

Additionally, the computational time was reduced by resorting to parallel computing:

- Carry out the assembly of the tangent matrix and the right hand side of Equation (8.10) on multiple CPU-cores in parallel.
- Use multiple CPU-cores for the solution of the linear system (8.10) in each iteration step by utilizing a parallel solver like MUMPS, [64] and [65].

8.2 Normal contact of a single asperity

This section summarizes a series of fundamental calculations on contact between a single asperity and a flat surface or between a pair of single asperities. Starting from the simplest possible case and adding complexity gradually, asperities with spherical or sinusoidal shape are used to illustrate many of the friction mechanisms discussed previously and the effect of size scale.

All asperity geometries considered in this section are characterized by a height h and a half-period a. The bulk material is characterized by its Young's modulus E, Poisson's ratio ν and an effective elasticity modulus defined as:

$$E' = \frac{E}{1-\nu^2} \tag{8.17}$$

Moreover, when plasticity is considered, a perfect elasto-plastic material with yield limit σ_y is assumed.

Based on these basic parameters, a characteristic pressure of the contact can be defined to be used as a reference for deriving dimensionless parameters. A reasonable choice for such a characteristic pressure is following:

$$p_{ref} = E' \frac{h}{a} \tag{8.18}$$

The normal load for the contact is defined through a corresponding pressure p. However, it will be shown convenient to use a corresponding dimensionless load parameter defined as:

$$\bar{p} = \frac{p}{p_{ref}} \tag{8.19}$$

in order to present all results in a generalized way.

8.2.1 Elastic contact of a sinusoidal asperity

The geometry of a single sinusoidal asperity with amplitude h and half-period a is defined in two dimensions as:

$$z_{sin}(x) = \frac{h}{2}(1 - cos\frac{\pi x}{a}) \tag{8.20}$$

Figure 8.4 illustrates the calculated contact area for sinusoidal asperities with different h and a values, but with constant effective elasticity modulus E'=1000 N/mm^2. The horizontal axis corresponds to the dimensionless load parameter $\bar{p}$, while the vertical axis represents the calculated contact area as a fraction of the total area corresponding to full contact. The overlapping curves in Figure 8.4 confirm that for h and a values with an average slope h/a varying from 0.1 to 0.0001, all given geometric, material and load parameters can be reduced to a single dimensionless load parameter $\bar{p}$, which is sufficient for estimating the contact area ratio with reasonable accuracy.

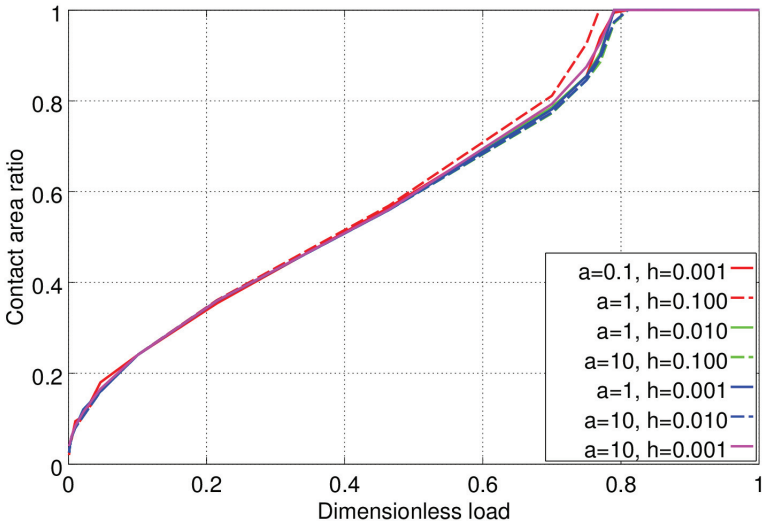

Figure 8.4: Real area of contact as a function of load for two-dimensional sinusoidal asperities under pure elastic conditions

8.2.2 Comparison between sinusoidal and spherical asperities

The geometry of a spherical asperity with radius R, truncated to a maximum height h can be defined in two dimensions as:

$$z_{sphere}(x) = min\left(R - \sqrt{R^2 - x^2},\ h\right) \tag{8.21}$$

In the two-dimensional case the term "spherical" should actually be replaced by the term "circular", however in a strictly mathematical sense it is valid to use the term "spherical" also in two dimensions.

By establishing a relationship between the sinusoidal and spherical asperities described in Equations (8.20) and (8.21) respectively, a relation between the sphere radius R and the half width a can also be established. Figure 8.5 shows two ways of approximating the originally considered sinusoidal asperity by a spherical one. The sphere can either be inscribed into the curvature of the sinus form at its peak or a sphere can be selected that intersects the sinus curve at a length of $a/2$, approximating in this way the overall sinus form.

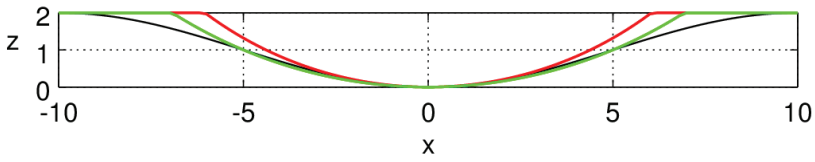

Figure 8.5: Geometry of two-dimensional sinusoidal (black), fitted spherical (green) and inscribed spherical (red) asperities for h=2 and a=10 mm

Equation (8.22) defines the radius of the inscribed sphere and Equation (8.23) provides the radius of the fitted sphere as a function of the reference sinus parameters h and a.

$$R_{inscr} = \frac{2a^2}{\pi^2 h} \tag{8.22}$$

$$R_{fitted} = \frac{h^2 + a^2}{4h} \tag{8.23}$$

Utilizing these two expressions for replacing the sinusoidal asperity, in the calculations of the previous section, with an either fitted or inscribed spherical asperity, one can generate similar curves for the real area of contact. Moreover, one can use the Hertzian theory for estimating the contact area ratio $\bar{A}$ in these cases:

$$\bar{A} = \sqrt{\frac{8Rh}{\pi a^2}\bar{p}} \tag{8.24}$$

and substituting the sphere radius from Equation (8.23) yields an expression for the Hertzian contact area ratio of a sphere, fitted to the original sinusoidal asperity:

$$\bar{A} = \sqrt{2\frac{(h/a)^2 + 1}{\pi}\bar{p}} \tag{8.25}$$

while using (8.22) yields an expression for the Hertzian contact area ratio of the corresponding inscribed sphere:

$$\bar{A} = \sqrt{\frac{16}{\pi^3}\bar{p}} \tag{8.26}$$

It should be noted that even if theoretically, Equation (8.25) depends on the asperity average slope h/a, for the range of average slopes considered here, $(h/a)^2$ is so much smaller than unity, that it can for practical purposes be neglected.

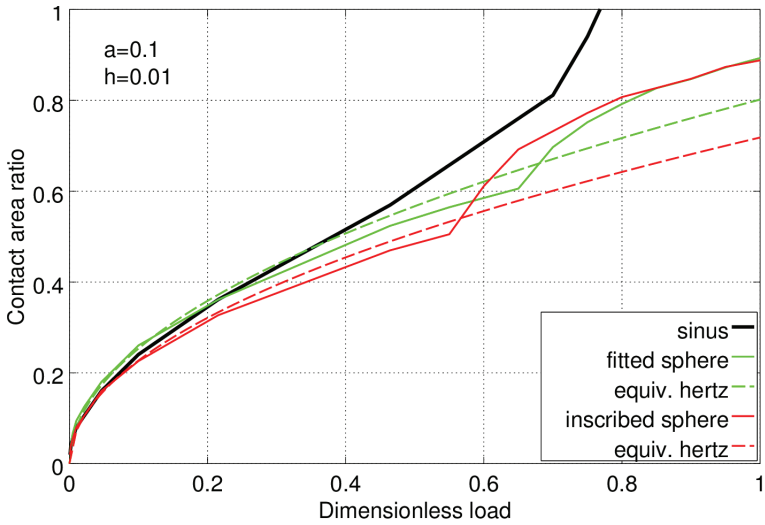

Figure 8.6: Real area of contact for two-dimensional sinusoidal and spherical asperities for h=0.01 mm and a=0.1 mm under pure elastic conditions

Figure 8.6 compares the calculated contact area for the original sinusoidal asperity with h=0.01 mm and a=0.1 mm as well as the corresponding fitted and inscribed spheres along with the theoretical curves according to Equations (8.25) and (8.26). As one would expect, for relatively low values of the dimensionless load parameter, the contact area predicted by the Hertzian theory resembles quite well the corresponding calculated curves. Moreover, one can observe that the inscribed sphere gives very similar results with the sinusoidal asperity only for very low loads, while the fitted sphere approximates the behavior of the sinusoidal asperity in a wider range of loads, practically up to dimensionless load value of 0.4.

8.2.3 Impact of plastic deformation

A first step of adding complexity to the very fundamental contact cases studied so far, is to assume that the bulk material can be deformed plastically beyond a yield limit σ_y. Like in the case of the normal load p, it will be shown very convenient to replace σ_y with a corresponding dimensionless parameter, also derived on basis of the characteristic pressure from Equation (8.18):

$$\bar{\sigma_y} = \frac{\sigma_y}{p_{ref}} \tag{8.27}$$

Figure 8.7 shows, how the calculated contact area is affected by varying the material yield limit. The assumed values for the dimensionless yield limit are in the range from 0.1 to 1.6.

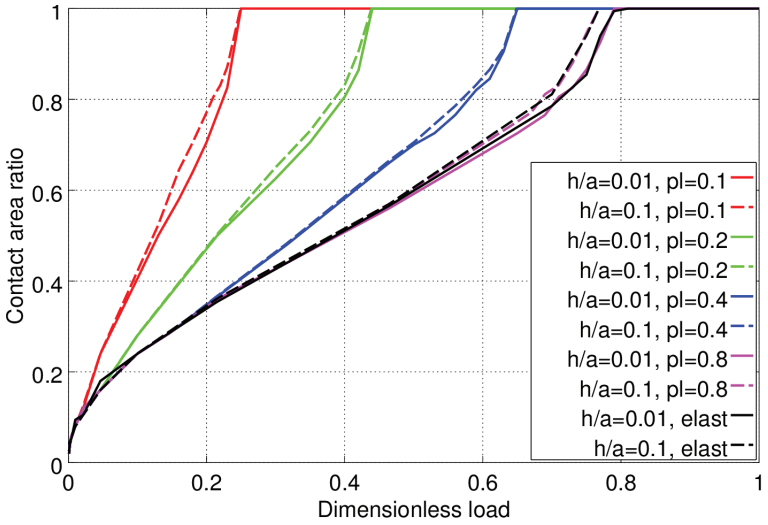

Figure 8.7: Impact of plasticity limit on the real area of contact for two-dimensional sinusoidal asperities with a=0.1 mm

The results show that for the curve sets corresponding to a dimensionless yield limit parameter $\bar{\sigma_y}$ equal to 0.1, 0.2 and 0.4, plastic deformation occurs beyond a certain load limit for each of the three curve sets. Below that limit for a given curve set, the calculated contact area coincides with the one of the pure elastic case. For curve sets at lower values of the dimensionless yield limit $\bar{\sigma_y}$ the load level where plastic deformation starts is also lower and the slope of the contact area curve for loads beyond that limit is steeper.

For a given value of the dimensionless yield limit $\bar{\sigma_y}$, one single curve can represent with reasonable accuracy asperities with different average slopes h/a, at least in the range of $h/a < 0.1$. This observation justifies the choice of Equation (8.27) for expressing the yield limit in dimensionless form.

8.2.4 Normal contact for three-dimensional asperities

The results presented so far for the calculated contact area between a two-dimensional sinusoidal asperity and a flat obstacle, can be extended to three dimensions by considering the following asperity form:

$$z_{sin}(x,y) = h \cdot (1 - cos^2 \frac{\pi x}{2a_x} \cdot cos^2 \frac{\pi y}{2a_y}) \tag{8.28}$$

with a_x and a_y standing for the half-period lengths in directions x and y respectively. For $a_x = a_y$ the asperity is equiaxial resembling a sphere and the reference pressure p_{ref} can straightforwardly be defined according Equation (8.18). In the general case of $a_x \neq a_y$ however, the asperity is elongated in one direction resembling an ellipsoid and the definition of the reference pressure has to be redefined as:

$$p_{ref} = E' \frac{h}{\min(a_x, a_y)} \tag{8.29}$$

Figure 8.8 shows the calculated contact area for elastic and plastic contact between an equiaxial three-dimensional sinusoidal asperity and a flat obstacle for two different average slopes and five levels of the plastic yield limit. As in all previous cases, the impact of the average slope is captured well by expressing the load through the dimensionless parameter $\bar{p}$. For this reason, the rest of the calculated examples in this section, will be limited to one average slope $h/\min(a_x, a_y) = 0.1$.

In the three-dimensional case, the periodic boundary conditions of the blocks in Figure 8.3 imply that the simulated single asperity belongs to an infinite rectangular lattice of identical asperities. An alternative arrangement of the considered asperities could be according to a rhombic lattice. The latter case can actually be studied by including at least two neighboring asperities in the representative surface sample to be simulated. Figure 8.9 presents the calculated contact area for asperities arranged in a rhombic lattice and Figure 8.10 compares the actual contact regions for the rectangular (square) and rhombic asperity lattices under pure elastic material behavior. The actually simulated domain is presented with brighter colors, while the dimmed domain, represents a periodic extension made for illustration purposes.

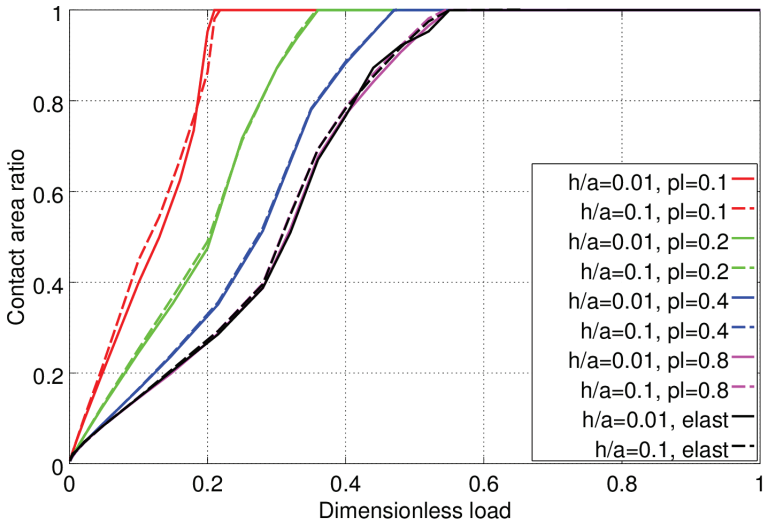

Figure 8.8: Impact of plasticity limit on the real area of contact for equiaxial three-dimensional asperities with a_x=a_y=0.1 mm arranged in a square lattice

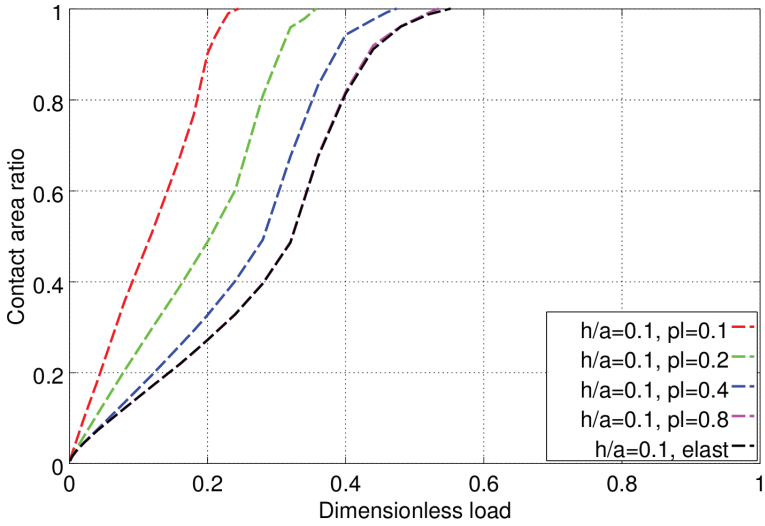

Figure 8.9: Impact of plasticity limit on the real area of contact for equiaxial three-dimensional asperities with a_x=a_y=0.1 mm arranged in a rhombic lattice

Considering only the diagram curves, the differences between the calculated areas for the two lattices are very small except at very high loads, when the real contact area ratio exceeds 90%. However, when looking at the actual contact regions, differences

appear already at lower loads, when the contact regions of neighboring asperities begin to merge together. For instance, a dimensionless load of $\bar{p} = 0.36$ yields in the elastic case a contact area ratio of approximately 70% for both lattices. Nevertheless, the shapes of the corresponding contact regions illustrated in Figure 8.10 are fundamentally different.

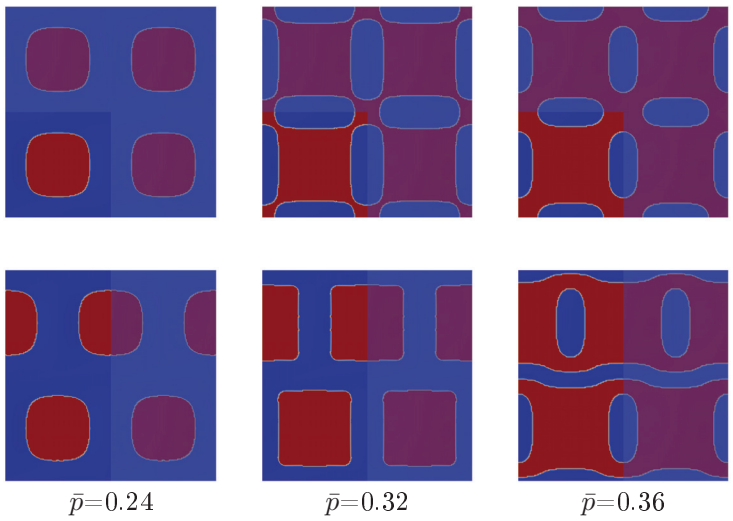

Figure 8.10: Real area of contact (in red) for equiaxial three-dimensional asperities with a_x=a_y=0.1 mm arranged in square and rhombic lattices (first and second row respectively) at different load levels under pure elastic conditions

A similar study can be made for non-equiaxial asperities. Figure 8.11 shows the calculated contact area ratios for asperities with different aspect ratios a_y/a_x, arranged in different lattice arrangements. Apart from the rectangular lattice shown in the first diagram, there are two possibilities for arranging non-equiaxial asperities in a rhombic lattice. The second diagram in Figure 8.11 refers to a rhombic lattice with asperities aligned along their short axis, while the third diagram refers to a rhombic lattice with asperities aligned along their long axis.

Figure 8.12 shows the actual contact regions at different load levels for purely elastic deformation and all three possible lattices with asperities of an aspect ratio $a_y/a_x = 4$.

The first two lattices exhibit very similar behavior not only with respect to the numerical value of the calculated contact area but also regarding the spatial distribution of the contact region. The third lattice, where the asperities are aligned along their long axis only, exhibits a fundamentally different behavior, both regarding the numerical results for the calculated contact area and regarding its spatial distribution. This

third case is actually the one that is closest to real surface topographies involving non-equiaxial asperities.

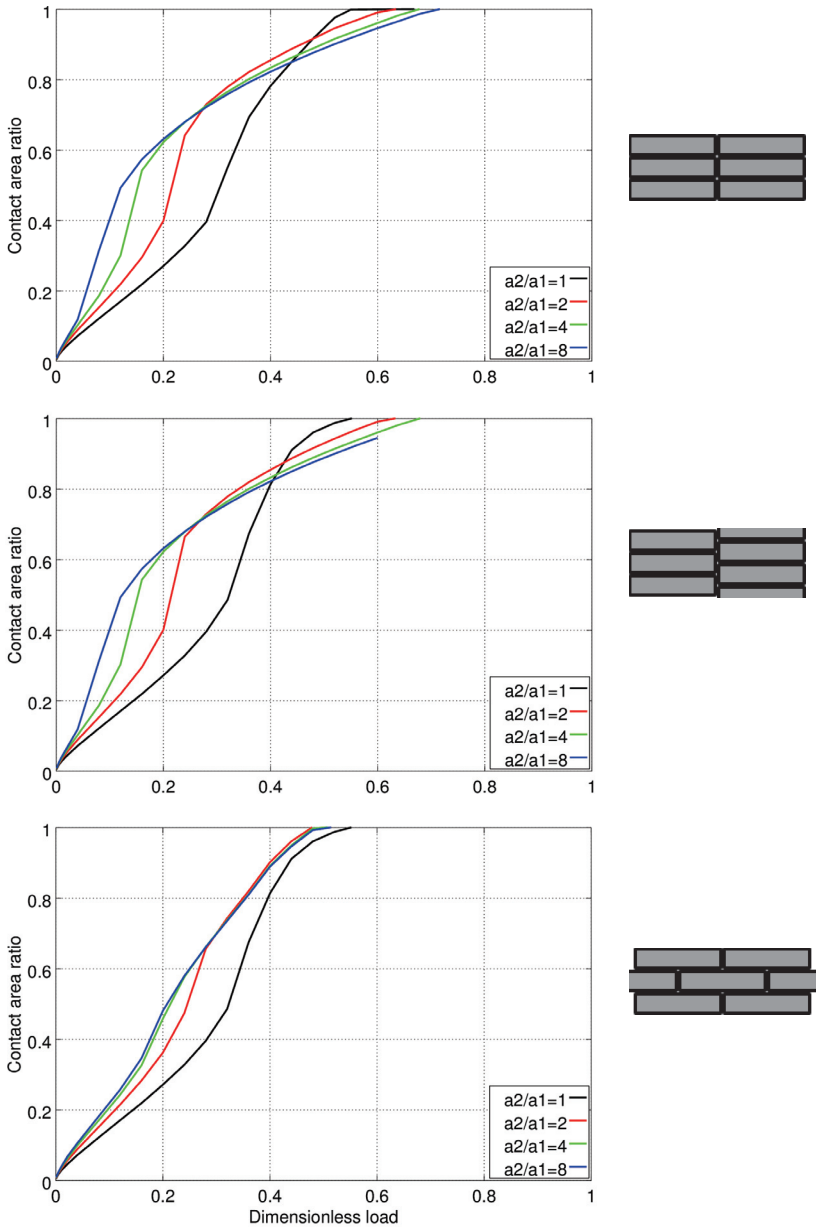

Figure 8.11: Impact of asperity aspect ratio on the real area of contact for non-equiaxial three-dimensional asperities with $a_x = 0.1$ arranged in different lattices under pure elastic conditions

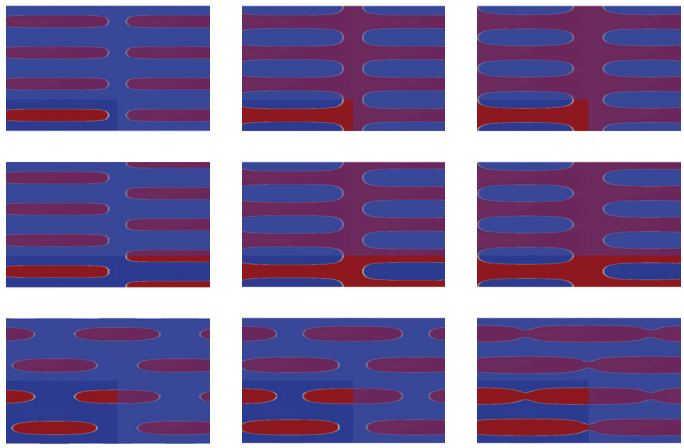

Figure 8.12: Real area of contact (in red) for non-equiaxial asperities with $a_x = 0.1$ and $a_y = 0.4$ arranged in different lattices at different load levels under pure elastic conditions

The contact regions shown in Figure 8.12 are important for practical applications requiring lubrication under relatively low sliding speeds and high pressures, because they predict cases where isolated valleys can be formed which can entrap lubricant and build up hydrostatic pressure between the contacting surfaces.

8.3 Normal contact of multiple asperities

The contact cases discussed in the previous section referred to a single asperity that was part of an infinite array of identical asperities. Real surfaces include peaks of different shapes and sizes, which are located at different heights with respect to the surface average plane. The important parameter in case of multiple asperities at different heights is the interaction between neighboring asperities. As explained in Chapter 7, the main drawback of the classical theory of Greenwood and Williamson is that it ignores this interaction assuming that the surrounding of an asperity peak is completely unloaded. A very simple but essential modification of the Greenwood and Williamson theory would be to replace the Hertzian relationship between the load and the contact area with the curves from Figures 8.7 or 8.8, where the impact of plasticity is included. This choice would additionally replace the assumption of a completely unloaded surrounding of each single asperity by the assumption of an asperity surrounded by equally loaded asperities, which is a better approximation to reality.

In this section however, the simplest case of neighbouring asperities with unequal heights will be considered, in order to estimate the impact of interaction between differently loaded neighboring asperities. A parameter study was carried out both in two and three dimensions with neighboring asperities of height h=0.01 mm and half-period a=0.1 mm, where the height difference between neighboring asperities was varied between 10 and 80% of the asperity height. The height difference was imposed by adding a sinus form of period equal to $4a$. Figure 8.13 shows the calculated contact area for the two-dimensional case and Figure 8.14 shows the corresponding result for the three-dimensional case. The dotted lines correspond to the case of asperities of same height, but with the dimensionless load adapted by a factor of two, as if only half of the asperities would take the same load.

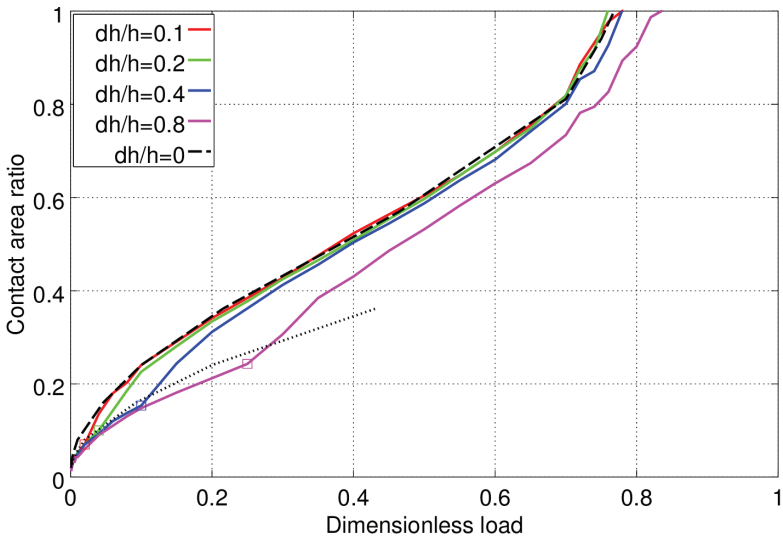

Figure 8.13: Impact of height difference between neighboring two-dimensional sinusoidal asperities on the real area of contact

It appears that for dimensionless loads higher than 0.2, height differences of up to 40% of the asperity height do not have any important impact on the calculated area. This practically means that in a surface with multiple asperities, if the roughness slopes at double wavelength are less than 40% of the asperity slopes of the currently considered wavelength, the long wavelength component has very little impact at moderate and high contact pressures.

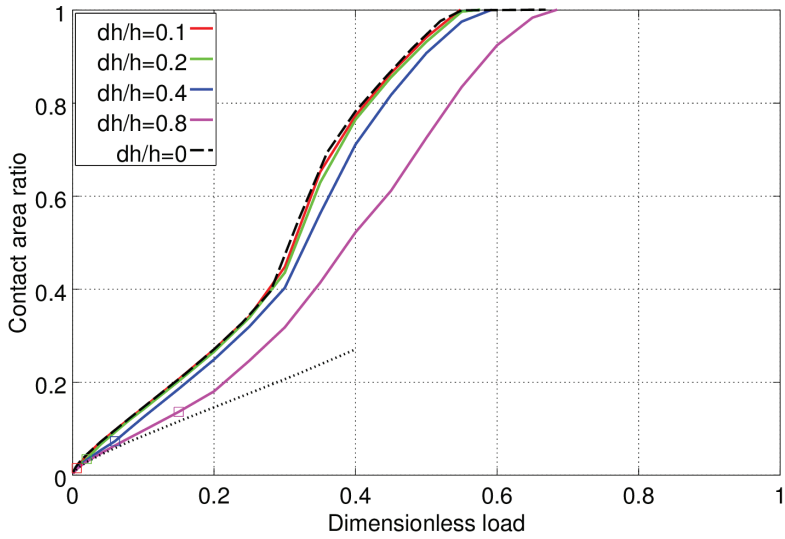

Figure 8.14: Impact of height difference between neighboring three-dimensional sinusoidal asperities on the real area of contact

8.4 Sliding and frictional contact of a single asperity

Including friction as an interfacial shear strength combined with a relative sliding between the contacting bodies increases the complexity of the system considerably. This section presents a study on the frictional sliding of a single asperity in contact with a rigid obstacle.

Figure 8.15 shows the geometry of the asperity in contact, scaled in the vertical direction in order to become easier to recognize. In the left-side case, the asperity is defined on the rigid obstacle represented in red color and the block surface is flat, while in the right-side case, the asperity is defined on the elastic block surface and the rigid counter surface is flat. The form of the asperity is sinusoidal with half-period a=0.1 mm and height h=0.01 mm. The material properties of the block correspond to PET thermoplastic with Young's modulus equal to 3000 MPa and Poisson's ratio equal to 0.43. The simulation included normal loading up to 0.294 N corresponding to a dimensionless load parameter $\bar{p}$ of 0.02, in a sequence of five increasing load steps and subsequent sliding for 0.05 mm in six further steps under constant normal load.

Figure 8.16 shows the calculated contact area for the cases shown in Figure 8.15. The right-side case of Figure 8.15 with the flat rigid obstacle is distinguished in the graphs by the identifier "flat". The results include both the case of a purely elastic deformation and the case with a yield limit σ_y equal to 75 N/mm^2. The contact area

is increased when plastic deformation is taken into account. Moreover the contact area is increased further when friction with a coefficient of 0.2 is included in the calculation additionally to plasticity. In the purely elastic case, inclusion of friction doesn't seem to affect the calculated contact area.

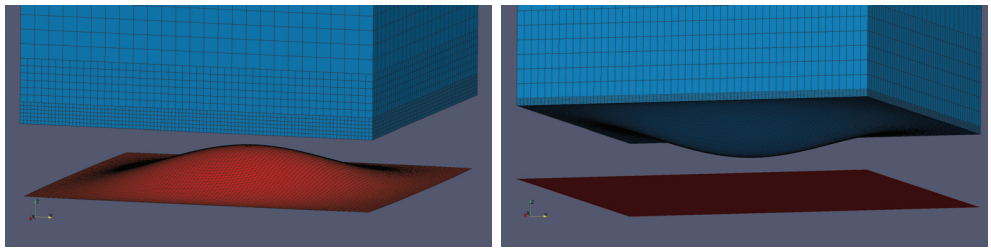

Figure 8.15: Reference geometry for studying the loaded contact and sliding of a single sinusoidal asperity between a perfectly elastic body and a rigid obstacle (scaled vertically by a factor of five)

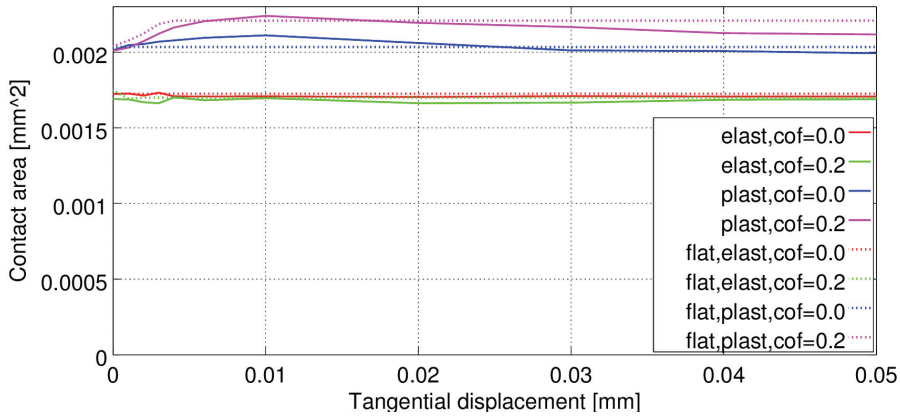

Figure 8.16: Calculated contact area for a single sinusoidal asperity in sliding under load

Figure 8.17 shows the horizontal component of the contact forces acting normal to the asperity surface. For the elastic cases and the cases with the flat rigid obstacle, the calculated horizontal force is, as expected equal to zero. For the case with plastic deformation and ploughing of the block surface, a horizontal force of 0.0034 N was calculated. With a normal force of 0.294 N, this horizontal force corresponds to a contribution of 0.012 to the coefficient of friction, due to ploughing, which is a small but not negligible amount.

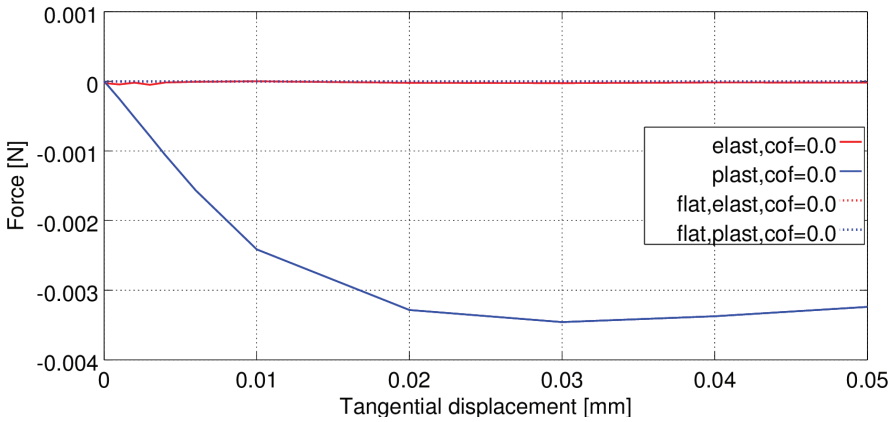

Figure 8.17: Calculated horizontal force due to normal forces applied to the sliding asperity

8.5 Calculation of practical cases

Three different cases of contact pairs corresponding to realistic conditions are presented in this section. The used surface roughness topographies correspond to pin specimens and discs used in pin-on-disc testing presented in Chapter 4. Areal topographies of the pin surfaces were measured using focus variation microscopy equipment and the topography of the disc track was reconstructed by revolving, around the disc axis, the disc roughness profiles from Figures 7.2 and 7.3. The actually utilized surface topographies are illustrated in Figure 8.18.

The assumed material parameters of the three simulated pins are summarized in Table 8.1, while typical material data for steel were considered for the disc.

Table 8.1: Material parameters used in the calculations

Pin Material	E [MPa]	ν [-]	σ_y [MPa]
TP1	3000	0.43	90
TP3	1600	0.44	50
FC1	7260	0.27	-

The dimensions of the discretized surface samples are 0.715 times 0.54 mm for the first two examples and 1.43 times 1.08 mm for the third one. The first and the second

dimensions refer to the tangential and the radial disc directions respectively. In all cases, the element size of the disc contact surface is 0.015 times 0.008 mm. For the pin contact surfaces the elements are square with a size of 0.0044 mm in the first two examples and 0.0088 mm in the third one.

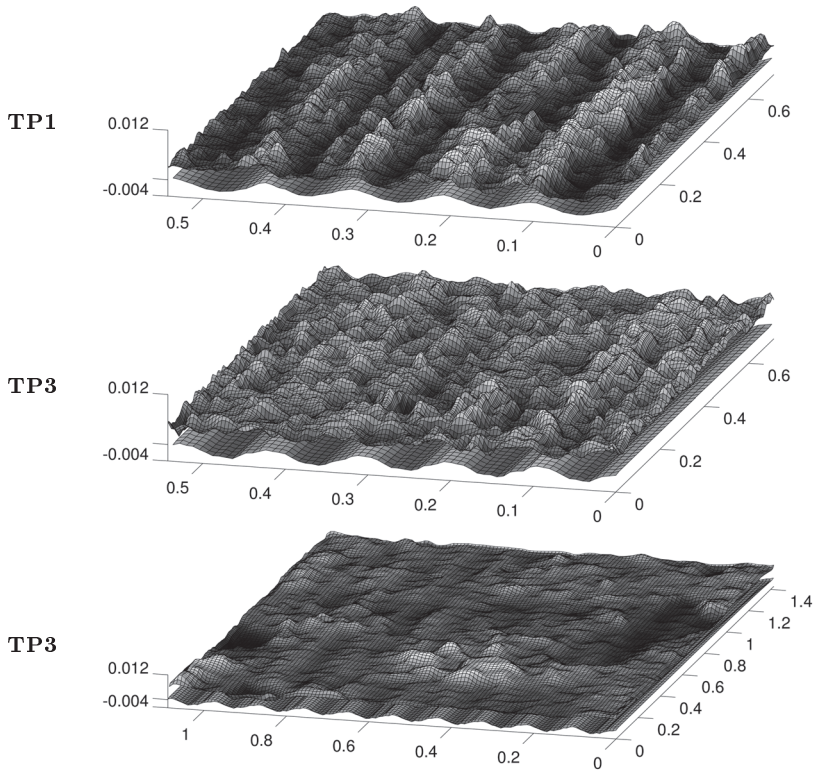

Figure 8.18: Pin and disc topographies for the three calculated examples

For each contact pair a series of load cases corresponding to nominal pressures from 3 to 24 MPa, increasing in steps of 3 MPa were calculated consecutively. For the cases of materials TP1 and TP3, that involve plastic deformation, the same load steps were repeated also in descending order.

Figure 8.19 shows the contact stress distribution on the disc surfaces for the three calculated examples at the maximum nominal pressure. The real contact area is distinguished by presence of non-zero contact stress. Figure 8.20 illustrates the evolution of the ratio between the real contact area and the apparent contact area during the variation of the nominal pressure. The lower and the upper branches of the curves for material TP1 and TP3 correspond to the loading and unloading phases respectively.

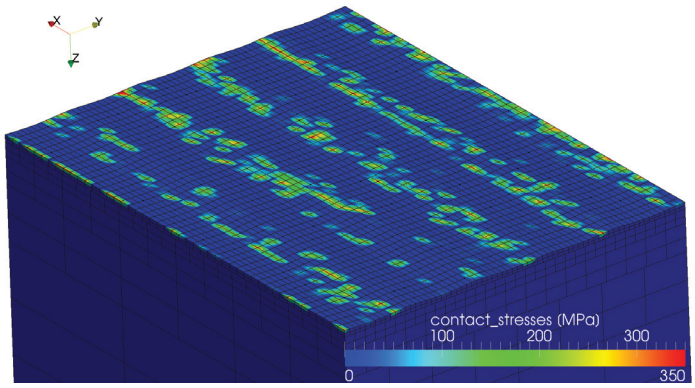

(TP1)

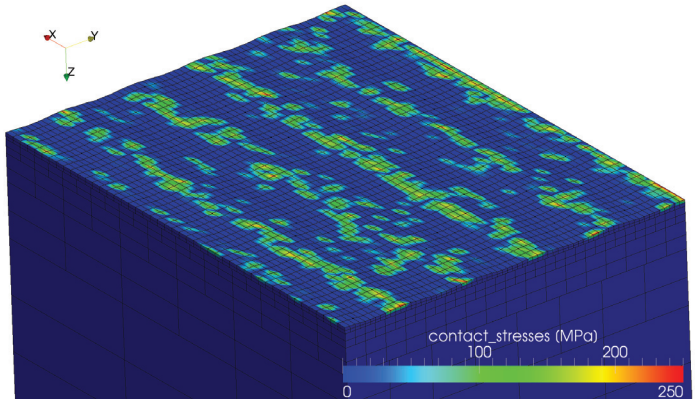

(TP3)

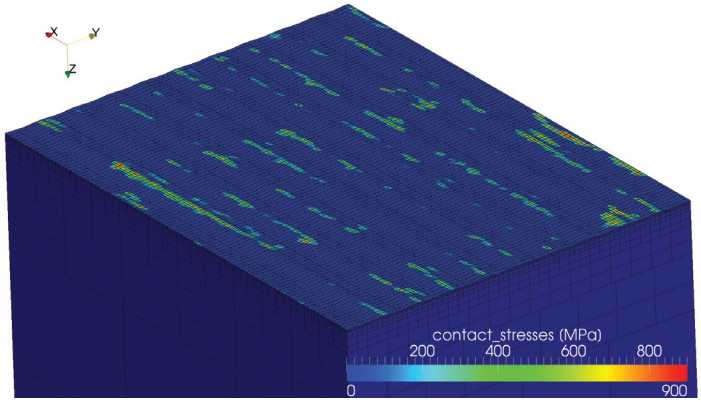

(FC1)

Figure 8.19: Contact stress on the disc surface for the three calculated cases at 24 MPa

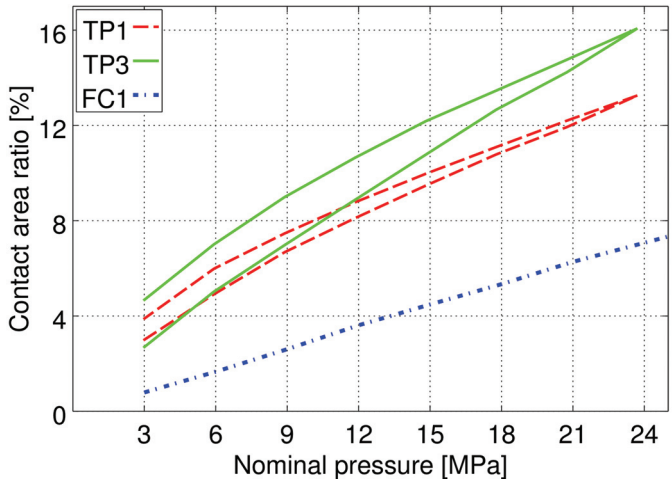

Figure 8.20: Relation between the nominal pressure and the real contact area ratio for the three calculated cases

Figure 8.21 shows the evolution of the mean contact pressure within the real contact area for varying nominal pressure. For the thermoplastic pin materials TP1 and TP3 the upper and the lower curve branches correspond to the loading and unloading phases respectively.

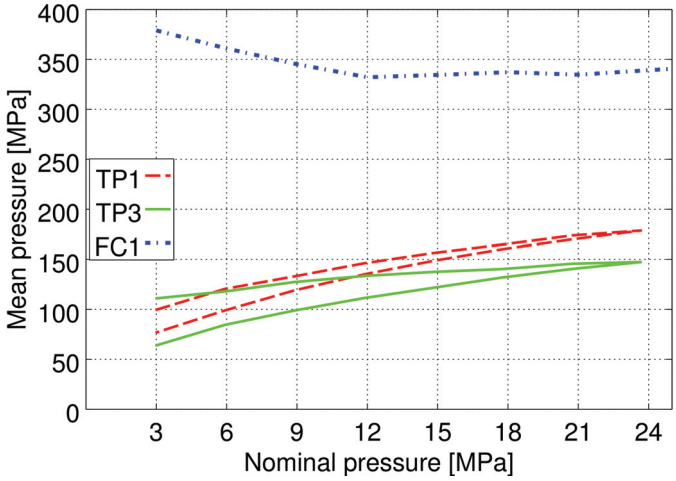

Figure 8.21: Relation between the nominal pressure and the mean contact pressure for the three calculated cases

From the graphs presented in Figures 8.20 and 8.21, it becomes obvious that there is both a quantitative and a qualitative difference between the fiber composite FC1 and the two thermoplastics TP1 and TP3. Material FC1 results in a significantly lower real contact area and correspondingly higher mean contact pressure. Moreover, the evolution of the mean contact pressure is qualitatively different. For increasing nominal pressure, in case of material FC1 the mean contact pressure remains approximately constant while for materials TP1 and TP3 it raises steadily.

The differences between materials TP1 and TP3 are smaller. Thermoplastic TP3 has lower Young's modulus and yield stress resulting in higher contact area and more extensive permanent deformations. The plastic deformation of the pin material is reflected in the difference between the ascending and the descending load branches of the curves in Figure 8.20.

Chapter 9

Conclusion and future aspects

Targeting a specific real life application, namely the yaw system of horizontal axis wind turbines, the present thesis was intended for providing a basic reference for material selection, material testing and dimensioning with respect to the considered system. In order to fulfill this goal, both experimental and theoretical subjects were dealt with.

The literature research presented as part of this work is an important contribution by itself. Apart from the synoptic listed references in Chapter 1, one can find in Chapter 2 further literature sources with information and examples on the operational conditions of the studied system. In Chapter 3 the technological aspects of most relevant friction materials was presented in a brief but concise way along with a number of selected references.

Chapter 2 aimed at establishing a connection between the overall wind turbine operational conditions and the corresponding mechanical behavior within each individual system segment. It was shown how a segmented wind turbine yaw system can be represented by a relatively simple but parametric finite-element model, for predicting the load distribution among the system segments, including the effect of nacelle stiffness. The practical numerical examples presented in Chapter 2, were considered as references for the conditions tested experimentally and they can also be considered as indicative for the wind turbine yaw system in general.

The experimental part of this work, including pin-on-disc and pin-on-plate testing, has provided a collection of friction coefficients and wear rate reference values for a variety of materials. Moreover, the testing procedures and the particularities with respect to reciprocating, low speed and high load conditions, were documented. All tested materials under both dry and grease-lubricated conditions, exhibited coefficients of friction that either decrease or remain approximately constant with increasing contact pressure. The impact of pressure on wear rate was determined experimentally for two different materials, which both exhibited a linear relationship between pressure and wear rate, but only one of them could be expressed by Archard's wear equation. A general conclusion from the conducted experimental testing is that thermoplastics and fiber composites are the most promising material groups for the considered application.

Chapter 7 presented practical cases from selected experimental tests, evaluating the results within the framework of well-established friction and wear mechanisms found in literature. The running-in effect, always observed in the tests as a period of increasing friction, was attributed through specific examples to changes in the roughness topographies and material transfer, normally from the friction material to the steel surface side. Optical microscope pictures and surface topography measurements corresponding to surfaces subject to dry testing, revealed the formation of load carrying local plateaus and indicated their shapes and sizes. Moreover, SEM pictures of the tested surfaces and the corresponding wear debris particles revealed a structure resulting from compaction of finer fragments. The role of material transfer in avoiding abrasive wear was also demonstrated in the case of dry testing of PET.

The finite-element model presented in Chapter 8 was utilized for mechanical contact studies of simple cases of single asperity contact between an elastic body and a rigid obstacle, but also for studying mechanical contact including plasticity and friction between realistic surface topographies. The results corresponding to the simple cases were expressed in terms of dimensionless parameters that can serve as references or be used as part of semi-analytical models.

Summarizing the present work, the considered main system was examined for mechanical behavior at machine elements level as a reference for experimental tribological testing and numerical algorithms in the field of contact mechanics were implemented. Due to its multidisciplinary structure however, the present work could reach only a certain level of detail within each of the studied fields. For this reason, it is natural to highlight the most important aspects that can be suggested for future research.

One material group, mentioned in the present thesis but not included in the conducted tests, are elastomers. It would be very interesting to investigate how elastomers compare in terms of friction and wear to the so far tested materials. The present work has also revealed, how material wear can depend on the contact pressure in

different ways. It would be interesting to extend the tests under variable pressures to further materials.

Finally, the implemented micro-contact model proved itself as a useful tool both for understanding friction mechanisms at theoretical level and for simulating specific cases of contact between real surfaces. Application of the model to more cases of real surfaces would provide further insight to the current understanding on friction and wear mechanisms, in a more quantitative manner. In particular, emphasis could be put on utilizing material properties that are experimentally determined in the size scale represented by the model, on applying relative sliding between realistic surfaces as well as on studying different interfacial constitutive laws. Moreover, an extension of the model to include viscoelastic material behavior and non-homogeneous or layered materials, would create new possibilities for realistic simulation of more complex systems.

Appendix A

Publications

This appendix includes two peer reviewed papers published in the framework of the present Ph.D. thesis (P1 and P2) in the journals "Tribology Letters" and "Wear" respectively, one additional paper that has been submitted for publication to the "Wear" journal (P3) and one publication that was presented in the 3rd International Tribology Symposium of IFToMM (P4).

Publication [P1]

Tribol Lett (2013) 51:191–198
DOI 10.1007/s11249-013-0107-0

ORIGINAL PAPER

Coefficient of Friction Measurements for Thermoplastics and Fibre Composites Under Low Sliding Velocity and High Pressure

K. Poulios · G. Svendsen · J. Hiller · P. Klit

Received: 14 November 2012 / Accepted: 22 January 2013 / Published online: 3 February 2013
© Springer Science+Business Media New York 2013

Abstract Friction materials for typical brake applications are normally designed considering thermal stability as the major performance criterion. There are, however, brake applications with very limited sliding velocities, where the generated heat is insignificant. In such cases it is possible that friction materials which are untypical for brake applications, like thermoplastics and fibre composites, can offer superior performance in terms of braking torque, wear resistance and cost than typical brake linings. In this paper coefficient of friction measurements for various thermoplastic and fibre composite materials running against a steel surface are presented. All tests were carried out on a pin-on-disc test-rig in reciprocating operation at a fixed sliding speed and various pressure levels for both dry and grease lubricated conditions. Moreover, a generic theoretical framework is introduced in order to interpret the changes of friction observed during the running-in phase.

Keywords Coefficient of friction · Thermoplastics · Fibre composites · Low speed · Reciprocating

1 Introduction

In general, the selection or design of friction materials for brake applications is based on factors like the coefficient of friction, the wear resistance, the thermal stability, the tendency for noise generation and the material cost.

The function of typical brake applications, such as vehicles, crane winches or a wind turbine drive train, is to bring the corresponding mechanical systems to standstill by converting their kinetic energy to heat. Such brakes are dimensioned for reaching a certain peak temperature and the friction materials to be used are required to exhibit good thermal stability up to this temperature level. The possible friction material choices include sintered or organic composites or fibre composites specially designed for thermal stability [1].

A different kind of brake applications are the so-called positioning or holding brakes. Their function is to maintain the relative position between two components and occasionally permit a relative motion at low sliding speeds. The heat generation in such cases is usually very low and the coefficient of friction and low-noise operation are the main criteria for the selection of friction materials. A typical application of this kind is the brakes in the wind turbine yaw system. In special cases the positioning brake functionality can be integrated in a slide bearing.

The main objective of this paper is to present coefficient of friction measurements for different thermoplastics and fibre composites running against steel. Moreover, it presents the particularities of using a pin-on-disc test-rig for studying the coefficient of friction with respect to positioning brakes applications. A simple but quite generic theoretical framework for interpreting the changes of friction observed during the running-in phase is also presented.

2 Testing Equipment and Methods

Figure 1 shows a simplified illustration of the used pin-on-disc test-rig. The normal load on the pin (1) is determined by the position of the mass (2) on the loading arm (3). The

K. Poulios (✉) · G. Svendsen · J. Hiller · P. Klit
Department of Mechanical Engineering, Technical University of Denmark, Nils Koppels Allé, Building 404, 2800 Kgs. Lyngby, Denmark
e-mail: kopo@mek.dtu.dk

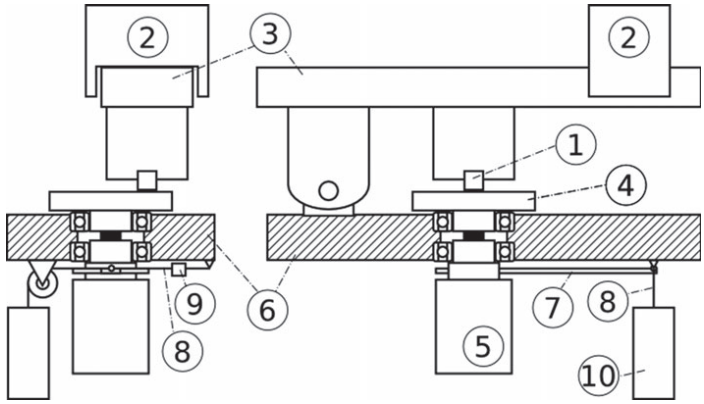

Fig. 1 Simplified illustration of the pin-on-disc test-rig

rotating disc (4) is driven by an electric motor (5). The rotation of the motor housing with respect to the test-rig frame (6) is restricted exclusively through the arm (7), the wire (8) and the load cell (9).

One of the particularities of positioning brakes is their intermittent operation in both sliding directions. In order to take this effect into account the sliding direction had to be alternated periodically during the testing. In order to enable the friction measuring in both rotational directions of the disc the wire (8) and the load cell (9) are preloaded through the weight of an additional mass (10).

In contrast to typical brake applications, positioning brakes operate at much lower sliding speeds and permit much higher pressure levels. A gearbox of transmission ratio 30 integrated in the test-rig motor (5) was used in order to permit testing speed as low as 20 mm/s and pressures of up to 20 MPa.

Part of the testing procedure is the calibration of the normal force applied to the pin and the friction force recording load cell (9). The normal force applied to the pin is determined by an initial load due to the weight of the loading arm and a variable load proportional to the linear position of the corresponding mass (2). A calibration line correlating the mass position with the normal force was determined by placing a compressive load cell below the pin and moving the mass to different positions. During the tests the position of the mass is adjusted through a stepper motor in order to achieve the desired nominal pressure on the pin surface. The calibration of the load cell (9) was done in-place by adding and removing weight to the corresponding mass (10).

The dimension of the pins used for all tests was 10 mm in diameter. The pin specimens were manufactured from the different materials to be tested by turning larger material samples provided in form of plates or bars. The disc material was alloy steel 34CrNiMo6 in unhardened condition and the disc surface was turned with surface roughness corresponding to arithmetic average values (Ra) varying from 0.7 to 1 μm for the different discs used in the tests.

Because of the flat form of the pin surface in contact with the disc, a good alignment between the pin and the disc surfaces is very important. For this purpose, pressure sensitive paper was used before every test in order to verify a uniform contact through the whole pin surface. Figure 2 shows two photos of a partial and a full pin contact.

For each of the tested materials an initial running-in test on the disc track with diameter of 80 mm ensured that any remaining geometrical misalignment between the pin and the disc would be eliminated through the wear process. During this initial running-in, the nominal pressure applied to the pin was 6 MPa and the sliding direction was alternated every 0.9 m. During this initial testing phase as well as in all following testing steps the rotational speed of the disc was adjusted to a fixed sliding speed of 20 mm/s in the middle of the respective testing track.

Following, the pin was moved on the disc track with diameter of 102 mm where the actual measurement took place. On this track a second running-in was carried out under the same conditions as the first one until the recorded coefficient of friction approximated a steady state. After that state was reached, the pressure was varied from 3 to 18 MPa in steps of 3 MPa. For each pressure level, a sliding distance of 10 m was covered with a reciprocation stroke length of 0.9 m.

After this phase, the pin was moved to a third track at disc diameter of 124 mm that was covered with an approximately 1-mm-thick layer of grease. During a similar running-in period like in the previous cases, the grease layer is removed from the track due to the motion of the pin. However, a small quantity of lubricant will remain in the contact either because of the strong adhesion of a very

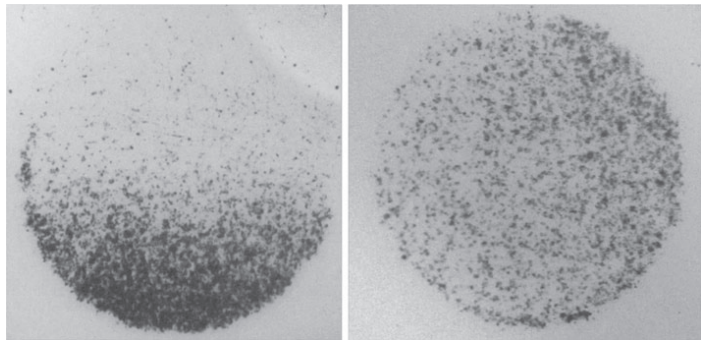

Fig. 2 Pin imprint on pressure sensitive paper for a case of bad (*left*) and good (*right*) alignment between the pin and the disc

thin layer of lubricant with the surfaces or because of the lubricant that is stored in the porous structure of the tested materials. It was observed in all tests that were carried out, that the pin runs under boundary lubrication conditions for distances longer than 300 m even if no further grease is added to the contact. The base oil viscosity of the grease used in the tests was 46 mm^2/s and its consistency corresponded to NLGI number 2.

3 Results

Table 1 summarizes the tested friction materials that will be presented in this section. All five materials are representative samples of commercially available products of their category. The first three ones can be categorized according to their major component as thermoplastics and the last two as fibre composites.

The first category includes semi-crystalline thermoplastic materials that are either in almost pure form like in the cases of PET and PA 6 or are combined with a relatively low amount of reinforcement and lubrication additives like chopped glass fibres and molybdenum disulphide, respectively, in the case of PA 66+. The pins of PET and PA 6 materials were manufactured from extruded bars so that the contact surface is perpendicular to the axis of the raw material bars. The pins for PA 66+ were machined out of extruded plates of the raw material with the contact face parallel to the mid-plane of plate.

Table 1 Description and abbreviated names of the tested materials

Symbol	Description
PET	Polyethylene terephthalate
PA 6	Polyamide 6
PA 66+	Polyamide 6.6 with glass fibres and molybdenum disulphide
FCF	Fine fibre composite with aramid
FCC	Coarse fibre composite

The second category, represented by the types FCF and FCC, refers to materials that are dominated by a high amount of fibres typically bond together with some kind of epoxy resin thermoset. FCF consists of randomly oriented cellulose and aramid fibres that result to a fine and homogeneous structure that resembles the corresponding pulp that is typically used in its manufacturing process. FCC consists of a woven yarn textile impregnated in a bonding resin. The material structure is coarse and oriented, with the direction of the crossed woven fibres parallel to the contact interface.

Figure 3 shows the evolution of the coefficient of friction during the second running-in phase of the three thermoplastics without lubrication, and Fig. 4 shows the corresponding curves for the two fibre composites.

It must be noted that the filtered curves shown in these diagrams demonstrate the long-term evolution of the coefficient of friction. However, after each alternation of the sliding direction a short-term transition may occur due to e.g. a reorientation of the surface asperities. This phenomenon was mostly pronounced for PA 6 while for other

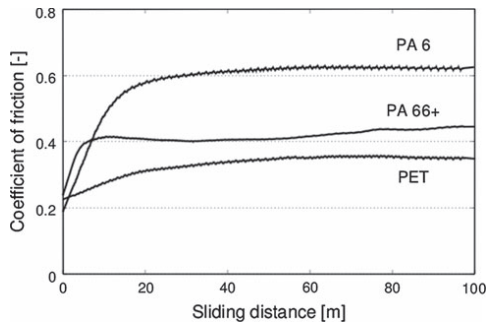

Fig. 3 Running-in of thermoplastics without lubrication

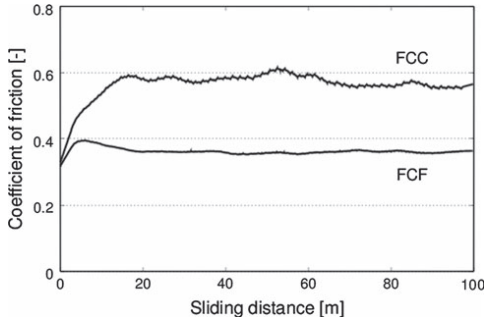

Fig. 4 Running-in of fibre composites without lubrication

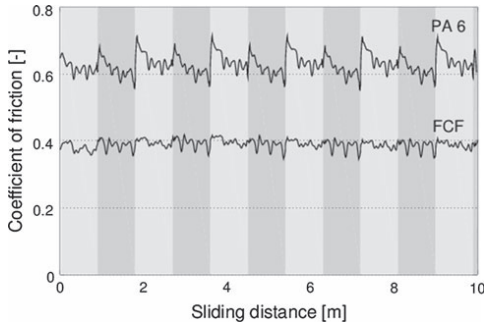

Fig. 5 Steady-state coefficient of friction measurement for PA 6 and FCF at the pressure of 6 MPa

materials like e.g. for the FCF one it could not be observed at all. Figure 5 shows the unfiltered coefficient of friction measurement during the steady-state phase for PA 6 and FCF. The light and dark background of the diagram illustrates the different sliding directions. It is evident that in the case of PA 6 the coefficient of friction increases significantly after each direction change.

Figure 6 shows the variation of the average coefficient of friction for all five materials over the tested pressure range. It seems that the measured coefficient of friction for all three thermoplastics is quite unaffected by the pressure level. Especially the PET thermoplastic exhibits a completely constant coefficient of friction over the whole pressure range. The measured coefficient of both fibre composites exhibits the same negative tendency with increasing pressure. The corresponding running-in and pressure variation measurements with the presence of grease lubricant are illustrated in Figs. 7, 8 and 9.

With lubrication, after the running-in phase all three thermoplastics exhibited similar coefficients of friction between 0.12 and 0.15. The glass fibre reinforced

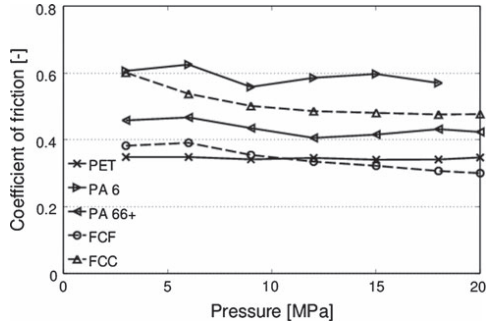

Fig. 6 Impact of the nominal contact pressure on the average coefficient of friction without lubrication

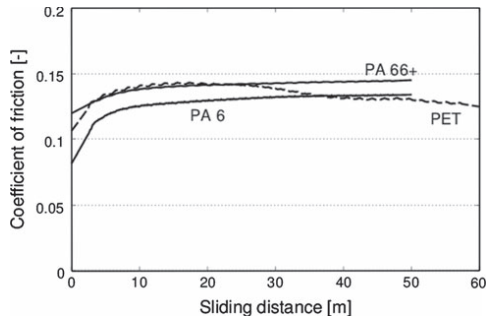

Fig. 7 Running-in of thermoplastics with grease lubrication

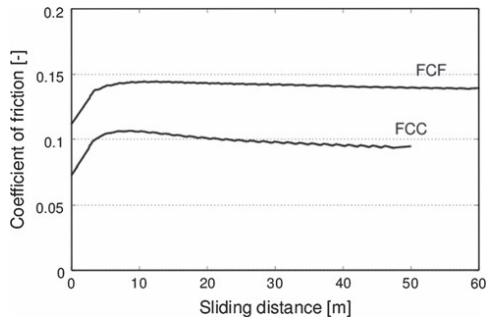

Fig. 8 Running-in of fibre composites with grease lubrication

polyamide PA 66+ had a tendency to higher friction values than the other two thermoplastics. Concerning the two fibre composites, the finer one behaved similar to the thermoplastics, while the coarse fibre composite FCC demonstrated a significantly lower coefficient of friction around 0.09.

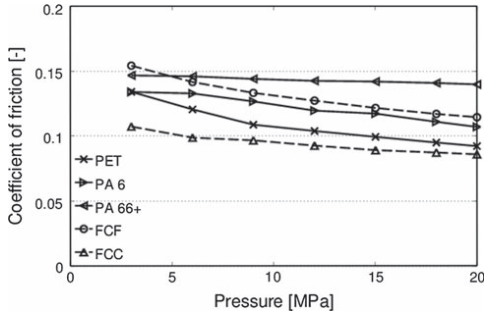

Fig. 9 Impact of the nominal contact pressure on the average coefficient of friction with grease lubrication

4 Discussion

In both dry and lubricated tests the observed coefficient of friction increases during the running-in period. In the lubricated case this increase is mainly due to the transition from mixed to boundary lubrication, as the quantity of the grease on the track is reduced to a minimum. However, the increasing coefficient of friction during the dry running-in occurs due to less evident phenomena.

Formation of transfer layers is the first phenomenon to be mentioned [2, 3]. Either material from the pin can adhere to the disc surface or particles from the disc like e.g. iron oxides can adhere to the pin surface. In this way the increased affinity between the two contacting surfaces normally yields to an increase of the interfacial shear strength.

Changes in the topography of the contacting surfaces during the running-in period can be mentioned as the second factor that contributes to the increasing coefficient of friction. Through the wear process the surfaces tend to become more conformal than initially. This may give rise to a higher real contact area between the two surfaces and an increased coefficient of friction.

All results presented in the previous section are related to the nominal pressure P that is an average pressure over the apparent contact area A_a corresponding to the pin diameter of 10 mm. More relevant for the understanding of

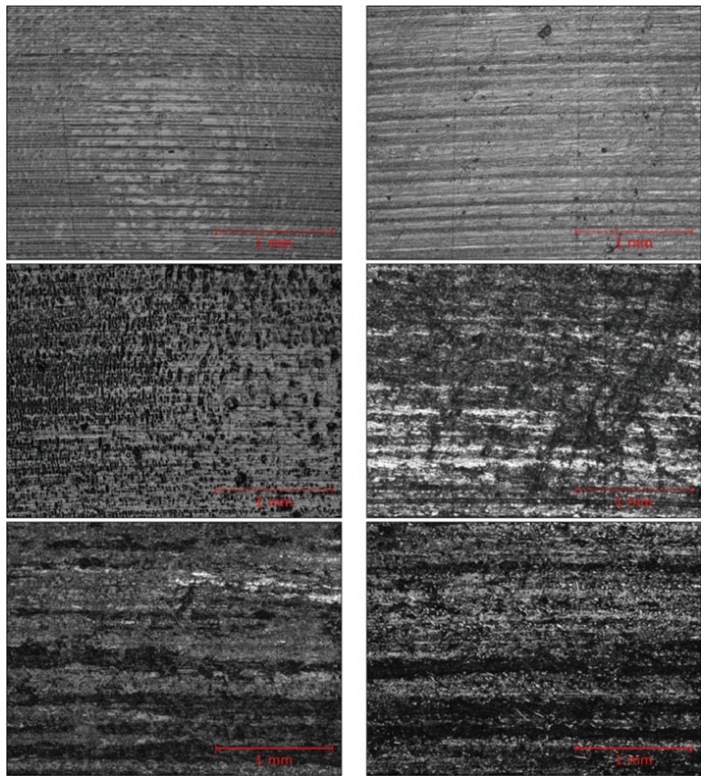

Fig. 10 Images of the pin surfaces for PET (*top*), PA 6 (*middle*) and PA 66+ (*bottom*) after dry and lubricated testing (*left* and *right column*, respectively). Dimensions: 2.84 × 2.15 mm

the tribological system is, however, the local pressure p which is distributed over the real contact area A_r. The real contact area is load dependent and much smaller than A_a. The macroscopically observed Amonton's first hypothesis about a pressure independent coefficient of friction can be explained only through consideration of the real contact area [4, 5]. Studying less ideal cases like the pressure dependent coefficients of friction shown in Figs. 6 and 9 requires consideration of the real contact area A_r as well.

Even if at macroscopical level the coefficient of friction is either independent or weakly dependent on the nominal pressure, microscopically the constitutive law for the interfacial shear may not be proportional to the normal stress. The following constitutive equation can be used for approximating the shear strength of the interface, [6]:

$$\tau = \tau_0 + c.p \tag{1}$$

In this equation τ_0 is a constant interfacial shear stress related to adhesion and c is a proportionality constant for the pressure dependent term.

The normal force F_N in the contact can be defined as the integral of the local pressure p over the real contact area A_r and the friction force F_T as the integral of the shear stress τ. By integration of Eq. 1 follows:

$$F_T = \tau_0 A_r + cF_N \tag{2}$$

and the coefficient of friction can consequently be expressed as:

$$\mu = \tau_0 A_r / F_N + c \tag{3}$$

Eq. 3 reveals the importance of the real contact area A_r for the observed coefficient of friction μ. During the running-in process, due to changes in the topographies of the contacting surfaces, A_r increases for constant F_N, causing the coefficient of friction to increase as well. Formation of transfer layers may additionally provoke changes in the constitutive law constants τ_0 and c [3].

The variation of the nominal contact pressure in Figs. 6 and 9 corresponds to variation of F_N in Eq. 3. The coefficient of friction μ will remain constant only if the real contact area A_r increases proportionally to F_N or if τ_0 is negligible (in comparison to the local pressure p). In most practical cases, τ_0 cannot be neglected and, therefore, it is important to study the relation between A_r and F_N. A constant ratio A_r/F_N means that the average local pressure in the real contact area remains constant with changing normal load. This is the case for both the model of Bowden and Tabor [4] that assumes fully plastic deformation and approximately also for the fully elastic models of Archard [7] and Greenwood and Williamson [5]. In the more general case, A_r and F_N are not proportional and their ratio depends on the elastic properties of the contacting bodies and their surface topographies.

The lower friction levels observed under boundary lubrication conditions are attributed to the impact of the lubricant film on the constants τ_0 and c in Eq. 1. However, changes of these two constants are not sufficient for explaining the increased or reduced dependence of the coefficient of friction on the pressure level that is observed with the addition of lubricant. In comparison to Fig. 6, the coefficient of friction dependence on the pressure in Fig. 9 becomes stronger for some materials (e.g. PET, PA 6) and weaker for others (e.g. FCA). A less evident factor

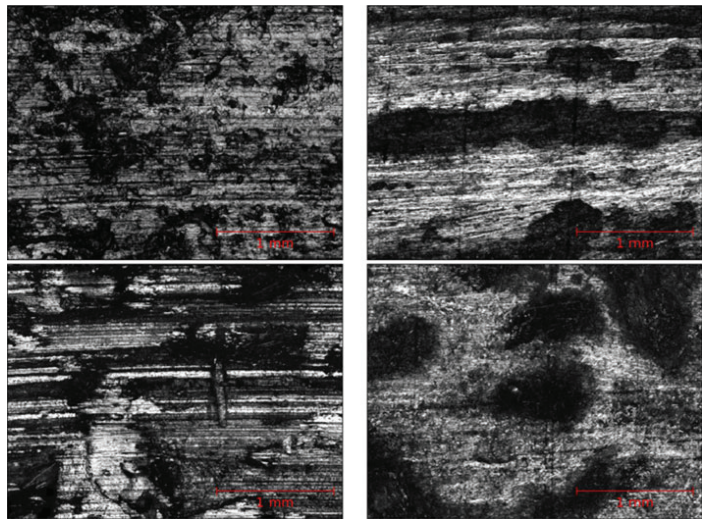

Fig. 11 Images of the pin surfaces for FCF (*top*) and FCC (*bottom*) after dry and lubricated testing (*left* and *right column*, respectively). Dimensions: 2.84 × 2.15 mm

affecting the slope of the coefficient of friction curves in these figures is the impact of lubrication on the surface topography. The different wear mechanisms under lubricated conditions yield to different surface topographies in comparison to the dry case. The modified surface topography affects the evolution of the ratio A_r/F_N in Eq. 3. Figure 10 shows optical microscope pictures of the three thermoplastic pin surfaces after dry and lubricated runs. Figure 11 contains similar pictures for the two fibre composites. From the different wear traces that are visible on the pictures corresponding to PA 6 and the fibre composites one can recognize how the presence of lubricant can yield to significantly different surface topographies.

Figure 12 shows the surface topographies obtained with a focus variation optical system for the three thermoplastics after the dry testing. In the first two cases, it is easy to recognize a characteristic wavelength in the vertical direction which corresponds to the turning marks of the steel counter surface. The surface topography for PA 66+ is quite different, covered by relatively flat patches with a characteristic dimension of approximately 0.5 mm. Hence, the wear process of relatively homogeneous materials like PET and PA 6 results in a surface similar to the surface of the counter material. Formation of patches of compacted debris in the vicinity of hard inclusions is a characteristic of reinforced materials like PA 66+.

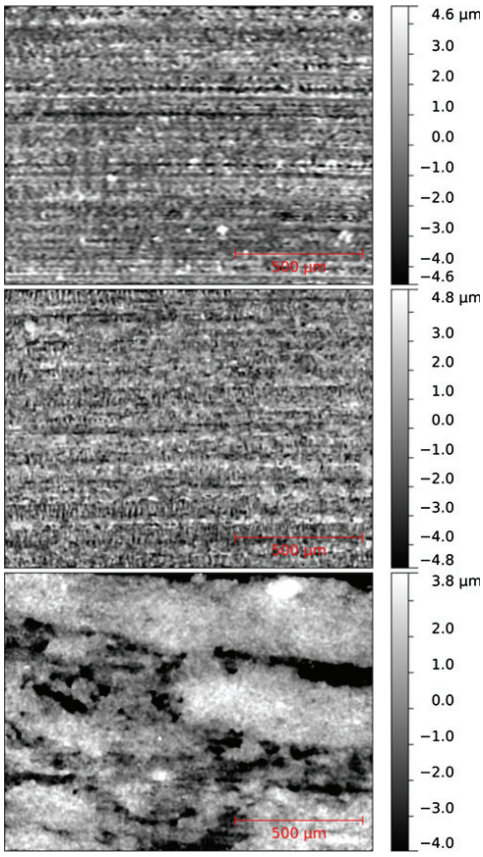

Fig. 12 Surface topographies for thermoplastics after dry testing, PET (*top*), PA 6 (*middle*) and PA 66+ (*bottom*). Dimensions: 1.43 × 1.09 mm

5 Conclusions and Future Work

Friction materials from two very dissimilar material categories were tested under conditions that are relevant for holding brake applications. Some of the practical conclusions that could be drawn are listed below:

- The measured coefficient of friction for all tested thermoplastics appeared to be independent from the nominal pressure under dry conditions.
- The coefficient of friction for fibre composites dropped significantly with increasing nominal pressure under dry conditions.
- With grease lubrication in all cases except one the coefficient of friction dropped with increasing pressure.
- For the design of holding brake applications with friction materials similar to the ones tested here, a coefficient of friction of 0.15 should be considered as an absolute maximum in case that grease reaches the contact surfaces even occasionally.
- Under dry conditions, thermoplastics like PA6 and fibre composites like FCC can offer high coefficient of friction close to values typically met in organic and sintered brake pads used in normal brake applications. However, wear and noise behaviour should also be considered.

In this work, some interesting cases concerning the coefficient of friction dependence on pressure were identified. In order to verify the corresponding assumptions and the qualitative explanations presented in this work the following tasks are proposed for future work:

- The wear process and its impact on the evolution of the friction force could be investigated. Due to expected variations of the material composition, multiple test repetitions will be necessary in order to provide statistically reliable quantitative conclusions.
- The relation between the normal load and the real contact area could be studied numerically in order to permit a quantitative comparison between the theoretical friction models and the experimental results.

- An experimental method for estimating the real contact area either in situ or through analysis of the worn surface topographies would contribute significantly to a more quantitative explanation of the discussed phenomena here.

References

1. Chan, D., Stachowiak, G.W.: Review of automotive brake friction materials. Proc. Inst. Mech. Eng. D **218**, 953–966 (2004)
2. Rhee, S.H., Ludema, K.C.: Mechanisms of formation of polymeric transfer films. Wear **46**, 231–240 (1978)
3. Zalisz, Z., Vroegop, P.H., Bosma, R.: A running-in model for the reciprocating sliding of nylon 6.6 against stainless steel. Wear **121**, 71–93 (1988)
4. Bowden, F.P., Tabor, D.: The Friction and Lubrication of Solids. Oxford University Press, New York (1958)
5. Greenwood, J.A., Williamson, J.B.P.: Contact of nominally flat surfaces. Proc. R. Soc. **295**, 300–319 (1966)
6. He, G., Müser, M.H., Robbins, M.O.: Adsorbed Layers and the Origin of Static Friction. Science **284**, 1650–1652 (1999)
7. Archard, J.F.: Elastic deformation and the laws of friction. Proc. R. Soc. Lond. A **243**, 190–205 (1957). doi:10.1098/rspa.1957.0214

Publication [P2]

Wear 303 (2013) 1–8

Contents lists available at SciVerse ScienceDirect

Wear

journal homepage: www.elsevier.com/locate/wear

Implementation and applications of a finite-element model for the contact between rough surfaces

K. Poulios *, P. Klit

Technical University of Denmark, Department of Mechanical Engineering, Solid Mechanics Nils Koppels All, Building 404, 2800 Kgs. Lyngby, Denmark

ARTICLE INFO

Article history:
Received 22 October 2012
Received in revised form
11 February 2013
Accepted 26 February 2013
Available online 6 March 2013

Keywords:
Real contact area
Finite-element
Micro-contact

ABSTRACT

Due to the rough nature of real mechanical surfaces, the contact between elastic bodies occurs at several size-scales. Statistical and fractal contact models can take a wide range of roughness wavelengths into account, without additional computational cost. However, deterministic models are more straightforward to understand and easier to extend to more complex cases like contacting bodies that demonstrate elasto-plastic behavior. This paper presents a finite-element model for studying the frictionless contact between nominally flat rough surfaces. Apart from a description of the model implementation, results from a series of calculations corresponding to theoretical and real life applications are included. Numerically generated surface topographies but also roughness measurements from a stylus instrument are used as input for the model. Elastic and perfectly elastic–plastic materials are included in the examples. Among the presented results one can find the distribution of the contact pressure at the interface and diagrams of the real area of contact as a function of the nominal contact pressure.

© 2013 Elsevier B.V. All rights reserved.

1. Introduction

Problems in contact mechanics can be roughly classified into two categories. The ones that refer to non-conformal contacting surfaces and those that treat the contact between macroscopically conformal surfaces. The latter case can often be reduced to a contact between rough but nominally flat surfaces. This kind of problem has many real life applications involving friction, wear and electrical or thermal conduction and was extensively studied since the classical works of Bowden and Tabor [1], Archard [2] and Greenwood and Williamson [3].

The real area of contact was very early identified as a key parameter in understanding and quantifying the phenomena that occur in the contact between conformal rough surfaces. For this reason a big number of either statistical or deterministic models were suggested for the calculation of the real area of contact and possibly the corresponding pressure distribution across and within a large number of contact spots. Statistical and fractal models work with surface parameters while deterministic models require a representative surface sample in the form of a topography matrix that is either measured or numerically generated.

Most of the fundamental questions that modern models for contact between rough surfaces are expected to solve in a quantitative manner, are already discussed in the three classical papers cited above. The role of the real contact area in the calculation of an approximately load independent coefficient of friction is highlighted in [1]. Moreover, even if that work overestimated the importance of plastic deformation in the asperities contact, plastic deformation is still a parameter which modern models often need to take into account in order to represent reality precisely. Archard in [2] states the importance of the surface topography in predicting a nearby linear relation between the normal load and the real contact area even under purely elastic deformations. For approximating such a relation he resorts to a multi-scale consideration of the surface roughness, in a way similar to modern fractal models. Finally Greenwood and Williamson show in [3] that an approximately linear relation between the real contact area and the normal load can be demonstrated even in a single size-scale consideration if a realistic statistical distribution of the asperities heights is taken into account. Ever since, this is recognized as the major effect in predicting how the real area of contact grows with the load.

More recent rough surface contact models consist to a large extent in refinements of the Greenwood and Williamson model, mainly in the directions of including inter-asperity interactions, variable asperity curvature and plasticity, see e.g. [4] and [5]. Models that intend to include multiple size-scales normally deviate from the Greenwood and Williamson approach. Typical examples are the fractal model proposed by Majumdar and Bhushan in [6] and the one introduced by Persson in [7].

* Corresponding author. Tel.: +45 4525 5776; fax: +45 4593 1475.
E-mail address: kopo@mek.dtu.dk (K. Poulios).

0043-1648/$ - see front matter © 2013 Elsevier B.V. All rights reserved.
http://dx.doi.org/10.1016/j.wear.2013.02.024

With respect to deterministic contact models, most of them are based on either an elastic half-space or a finite-element formulation, see e.g. [8,9] and [10,11], respectively. The present work includes implementation details and applications of a finite-element based model, that is capable of calculating the deformations, the contact pressure distribution and the real contact area between flat rough surfaces of two elasto-plastic bodies that are in contact under normal loading.

2. Methods

2.1. Continuous problem formulation

In continuum mechanics, the deformations u_1 and u_2 of two elastic bodies identified through the indices $i=1$ and 2 can be studied by considering the following equations:

$$\nabla\sigma_i(u_i)+f_i=0 \tag{1}$$

$$\sigma_i(u_i)=\mathcal{A}_i\epsilon_i(u_i) \tag{2}$$

in the corresponding domains Ω_i shown as an e.g. in Fig. 1.

With σ denoting the three by three stress tensor, Eq. (1) expresses the forces equilibrium in the bulk material under field forces f and Eq. (2) represents a constitutive law for elastic deformations with $\mathcal{A}$ and ϵ corresponding to the elasticity and the linearized strain tensors, respectively.

Additionally, homogeneous Dirichlet conditions on the boundaries $\Gamma_{D,i}$ and surface normal forces t_i on the boundaries $\Gamma_{N,i}$ can be expressed through the following equations, respectively:

$$u_i=0 \quad \text{on } \Gamma_{D,i} \tag{3}$$

$$\sigma_{N,i}=t_i \quad \text{on } \Gamma_{N,i} \tag{4}$$

with the stress component $\sigma_{N,i}$ in direction n_i normal to the body surface, defined as

$$\sigma_{N,i}(u_i)=\sigma_i(u_i)n_i \tag{5}$$

For studying the contact interaction between the two elastic bodies, the non-penetration condition can be described on a portion $\Gamma_{C,1}$ of the surface of the first body by using the so-called Karush–Kuhn–Tucker conditions,

$$\sigma_{N,1}(u_1)\le 0 \quad \text{on } \Gamma_{C,1} \tag{6}$$

$$g_N(u_1,u_2)\ge 0 \quad \text{on } \Gamma_{C,1} \tag{7}$$

$$g_N(u_1,u_2)\sigma_{N,1}(u_1)=0 \quad \text{on } \Gamma_{C,1} \tag{8}$$

with the normal gap g_N between the bodies, defined as

$$g_N(u_1,u_2)=g_{N0}-(u_1-P_1(u_2))n_1 \tag{9}$$

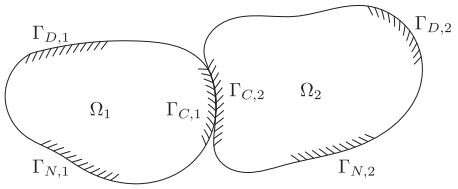

Fig. 1. Deformable bodies in contact.

The variable g_{N0} corresponds to the initial gap between the unloaded bodies and P_1 represents a projection operation on the surface of the first body. In the case of Eq. (9) the projected quantity is the displacement field u_2.

Eq. (6) enforces that only compressive stresses can be exerted between the contacting bodies and Eq. (7) enforces the actual non-penetration condition. Finally, Eq. (8) expresses that at a specific point either contact will occur or the contact pressure will be zero. A more detailed description of the fundamental problem formulation can be found in [12].

2.2. Finite-element discretization

For geometrically complex contacting bodies, the problem stated in the previous section cannot be solved analytically and is typically discretized by using the finite-element method. In the case of a nominally flat rough surface and for relatively small roughness asperity slopes the complexity of the geometry cannot justify resorting to a finite-element model, half-space models can solve this problem in a more efficient way, see e.g. [9]. However, if the effect of asperity slopes has to be taken into account or if the bulk material is expected to deform plastically, the finite-element method provides a very straightforward approach in solving this problem.

Two further steps that are typically required before the actual discretization are the conversion of the problem statement into the corresponding weak formulation and the introduction of Lagrange multipliers in Eqs. (6)–(8). Both these steps are described in detail in [13] and [14]. With respect to the discretization of the contact conditions, the latter paper describes two possible approaches, a nodal one that enforces Eqs. (6)–(8) at each finite-element node and an integral one that enforces the condition in an average sense over the contacting face of each finite-element. In the present work the integral approach is used.

The final form of this problem after its conversion into a series of linear steps according to the Generalized-Newton-Method algorithm presented in [13] is described below,

$$\begin{bmatrix} K_1^k & 0 & C_{N,1} \\ 0 & K_2^k & C_{N,2} \\ B_{N,1}^k & B_{N,2}^k & D^k \end{bmatrix} \cdot \begin{bmatrix} \delta u_1 \\ \delta u_2 \\ \delta\lambda_N \end{bmatrix} = \begin{bmatrix} R_1^k \\ R_2^k \\ R_\lambda^k \end{bmatrix} \tag{10}$$

$$\begin{bmatrix} u_1^{k+1} \\ u_2^{k+1} \\ \lambda_N^{k+1} \end{bmatrix} = \begin{bmatrix} u_1^k \\ u_2^k \\ \lambda_N^k \end{bmatrix} + \alpha \cdot \begin{bmatrix} \delta u_1 \\ \delta u_2 \\ \delta\lambda_N \end{bmatrix} \tag{11}$$

with the index k corresponding to the current step of the iterative solving process.

The factor α for calculating the next iteration step is determined by performing a line search operation. For linear elastic bulk materials the stiffness sub-matrices K_i are actually independent of the iteration index k. However, for elasto-plastic materials they have to be recalculated at every iteration and can be expressed as $K_i(u_i)$. Sub-matrices $C_{N,i}$ are constant and sub-matrices $B_{N,i}$ and D change as the contact area changes during the numerical iterations and can actually be written as $B_{N,i}(u_1,u_2,\lambda_N)$ and $D(u_1,u_2,\lambda_N)$. The right-hand-side terms of Eq. (10) are also functions of u_1, u_2 and λ_N.

All components that were described in this subsection are available in the public domain finite-element library GetFem++[1] that was utilized for the implementation of the present model.

[1] http://download.gna.org/getfem/html/homepage/

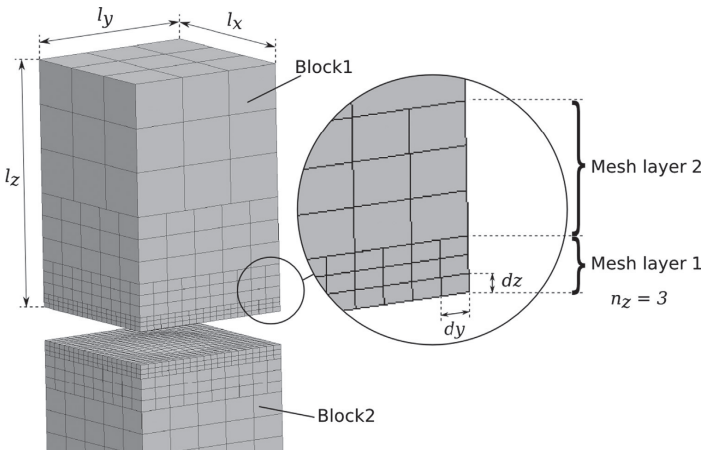

Fig. 2. Finite-element mesh.

2.3. Mesh generation

Fig. 2 shows the mesh discretization used in the model consisting of two rectangular parallelepiped blocks corresponding to the two contacting bodies. Each block is discretized using 8-node hexahedral elements and is divided in layers of different mesh size. Instead of using transition elements, the continuity between the non-matching meshes of neighbouring layers is enforced by applying additional constraints using Lagrange multipliers defined on the finite-element nodes of the finest of the neighbouring layers. More details and examples about this technique for connecting non-matching meshes can be found in [15].

The parameters describing the mesh of each block consist of the block dimensions l_x, l_y, l_z, the number of elements in z-direction per layer, n_z and the mesh sizes dx, dy and dz at the finest mesh layer. The mesh size in the other layers is determined by a coarsening factor as close to the value of two as possible and the number of layers is such that the prescribed block height l_z is fulfilled.

For each block, the roughness topography of the contacting surface is read as a matrix stored in a file and is applied to the nodes of the finest mesh layer as displacements in the z-direction weighted by a factor of one for the nodes on the surface and decreasing to zero for the nodes at the interface with the second mesh layer.

2.4. Boundary conditions

All results presented later in this paper correspond to a normal loading between the upper and the lower blocks. This condition is achieved by fixing the z displacement of all nodes on the bottom surface of the lower block and loading the top surface of the upper block with a uniform load in z-direction. The movement in x and y-directions for both the bottom surface of the lower block and the top surface of the upper block is restricted in an average sense, this means that the individual nodes are free to move in these directions but the average movement over each surface is zero.

The blocks shown in Fig. 2 correspond to only a small, possibly representative, portion of the two bodies in contact. In order to take this into account and assuming that macroscopically the contact pressure distribution is uniform, periodicity conditions are introduced to the model. The lateral block surfaces in the positive and negative x-directions are connected together and this is also the case for the other two lateral surfaces perpendicular to the y-direction. The connection is implemented through elimination of finite-element nodes. The DOFs corresponding to one of the connected surfaces are removed and replaced by the corresponding DOFs of the opposite surface. The resulting model should ultimately be interpreted as a rectangular array of infinite blocks like the ones shown in Fig. 2 extending in x and y-directions.

2.5. Material properties

Two different material laws, that were already implemented in the GetFem++ library, are supported by the present model. Ideally elastic isotropic materials, expressed by Eq. (2), and perfectly elastic–plastic materials can be taken into account.

Plastic deformation can be considered only in the context of a time dependent process, where the previous time or load step provides the current deformations and stresses, u^0 and σ^0, respectively, as a reference. In this case, a hypothetical elastic relationship between the deformations and stresses can be expressed in incremental sense with respect to the current state as

$$\tilde{\sigma}(u) = \sigma^0 + \mathcal{A}(\epsilon(u) - \epsilon(u^0)) \tag{12}$$

Eq. (12) is equivalent to Eq. (2) with the body index i omitted for the sake of simplicity. According to the closest-point projection method described in [16, Chapter 10.7], plastic behavior of a material can be taken into account by projecting the hypothetical elastic stresses $\tilde{\sigma}$ to the space of admissible stresses. By introducing the yield limit σ_y with respect to the Von Mises yield criterion, the constitutive law for a perfectly elastic–plastic material behavior can be expressed based on Eq. (12), as

$$\sigma(u) = \begin{cases} \tilde{\sigma}, & \text{for } \tilde{\sigma}_{\text{vm}} \le \sigma_y \\ \tilde{\sigma}_m + \frac{\sigma_y}{\tilde{\sigma}_{\text{vm}}} \cdot \tilde{\sigma}_d & \text{for } \tilde{\sigma}_{\text{vm}} > \sigma_y \end{cases} \tag{13}$$

whereby, the hydrostatic and deviatoric stress tensors, $\tilde{\sigma}_m$ and $\tilde{\sigma}_d$, are defined, respectively as following:

$$\tilde{\sigma}_m = \frac{\tilde{\sigma}_{11} + \tilde{\sigma}_{22} + \tilde{\sigma}_{33}}{3} \cdot I \tag{14}$$

$$\tilde{\sigma}_d = \tilde{\sigma} - \tilde{\sigma}_m \tag{15}$$

and the scalar function representing the Von Mises stresses can be defined using the euclidean norm of $\tilde{\sigma}_d$,

$$\tilde{\sigma}_{\mathrm{vm}} = \sqrt{3/2} \cdot |\tilde{\sigma}_d| \tag{16}$$

Considering the incremental nature of plasticity phenomena, if at least one of the contacting bodies is expected to deform plastically, the corresponding Eq. (2) is replaced by Eq. (13) and a series of quasi-static load steps, beginning from the unloaded state, has to be simulated.

It should be noted that both the elastic and the elasto-plastic material laws, that were included in the present model, are based on the assumption of geometric linearity that is valid only for small deformations.

2.6. Performance

As described in Section 2.4, each of the blocks shown in Fig. 2 can be interpreted as part of a periodic space that consists of infinite repetitions of the considered block in form of a rectangular array. In order for the model to represent reality adequately, the dimensions l_x and l_y of each block must be higher than the longest wavelength of interest that is pronounced on the corresponding real surface. In case that this wavelength can be identified as a deterministic pattern on the surface, the corresponding block dimension has to be an exact multiple of it. Additionally, the mesh discretization sizes dx and dy should be lower than the shortest wavelength of interest on the corresponding real surfaces and directions. For this reason, a very high number of elements $n_x = l_x/dx$ and $n_y = l_y/dy$ is necessary in order to cover a range of roughness wavelengths as wide as possible. Therefore, the model size in terms of DOFs and the corresponding computational cost are considerably high.

The following measures were taken in order to reduce the computational cost:

- Use variable mesh size in the depth direction in order to reduce the complexity of the problem.
- Reduce the number of Newton–Raphson iterations by using robust contact algorithms like the one mentioned in Section 2.2.

Additionally, the computational time was reduced by resorting to parallel computing:

- Carry out the assembly of the tangent matrix and the right hand side of Eq. (10) on multiple cpu-cores in parallel.
- Use multiple cpu-cores for the solution of the linear system (10) in each iteration step by utilizing a parallel solver like MUMPS [17] and [18] in our case.

3. Results and discussion

In this section a series of examples are presented in order to compare the implemented model with the Greenwood and Williamson theory, to show its utility for real life applications and to give an impression about the computational performance that can be achieved utilizing publicly available numerical tools.

3.1. Comparison with Greenwood and Williamson

In order to compare to the Greenwood and Williamson theory [3], surface topographies that fulfil the corresponding assumptions were generated numerically. Fig. 3 illustrates the sum topography of the contacting surfaces for the four examples presented in this section and Fig. 4 shows the individual topographies corresponding to the upper and lower contacting surfaces for examples 3 and 4. In all cases the dimensions of the surface samples are $l_x = 1.8$ by $l_y = 1.8$ mm, and the surfaces include 81 spherical bumps of constant radius.

In the first two examples, one of the contacting surfaces is rigid and flat, whereas the other contacting surface is provided with bumps of radius equal to 1 mm arranged in a rectangular array. The discretization length is $dx = dy = 0.02$ mm for the first example and $dx = dy = 0.01$ mm for the second one. Apart from the different mesh size, examples 1 and 2 are identical. The heights of the spherical bumps were generated randomly according to a normal distribution with standard deviation of 0.7 μm. The bulk material is considered isotropic and ideally elastic corresponding to steel against steel and with the Young's modulus $E = 1.05 \cdot 10^5$ N/mm^2 and Poisson's ratio $\nu = 0.3$ representing an equivalent elastic body in contact with a rigid body.

The third example takes two elastic bodies into account with $E = 2.1 \cdot 10^5$ N/mm^2 and $\nu = 0.3$, provided with spherical bumps like in the first two examples but with radius equal to 2 mm and height standard deviations of 0.43 μm and 0.55 μm for the upper and the lower contacting surfaces, respectively. In this way the equivalent radius for the contact between two bumps is equal to 1 mm and the standard deviation of the sum of the two surfaces will correspond to $\sqrt{0.43^2 + 0.55^2} \approx 0.7$ μm. This choice makes this example statistically equivalent to the first two ones.

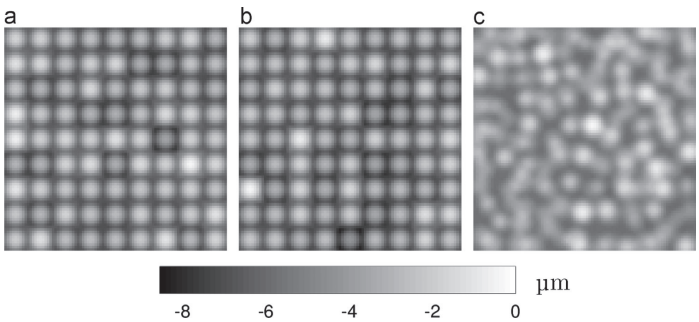

Fig. 3. Combined surface topographies used in examples 1–4. (a) cases 1 and 2, (b) sum for case 3 and (c) sum for case 4.

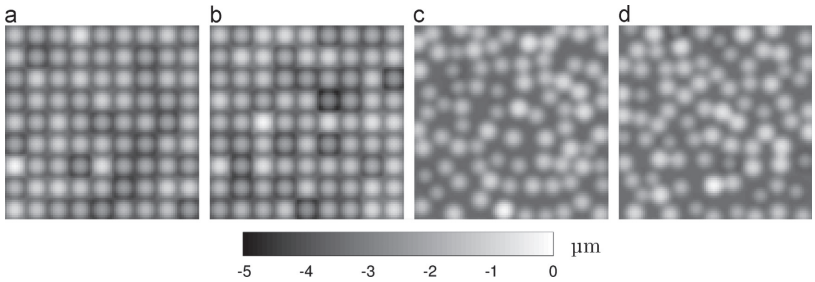

Fig. 4. Individual surface topographies used in examples 3 and 4. (a) case 3, upper, (b) case 3, lower, (c) case 4, upper and (d) case 4, lower.

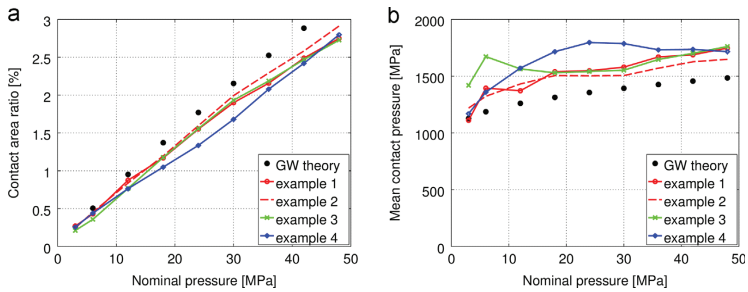

Fig. 5. Calculated real contact area (a) and mean contact pressure (b) for examples 1–4.

The fourth example has similar characteristics to the third one. The same material parameters, bump radius and bump height distribution samples were utilized, however the locations of the surface bumps between the two surfaces do not match each other. They are generated by a random function following the uniform distribution with the additional constraint that the overlap with any pre-existing bump will not exceed 40% of the bump meniscus radius.

The simulation results for examples 1–4, corresponding to applied nominal pressures of 3, 6, 12, 18, … up to 48 MPa, are summarized in Fig. 5. In all cases the calculated real area of contact increases almost proportionally with the applied nominal pressure. For a perfectly linear relationship the mean pressure, defined as the total normal load divided by the real contact area, would remain constant. However, the right graph in Fig. 5 shows that there is a small increasing tendency in the mean pressure for increasing nominal pressure.

A comparison of the real contact area and mean pressure curves between examples 1 and 2 shows that the relatively coarse mesh used in the first example can give results that do not deviate more than 5% from the ones with a twice as fine mesh size. This justifies the use of the same discretization length also in examples 3 and 4 and gives an impression about the expected accuracy for these calculations as well.

The diagrams in Fig. 5 also include the real contact area and the mean pressure calculated according to the Greenwood and Williamson theory. The match with the numerical results, especially for the fine mesh of example 2, is relatively good. The real contact area calculated by the finite-element model seems to be in general lower than the one predicted by the theoretical model. It should be noted, however, that the limitation of the Greenwood and Williamson theory of not accounting for the interaction between the roughness asperities is, by the nature of the finite-element model, not possible to reproduce. Nevertheless, at least for examples 1–3, the provided distance between neighbouring bumps indicates that for moderate loads the interaction between them is limited.

3.2. Polymer against steel

Examples 5–8 refer to surface topographies that were measured on real specimens and are illustrated in Fig. 6. The upper topography on each graph corresponds to the surface of a polyethylene-terephthalate polymer pin used in a pin-on-disc test-rig [19], whereas the lower one represents the corresponding steel disc surface. The left graph illustrates the initial contacting surfaces and the right one shows the measured contacting surfaces after 40 m of sliding under nominal pressure of 6 MPa. In all cases, the dimensions of the surface samples are $l_x = 0.53$ by $l_y = 0.47$ mm and the direction of sliding between the pin and the disc is parallel to the y-axis. On the initial pin surface turning marks from the machining can be distinguished whereas the final surface seems to have adopted a topography that matches the steel disc surface.

Examples 5 and 6 corresponding to the initial and final surface, topographies respectively, were calculated including the plastic deformation of the pin material. The properties of the purely elastic disc material were $E = 2.1 \cdot 10^5$ N/mm^2 and $\nu = 0.3$, whereas the pin bulk material was assumed to exhibit a perfectly elastic–plastic behavior with $E = 3.5 \cdot 10^3$ N/mm^2, $\nu = 0.43$ and yield strength limit $\sigma_y = 75$ N/mm^2.

Examples 7 and 8 represent the same conditions like cases 5 and 6, respectively, with the only modification of removing the yield strength limit and considering the polymer perfectly elastic.

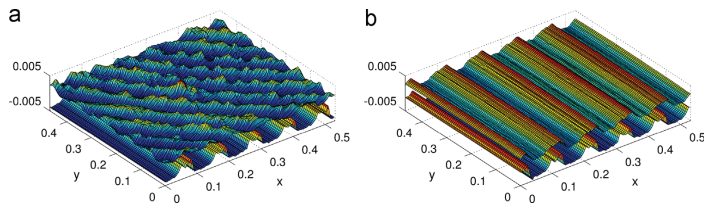

Fig. 6. Surface topographies used in examples 5–8. (a) cases 5 and 7 and (b) cases 6 and 8.

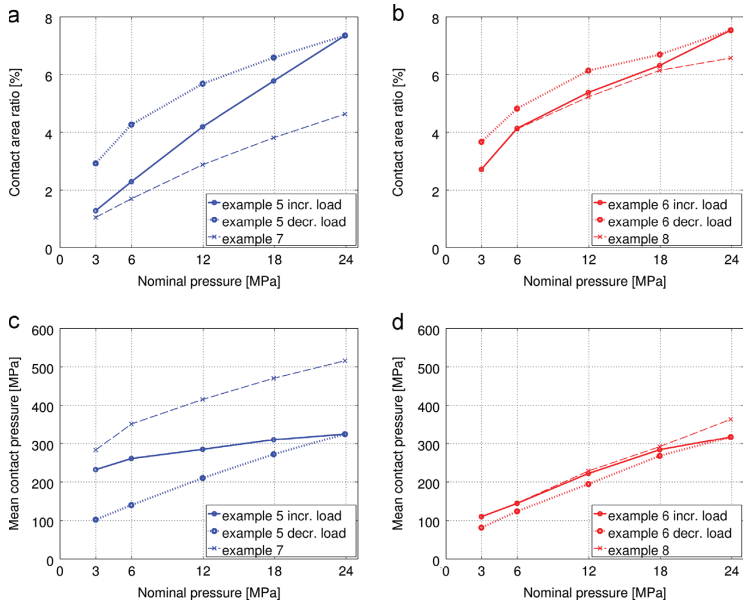

Fig. 7. Calculated real contact area (a) and (b) and mean contact pressure (c) and (d) for examples 5–8.

This is an academic case serving as a reference for demonstrating the effect of plastic deformation on the real contact area and the solving performance of the model.

The loading conditions for examples 5 and 6 include an increase of the normal load in steps corresponding to nominal pressures of 3, 6, 12, 18 and 24 MPa and a consequent decrease following the same steps in reverse order. Examples 7 and 8 include exclusively elastic materials, hence the decreasing load phase was omitted as it was expected to give identical results as the increasing load phase. Fig. 7 shows the relationship between the applied nominal pressure and the calculated real area of contact on the upper diagrams and the mean contact pressure on the lower diagrams. The diagrams on the left and the right side of the figure refer to the initial and final surface topographies, respectively.

One can observe that during the unloading phase of examples 5 and 6 the real area of contact is higher than during loading and consequently the mean contact pressure is lower. The difference between the loading and the unloading branch of the curves indicates the extend of permanent deformations due to plasticity and it is higher in the case of the initial pin surface (see example 5) than for the final one (see example 6). According to [20], that studies the impact of plastic deformation on the contact area ratio during the unloading phase, the span between the loading and the unloading branch increases with increasing plasticity index ψ. It is difficult to define a plasticity index for examples 5 and 6 because the corresponding surfaces do not fulfil the assumptions of [3]. However the transition from the surfaces in Fig. 6(a) to the more conformal ones in Fig. 6(b) corresponds to a reduced peak curvature radius and consequently to a lower plasticity index.

Examples 7 and 8 show that by neglecting the plastic deformation of the polymer the calculated real area of contact is reduced and the mean contact pressure becomes higher. The difference with respect to examples 5 and 6, respectively, is another indicator of the extent of plastic deformation and it is clearly higher in the case of the initial pin surface (compare examples 5 and 7).

An interesting observation can be extracted from graph (b) of Fig. 7 which shows that during the loading phase no plastic

deformation occurs up to a nominal pressure level of 6 MPa. The two curves that were calculated with elastic and elasto-plastic conditions, respectively, coincide up to this pressure. This is in accordance with the testing conditions of the pin in the real set-up. Since the pin was loaded with a nominal pressure of 6 MPa, any plastic deformation that would occur under this load has already occurred during the running-in of the pin within the sliding distance of 40 m. The pin topography shown in Fig. 6(b) should already include this permanent deformation, so that no further plastic deformation is expected without a further increase of the load.

Fig. 8 shows the distribution of the contact pressure over the disc surface for the contact with the original pin under the maximum nominal pressure of 24 MPa. The corresponding mean contact pressure that can be read from Fig. 7(c) is around 325 MPa.

3.3. Performance

Table 1 summarizes the sizes of the calculated examples in terms of DOFs, the calculation times, the average number of Newton–Raphson iterations per load-step and the peak memory usage for each calculation. All calculation times in the table are wall-clock times for parallel runs on 10 cpu-cores. These results should not be considered as accurate benchmarking data but they can serve as indicative values for the overall performance of the model as well as for a rough comparison between the different cases presented above.

Concerning the number of DOFs listed in the table, it should be noted that the major part of the model DOFs describes the displacements field in the contacting blocks. A smaller portion corresponds to Lagrange multipliers that are necessary for describing the contact condition, the continuity between the different mesh layers and the enforcement of the Dirichlet boundary condition at the bottom of the lower block.

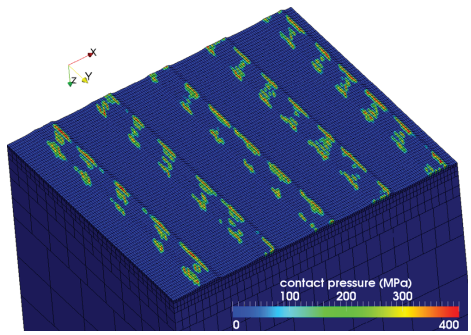

Fig. 8. Contact pressure distribution on the disc surface for example 5 at 24 MPa.

Table 1
Summary of model size, calculation time, Newton–Raphson iterations and memory usage.

Example	DOFs	Calculation wall-clock time	Iterations per load step	Peak memory usage (GB)
1	138,096	1 h 24 min	3.8	0.85
2	551,376	29 h 42 min	6.3	3.67
3	267,936	2 h 25 min	3.2	2.58
4		2 h 40 min	3.2	2.60
5	426,976	12 h 47 min	10.9	4.52
6		11 h 17 min	7.4	3.80
7		5 h 20 min	3.1	3.75
8		4 h 28 min	2.8	3.67

A comparison between the first two examples shows that a mesh refinement by a factor of two causes an increase in the number of DOFs by a factor of approximately four. Because of the variable mesh size in the depth direction the total number of DOFs depends on the second instead of the third power of the refinement factor. Nevertheless, the impact of the increased number of DOFs on the computational time is high.

For examples 7 and 8 to be comparable with examples 5 and 6 in terms of performance, the data contained in Table 1 include the decreasing load phase also for these purely elastic cases even if the results are identical with the same load steps during the increasing load phase. It seems that including plasticity for one of the two contacting bodies increases the computation time by a factor around 2.5. This change should be attributed to the similar increase in the number of Newton–Raphson iteration per load step and not to the higher computational cost of the stiffness matrix assembly in each iteration as one may expect.

3.4. Multi-scale

Considering the above listed model sizes and calculation times it becomes evident that in order to model bigger surface samples while maintaining very short wavelength components of the surface roughness, several millions of DOFs may be necessary, making the memory requirements and the calculation times increase considerably.

A different approach to this problem would be the implementation of a multi-scale model. The interaction between the asperities in longer wavelengths could be taken into account in a coarse mesh while the asperities in contact could be calculated individually with a finer mesh that takes shorter wavelengths into account. The here presented model could be utilized as a fundamental building element for the implementation of such a multi-scale reduced model, similar to the one presented in [21].

4. Conclusions and future work

In this paper the theoretical foundation and some implementation details of a finite-element model for the frictionless contact between nominally flat rough surfaces were presented. A series of calculation examples have shown that a model based on publicly available numerical libraries can achieve decent performance and provide sensible and useful results.

The first part of the calculated examples aimed to compare the model with the Greenwood and Williamson theory. The results demonstrated a relatively good agreement with the theory. The real area of contact increases approximately proportional with the applied load while the mean contact pressure increases only slightly.

In the second part of the calculated examples, real surface topographies and an elasto-plastic material behavior were considered. The corresponding results seem to be coherent. The extent of plastic deformation is higher for less conformal contacting surfaces. Moreover, the model predicted correctly that loads higher than the ones applied during the operation of the real surfaces are necessary in order to cause further plastic deformation to the measured after the operation surfaces. It was also shown that for the specific materials pair studied in these examples, neglecting plasticity would have a significant influence on the calculated area of contact and mean contact pressure.

As a future work, the presented model is intended to be extended by including friction in form of shear stresses between the contacting surfaces and by implementing a multi-scale calculation scheme. A further interesting application of the presented model would be to study the changes in the asperity heights distribution on unloaded surfaces that contain plastically deformed asperities.

References

[1] F.P. Bowden, D. Tabor, The area of contact between stationary and between moving surfaces, Proceedings of the Royal Society of London Series A—Mathematical and Physical Sciences 169 (1939) 391–413.
[2] J.F. Archard, Elastic deformation and the laws of friction, Proceedings of the Royal Society of London Series A—Mathematical and Physical Sciences 243 (1957) 190–205.
[3] J.A. Greenwood, J.B.P. Williamson, Contact of nominally flat surfaces, Proceedings of the Royal Society 295 (1966) 300–319.
[4] M. Ciavarella, J. Greenwood, M. Paggi, Inclusion of interaction in the Greenwood and Williamson contact theory, Wear 265 (2008) 729–734.
[5] R.L. Jackson, I. Green, A statistical model of elasto-plastic asperity contact between rough surfaces, Tribology International 39 (2006) 906–914.
[6] A. Majumdar, B. Bhushann, Fractal model of elastic–plastic contact between rough surfaces, Journal of Tribology—Transactions of the ASME 113 (1991) 1–11.
[7] B.N.J. Persson, F. Bucher, B. Chiaia, Elastic contact between randomly rough surfaces: comparison of theory with numerical results, Physical Review B 65 (2002) 184106.
[8] Y. Ju, L. Zheng, A full numerical solution for the elastic contact of three-dimensional real rough surfaces, Wear 157 (1992) 151–161.
[9] H.M. Stanley, T. Kato, An FFT-based method for rough surface contact, Journal of Tribology—Transactions of the ASME 119 (1997) 481–485.
[10] S. Hyun, L. Pei, J.F. Molinari, M.O. Robbins, Finite-element analysis of contact between elastic self-affine surfaces, Physical Review E 70 (2004) 26117.
[11] L. Pei, S. Hyun, J. Molinari, M.O. Robbins, Finite element modeling of elasto-plastic contact between rough surfaces, Journal of the Mechanics and Physics of Solids 53 (2005) 2385–2409.
[12] P. Wriggers, Computational Contact Mechanics, Springer, 2006.
[13] P. Alart, A. Curnier, A mixed formulation for frictional contact problems prone to newton like solution methods, Computer Methods in Applied Mechanics and Engineering 92 (1991) 353–375.
[14] Y. Renard, Generalized newton's methods for the approximation and resolution of frictional contact problems in elasticity, Computer Methods in Applied Mechanics and Engineering 256 (2013) 38–55.
[15] B. Herry, L. Di Valentin, A. Combescure, An approach to the connection between subdomains with non-matching meshes for transient mechanical analysis, International Journal for Numerical Methods in Engineering 55 (2002) 973–1003.
[16] A. Anandarajah, Computational Methods in Elasticity and Plasticity: Solids and Porous Media, Springer, 2010.
[17] P.R. Amestoy, I.S. Duff, J. Koster, J.-Y. L'Excellent, A fully asynchronous multifrontal solver using distributed dynamic scheduling, SIAM Journal on Matrix Analysis and Applications 23 (2001) 15–41.
[18] P.R. Amestoy, A. Guermouche, J.-Y. L'Excellent, S. Pralet, Hybrid scheduling for the parallel solution of linear systems, Parallel Computing 32 (2006) 136–156.
[19] K. Poulios, G. Svendsen, J. Hiller, P. Klit, Coefficient of friction measurements for thermoplastics and fibre composites under low sliding velocity and high pressure, Tribology Letters (2013).
[20] Y. Kadin, Y. Kligerman, I. Etsion, Unloading an elastic–plastic contact of rough surfaces, Journal of the Mechanics and Physics of Solids 54 (2006) 2652–2674.
[21] V.A. Yastrebov, J. Durand, H. Proudhon, G. Cailletaud, Rough surface contact analysis by means of the finite element method and of a new reduced model, Comptes Rendus Mecanique 339 (2011) 473.

Publication [P3]

A reciprocating pin-on-plate test-rig for studying friction materials for holding brakes

K. Poulios[a,*], N. Drago[b], P. Klit[a], L. De Chiffre[b]

[a] *Technical University of Denmark, Department of Mechanical Engineering, Solid Mechanics Nils Koppels Allé , Building 404, 2800 Kgs. Lyngby*
[b] *Technical University of Denmark, Department of Mechanical Engineering, Manufacturing Engineering Produktionstorvet, Building 425, 2800 Kgs. Lyngby*

Abstract

This paper refers to testing of friction materials for holding brakes. In contrast to the more typical case of high energy brakes, holding brakes operate usually in a reciprocating sense, at very low sliding speeds and allow significantly higher clamping pressures. The design of a reciprocating pin-on-plate test-rig for studying the evolution of wear by monitoring the pin height reduction using Eddy-current proximity sensors, is presented. Moreover, a new mechanism for recording the friction force is suggested. Apart from the design of the test-rig, friction force and wear rate measurements for two different friction materials running against an unhardened steel surface are presented as a usage case.

Keywords: pin-on-plate, wear, friction, holding brakes

1. Introduction

Holding brake applications are generally not as extensively studied as typical high energy brake applications. Their particularities compared to high energy brakes include low sliding speeds, high clamping pressures, bidirectional motion and low temperatures. Theoretically, holding brake materials should experience relative sliding only in completely released state and thus exhibit insignificant wear. In praxis however, it is not uncommon that during sliding, significant normal load is present, e.g. either because the brake is not supposed to be released completely or because it is designed to be functioning as sliding bearing at the same time. Typical holding brake applications are e.g. the yaw system brakes in cranes and wind turbines.

The clamping force in holding brakes can be either passive, generated through preloaded springs or active, generated through hydraulic or pneumatic actuators. Especially in the first case, the wear of the friction materials is a very important parameter to take into account for a proper operation of the equipment in long term. But wear is also important for active holding brakes, in cases where very long lifetime and maintenance intervals are required.

*Corresponding author
Email address: kopo@mek.dtu.dk (K. Poulios)

Friction material candidates for holding brake applications include paper like or woven fiber composites but also thermoplastics either in pure form or reinforced with short fibers, e.g. glass, aramid and carbon fibers. Available friction and wear-rate data for such friction materials usually refer to relatively low pressure ranges and relatively high sliding velocities, typical for sliding bearing applications, see e.g. [1]. Regarding holding brakes, a sliding speed range between 1 and 50 mm/sec can be considered as indicative, while the clamping pressure can vary from 2 MPa to more than 20 MPa.

Such operational conditions can be reproduced in both pin-on-disc and pin-on-plate test-rigs, see Sec. 9.2.8 and 9.2.11 of [2]. Pin-on-plate test-rigs are inherently reciprocating while pin-on-disc test-rigs can be set up to operate also in reciprocating sense, like in [3].

In literature, different methods for quantifying wear in pin-on-disc and pin-on-plate testing are suggested. ASTM standards [4] and [5] as well as Appendix B, Sec. 3 of [6], provide a more detailed discussion on the different possibilities for wear measurements during and after the testing. After the test, measuring weight loss and dimensional changes can provide information about pin wear, while profilometric measurements can indicate wear on the disc or plate. During the test, the so called wear displacement, i.e. the displacement of the pin with respect to the counter surface, can be monitored. For this purpose, the above mentioned ASTM standards suggest using a linear displacement sensor that records the vertical displacement of the loading arm with respect to the test-rig frame. The present paper suggests a slightly improved implementation of monitoring the wear displacement utilizing Eddy-current proximity sensors [7], mounted very close to the pin sample.

An important aspect in both pin-on-disc and pin-on-plate testing is the form of the pin end. Usually pins with spherical or tapered ending are recommended, like e.g. in [4] and [5], but other forms including flat ended pins are also possible and discussed in more detail in Sec. 9.2.8 of [2]. The main advantage of using spherical pins is that a very high contact pressure can be achieved through a moderate normal force. However, the contact pressure is not even approximately constant and its actual distribution depends on the wear process. Moreover, as wear progresses the contact area grows resulting to a decreasing average pressure. Flat ended pins do not exhibit these drawbacks, however they may suffer from high edge loads when the pin material is stiffer than the counter surface material or when material pairs of similar stiffness are tested. Edge loads do not represent an issue for testing typical friction materials for holding brakes against a steel surface because these materials are normally considerably more compliant than steel.

With respect to the measurement of the friction force, there are basically two possibilities. One is to record the reaction forces on the pin side and the second option is to record the reaction forces or moments on the plate or disc side, Sec. 4.2 of [8]. Utilizing strain gauges or commercial force transducers for measuring these forces is a very common approach, Sec. 8.6 of [2] and Appendix B, Sec. 3 of [6]. The present paper suggests a new mechanism for recording the reaction of the friction force on the loading arm, the pin is mounted on, utilizing common tensile/compressive force transducers (load-cells).

The normal force applied to the pin can be exerted either by hydraulic actuators or a dead weight and possibly through a lever arm, Appendix B, Sec. 1 of [6]. The normal force can also be monitored through a force transducer or it may be assumed as known if it was appropriately calibrated before the test, Appendix B, Sec. 3 of [6].

2. Methods

2.1. The pin-on-plate test-rig design

Fig. 1 illustrates the concept of the implemented pin-on-plate test-rig. The tested material is in form of a flat ended cylindrical pin (1) that is vertically loaded through a dead weight (3) and a lever arm (2). This loading arm is connected to the intermediate lever (5) at the pivot point (A). With respect to the fixed sub-frame (6), lever (5) is free to rotate around pivot (B). Its rotation is restricted exclusively through load-cell (4). According to the equilibrium of moments for lever (5) around pivot (B), the horizontal force component transferred from loading arm (2) to lever (5) through pivot (A), generates a proportional force in load-cell (4). By choosing the vertical distances between pivot (B) and pivots (A) and (C) to be equal, the horizontal force recorded by load-cell (4) is equal to the horizontal force component applied to pivot (A) and consequently equal to the friction force exerted on pin (1).

The counter surface consists of the interchangeable insert plate (8) which is mounted on the moving plate (7). Plate (7) is connected with the stationary frame (9) through linear bearings and it is driven by a motor through a worm gear and a threaded shaft that are not included in the illustration. Its motion is linear apart from a limited distance near the stroke ends, where the plate motion is reversed.

This test-rig concept allows multiple instances of the loading arm substructure (1-6) and the insert plate (8) to be implemented against a common moving plate (7). The tests presented in the next section were conducted on a quadruplet implementation of the here presented pin-on-plate test-rig.

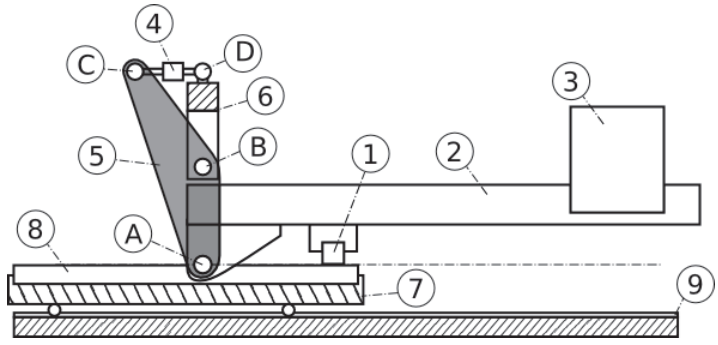

Figure 1: Pin-on-plate test-rig design

The construction of pivots (A) and (B) is a practical aspect that requires some further attention. Friction in pivot (A) affects the normal force applied on the pin, while friction in pivot (B) can yield to a reduced measured force in load-cell (4). In the present work, oil lubricated bronze bushings were utilized for both pivots (A) and (B). In comparison to roller element bearings, lubricated sliding bushings exhibit relatively higher static friction. However, they are more robust and they can consequently be designed with a smaller diameter so that the total friction torque will remain low. Moreover, roller element bearings under stationary load are prone to plastic deformation between the roller elements and the bearing races, which may compromise the function of the bearing and yield to unpredictable behavior.

2.2. Wear displacement monitoring

Fig. 2 shows the structure that supports the pin made of the sample material. Pin (1a) with dimensions of 10 mm in diameter and 8 mm in height is glued in holder (1b) which is bolted with the intermediate plate (1c). The purpose of the intermediate plate (1c) is to provide a rigid support for the Eddy-current proximity sensor (11). Plate (1c) is connected directly to loading arm (2) and its position in height is adjustable through an appropriate screw (10).

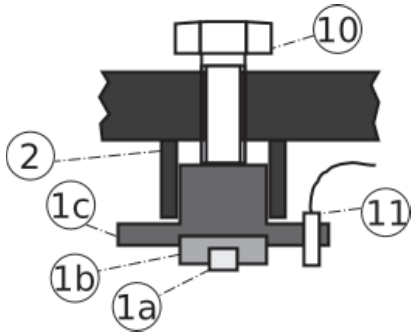

Figure 2: Pin holder design

The Eddy-current proximity sensor (11) provides a signal that is proportional to the gap between its free end and the counter surface (8). In case that the protruding part of sensor (11) with respect to its holder (1c) is too small its linearity may be disturbed significantly, because the steel part (1c) intersects the magnetic field of the sensor. For the 5 mm in diameter sensor that was used in our implementation, the holding system shown in Fig. 2 was dimensioned in such a way that a minimum distance of 7 mm between the free end of sensor (11) and its holder (1c) was available, when the sensor was adjusted at a distance of 1.5 mm from the counter surface (8). The linearity of the assembled sensor was verified by mounting the compound (1b), (1c) and (11) on a height gauge and varying its vertical position in steps of 0.1 mm. At the same time the linearity coefficients between measured signal and monitored gap were specified for a gap range between 0.5 and 2.5 mm.

In order to estimate the wear displacement based on the monitored gap, one has to also take into account the different axial positions of pin (1a) and sensor (11) with respect to the pivot point (A). The wear displacement δh is equal to the difference between the monitored gap g at the current time point during a test and the gap g_0 at a reference time point, multiplied by a geometrical factor:

$$\delta h = \frac{x_{(1)}}{x_{(11)}} \cdot (g - g_0) \tag{1}$$

with $x_{(1)}$ and $x_{(11)}$ representing the axial distance from pivot point (A) to the center of the pin and the Eddy-current sensor respectively.

It should be noted that due to geometrical deviations, elastic deflections and local changes in the magnetic properties of the counter surface, the signal of the proximity sensor may oscillate during a single stroke significantly. In order to compensate such

local effects, the average value of δh per stroke is used for indicating the evolution of the wear displacement. This per stroke averaging can also be seen as a filtering of the measured signal.

In comparison to other systems that record the wear displacement on the loading arm, the advantage of mounting the proximity sensor close to the pin sample is the minimization of possible errors from deformation and thermal expansion of the parts between the pin sample and the displacement sensor. Moreover, this setup utilizes directly the counter surface as the reference surface. In this way, many deviations of the involved components with respect to the fixed world reference are compensated mutually.

The impact of ambient temperature changes on the monitored gap could be estimated in the implemented test-rig by testing a sliding material under grease lubrication and wear rate much lower than for friction material in holding brakes. During a testing period of 55 hours, long-term fluctuations of the measured gap in the order of 4 µm could be observed. Therefore, a reliable wear rate estimation requires sufficient testing distance for the total wear displacement to be at least one order of magnitude higher.

The choice of Eddy-current proximity sensors instead of capacitive sensors was based on their lower sensitivity to contaminants on the target surface. Their main disadvantage is that they normally have to be pre-calibrated by the manufacturer for a specific counter surface material, which additional has to be conductive. For testing different friction materials running against a steel surface, which is the typical case in holding brake application, these limitations are of less importance.

2.3. Specimen preparation and installation

Pin samples are normally machined by turning either a bar or a plate of the raw material. Unless otherwise required, the pin axis should correspond to the axis of the raw material bar or it should be perpendicular to the mean plane in case of raw material plates.

The surface of the insert plate (8) can be either ground or also polished if required. Polished surfaces are appropriate for fundamental tribological testing, whereas simply ground surfaces are relevant for testing with respect to a specific real life application with similar roughness characteristics, [5].

Both the pin sample and the corresponding plate have to be cleaned before testing. Cleaning with ethyl alcohol and consequently drying can be repeated one or more times. Cleaning in ultrasound bath and drying in an oven is recommended by the ASTM standards [4] and [5]. For each test, an unused track on plate (8) has to be used. Reusing the same track for tests with different pin materials should be avoided, because, in most cases, the presence of an already formed transfer film is expected to have a non-negligible impact on the new test.

In order to ensure a correct operation of the test-rig a few alignments are required before each test. As a first step, a digital level is used in order to check that the pivot points (A) and (B) of Fig. 1 are aligned on the same vertical line. If not, the distance CD is adjusted by modifying the length of the connectors of load-cell (4).

In a second step, in order to avoid self energizing and de-energizing of the friction force, it is checked that the free surface of pin (1a) and the center of pivot (A) lie in the same horizontal plane, when the loading arm (2) is horizontal. If not, screw (10) is adjusted until this condition is fulfilled. Next, it is checked that when the pin is loaded

against plate (8), the loading arm is horizontal and the pressure on the pin surface is uniform. For this purpose, pressure sensitive paper is put between pin (1) and plate (8) and the height of the sub-frame (6) is adjusted iteratively until a uniform imprint of the pin on the pressure sensitive paper is achieved, see Fig. 3.

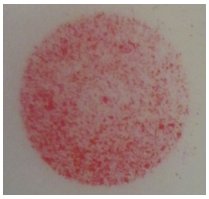

Figure 3: Pin imprint on pressure sensitive paper, after alignment

2.4. Normal load calibration

The normal load applied on the pin could theoretically be calculated based on the weight and center of gravity of arm (2) along with the weight and position of mass (3). However, in order to avoid the complex calculation of the arm center of gravity and account for deviations in the geometry and density of the involved parts, it is more practical to use a compressive load-cell placed below the pin and move the dead weight until the recorded normal force corresponds to a predetermined value. In this way, one can mark several positions of the dead weight on the arm, which provide the required pressure levels on the pin surface.

2.5. Comparative advantages and disadvantages

Depending on the materials to be tested as well as the load, speed and environmental conditions, different experimental setups may be preferred for friction and wear testing. However, the same fundamental difficulties have to be overcome in almost every case. For measuring the friction force it is necessary to incorporate a force transducer in the structure supporting one of the contacting bodies, parallel to the sliding direction. This force transducer has to be incorporated in such a manner that it will not compromise the stiffness of the support and no significant tilting between the contacting bodies will occur. For monitoring the wear displacement it is essential to minimize the impact of thermal expansion and deflection of other components on the measurement. Some of the advantages and disadvantages of the proposed test-rig concept with respect to the above mentioned aspects are summarized below:

+ Inexpensive longitudinal force transducers can be utilized.

+ The friction force in the contact does not contribute to tilting of the pin specimen.

+ Deviations with respect to the fixed world reference are partially compensated in the wear displacement measurement because the latter is based on the relative position of the pin and the counter surface.

+ The proposed test-rig concept is suitable for an implementation with multiple pins tested in parallel.

– Good alignment of pivot points (A) and (B) is essential for the accuracy of the friction force measurement.

– Friction losses in pivots (A) and (B) affect the applied normal force and the measured friction force respectively.

– Wear monitoring though Eddy-current proximity sensors is possible only for conductive counter surface materials.

– Eddy-current proximity sensors need to be pre-calibrated for a specific counter surface materials.

Many of these characteristics also apply to reciprocating test configurations described in references [2], [5] and [8]. However, the proposed concept is believed to combine many of the positive characteristics, while its negative aspects are normally of little or no relevance for the study of friction materials for holding brake applications.

3. Results and discussion

In this section representative testing results from a quadruplet pin-on-plate test-rig are presented. In each test, four pins made of the same material were tested in parallel. Since the environmental conditions are common for each group of pins, the observed differences among them can be attributed either to random differences in the material composition and the counter surfaces or to inaccuracies in the test-rig itself and the calibration of its sensors.

The first example shows detailed testing results for glass and aramid fiber reinforced polyamide 6.6 (PA66) as the pin material. In the second example, more synoptic results of friction force and wear evolution for pins made of polyethylene-terephthalate (PET) are presented. For the latter case, the final wear height measured through the Eddy-current proximity sensors is compared with two conventional methods, pin weighing and pin height measurement using a coordinate measuring machine (CMM). The pin dimensions are those given in section 2.2.

In all cases, the counter part corresponding to part (8) of Fig. 1 is made of alloy steel 42CrMo4 in unhardened condition and its functional surface is ground in the direction parallel to the sliding. The arithmetic average roughness Ra, was measured on each plate at six different positions in direction perpendicular to the sliding. Despite the fact, that all eight plates used in both tests presented below were ground in the same pass of the grinding machine, the mean Ra value per plate varied from 0.48 to 0.76 µm.

The stroke length for both tests presented below was 0.668 m. When referring to stroke counting, one stroke is meant as a complete forward and reverse movement corresponding to a cumulative sliding distance of 1.336 m.

3.1. Testing of reinforced PA66

Reinforced PA66 pins were tested under nominal pressures of 6, 9 and 12 MPa and a sliding velocity of 20 mm/s. The results presented below refer to the highest load case of 12 MPa. Figures 4 and 5 show the evolution of the measured friction force and wear displacement respectively, in two individual strokes for the first of the four pins.

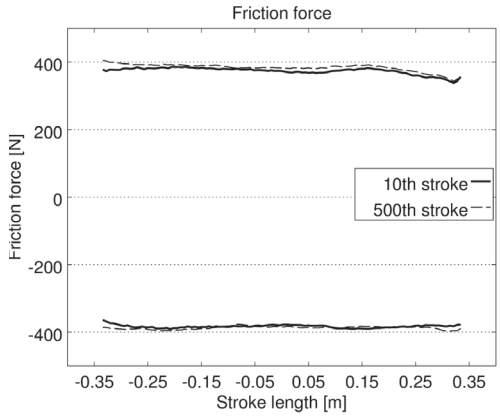

Figure 4: Measured friction force in the 10th and the 500th stroke for the first pin of reinforced PA66 at 12 MPa

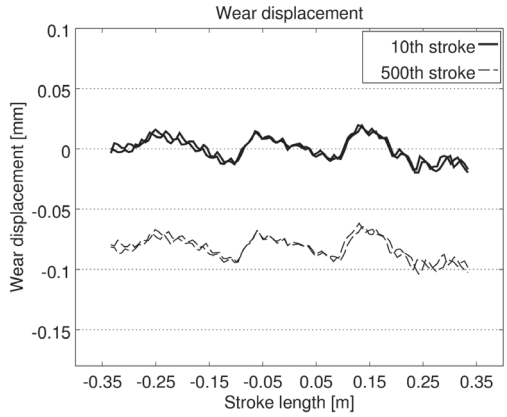

Figure 5: Measured wear displacement in the 10th and the 500th stroke for the first pin of reinforced PA66 at 12 MPa

In Fig. 4 one can recognize the forward and reversing part of the stroke based on the sign of the measured force. There are no significant differences between the 10th and the 500th stroke. This indicates that the contact between the pin and the plate at the 10th stroke was already in steady state. This is because of the testing at 6 and 9 MPa that occurred prior to the here presented test at 12 MPa.

Fig. 5 illustrates fluctuations in the measured wear displacement that may be observed within each individual stroke. In section 2.2, such discrepancies were attributed to geometrical deviations, elastic deflections and local variation of magnetic properties. The results presented here show that the fluctuation pattern is very reproducible even after 1 km of testing. Moreover, the differences between forward and reversing directions are very small. Based on these observations, it is expected that, despite the important variation of the apparent wear displacement within each stroke, the offset between per

stroke averages can represent the wear displacement adequately. It should be noted, that by considering the 10th stroke as a reference, the average wear displacement for this stroke in Fig. 5 is by definition equal to zero.

Figures 6 and 7 show the overall evolution of the friction force and the wear displacement respectively, for all four pins during the 1 km long testing at 12 MPa. Each single point in these curves is an average value per stroke. This means that each curve of Fig. 4 or Fig. 5 is represented by its average as a single point in Fig. 6 or Fig. 7 respectively. Especially for negative friction forces, their absolute value is considered.

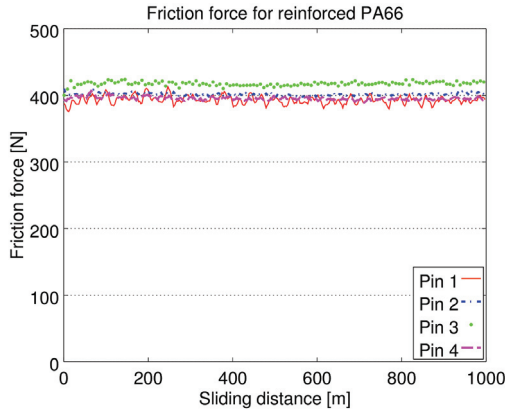

Figure 6: Evolution of friction force for reinforced PA66 at 12 MPa

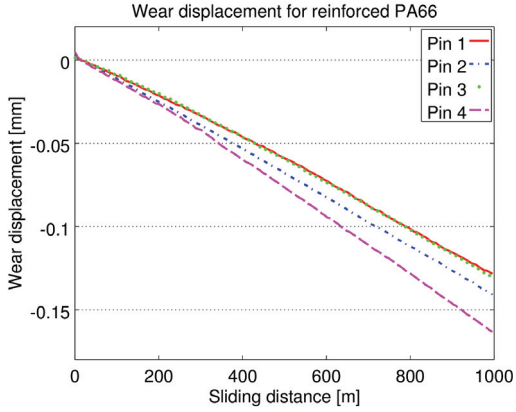

Figure 7: Evolution of wear displacement for reinforced PA66 at 12 MPa

Table 1 summarizes wear rate and coefficient of friction values extracted from Figures 7 and 6. The wear rate values presented here correspond to the slope of a line fitted to the wear displacement curves within the last 500 m of testing. The calculated coefficients of friction are based on the average friction force in the last 500 m of testing, divided by the prescribed normal force of 943 N that corresponds to a nominal pressure

of 12 MPa. The coefficient of variance for the four presented wear rate and coefficient of friction values is 10.6 and 2.8% respectively. It should be noted that the here tested variant of fiber reinforced PA66 was also included in the pin-on-disc testing presented in [3]. Despite the different surface finishing of the steel plates used in the here presented tests and the steel disc used in [3], the reported friction coefficient of 0.4 at 12 MPa from reference [3], is very close to the average friction coefficient of 0.43 reported in Table 1.

	Wear rate [µm/km]	Coefficient of friction
Pin 1	139	0.42
Pin 2	146	0.43
Pin 3	141	0.44
Pin 4	173	0.42
Average	150	0.43

Table 1: Wear rate and coefficient of friction for reinforced PA66 at 12 MPa

3.2. Testing of PET

Figures 8 and 9 show the evolution of the friction force and the wear displacement respectively, during a 5.3 km long test of PET pins under a nominal pressure of 6 MPa and sliding velocity of 20 mm/s.

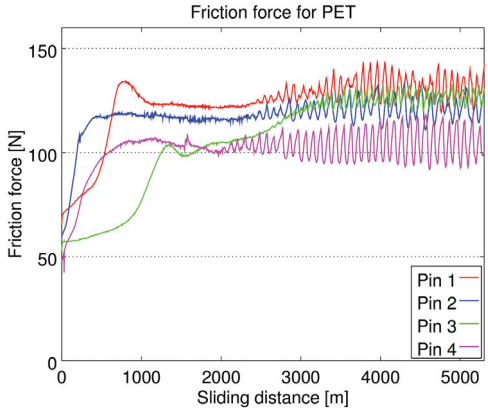

Figure 8: Evolution of friction force for PET at 6 MPa

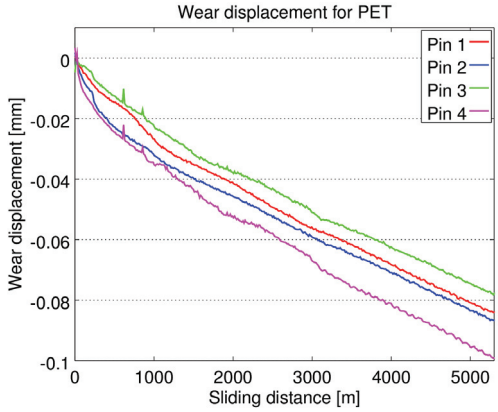

Figure 9: Evolution of wear displacement for PET at 6 MPa

Regarding the friction force graph in Fig. 8, two phenomena can be observed. During the first 1.5 km the contact between pin and moving plate runs in and the friction force is approximately doubled with respect to its initial level. The running-in distance varies among the four pins from 0.5 to 1.5 km. The second phenomenon is observed in the last 3 km. It is a periodic build up and decrease of the friction force. The period of this variation is about 75 strokes corresponding to approximately 100 m of sliding distance which is covered in circa 1.5 hours. It is assumed that the cause of such oscillation is an unstable transfer layer thickness on the steel surface. However, further investigation is required in order to prove this assumption. Both the period and the amplitude of the friction force oscillation vary among the four pins.

Table 2 summarizes the average wear rate and coefficient of friction values estimated in the last 500 m of the graphs in Figures 9 and 8. The coefficient of variance for the four presented wear rate and coefficient of friction values is 8.8 and 9.6% respectively.

	Wear rate [µm/km]	Coefficient of friction
Pin 1	11.7	0.28
Pin 2	12.3	0.26
Pin 3	11.9	0.27
Pin 4	14.1	0.22
Average	12.5	0.26

Table 2: Wear rate and coefficient of friction for PET at 6 MPa

Table 3 compares three different methods for estimating the total wear height. The wear values according to the proximity sensors method correspond to the final point of the curves in Fig. 9.

Regarding the weighing method, the four pins, including the pin holder (1b) of Fig. 2 were weighed before and after the test. The pin holder (1b) was made of aluminum in order to reduce the total weight of the compound and increase the accuracy of weighing. Before each weighing the pins were repeatedly cleaned with isopropyl alcohol and dried

with pressurized air. A weighing device with a resolution of 1 mg was used and the observed weight differences were converted to equivalent heights under consideration of the pin diameter of 10 mm and a density of 1.38 mg/mm^3 for the PET material.

	Total wear height [µm]		
	Proximity sensors	Weighing	CMM
Pin 1	85	83	92
Pin 2	88	88	91
Pin 3	79	74	79
Pin 4	100	92	95

Table 3: Total wear height for PET at 6 MPa

Regarding the CMM pin height measurement, the surface of the pin holder (1b) was used as a reference by calculating the average plane of points probed at a radius of 20 mm, see Figures 10 and 2. In order to specify the height of the protruding part of pin (1a) with respect to the pin holder (1b), nine points on the pin surface, illustrated in Fig. 10, were probed. The pin height was evaluated as the average z-coordinate of these nine probed points. Carrying out the height measurement for each pin before and after the test gave the possibility to calculate the wear height as the corresponding heights difference.

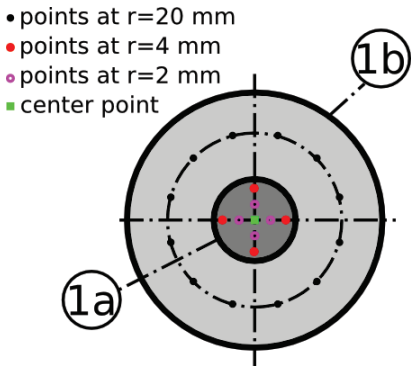

Figure 10: Probing points for the pin height measurement with CMM.

The CMM method is considered as the most accurate one and consequently the third column of Table 3 will be used as a reference for the other two methods. A paired Student's t-test between columns one and three yields a t-value of -0.49, whereas a comparison between columns two and three gives a t-value of -3.54. For a significance level of 10% and the given number of samples the confidence interval for the t-value is between -2.35 and 2.35. This means that no systematic difference between the Eddy-current sensor and the CMM method could be detected. On the other side, the differences between the weighing method and the CMM method are statistically significant. The weighing method seems to underestimate the reduction of the pin height. This can be explained by the fact that the measurand in this case is the mass, whereas the other two methods both involve the pin height directly. The assumed relation between mass

and height reduction relies on a previously determined material density and neglects any possible plastic deformation of the pin sample.

Another interesting observation is that even for a very homogeneous material like PET, there seem to be important deviations between different pin samples. This fact underlines the importance of running multiple tests under the same conditions in parallel, in order to obtain a minimal statistical sample to draw conclusions from.

Apart from verifying the in situ wear displacement monitoring results, the CMM pin height measurements can also be utilized for examining the form of the pin surfaces after testing. For each of the four tested PET pins, Fig. 11 shows the surface profile along the sliding direction. The five points defining each curve correspond to the five probe points on the horizontal symmetry line of Fig. 10. All four pin surfaces exhibit a convex form which is due to tilting of the pin because of elastic deformations of the test-rig. However, the deviations from the flat form are limited to less than 2 µm on a diameter of 8 mm, which is indicative for the very stiff implementation of the presented test-rig.

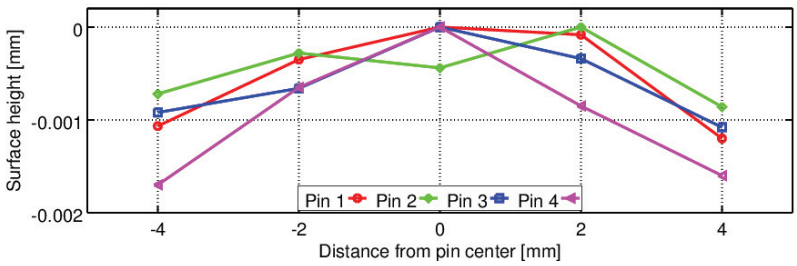

Figure 11: Profiles of the PET pin surfaces along the sliding direction.

4. Conclusions

In this paper a novel pin-on-plate test-rig concept was presented along with corresponding examples of measured friction and wear. The novelty of the design consists in the way that the friction force is transferred to a load-cell, while at the same time self energizing and de-energizing of the friction force between the pin and the plate is avoided.

Moreover, a successful implementation of in situ wear displacement monitoring based on Eddy-current proximity sensors was reported. Details about the mounting of such sensors and the interpretation of the measured signal were presented. The obtained final wear heights were compared to classical methods like weighing and CMM dimensional measurements on the pins. A good correlation between the results from the proximity sensors system and the CMM pin height measurements could be found, whereas the weighing method seemed to underestimate the reduction of the pin height.

Apart from demonstrating the operation of the presented test-rig, the included testing results are also relevant for holding brake applications, providing reference values for the coefficient of friction and wear rate of two thermoplastic material types running against a ground steel surface.

References

[1] J. Byett, C. Allen, Dry sliding wear behaviour of polyamide 66 and polycarbonate composites, Tribology International 25 (1992) 237–246.

[2] R. Bayer, Mechanical Wear Fundamentals and Testing, Revised and Expanded, Dekker Mechanical Engineering, Taylor & Francis, 2004.

[3] K. Poulios, G. Svendsen, J. Hiller, P. Klit, Coefficient of friction measurements for thermoplastics and fibre composites under low sliding velocity and high pressure, Tribology Letters (2013).

[4] ASTM International, G99-05 standard test method for wear testing with a pin-on-disk apparatus, 2010.

[5] ASTM International, G133-05 standard test method for linearly reciprocating ball-on-flat sliding wear, 2010.

[6] M. Neale, M. Gee, Guide to wear problems and testing for industry, William Andrew Pub, 2001.

[7] J. Fraden, Handbook of Modern Sensors. ; Physics, Designs, and Applications, Springer, 2010.

[8] G. Stachowiak, A. Batchelor, Experimental Methods in Tribology, Tribology and Interface Engineering, Elsevier Science, 2004.

Publication [P4]

Real Contact Area Study Using a Micro-Contact FEM Model

K. Poulios[1,*]

[1]**Technical University of Denmark, Department of Mechanical Engineering, Nils Koppels All , Building 404, 2800 Kgs. Lyngby, Denmark**

[*]**Corresponding author: kopo@mek.dtu.dk**

Abstract: This paper presents a set of finite-element calculations of the real contact area and the pressure distribution between nominally flat rough surfaces. The calculated examples include cases that take plastic deformation into account. All cases are based on measured roughness topographies and material and loading parameters corresponding to real life conditions. Graphs showing the dependence between the nominal contact pressure and the real area of contact are presented.

Key words: Real contact area, finite-element, roughness.

1. INTRODUCTION

The real area of contact is a key parameter for studying the friction force or the thermal and electrical resistance between two nominally conformal solid bodies pressed against each other under some known load. Even if the macro-geometries of the contacting surfaces match, the real area of contact and consequently the functional behaviour of the contact may depend strongly on the micro-geometry of the surfaces' roughness.

Since the classical works of Bowden & Tabor [1] and Greenwood & Williamson [2], numerous statistical and deterministic models have been suggested for studying the contact between rough surfaces. The finite-element method is one of the deterministic approaches that have been used for studying this problem. Due to the fact that within the contact region, phenomena in multiple size scales take place, the applicability of the finite-element approach is often connected with significantly high computational cost. Despite this difficulty, a finite-element micro-contact model can be useful as a generic tool for predicting the real contact area and the pressure distribution at some specific size scales range or as part of a semi-analytical multi-scale model.

In this paper a finite-element model is used for studying the relation between the real area of contact and the applied nominal pressure. The presented case study is based on areal topographies measured on real specimens.

2. METHODS

The finite-element model used in the context of this paper includes two rectangular parallelepiped volumes representing samples of the two bodies in contact, see Figure 1. Each volume is discretized with first order hexahedral elements structured in layers of progressively finer mesh sizes as one approaches the contacting faces. The non-matching nodes at the interface between the different mesh layers were treated through additional continuity constraints. Moreover, periodicity con-

ditions were applied at the four lateral faces of each parallelepiped volume.

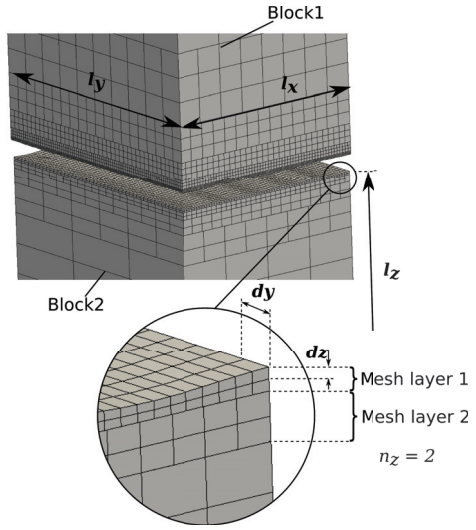

Figure 1. Meshes of the finite-element model

At the contacting interface between the two bodies, a frictionless non-penetration condition was imposed through augmented Lagrange multipliers [3]. Areal topographies originating from real surface roughness scans are applied on the contacting surfaces by moving the nodes of the finest mesh layer in the vertical direction accordingly.

The boundary condition imposed on the bottom free surface of the lower body restricts all displacement components of the corresponding nodes. On the top free surface of the upper body the lateral displacement components are restricted in an average sense over all nodes. In the vertical direction, uniformly distributed forces corresponding to the applied nominal pressure are exerted on all nodes.

The solution process consists in solving the system of non-linear equations representing the elasticity of the bulk materials and the boundary and contact conditions for a series of load cases. A Newton like algorithm with line search is applied for each load case [3].

Materials that are expected to undergo plastic deformation are taken into account by assuming a perfect elastic-plastic behaviour with a yield threshold stress σ_y referring to the Von Mises yield criterion.

3. RESULTS & DISCUSSION

Three different cases of contact pairs were calculated and are presented in this section. The topographies of the surfaces in contact originate from real samples tested on a pin-on-disc test-rig. Areal topographies corresponding to the pin surface were measured by means of focus variation microscopy equipment [4]. Line profiles corresponding to the radial direction of disc surface were extracted using a stylus profilometer. The areal topography of the turned disc surface was assumed to be approximately axisymmetric and could be reconstructed from the line profile and the radius of the testing track on the disc.

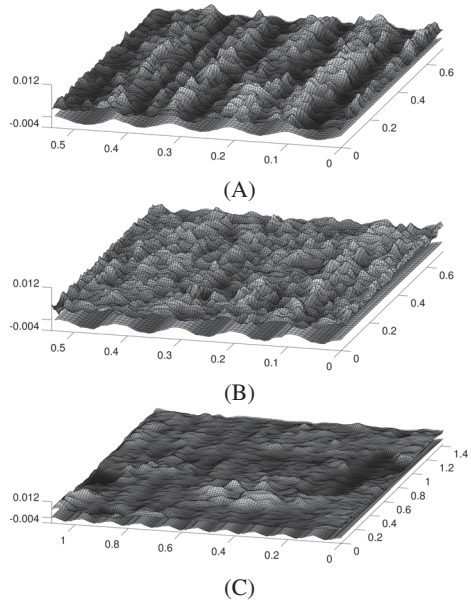

Figure 2. Pin and disc topographies for the three calculated examples

Figure 2 shows the three pin topographies on top of the corresponding disc topographies used in the calculations. All disc topographies have a

sinus-like form with small differences in each case whereas the pin surfaces vary depending on the pin material. Table 1 contains the most important roughness parameters for the surfaces shown in Figure 2.

Table 1. Roughness parameters for the surfaces used in the calculations

Case	Surface	R_a	R_q	R_{sk}	R_{ku}
		10^{-3} mm		-	
A	Pin	1.18	1.47	-0.62	3.01
B	Pin	0.99	1.24	0.01	3.08
C	Pin	1.08	1.50	-0.25	4.98
A	Disc	0.74	0.84	0.13	1.75
B	Disc	0.88	0.99	-0.02	1.68
C	Disc	0.92	1.09	-0.03	4.86

The disc material in all three cases is assumed to be steel with Young's Modulus and Poisson's ratio equal to 210000 MPa and 0.3 respectively. The materials corresponding to the three pin surfaces presented in Figure 2 are polyethylene terephthalate (PET), polyamide 6 (PA 6) and friction paper for the cases A, B and C respectively. The elasticity pparameters of the three pin materials are summarized in Table 2.

Table 2. Elasticity parameters for the pin materials used in the calculations

Case	Pin Material	E	ν	σ_y
		[MPa]	[-]	[MPa]
A	PET	3000	0.43	90
B	PA 6	1600	0.44	50
C	Friction paper	7260	0.27	-

The dimensions of the discretized surface samples are 0.715 times 0.54 mm for the first two examples and 1.43 times 1.08 mm for the third one. The first and the second dimensions refer to the tangential and the radial disc directions respectively. In all cases, the element size of the disc contact surface is 0.015 times 0.008 mm. For the pin contact surfaces the elements are square with a size of 0.0044 mm in the first two examples and 0.0088 mm in the third one.

For each contact pair a series of load cases corresponding to nominal pressures from 3 to 24 MPa, increasing in steps of 3 MPa were calculated consecutively. For the cases A and B, that involve plastic deformation, the same load steps were repeated in descending order.

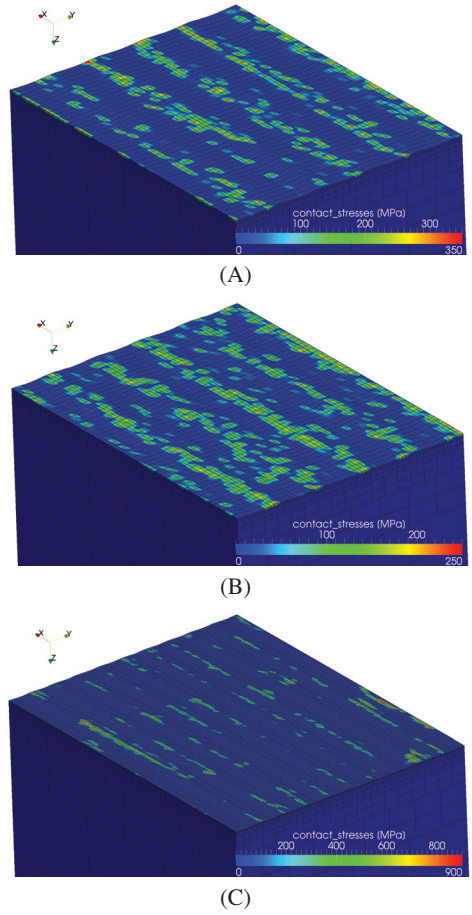

Figure 3. Contact stress on the disc surface for the three calculated cases at 24 MPa

Figure 3 shows the contact stress distribution on the disc surfaces for the three calculated examples at the maximum nominal pressure. The real contact area is distinguished by the presence of nonzero contact stress. Figure 4 illustrates the evolution of the ratio between the real contact area and the apparent contact area during the variation of the nominal pressure. The lower and the upper

branches of the curves for cases A and B correspond to the loading and unloading phases respectively.

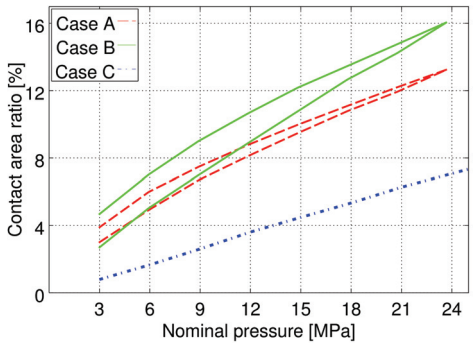

Figure 4. Relation between the nominal pressure and the real contact area ratio for the three calculated cases

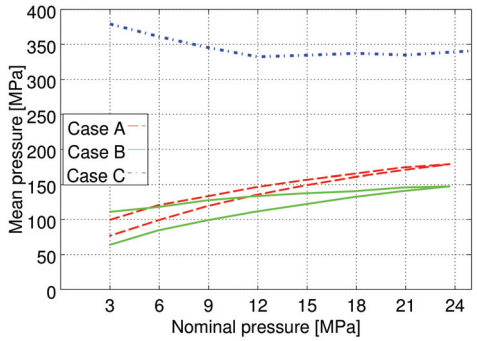

Figure 5. Relation between the nominal pressure and the mean contact pressure for the three calculated cases

Figure 5 shows the evolution of the mean contact pressure within the real contact area for varying nominal pressure. For cases A and B the upper and the lower curve branches correspond to the loading and unloading phases respectively.

From the graphs presented in Figures 4 and 5 it becomes obvious that there is both a quantitative and a qualitative difference between case C and cases A and B. With respect to these two cases, case C exhibits a significantly lower real contact area and correspondingly higher mean contact pressure. Moreover, the evolution of the mean contact pressure in case C is qualitatively different with respect to the other two cases. For increasing nominal pressure, in case C the mean contact pressure remains approximately constant while in cases A and B it raises steadily.

The differences between cases A and B are smaller. The pin material of case B has lower Young's modulus and yield stress resulting to a higher contact area and more extensive permanent deformations respectively. The plastic deformation of the pin material is reflected in the difference between the ascending and the descending load branches of the curves in Figure 4.

4. CONCLUSIONS

The case study presented in this paper demonstrates how a finite-element micro-contact model can be used for estimating the effective area of contact in real life applications. The contact between three different materials and a steel surface under nominal pressures varying from 3 to 24 MPa was studied. The softest material (PA 6, case B) exhibited a contact area ratio of 16 % under 24 MPa, while the next stiffer material (PET, case A) and the stiffest one (friction paper, case C) exhibited contact area ratios around 13 % and 7 % respectively.

The observed behaviour of case A (PET) and case B (PA 6) was expressed through similar curves with small quantitative differences mainly due to the different material properties. With respect to case C, a comparison of the calculated mean contact pressures reveals that the impact of the nominal pressure on the real contact area is qualitatively different than in the first two cases.

None of the observed differences could be attributed exclusively to the material properties because different surface topographies were involved in the three calculations. In the future, an extended study with the same materials but with a common surface topography could help in separating the impact of the material properties from the impact of the surface topographies.

References

[1] F. P. Bowden and D. Tabor. The area of contact between stationary and between moving surfaces. *Proceedings of the Royal Society of London. Series A. Mathematical and Physical Sciences*, 169(938):391–413, 1939.

[2] J. A. Greenwood and J. B. P. Williamson. Contact of nominally flat surfaces. *Proceedings of the Royal Society*, 295:300–319, 1966.

[3] P. Alart and A. Curnier. A mixed formulation for frictional contact problems prone to newton like solution methods. *Computer Methods in Applied Mechanics and Engineering*, 92(3):353 – 375, 1991.

[4] R. Danzl, F. Helmli, and S. Scherer. Focus variation - a robust technology for high resolution optical 3d surface metrology. *Strojniški vestnik - Journal of Mechanical Engineering*, 57(3), 2011.

Appendix B

Input data for the parametric yaw system model

Tables B.1 and B.2 summarize all mandatory and optionally input parameters for the parametric finite-element model of the wind turbine yaw system. The dimensions referring to the tower, transition and flange are self-explanatory and the dimensions of the segment refer to Figure 2.4. If the parameter SEGMENT_LENGTH2 is not given it is replaced by SEGMENT_LENGTH and the optional parameter SEGMENT_OPENING is set equal to FLANGE_THICKNESS if omitted. Otherwise the yaw system will include clearance, if the segment opening is given a value higher than the flange thickness or pretension if the segment opening is smaller. The optional parameter SEGMENT_DIAMETER is treated in a similar way with respect to the flange inner diameter.

The elasticity parameters E and NU are considered by default as common among all system components. Alternatively, the Young's modulus of the nacelle can be specified independently through the optional parameter E_NACELLE.

The supported formats for the nacelle mesh file include the GMSH "*.msh" format and the ANSYS "*.cdb" format. The software that can be used for generating the nacelle mesh file from a CAD STEP file include among others, ANSYS, NETGEN and GMSH. In order to orient the nacelle correctly with respect to the tower, the vertical upward direction and the downwind direction should be given in terms of

the coordinate system axes of the nacelle mesh file. Valid inputs for these directions are the expressions: "X", "-X", "Y", "-Y", "Z" and "-Z".

Table B.1: Mandatory input parameters for the yaw drive unit model

E	N/mm^2	Young's Modulus
NU	-	Poisson's ratio
TOWER_DIAMETER	mm	Tower outer diameter
TOWER_THICKNESS	mm	Tower thickness
TOWER_HEIGHT	mm	Tower height
TRANSITION_DIAMETER	mm	Transition outer diameter
TRANSITION_THICKNESS	mm	Transition thickness
TRANSITION_HEIGHT	mm	Transition height
FLANGE_DIAMETER	mm	Flange outer diameter
FLANGE_WIDTH	mm	Flange width (radial)
FLANGE_THICKNESS	mm	Flange thickness (vertical)
SEGMENT_LENGTH	mm	Segment length (circumferential)
SEGMENT_BODY_THICKNESS	mm	Segment body thickness (radial)
UPPER_SEGMENT_PLATE_WIDTH	mm	Upper segment plate width
UPPER_SEGMENT_PLATE_THICKNESS	mm	Upper segment plate thickness
LOWER_SEGMENT_PLATE_WIDTH	mm	Lower segment plate width
LOWER_SEGMENT_PLATE_THICKNESS	mm	Lower segment plate thickness
SEGMENT_LOCATIONS	$\circ$	Array of circumferential locations of the segments
THRUST_FORCE	N	Thrust force (Fx)
LATERAL_FORCE	N	Lateral force (Fy)
VERTICAL_FORCE	N	Vertical force (Fz)
ROLL_MOMENT	$N.mm$	Roll moment (Mx)
TILT_MOMENT	$N.mm$	Tilt moment (My)
YAW_MOMENT	$N.mm$	Yaw moment (Mz)
NACELLE_MESH_FILE	-	Mesh file for the nacelle
NACELLE_CS_VERTICAL_AXIS	-	Vertical (upwards) axis in the nacelle mesh coordinates system
NACELLE_CS_DOWNWIND_AXIS	-	Downwind axis in the nacelle mesh coordinates system
NACELLE_UNITS_SCALE	-	Scaling factor for converting nacelle mesh dimensions into mm

The model is available in form of a standalone executable file but it can also be executed through an appropriate Matlab/Octave script. This script generates

Table B.2: Optional input parameters for the yaw drive unit model

SEGMENT_LENGTH2	mm	Minimum length of the segment on its back side
SEGMENT_DIAMETER	mm	Dimension corresponding to the flange inner diameter
SEGMENT_OPENING	mm	Dimension corresponding to the flange thickness
NACELLE_WEIGHT	N	Weight of the nacelle and its contents
NACELLE_WEIGHT_LOCATION	mm	Gravity center of the nacelle weight (positive downwind)
ELEMENTS_TOWER_CIRCUMFERENTIAL ELEMENTS_TOWER_THICKNESS ELEMENTS_TOWER_HEIGHT ELEMENTS_TRANSITION_CIRCUMFERENTIAL ELEMENTS_TRANSITION_THICKNESS ELEMENTS_TRANSITION_HEIGHT ELEMENTS_FLANGE_CIRCUMFERENTIAL ELEMENTS_FLANGE_WIDTH ELEMENTS_FLANGE_THICKNESS ELEMENTS_SEGMENT_LENGTH ELEMENTS_SEGMENT_BODY ELEMENTS_SEGMENT_OPENING ELEMENTS_UPPER_SEGMENT_PLATE_WIDTH ELEMENTS_UPPER_SEGMENT_PLATE_THICKNESS ELEMENTS_LOWER_SEGMENT_PLATE_WIDTH ELEMENTS_LOWER_SEGMENT_PLATE_THICKNESS		Number of elements
OUTPUT_DIRECTORY		Directory for output files

graphs with the calculated load distribution across the segments and provides some additional input possibilities for the parameter SEGMENT_LOCATIONS that are listed in the appendix table B.3 and facilitates the calculation of optimization case studies. The last four possibilities in this table are based on the input of three numbers, N_F, N_L and N_B, corresponding to the segments at the front, lateral and back sides within an angle of 90° in each case. The total number of segments will be: $N_F + 2 \cdot N_F + N_B$.

Table B.3 lists additional input possibilities with respect to the position and the number of the yaw system segments.

Table B.3: Additional input possibilities for the yaw drive unit model, when it is invoked through Matlab/Octave

SEGMENT_LOCATIONS	-	Number of evenly distributed segments (with the first one in the downwind direction)
SEGMENT_LOCATIONS	{-,-,-}	Number of evenly distributed segments in the front, lateral and back quadrants
SEGMENT_LOCATIONS	{-,-,-,'optim1'}	Similar to the second one with variation of the total number of segments
SEGMENT_LOCATIONS	{-,-,-,'optim2'}	Similar to the second one with variation of the segments distribution
SEGMENT_LOCATIONS	{-,-,- ; -,-,- ; ...}	Similar to the second one with multiple user defined cases

Bibliography

[1] D. Chan and G. W. Stachowiak, "Review of automotive brake friction materials," *Proceedings of the Institution of Mechanical Engineers, Part D: Journal of Automobile Engineering*, vol. 218, pp. 953–966, 2004.

[2] P. Blau, "Compositions, functions, and testing of friction brake materials and their additives," tech. rep., ORNL, 2001.

[3] M. Eriksson and S. Jacobson, "Tribological surfaces of organic brake pads," *Tribology International*, vol. 33, pp. 817–827, 2000.

[4] W. Österle, H. Kloß, I. Urban, and A. Dmitriev, "Towards a better understanding of brake friction materials," *Wear*, vol. 263, pp. 1189–1201, 2007.

[5] R. Mäki, *Wet Clutch Tribology - Friction Characteristics in Limited Slip Differentials*. PhD thesis, Luleå University of Technology, Department of Applied Physics and Mechanical Engineering, Division of Machine Elements, 2005.

[6] W. Bartz, *Selbstschmierende und wartungsfreie Gleitlager: Typen, Eigenschaften, Einsatzgrenzen und Anwendungen ; mit 144 Literaturstellen*. Kontakt & Studium: Tribologie, Expert-Verlag GmbH, 1993.

[7] Z. Lawrowski, "Polymers in the construction of serviceless sliding bearings," *Archives of Civil and Mechanical Engineering*, vol. 7, no. 4, pp. 139–150, 2007.

[8] G. Stachowiak and A. Batchelor, *Experimental Methods in Tribology*. Tribology and Interface Engineering, Elsevier Science, 2004.

[9] R. Bayer, *Mechanical Wear Fundamentals and Testing, Revised and Expanded*. Dekker Mechanical Engineering, Taylor & Francis, 2004.

[10] H. Czichos, K. Habig, J. Celis, R. Cowan, A. Fischer, K. Gerschwiler, T. Gradt, E. Kleinlein, F. Klocke, G. Knoll, *et al.*, *Tribologie-Handbuch: Tribometrie, Tribomaterialien, Tribotechnik*. Vieweg+Teubner Verlag, 2010.

[11] M. Neale and M. Gee, *Guide to wear problems and testing for industry*. William Andrew Pub, 2001.

[12] E. R. Booser, S. of Tribologists, and L. Engineers., *Tribology data handbook*. CRC Press, 1997.

[13] J. Anderson, "Wear of commercially available plastic materials," *Tribology International*, vol. 15, no. 5, pp. 255–263, 1982.

[14] P. J. Blau and A. S. for Metals International. Handbook Committee., *ASM handbook*. 1992.

[15] Z. Zalisz, P. H. Vroegop, and R. Bosma, "A running-in model for the reciprocating sliding of nylon 6.6 against stainless steel," *Wear*, vol. 121, pp. 71–93, 1988.

[16] J. Byett and C. Allen, "Dry sliding wear behaviour of polyamide 66 and polycarbonate composites," *Tribology International*, vol. 25, no. 4, pp. 237–246, 1992.

[17] A. Golchin, G. F. Simmons, and S. B. Glavatskih, "Break-away friction of ptfe materials in lubricated conditions," *TRIBOLOGY INTERNATIONAL*, vol. 48, pp. 54–62, 2012.

[18] F. P. Bowden and D. Tabor, "The area of contact between stationary and between moving surfaces," *Proceedings of the Royal Society of London. Series A. Mathematical and Physical Sciences*, vol. 169, no. 938, pp. 391–413, 1939.

[19] J. F. Archard, "Elastic deformation and the laws of friction," *Proceedings of the Royal Society of London. Series A. Mathematical and Physical Sciences*, vol. 243, no. 1233, pp. 190–205, 1957.

[20] J. A. Greenwood and J. B. P. Williamson, "Contact of nominally flat surfaces," *Proceedings of the Royal Society*, vol. 295, pp. 300–319, 1966.

[21] B. Bhushan, *Modern Tribology Handbook*. The mechanics and materials science series, CRC Press, 2001.

[22] G. W. Stachowiak and A. W. Batchelor, *Engineering tribology*. Elsevier Butterworth-Heinemann, 3rd ed. ed., 2005. Includes bibliographical references and index.

[23] Zmitrowicz, "Wear patterns and laws of wear-a review," *Journal of Theoretical and Applied Mechanics*, vol. 44, no. 2, pp. 219–253, 2006.

[24] Majumdar and Bhushan, "Fractal model of elastic-plastic contact between rough surfaces," *Transactions of the ASME. Journal of Tribology*, vol. 113, no. 1, pp. 1–11, 1991.

[25] B. Persson, "Elastoplastic contact between randomly rough surfaces," *Physical Review Letters*, vol. 87, no. 11, pp. 116101/1–116101/4, 2001.

[26] Stanley and Kato, "An fft-based method for rough surface contact," *Transactions of the ASME. Journal of Tribology*, vol. 119, no. 3, pp. 481–485, 1997.

[27] Sellgren, Bjorklund, and Andersson, "A finite element-based model of normal contact between rough surfaces," *Wear*, vol. 255, no. 11, pp. 1180–1188, 2003.

[28] L. Pei, S. Hyun, J. Molinari, and M. O. Robbins, "Finite element modeling of elasto-plastic contact between rough surfaces," *Journal of the Mechanics and Physics of Solids*, vol. 53, no. 11, pp. 2385–2409, 2005.

[29] V. A. Yastrebov, J. Durand, H. Proudhon, and G. Cailletaud, "Rough surface contact analysis by means of the finite element method and of a new reduced model," *Comptes Rendus Mecanique*, vol. 339, no. 8-8, p. 473, 2011.

[30] M. Renouf, F. Massi, N. Fillot, and A. Saulot, "Numerical tribology of a dry contact," *Tribology International*, vol. 44, no. 7-8, pp. 834–844, 2011.

[31] "Iec 61400–1 ed.3. wind turbines - part 1: Design requirements," 2005.

[32] T. Burton, N. Jenkins, D. Sharpe, and E. Bossanyi, *Wind Energy Handbook*. Wiley, 2011.

[33] U.S. Government, *Wind Turbine Design Guideline Dg03: Yaw and Pitch Rolling Bearing Life*. General Books, 2009.

[34] R. van Rooij, "Terminology, reference systems and conventions." In the project: Design Methods for Offshore Wind Turbines at Exposed Sites, October 2001.

[35] K. C. Park, C. A. Felippa, and G. Rebel, "A simple algorithm for localized construction of non-matching structural interfaces," *International Journal for Numerical Methods in Engineering*, vol. 53, no. 9, pp. 2117–2142, 2002.

[36] "En 100083-3: Steels for quenching and tempering - part 3: Technical delivery conditions for alloy steels," 2006.

[37] "En 1337-2: Structural bearings - part 2: Sliding elements," 2004.

[38] M. G. Jacko, P. H. S. Tsang, and S. K. Rhee, "Automotive friction materials evolution during the past decade," *Wear*, vol. 100, pp. 503–515, 1984.

[39] P. K. Mallick, *Fiber-reinforced composites: materials, manufacturing, and design*. CRC Press, 3rd ed. ed., 2008. Series: Dekker mechanical engineering.

[40] D. Krevelen and K. Te Nijenhuis, *Properties of Polymers: Their Correlation With Chemical Structure; Their Numerical Estimation and Prediction from Additive Group Contributions*. Elsevier, 2009.

[41] J. Margolis, *Engineering plastics handbook*. McGraw-Hill handbooks, McGraw-Hill, 2006.

[42] "Material property data, online database." `http://www.matweb.com/`. Last accessed 2013.

[43] "Designer data, online database." `http://www.designerdata.nl/index.php?lang=en`. Last accessed 2013.

[44] W. F. Gale and T. C. Totemeier, eds., *Smithells Metals Reference Book*. Elsevier, 8th ed., 2004.

[45] R. M. Mortier, M. F. Fox, and S. T. Orszulik, *Chemistry and Technology of Lubricants*. Springer, 3rd ed., 2010.

[46] M. D. Jacobsen and C. K. Christiansen, "Udvikling af pin-on-disk testmaskine," bachelor thesis, DTU, 2010.

[47] Y.-K. Cho, L. Cai, and S. Granick, "Molecular tribology of lubricants and additives," *Tribology International*, vol. 30, no. 12, pp. 889–894, 1997.

[48] ASTM International, "G99-05 standard test method for wear testing with a pin-on-disk apparatus," 2010.

[49] ASTM International, "G133-05 standard test method for linearly reciprocating ball-on-flat sliding wear," 2010.

[50] F. Chen, C. A. Tan, and R. L. Quaglia, *Disc Brake Squeal: Mechanism, Analysis, Evaluation, and Reduction/Prevention*. SAE International (Publishing), 2005.

[51] T. Thomas, "The elastic contact of a rough surface," *Wear*, vol. 35, no. 1, pp. 87–111, 1975.

[52] M. Ciavarella, J. Greenwood, and M. Paggi, "Inclusion of "interaction" in the greenwood and williamson contact theory," *Wear*, vol. 265, no. 5-6, pp. 729–734, 2008.

[53] M. Paggi and M. Ciavarella, "The coefficient of proportionality between real contact area and load, with new asperity models," *Wear*, vol. 268, no. 8-8, p. 1020, 2010.

[54] P. J. Blau, *Friction science and technology : from concepts to applications*. CRC Press, 2nd ed. ed., 2009.

[55] G. He, M. Muser, and M. Robbins, "Adsorbed layers and the origin of static friction," *Science (New York, N.Y.)*, vol. 284, no. 5420, pp. 1650–1652, 1999.

[56] T. Wanheim and N. Bay, *Friction and Tools*, vol. Chapter 6, pp. 199–226. 1986.

[57] J. R. Barber, "Multiscale surfaces and amontons' law of friction," *Tribology Letters*, vol. 49, no. 3, pp. 539–543, 2013.

[58] Archard and Hirst, "The wear of metals under unlubricated conditions," *Proceedings of the Royal Society of London, Series A. Mathematical and Physical Sciences*, vol. 236, no. 1206, pp. 397–410, 1956.

[59] P. Wriggers, *Computational Contact Mechanics*. Springer, 2006.

[60] P. Alart and A. Curnier, "A mixed formulation for frictional contact problems prone to newton like solution methods," *Computer Methods in Applied Mechanics and Engineering*, vol. 92, no. 3, pp. 353–375, 1991.

[61] Y. Renard, "Generalized newton's methods for the approximation and resolution of frictional contact problems in elasticity," *Computer Methods in Applied Mechanics and Engineering*, vol. 256, no. 0, pp. 38 – 55, 2013.

[62] B. Herry, L. Di Valentin, and A. Combescure, "An approach to the connection between subdomains with non-matching meshes for transient mechanical analysis," *International Journal for Numerical Methods in Engineering*, vol. 55, no. 8, pp. 973–1003, 2002.

[63] A. Anandarajah, *Computational methods in elasticity and plasticity : solids and porous media*. Springer, 2010.

[64] P. R. Amestoy, I. S. Duff, J. Koster, and J.-Y. L'Excellent, "A fully asynchronous multifrontal solver using distributed dynamic scheduling," *SIAM Journal on Matrix Analysis and Applications*, vol. 23, no. 1, pp. 15–41, 2001.

[65] P. R. Amestoy, A. Guermouche, J.-Y. L'Excellent, and S. Pralet, "Hybrid scheduling for the parallel solution of linear systems," *Parallel Computing*, vol. 32, no. 2, pp. 136–156, 2006.

DTU Mechanical Engineering
Section of Solid Mechanics
Technical University of Denmark

Nils Koppels Allé, Bld. 404
DK- 2800 Kgs. Lyngby
Denmark
Phone (+45) 4525 4250
Fax (+45) 4593 1475
www.mek.dtu.dk
ISBN: 978-87-7475-367-4

DCAMM
Danish Center for Applied Mathematics and Mechanics

Nils Koppels Allé, Bld. 404
DK-2800 Kgs. Lyngby
Denmark
Phone (+45) 4525 4250
Fax (+45) 4593 1475
www.dcamm.dk
ISSN: 0903-1685